Andreas Steinegger, MSc

New Indicators for Optical Sensing by Manipulating the Intersystem Crossing in Luminescent Dyes

DOCTORAL THESIS

to achieve the university degree of

Doktor der technischen Wissenschaften

submitted to

Graz University of Technology

Supervisor

Assoc. Prof. kand. Sergey Borisov

Institut für Analytische Chemie und Lebensmittelchemie

Graz, October 2020

"It's a dangerous business beginning a PhD. You step into the lab, and if you don't keep your ideas, there's no telling where you might be swept off to."

freely adapted from Bilbo Baggins

AFFIDAVIT

I declare that I have authored this thesis independently, that I have not used other than the declared sources/resources, and that I have explicitly indicated all material which has been quoted either literally or by content from the sources used. The text document uploaded to TUGRAZonline is identical to the present master's thesis.

EIDESSTATTLICHE ERKLÄRUNG

Ich erkläre an Eides statt, dass ich die vorliegende Arbeit selbstständig verfasst, andere als die angegebenen Quellen/Hilfsmittel nicht benutzt, und die den benutzten Quellen wörtlich und inhaltlich entnommenen Stellen als solche kenntlich gemacht habe. Das in TUGRAZonline hochgeladene Textdokument ist mit der vorliegenden Dissertation identisch.

_____   _____
        Datum/Date   Unterschrift/Signature

Abstract

This thesis presents new indicators and sensor materials for optical luminescent sensing. It is mainly focused on temperature indicators and cyclometalation as a method to control the photophysical properties of indicator dyes. The temperature indicators are based on thermally activated delayed fluorescence (TADF) emitters. A design is presented to eliminate oxygen-cross talk from temperature sensing materials based on indicators with long luminescent decay times. An advanced data processing method enables dual sensing of oxygen and temperature with a single indicator using only single-wavelength readout. The results of this thesis are presented in chapters 3 to 6 that have been published as full papers in peer reviewed journals and in chapter 7.

The first chapter about TADF emitters presents two dye classes and their performance when applied in optical sensors for oxygen and temperature. The new sensing materials do not offer any improvement with regard to optical oxygen sensing. In contrast, the high temperature sensitivity of their TADF decay times is particularly advantageous for optical thermometry. Immobilized into a nearly oxygen impermeable poly(vinylidene chloride-co-acrylonitrile) matrix, they display excellent temperature sensitivity of 1.4 to 3.7% K^{-1} change of TADF decay time at 298 K. In form of indicator-loaded cell penetrating nanoparticles, the materials allow temperature imaging and feature sensitivities from 2.2 to 2.8% K^{-1} change of TADF lifetime at 298 K. This chapter demonstrates the high potential of TADF emitters for optical luminescent temperature sensing and imaging.

In chapter 4, Zn(II) Schiff base complexes are presented as a new class of TADF emitters. They possess excellent brightness and high temperature sensitivity of the TADF decay time with a change of 4.1%/K at 298 K. Respective sensing materials enable temperature sensing with a resolution better than 0.03 °C. Notorious oxygen cross-sensitivity is eliminated by a new sensor design based on an off-stoichiometry thiol-ene polymer layer as an oxygen-consuming layer covering the sensing layer. These layers are then coated with a poly(vinylidene chloride-co-acrylonitrile) layer as an additional oxygen barrier. The material shows no influence of oxygen after more than 2 months of storage at ambient air, which proves suitability fo long-term temperature monitoring.

In chapter 5, an alkylsulfone-substituted Zn(II)-$meso$-tetraphenyltetrabenzoporphyrin is presented as an indicator for simultaneous measurement of oxygen and temperature at a single wavelength. The benzoporphyrin emits prompt and thermally activated delayed fluorescence. TADF is differently affected by oxygen and temperature. During measurement, it is referenced

against prompt fluorescence (PF) that acts as the virtually inert reference signal. The information on both parameters is accessed via multifrequency phase fluorometry and sophisticated data processing. After measurement and data processing, the decay time of TADF and the ratio of TADF and PF are extracted and used to calculate oxygen concentration and temperature. Planar optodes, made from poly(styrene-*co*-acrylonitrile) and the benzoporphyrin, enable temperature-compensated trace oxygen sensing in the oxygen concentration range 0.002 - 6 hPa pO$_2$ at ambient conditions. The presented system offers a significantly simplified experimental setup and eliminates effects of different leaching or photobleaching rates compared to systems using two indicators for dual sensing.

Chapter 6 describes the investigation of cyclometalation as a method to control the photophysical properties of phosphorescent metallo(benzo)porphyrins. Motifs for cyclometalation with Pt(II) were integrated into three Pd(II) porphyrin complexes. The integration of 2-phenylpyridyl in the *meso*-position only affects the luminescence decay time (about 2-fold decrease) in solution. In contrast, decay time remains unchanged for the dyes in frozen glass at 77K or immobilized into a rigid polymeric matrix. Cyclometalation based on a 2-pyridyl unit in *meso*-position with C-H activation of β-H of the porphyrin results in about 100 nm large bathochromic shift of absorption and emission spectra. Additionally, the phosphorescence decay time drastically decreases (about 20-fold). Unfortunately, also the phosphorescence quantum yield decreases significantly. For this structure, cyclometalation, however, is accompanied by an increase of singlet oxygen quantum yield to 85%. This makes the new dye a powerful red-light excitable ^{1}O$_2$ photosensitizer.

The short chapter 7 presents the photophysical properties of two cyclometalated 1,8-naphthalimide structures. The naphthalimides were modified with motifs for cyclometalation in 4-position and in imide position. Cyclometalation in 4-position generated room temperature phosphorescence. The cyclometalation in imide position only reduced the quantum yield. The tedious and difficult purification of the dyes, however, suggested not to further investigate cyclometalation of 1,8-naphthalimide or closely related rylene dyes.

Kurzfassung

Im Zuge dieser Arbeit wurden im Bereich der optischen Sensorik neue lumineszierende Indikatoren und Sensormaterialien hergestellt. Die neuen Indikatoren basieren auf Farbstoffen die thermisch aktivierte verzögerte Fluoreszenz (TADF) emittieren und der Cyclometallierung von bekannten Farbstoffen. Cyclometallierung wurde als Methode zur Anpassung der photophysikalischen Eigenschaften von Indikatoren untersucht. Im Rahmen der Entwicklung neuer Temperatursensoren wurde ein Konzept entwickelt um die oft vorhandene Sauerstoffquerempfindlichkeit von lumineszierenden Temperaturindikatoren mit langen Lumineszenzabklingzeiten zu eliminieren. Zur simultanen Messung der Sauerstoffkonzentration und der Temperatur wurde ein neuer Indikator entwickelt. Dieser ermöglicht ein Messsetup mit minimaler Komplexität. Unter Verwendung komplexer Auswerteverfahren reicht es eine Emissionswellenlänge zu detektieren. Die Ergebnisse dieser Arbeit wurden in mehreren Publikationen nach Begutachtung von externen Experten veröffentlicht und stellen die Kapitel 3 bis 7 dar.

Im 3. Kapitel wurde die Anwendbarkeit von zwei Klassen von TADF-Emittern in der optischen Sensorik untersucht. Die Farbstoffe wurden verwendet um Sensoren für die optische Messung der Sauerstoffkonzentration und der Temperatur herzustellen. Nach Charakterisierung der Sensormaterialien ergab sich, dass die Farbstoffe keine Verbesserung im Bereich der Sauerstoffsensorik darstellen. Im Gegensatz dazu überzeugen die Farbstoffe durch ihre hohe Temperaturempfindlichkeit der TADF Abklingzeit. Eingebaut in ein Polymer mit geringer Sauerstoffpermeabilität wiesen die Farbstoffe Werte für die Temperaturempfindlichkeit im Bereich von 1.4-3.7% K^{-1} Änderung der TADF Abklingzeit auf. Um die Anwendbarkeit für bildgebende Verfahren im Bereich der Medizin und Biologie zu demonstrieren wurden zellpenetrierende Nanopartikel mit den Farbstoffen markiert. Die Materialien wiesen Temperaturempfindlichkeiten im Bereich von 2.2 bis 2.8% K^{-1} Änderung der TADF Lebenszeit auf. In diesem Kapitel wird das hohe Potential der TADF Emitter in der optischen Sensorik präsentiert.

Kapitel 4 beschreibt Zn(II) Komplexe mit Schiffbasen als neue Klasse von TADF-Emittern. Die Farbstoffe überzeugen durch ihre hohe Helligkeit und ihre exzellente Temperaturempfindlichkeit der TADF Abklingzeit. Die daraus erzeugten Sensormaterialien weisen eine Temperaturempfindlichkeit von 4.1%/K Änderung der TADF Abklingzeit auf und überzeugen mit einer Auflösung von unter 0.03 °C. Die inhärente Sauerstoffquerempfindlichkeit wurde durch die Verwendung einer Sauerstoff verbrauchenden Schicht aus einem „off-stoichiometry thiol-ene"-Polymer eliminiert. Um die Langlebigkeit der Sauerstoff verbrauchenden Schicht zu erhöhen wurde zusätzlich

eine Polymerschicht mit geringer Sauerstoffpermeabilität aufgetragen. Das Sensormaterial zeigt auch nach 2 Monaten Lagerung an Luft keine Sauerstoffquerempfindlichkeit. Es bietet sich daher auch als Sensormaterial zur Langzeittemperaturmessung an.

In Kapitel 5 wird ein neues alkylsulfon substituiertes Zn(II) Tetraphenyltetrabenzoporphyrin als neuer Indikator für die temperaturkompensierte Spurensauerstoffmessung präsentiert. Der Indikator ermöglicht die simultane Messung der Sauerstoffkonzentration und der Temperatur unter Verwendung/Detektion nur einer Emissionswellenlänge. Die Messung wird ermöglicht durch die duale Emission von prompter und verzögerter Fluoreszenz. Die prompte Fluoreszenz ist weitestgehend inert und wird daher als Referenzsignal verwendet. Die verzögerte Fluoreszenz wird von Temperatur und Sauerstoff auf unterschiedliche Art und Weise beeinflusst. Unter Verwendung multifrequenter Phasenfluorimetrie ergeben sich aus ihr die Werte für Temperatur und Sauerstoff. Planare Optoden aus Poly(styrene-*co*-acrylonitril) und dem Indikator ermöglichen temperaturkompensierte Spurensauerstoffmessung im Bereich von 0.002 - 6 hPa pO$_2$ bei Raumtemperatur. Das präsentierte System überzeugt durch sein reduzierte Komplexität im Bezug auf den optischen Aufbau und seine verringerte Anfälligkeit gegenüber Photobleichung und Leaching.

In Kapitel 6 werden die Auswirkungen der Cyclometallierung auf die photophysikalischen Eigenschaften phosphoreszierender Metallo(benzo)porphyrine untersucht. Dafür wurden für Cyclometallierung geeignete Motive in *meso*-Position dreier Pd(II)(Benzo)porphyrine integriert. Cyclometallierung der 2-Phenylpyridine Einheiten hat in Lösung nur eine Verkürzung der Abklingzeiten zur Folge. Im Gegensatz dazu ändern sich die Abklingzeiten nicht, wenn die auf diese Weise cyclometallierten Porphyrine in einer rigiden Umgebung, bei 77 K in gefrorenen Glass oder immobilisiert in Polystyrol, sind. Cyclometallierung der 2-Pyridyl Einheit unter C-H Aktivierung des β-H am Porphyrin führen zu einer bathochromen Verschiebung der Absorptions- und Emissionspektren. Gleichzeitig wir die Phosphoreszenzabklingzeit um den Faktor 20 reduziert. Unglücklicherweise geht mit diesen Änderungen auch eine Reduktion der Phopshoreszenzquantenausbeute einher. Die Singulettsauerstoffquantenausbeute hingegen erhöht sich auf etwa 85 %. Daher ist dieser Farbstoff als interessanter rot-anregbarer ^{1}O$_2$ Photosensitizer zu sehen.

Das kurze Kapitel 7 präsentiert die Auswirkungen der Cyclometallierung auf die photophysikalischen Eigenschaften zweier 1,8-Naphthalimide. Die Strukturmotive zur Cyclometallierung wurden in zwei Positionen, Imidposition und 4-Position, eingefügt. Die Cyclometallierung in 4-Position generierte Phosphoreszenz, die auch bei Raumtemperatur besteht. Die Cyclometallierung in Imidposition hatte abgesehen von der Reduktion der Fluoreszenzquantenausbeute, keinen weiteren Effekt auf die photophysikalischen Eigenschaften. Die aufwändige und schwierige Aufreinigung der Farbstoffe schloss eine weitere Erforschung der Cyclometallierung von Naphthalimiden oder Rylenfarbstoffen aus.

Danksagung

...zum Selbstaussuchen. Es gibt viele Menschen, bei denen ich mich hier herzlichst bedanken möchte und andere die trotzdem erwähnt werden. Damit keiner traurig sein muss und sich jeder den Dank, den er verdient, aussuchen kann, gibt es jetzt einfach einen Danksagungslückentext. Am Ende stehen dann die Namen die vielleicht gemeint sind.

Danke, _____. Beste Freunde fürs Leben würde ich mal sagen und Schmusen kannst auch sehr gut. Du bist für mich das, was der Spritzer für Häupl ist. Ich bin dir echt dankbar, dass du mich schon so lang aushältst, so sehr unterstützt und mein Leben schöner machst. Ente!!!

Danke,_____, für deinen wertvollen Input und die unterhaltsamen persönlichen Gespräche. Du hast meine Arbeit immer sehr (un)genau verfolgt und unterstützt, ohne dich hätte ich nie so viel über J-Aggregate erfahren.

_____, ich bin dir sehr dankbar, für deine Fairness und deine Unterstützung in allen Bereichen. Du hast mich zu einem besseren Wissenschaftler (wenn ich mich das schimpfen darf) gemacht. Ich konnte, glaube ich, sehr viel von dir lernen.

_____, du hast mir gezeigt, dass manche Sachen gar nicht mal so gut sind und man trotzdem nicht den Mut verlieren sollte! Manchmal verliert man und manchmal gewinnen die Anderen.

Danke, _____! Das reicht vermutlich eh schon um zu wissen wer gemeint ist und mehr müsste ich auch nicht sagen. Ich möchte dir trotzdem danken, dass du immer so hilfsbereit warst und bist; für deine ruhige, unaufgeregte Herangehensweise an (meine) Probleme und deinen Humor. Du hast mir die Zeit am Institut so viel schöner und lustiger gemacht.

Danke, _____, du cooler Karpfen! Manchmal bist du zwar fünf Mal so anstrengend wie andere, aber schön, dass du hier bist.

_____, "du stinkst" habe ich dir früher öfter mal gesagt. Stimmt aber noch immer nicht. Es war eine sehr schöne Zeit mit dir im Büro und ich bin froh, dass wir noch immer Freunde sind. :)

Danke, _____ und _____, ihr seid echt wichtige Menschen in meinem Leben geworden. Wenn ich Probleme mit wuchernden Genitalwarzen hätte, euch könnte ich das erzählen und ihr würdet mich trotzdem noch unterstützen!

_____, du bist fürs ACFC das, was Käse für die vegetarische Ernährung ist. Ohne gehts auch, aber wer will das wirklich? Dein Wissen über Chemie, Verschwörungstheorien, Korruption, Fahrräder und die DSVGO beeindruckt mich immer wieder. Danke!

Contents

1 Scope and Outline

Optical luminescent sensing has become an integral part of analytical chemistry. It offers certain characteristics that are unmatched by other sensing methods. Yet, the selection of an analytical method needs to be evaluated on a case to case basis and is not always in favor of optical sensing. The features, however, that are universally attractive compared to most other methods are: the possibility of contactless sensing and imaging and the resolution down to the nanoscale.

Optical sensing as field of research has advanced far since its beginnings, but is still left with limitations and is overlooked in many possible areas of application. The concrete industry, for example, is a billion dollar business and issues such as corrosion are researched intensely. However, only recently, optical luminescent sensors found application in this area of research.

The general limitations for nearly all applications include issues related to: (a) stability (photo-, physical, chemical), (b) operational lifetime, (c) response time, (d) cross-sensitivity (especially to temperature), (e) calibration and (f) referencing. However, other limitations are specific to the physical or chemical parameter that is measured. These current limitations are addressed or can be overcome by new sensing concepts, new materials (polymers, indicators, additives, optoelectronic and microelectronic components) and new data processing methods. In this thesis, advances based on new materials, and application of a new data processing method for dual sensing are presented.

For advances, it is not always necessary to reinvent the wheel. By carefully looking at other areas of research, materials or concepts can be found that can improve "your" area of research. This was the case for the application of dyes as temperature indicators that were originally investigated as emitters for OLEDs (**chapter 3**). These dyes display thermally activated delayed fluorescence (TADF) that is used to increase the efficiency of OLEDs. This is accomplished by utilizing TADF as mechanism to "harvest" triplet excitons, which in 75 % are generated from electrical excitation. Since TADF relies on reverse intersystem crossing, it also displays temperature-dependent luminescence and consequentially can enable optical temperature sensing. Applicability of TADF emitters for time-resolved imaging has been proposed[1] and application of acridine yellow[2] and C_{70}-fullerenes[3–5] for optical temperature sensing has already been demonstrated. Consequentially, in chapter 3, dyes from OLED research were characterized for their performance as temperature indicators. However, not only the dyes, also the concepts for design of TADF molecules were to a large extent investigated by OLED researchers. These concepts were applied to Schiff bases and benzoporphyrins in chapter 4 and 5, respectively. In **chapter 4**, high resolution temperature sensing and an

approach to eliminate oxygen cross-sensitivity of indicators with long decay times are treated. **Chapter 5** presents a Zn(II) tetrabenzoporphyrin as an indicator that allows simultaneous measurement of oxygen and temperature at a single wavelength. This dual sensing required multifrequency phase fluorometry and sophisticated data processing and analysis. Also the concept for cyclometalation of indicator dyes was inspired by work that is not aimed towards optical sensing. Cyclometalation was reported to produce highly phosphorescent Pt(II) and Ir(III) complexes. Additionally, the introduction of further cyclometalated structures in these complexes resulted in red-shifted absorption and emission spectra and increased molar absorption coefficients. Also, their radiative rate constants and hence their quantum yields increased. In **chapters 6 and 7**, it is investigated if cyclometalation can modulate the photophysical properties of already luminescent indicator dyes. The intention was to obtain a tool that makes indicators with outstanding photophysical properties (molar absorption coefficient, quantum yield, stability) applicable to sensing of chemical species or physical parameters that require different decay times or spectral properties.
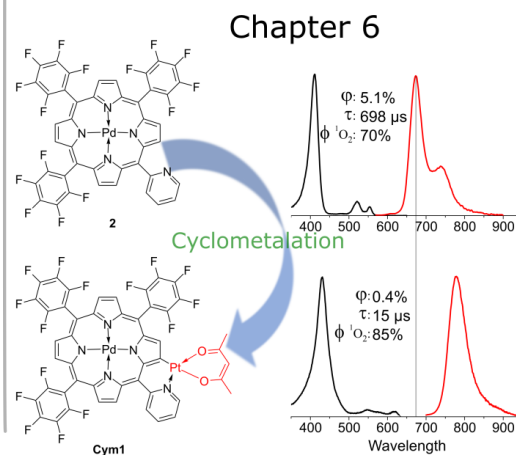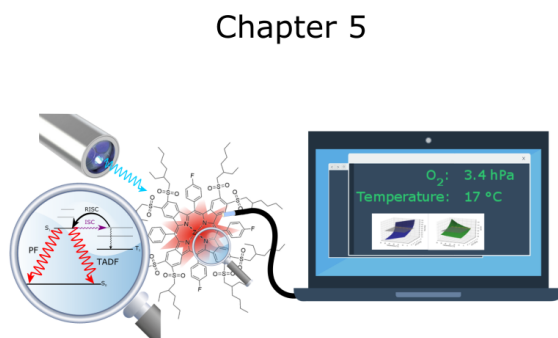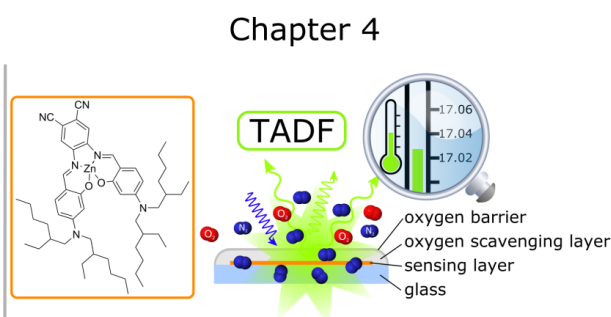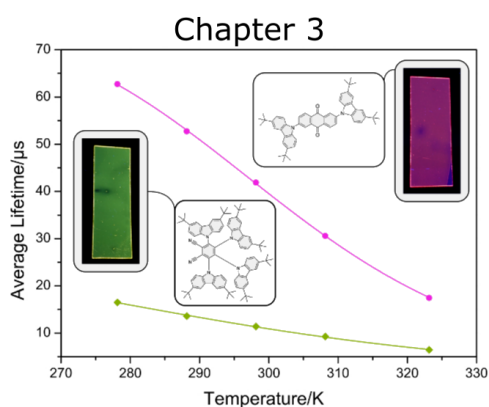
2 Theoretical Background

2.1 Optical Sensing based on Luminescence

Sensors are miniaturized devices that enable continuous monitoring of chemical or physical parameters. Optical sensors are based on the detection of photons to measure these parameters. The detection of photons can mean the measurement of the refractive index or of absorption, reflectance, intensity or decay time of photon emission. Optical sensors based on luminescence make use of materials that have luminescence properties sensitive to chemical or physical parameters. Among these materials are organic dye molecules, metal organic complexes, conjugated polymers, phosphors and nanomaterials. The analyte- or parameter sensitive part is called indicator or probe. In many cases, it can be necessary to incorporate the indicator in a host material. The combination of indicator and host material is called sensing material. For actual measurement, the sensing material is combined with a read-out device that illuminates the sensing material and detects photons. This in total is called sensor (Figure 2.1).
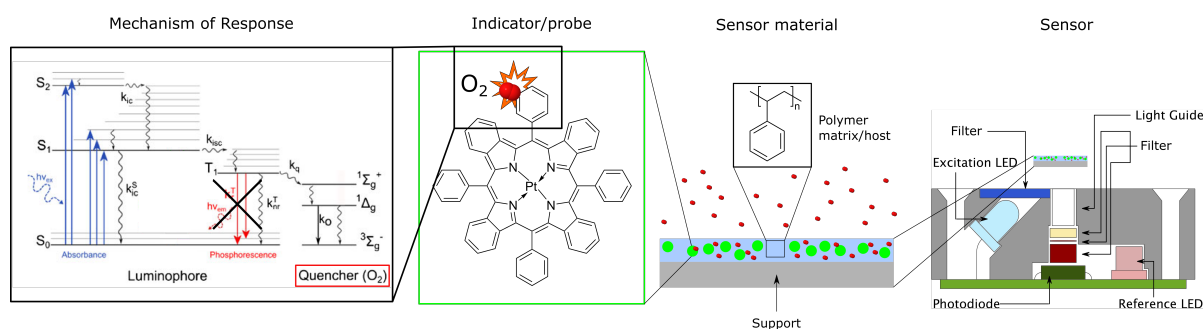
Figure 2.1: Illustration of the main components of a sensor. The Jablonski Diagramm was reprinted from ref.[6] with public license. The depicted sensor is adapted from ref.[7] with public licence.

The term sensor, however, is often ambiguously used for the sensor material or the indicator. Especially nanomaterials are often called nanosensors. Here, the distinction between sensing material and probe gets especially blurry considering genetically encoded fluorescent proteins or dendrimers.

The general advantages of optical sensors are that they are virtually free from electromagnetic disturbances, inexpensive, miniaturizable, non-invasive, allow contactless measurements, and are suitable for imaging of analyte distribution. The general disadvantages often include limited

operating lifetime/long-term stability, chemical and physical stability, interference with ambient light and that the sensors are often limited to certain applications due to their properties. Yet, their properties can be optimized for almost any desired application by proper choice of format, matrix, indicator chemistry and underlying physics. This, however, still requires intensive research and development.

In the following sections, the most important aspects of sensor materials based on luminescence are discussed.

2.2 Luminescence and Sensing

Photoluminescence is the emission of a photon after photoexcitation of a molecule. Photoexcitation means that the molecule absorbs a photon and is brought into an excited state. Here, several transition can happen that change the energetic state of the molecule. The involved transitions can be illustrated by the Perrin-Jablonski diagram (Figure 2.2). The singlet and triplet state derive from the multiplicity of the system or in other words the sum of electron spins plus one. Depending on the state of molecule, the luminescence emission is called either fluorescence or phosphorescence (c.f. Figure 2.2). The same holds true for more complex systems such as metal complexes with metal-to-ligand charge transfer. A representative absorption and emission spectrum of a benzoporphyrin is depicted in Figure 2.3.
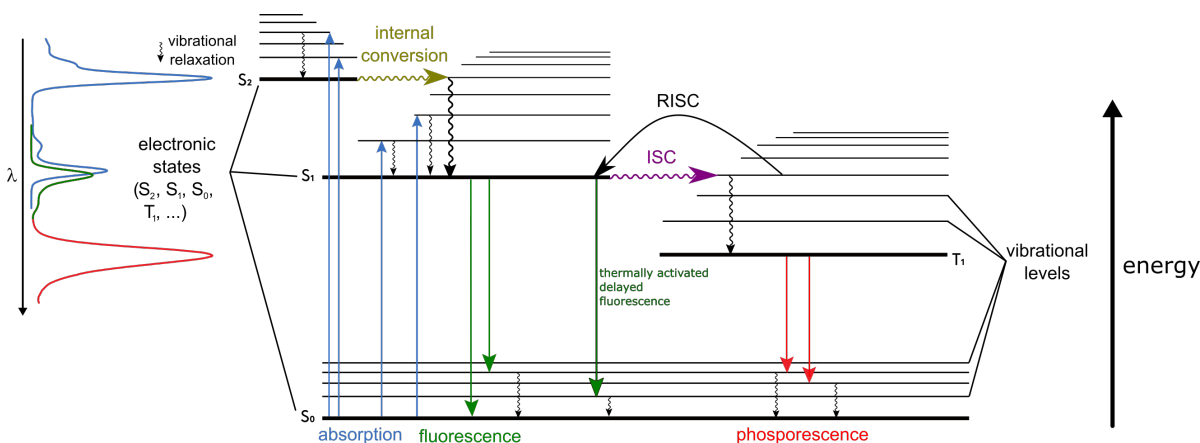
Figure 2.2: The Perrin-Jablonski diagram. It visualizes the involved transitions between the electronic and vibrational states of the molecule and as a result, the relative positions of the corresponding spectra. Here, they are illustrated by the absorption and emission spectra of a tetrabenzoporphyrin with (delayed) fluorescence and phosphorescence (left).

Both absorption and luminescence emission can be used for optical sensing if they change with a physical parameter or the concentration of an analyte. The change can be in wavelength, intensity, decay time or anisotropy. For some types of luminescence, the response is inherent, such as the phosphorescence of metalloporphyrins that is quenched by dioxygen (Figure 2.1). For others, the analyte sensitivity has to be introduced by a receptor part to the luminophore or by addition of a distinct analyte sensitive molecule or material. In the following subsections, the prerequisites and types of photophysical transitions and how they can be used for optical sensing are discussed.

2.2.1 Absorption

The absorption of a photon is a fast process. It takes around $1*10^{-15}$ s.[8] Absorption in the UV-vis region usually brings the molecule from the singlet ground state S_0 into the first S_1 or second S_2 excited singlet state (Figure 2.2) (c.f. the two bands in Figure 2.3). The
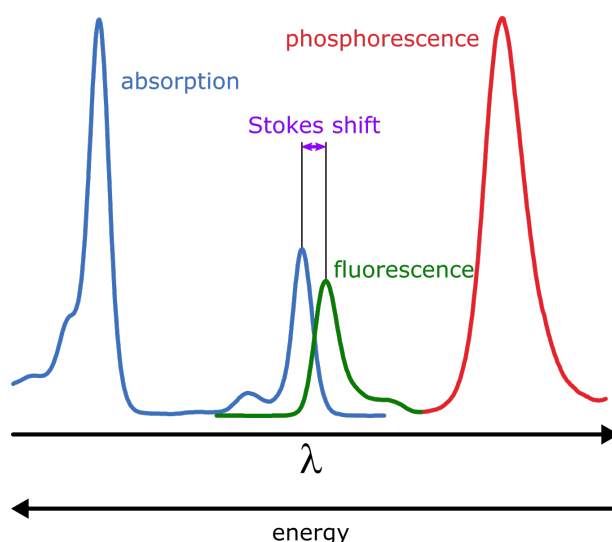
Figure 2.3: Representative absorption and emission spectrum of a tetrabenzoporphyrin with fluorescence and phosphorescence.

Franck-Condon principle states that this electronic excitation is much faster ($1*10^{-15}$ s) than molecular movements/vibrations ($1*10^{-10}$-$1*10^{-12}$ s).[8] The vibrational ground states of the two electronic states, however, have different molecular conformations. Therefore, the absorption produces a molecule not only electronically, but also vibrationally excited. Each of the electronically excited states has numerous vibrational sublevels. As a result, absorption bands are broad/broadened. They sharpen with decreasing temperatures due to the reduction of molecular vibrations. After excitation, there are various pathways to a final deexcitation. Molecules in excited states can undergo **internal conversion** with subsequent vibrational relaxation. Internal conversion is a horizontal transition (the energy stays the same) from a higher to a lower electronically excited state. As the electronic transition alone would reduce the energy, the molecule is transferred to a vibrationally highly excited state of the same energy. Then **vibrational relaxation** can occur that returns the molecule to the vibrational ground state of the same electronic state. Vibrational relaxation also happens directly after the excitation from S_0 to a vibrationally excited state of S_1. The energy gap between this state and the vibrational ground state of S_1 is the reason for the Stokes shift (Figure 2.3). Apart from the typical absorption, there is also the possibility for excited state absorptions, such as triplet-triplet transitions due to absorption. They are not commonly used in sensing.

Another type of absorption, two-photon-absorption, however, is of significant interest for research. Here, excitation is achieved by simultaneous absorption of two photons of the same energy. In other words, excitation can be done by using photons of half the energy/twice the wavelength. For measurement, this is an advantage compared to shorter wavelength excitation regarding scattering, absorption of biological tissues and photochemical damage. In contrast to standard absorption, the two-photon absorption increases with the square of the light intensity. This results in a better resolution for microscopy and other applications

such as microfabrication. Unfortunately, intense two-photon absorption is not that common in molecules and characterization is difficult with errors generally greater than 10 %.[9]

2.2.2 Fluorescence

For a molecule with a singlet ground state, emission from an excited singlet state is called fluorescence (Figure 2.2). More general, luminescence without a spin change during emission is called fluorescence. Prompt fluorescence describes emission after absorption and no involvement of the triplet state in the de-excitation pathway. For delayed fluorescence, the triplet state is involved and can be left by one of two pathways, via thermal activation or via triplet-triplet annihilation.

Prompt Fluorescence

The time it takes for absorption and emission to happen is relatively short. Typically absorption or emission of a photon takes around $1*10^{-15}$ s.[8] In between, the molecule stays in the excited singlet state typically in a range from $1*10^{-10}$ to $1*10^{-7}$s.[8] For a set of molecules, their stay in the excited state is described by an exponential decay function. A measure for this is the lifetime or decay time. It describes how long it takes for all but 1/e molecules to have returned to the ground state. For fluorescence, the lifetime of most fluorophores is in the single-digit nanosecond range. This is the time available for fluorescence to be bypassed by other transitions or reactions. This includes non-radiative deactivation by internal conversion, intersystem crossing, energy or electron transfer or quenching reactions from an external quencher or by a non-conjugated receptor part. In other words, rate constants for these reactions have to be in the same magnitude as the rate constant of fluorescence emission or greater to significantly affect it. The presence of other reactions that are similiarly fast reduces the decay time of fluorescence emission. This is due to the fact that with increasing time spent in the excited state the probability for the other reactions to happen increases. This effect can also be seen in equation 2.1, which demonstrates the dependence of the prompt fluorescence lifetime τ on the rate constants of transitions from S_1.

$$\tau = \frac{1}{k_r^s + k_{nr}^s + k_x^s} \tag{2.1}$$

k_r^s is the rate constant for radiative deactivation, here the emission of fluorescence. k_{nr}^s includes internal conversion and intersystem crossing. k_x represents any process that can/may occur while the molecule is in the excited state. This may be dynamic quenching, energy or electron transfer or any other process. The fluorescence can also change if an analyte sensitive group or receptor is part of the color-forming system. Analyte recognition then changes the color-forming system itself either by coordination or bond-formation, such as protonation. This can change both fluorescence and/or absorption, which as prerequisite to fluorescence also affects it.

As nearly every process, prompt fluorescence is temperature sensitive. According to Boltzmann, the temperature of the environment affects the distribution of the molecules over vibrational energy levels in the electronic ground state. An increased temperature broadens the spectrum. Additionally, increased temperature results in more thermal agitation. Thermal agitation includes collisions with solvent molecules, molecular vibrations, rotations, and etc.[8] All these processes promote non-radiative deactivation and consequentially decrease fluorescence. Often it is only to a minor extent so that sensing is not (heavily) affected. Yet, there are indicator dyes with prompt fluorescence that are sensitive enough for temperature measurement.[10] Apart from the decrease in fluorescence intensity, also the decay time shortens with increasing temperature as k_{nr}^s in eq. 2.1 increases with thermal agitation.

As typical oxygen indicators feature luminescent lifetimes of 6 μs and longer, prompt fluorescence is usually not utilized for O_2 sensing. However, there are some exceptions where prompt fluorescence is (effectively) quenched by oxygen. Osmium polypyridyl complexes have short decay times in the range of 5 - 15 ns[6] and polycyclic aromatic hydrocarbons have fluorescence decay times in the range of 100-450 ns.[6] Both indicator classes are quenched by oxygen. Even for short fluorescence lifetimes such as 5 ns from HPTS, influence of oxygen is visible and can be theoretically even used for dual sensing.[11] However, the influence is still small enough to be neglected for most applications.

Delayed Fluorescence

Thermally activated delayed fluorescence

Molecules in the first excited singlet state can undergo intersystem crossing, a principally spin forbidden transition to the triplet state. Although principally forbidden, the process occurs due to spin-orbit coupling. As a consequence of spin-orbit coupling, the singlet states are described by wave functions that have some small triplet character mixed in. Consequently, the spin selection rule loses effect. In the triplet state, there are various possibilities to de-excite. One of them is using the thermal energy of the environment for reverse intersystem crossing (RISC) to the first excited singlet state and subsequent emission of fluorescence (Figure 2.2). For this to happen, the singlet-triplet energy gap has to be small so thermal energy of the environment is sufficient for the reverse intersystem crossing. Additionally, the resulting rate constant for RISC has to be large enough to compete with other transitions from the triplet state such as non-radiative deactivation processes and phosphorescence. The kinetics describing TADF are a complex interplay of all involved processes. Hence, after RISC, ISC can happen again (many times) resulting in a cycling between the singlet and triplet state.[12]

On molecular level, many design strategies have been proposed for efficient TADF to

occur.[13–15] A small ΔE_{ST} can be realized by designing intramolecular push-pull systems, Donor (D) – Acceptor (A) structures, with appropriate spatial separation between HOMO and LUMO achieved by large steric hindrance or twisted structures. Rigidity is important to reduce the efficiency of non-radiative deactivation pathways related to molecular vibrations. This can be achieved by planar polycyclic aromatic structures, steric hindrance that minimizes rotations, π-conjugation or other intra- or inter-molecular interactions.[16] Other than the mentioned ΔE_{ST}, lifetime, quantum yields and stability are crucial parameters, but optimization of the parameters with little sacrifice of other parameters is not easily achieved.

Regarding optical sensing, TADF is a type of luminescence with intermediate properties between fluorescence and phosphorescence; similar to fluorescence, the emission of photons occurs from the excited singlet state and analogously to phosphorescence, the triplet state with correspondingly long lifetimes is involved. The long TADF lifetimes allow simple discrimination from autofluorescence and measurement with cheap phase fluorometers. Since TADF relies on reverse intersystem crossing, it displays temperature-dependent behavior and consequentially can enable optical temperature sensing. Additionally, the inherently long lifetimes of TADF can render the dyes also susceptible to oxygen quenching, and therefore allow oxygen sensing.

Triplet-triplet annihilation

For a molecule in the triplet state, another possibility to return to the ground state is triplet-triplet annihilation (TTA). Here, two molecules in the triplet state collide. One of them is returned to the first excited singlet state, the other one returns to the ground state. TTA requires high dye concentrations and high light intensities. This produces enough molecules in the triplet state and a high probability of them colliding. The process has different characteristics compared to TADF: Its decay time is half the lifetime of the triplet state of the molecule in dilute solutions. TTA has a quadratic dependence to the excitation light intensity.

2.2.3 Phosphorescence

Emission with a spin change is called phosphorescence. Typically, phosphorescence occurs from the first triplet state back to the singlet ground state (Figure 2.2).

After absorption of a photon, the molecule in the first excited singlet state can undergo intersystem crossing. Intersystem crossing is the transition into the triplet state. As described above, the principally spin forbidden ISC is enabled by spin-orbit coupling. The spin orbit coupling increases with atomic number. This is called heavy atom effect. The heavy atom effect of e.g. Pt(II) induces rate constants for intersystem crossing up to 10^{12} s^{-1}.[17] This rate constant exceeds the radiative rate constants for fluorescence (often around 10^8 s^{-1}). Phosphorescence is mainly competing with reverse intersystem crossing and non-radiative deactivation. Both processes are favored at high temperatures. Non-radiative deactivation is additionally favored by molecular vibrations and collisions with other molecules. Consequently,

phosphorescence is favored in rigid molecules at low temperatures and incorporated in rigid systems, such as polymers or in host-molecules such as cyclodextrins. Phosphorescent molecules often are complexes of Pt(II), Pd(II) or Ir(III) or contain high numbers of bromine or iodine atoms. These heavy atoms introduce sufficient spin-orbit coupling so that the rate constant for phosphorescence (e.g. for Pt(II) complexes 10^5-10^7 s^{-1}) is large enough to compete with other transitions. There are solely organic molecules that have a small singlet-triplet gap. In these molecules, the triplet state is reached, but phosphorescence is so slow[16] that either thermal motion and oxygen diffusion lead to de-excitation or reverse intersystem crossing with subsequent thermally activated delayed fluorescence. The design of phosphorescent molecules is described in various reviews.[16,18,19]

For optical sensing, phosphorescence is interesting due to ideal separation from excitation light and long decay times from 10^{-6} s up to minutes at low temperatures. The long decay times allow temporal separation from autofluorescence background in biological samples. The phosphorescence is often inherently sensitive to oxygen and therefore basis for optical luminescent oxygen sensing.

2.2.4 Upconversion

The conversion of two or more photons of lower energy into one of higher energy is called upconversion. There are two main types of upconversion, lanthanide upconversion with the mechanisms mentioned below and "organic upconversion" due to triplet-triplet energy transfer reactions and triplet-triplet annihilation (TTA). Lanthanide upconversion typically occurs in lanthanide ion (activator) doped nanomaterials. The host materials are optically transparent and serve to appropriately distribute the activator ions and other additives in three-dimensional space. Prequesite for upconversion is the existence of multiple, long lived (metastable) excited states with close energy levels in a ladder like fashion. Within the 4f electron shells of the lanthanide ions, there is a great number of possible electronic transition that are suitable for upconversion.

There are five possible mechanism how upconversion can occur: excited state absorption, cooperative upconversion, photon avalanche, energy transfer upconversion, and energy migration upconversion.[20] All mechanism are based on the sequential absorption of two or more photons and have to be distinguished from two-photon or multi-photon absorption.[21]

For **excited state absorption**, one single lanthanide ion successively absorbs photons. Hence, after ground state absorption, excited state absorption happens before up-converted emission occurs.

Also **energy transfer up-conversion** involves sequential excitation of one ion. Here, instead of excited state absorption of a second photon, the energy is received from a second excited neighboring ion (sensitizer). Typically, sensitizers with high absorption cross-sections are used to increase the efficiency of the process.

In **cooperative up-conversion**, the excitation occurs analogously to energy transfer up-

conversion, but here a third ion is involved, which renders the whole process a second order transition/reaction.

For **energy migration up-conversion**, four different types of ions are involved in the up-conversion. This type is typically found in core-shell type nanoparticles. In the core, one type of ion, the sensitizer, is used for ground state absorption. This energy is then transferred to the accumulator ion, which is promoted stepwise to high-lying excited states. Then, migrator ions help to transfer the energy to the shell, where the activator ion is located and emits up-converted photons.

The **photon avalanche** type is a complex cascade of up-conversion processes and cross-relaxation processes. It relies on both excited state absorption and energy transfer reactions to achieve a population of ions in the excited state capable of generating up-converted emission.[20]

Although the efficiency of up-conversion is poor, this phenomenon offers some distinct advantages. When it is used with longwave excitation in the NIR, it provides low auto fluorescence background, large anti-Stokes shifts, sharp emission bandwidths, high resistance to photobleaching, and high penetration depth and temporal resolution.[22] This is especially interesting for bioanalytical purposes. Resulting from the poor quantum yield, another downside is, however, the high light intensity that is required. This may cause heating of the sample as water absorbs at 970nm (typical excitation for Yb^{3+}UPcons 980 nm).[23] The 808 nm excitation (using Nd^{3+} absorption) may be a preferable alternative, but the problem is that characterization is challenging and results are difficult to compare.[23]

2.2.5 Parameters Measured in Optical Sensors

Intensity

Luminescence intensity is the most basic parameter and simplest to measure. One just needs a light source, a photodetector and a data logger. In compact devices, this can be an LED, a filter to cut off excitation light, and a photodiode. Apart from analyte-dependent changes, the luminescence intensity L depends on the excitation light intensity I, luminophore concentration c, molar absorption coefficient ε, penetration length l, quantum yield φ, and a factor for the optical setup k. This is described by Parkers law:

$$L = I * \varepsilon * c * l * \varphi * k \tag{2.2}$$

Physical or chemical parameters influence luminophore concentration (static quenching, bond-formation or complexation), quantum yield (via (various) rate constants c.f. eq 2.3), and molar absorption coefficient (bond formation, complexation). The luminescence quantum yield of a given state (the quantum yield for reaching this state is omitted) is,

$$\varphi = \frac{k_r}{k_r + k_{nr}} \tag{2.3}$$

where k_r and k_{nr} are the radiative and non-radiative rate constants, respectively. Especially k_{nr} is influenced by the environment and temperature. Rate constants of all other processes competing with luminescence, such as internal conversion, quenching, energy transfer and others can also be summarized under this term or added as distinct rate constants in the fraction below. All these parameters allow introduction of various interferences. The devices/optical setup introduce fluctuations in excitation light intensity, detector sensitivity and fluctuation due to changes/movements of the optical components (such as fibers, mirrors, filters). Luminophore concentration can change due to leaching, bleaching or aggregation and if it is too high, reabsorption of emitted photons, called inner filter effect, can occur. Other parameters that influence the intensity measurement are/include: sample turbidity, homogeneity of the sensing materials, swelling of the sensing material and background fluorescence from the sample or the measurement setup. To (partially) compensate for some of these effects, referencing schemes are required to ensure the correctness of intensity based measurement. Possibilities for referencing include two-wavelength ratiometric measurement and dual-lifetime referencing.

Two-wavelength ratiometric measurement includes various read-out schemes. In general, a second signal is measured that is analyte independent or differently affected by the analyte. In practice this includes measuring emission at a single wavelength after excitation at 2 different wavelengths (c.f. pH indicator HPTS), measuring at 2 emission wavelengths after excitation at a single wavelength and measuring at 2 emission wavelengths after excitation at 2 different wavelengths.

Dual-lifetime referencing is a scheme to extract a ratio of two components from a single wavelength read-out.[24] The scheme is based on the addition of an inert luminescent reference material with largely (≥ 10 times) different decay time but ideally identical but at least overlapping excitation and emission spectrum. The scheme can be used in the time or in the frequency domain.

In the time domain, intensity is measured during and after a light pulse (with some delay). During the light pulse, the intensity is the sum of the slow and the fast decaying component. After the the light pulse, the short component decays before the second measurement. Consequently, only the slow decaying component is measured. As only one component is parameter/analyte sensitive, the ratio is proportional to the parameter/analyte concentration.

For the frequency domain, both components are excited with sinusoidally modulated light intensity as typical for phase fluorometry. Both components are contributing to the overall phase shift that changes with a changing ratio of the two components.

Decay Time

After a luminophore is excited with a pulse of light, the de-excitation occurs according to an exponential decay function.

$$[A^*] = [A^*]_0 e^{-(k_r + k_{nr})t} \tag{2.4}$$

with $[A^*]_0$ and $[A^*]$ being the number of luminophore molecules in the excited state at time zero and at a given time t after excitation, respectively. k_r is the radiative, k_{nr} the non radiative rate constant. The luminescence intensity I_L at any time is proportional to the number of molecules in the excited state. The proportionality factor is the rate constant for radiative decay. This then gives:

$$I_L = k_r [A^*]_0 e^{-(k_r + k_{nr})t} \tag{2.5}$$

For practical purposes, the lifetime or decay time τ is used as a measure for the time it takes for all but 1/e luminophore molecules to have returned to the ground state:

$$\tau = \frac{1}{(k_r + k_{nr})} \tag{2.6}$$

This parameter is characteristic for a luminophore at given conditions. It can change with a given physical parameter or concentration of an analyte. These parameters influence both rate constants or add additional rate constants to the equation, hence the decay time is changed. Temperature, for example, always increases the non-radiative rate constant and for TADF also increases the radiative rate constant, consequentially decay time is drastically shortened, but e.g. TADF intensity could increase (c.f. eq 2.3). Quenching or energy transfer both add additional rate constants in the fraction below. Therefore, the decay time can be used for self-referenced determination of physical or chemical parameters. It is (largely)

independent of luminophore concentration and hence is not affected by leaching, photobleaching or inhomogeneous distribution of components in sensor materials. It is very robust against changes in the optical setup, scattering of the sensor material, and color/absorption of samples. Background fluorescence can be cut off when measurement is performed in the time domain. It is also independent of the excitation light intensity, unless when working with very high intensities or very long decay times.[25] For these conditions, a depopulation of the ground state of the luminophore can occur, which can lead to a decrease in apparent lifetime. To differentiate whether the source of decrease in lifetime is TTA, stimulated emission or excited state absorption, further investigation is necessary.[25]

In the simplest case, the decay curve originates from one species with a mono-exponential behaviour. If there are two contributing species with different decay times, the decay curve becomes bi-exponential. Then, a changing parameter results in changing relative amplitudes/shares of the two components. Using time-correlated single photon counting, this can be measured or an average lifetime is received. Also an average lifetime τ_{av} can be calculated from the relative amplitudes B_1, B_2 and the corresponding decay times τ_1, τ_2:

$$\tau_{av} = B_1\tau_1 + B_2\tau_2 \tag{2.7}$$

The decay time can be determined in the time domain or in the frequency domain.

In the **time domain**, a pulse of light is used for excitation and the luminescence decay is measured by one of various means. In time-correlated single photon counting, the time between an excitation pulse and the first detected photon is measured and assorted to a time channel. By monitoring a large number of these events, a histogram is constructed that represents the luminescence decay curve. This is based on the fact that the probability of detecting a photon at a certain time after an excitation pulse is proportional to the luminescence intensity at that time. The decay is then extracted from curve fitting with an exponential decay function. To reduce the amount of single measurements, the intensity in several time gates can be used to reconstruct the decay curve. This goes down to two measurements for the **rapid lifetime determination method**.[26] The luminescence intensity is measured in two windows after an excitation pulse with a gated detector. From the integrated emission during these windows, A_1 and A_2, and the starting times of the gates, t_1 and t_2, the decay time can be estimated, according to the following equation:

$$\tau = \frac{t_2 - t_1}{ln(\frac{A_1}{A_2})} \tag{2.8}$$

For **frequency domain measurement**, light of sinusoidally modulated intensity is used for excitation. The luminescence emission or "response" is sinusoidally modulated at the same frequency but shifted/delayed in time due to its lifetime. The delay is measured as a phase

shift Φ (Figure 2.4) and is related to the decay time according to the following equation:

$$\tau = \frac{tan\Phi}{2\pi f} \qquad (2.9)$$

where f is the modulation frequency. Also the amplitude is partially demodulated compared to the excitation. This demodulation is described by the modulation ratio M that is also related to the decay time by the following equation:

$$M = \frac{1}{(1 + (2\pi f)^2 \tau^2)^{1/2}} \qquad (2.10)$$
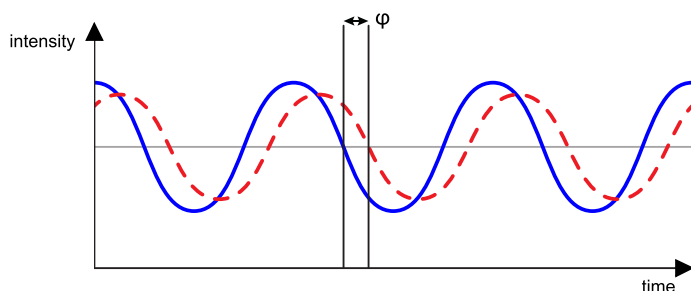
Figure 2.4: Illustration of the phase shift that is measured in frequency domain decay time measurements.

The distinct advantages of the lifetime-based measurements is its self referenced nature, precision, and robustness. The downsides include the complex and expensive instrumentation for indicators with short decay times that require high modulation frequencies for excitation. Except for oxygen and temperature sensing, the number of available indicator dyes suitable for lifetime-based measurement is limited. This is due to the mechanism of response that are applicable for these parameters (c.f. 2.2.6). For sensing oxygen, dynamic quenching affects the decay time of the indicator. For temperature sensing, changing rate constants of thermal quenching or reverse intersystem crossing affect the decay time. Sensors for pH or ions are usually based on indicators that bind or complex the analyte. This results in two forms of the indicator. If these two forms have different decay times, decay time based sensing is applicable. Often, however, the luminescence for the two forms is changed between completely on or off. This is the case for commonly used class of PET-based indicators. The luminescence is either on or quenched by PET and those that are turned on show a constant decay time.

Spectral Change

This section includes probes that continuously change their emission peak with a changing physical or chemical parameter. Probes with two analyte dependent forms (e.g. protonated/deprotonated) that have different emissions peaks are not treated here and fall under intensity-based measurement. Spectral changes can include a changing emission peak wave-

length or a change in linewidth. Shifting emission peak wavelenghts can be induced by a change in polarity for polarity probes, swelling/shrinking for photonic crystalls, or temperature for twisted intramolecular charge transfer states.[27] Also temperature dependent linewidth broadening can occur (e.g. rare-earth doped crystals[28]). To detect spectral changes, generally a spectrometer is necessary for measurement or at least multi-wavelength read-out. This increases the complexity of the instrumentation compared to intensity based measurement. Compared to intensity and decay time-based measurements, spectral change is rarely used to determine chemical or physical parameters except for polarity.

Anisotropy

Anisotropy is also a less commonly used technique. Upon excitation with polarized light, the emitted light is also polarized. The luminophores, however, can rotate during their time in the excited state. This results in a change of emission light intensity from its initial polarization. This can be measured by detection of the emission behind polarizers parallel and perpendicular to the direction of the polarized excitation light. The measure for this is called anisotropy r, given by equation 2.11, which is normalized by the total intensity[29].

$$r = \frac{I_\parallel - I_\perp}{I_\parallel + 2I_\perp} \tag{2.11}$$

where $I_\parallel$ and $I_\perp$ are the intensities with the polarizer being parallel or perpendicular to the polarization of the incident light. The rotation during the lifetime naturally changes with temperature and consequentially can be used for temperature measurement. Also some literature is available on pH sensors based on anisotropy.[30] Yet, anisotropy measurements are rather used in research (biological membranes, molecular biology, immunology, polymer research)[8] than in applied optical sensing.

2.2.6 Mechanism of Response

The sensitivity towards chemical or physical parameters can be based on different response mechanism. The response mechanism can affect certain aspects of the performance of optical sensors. Bleaching or leaching heavily affect concentration dependent mechanism like FRET or inner filter effect based schemes. Complexation based schemes often come with cross-sensitivities towards ions/ligands of similar size. Complexation behavior and dissociation constants are affected by the polarity of the environment.

Static and Dynamic Quenching

The term "quenching" is often ambiguously used. It does not include a decrease in luminescence intensity due to a reduction of molar absorption coefficient or light reabsorption. This, however, is sometimes called "apparent quenching". **Static quenching** decreases the luminescence intensity but does not change the luminescence lifetime. As depicted in Figure 2.5, two mechanism for static quenching are distinguished. One based on a sphere of effective quenching and the other based on a non-fluorescent ground state complex. For the sphere of effective quenching, the luminescence is quenched if the quencher is inside a certain active sphere around the excited molecule. Outside of it, there is no effect on the luminescence. For the second possibility, the quencher Q and the molecule M form a ground state complex QM that does not emit if excited or is not excitable (Figure 2.5, right side). This does not change the decay time of the overall emission as the excited state is not involved. Instead it reduces the luminescence-active amount of luminophore.
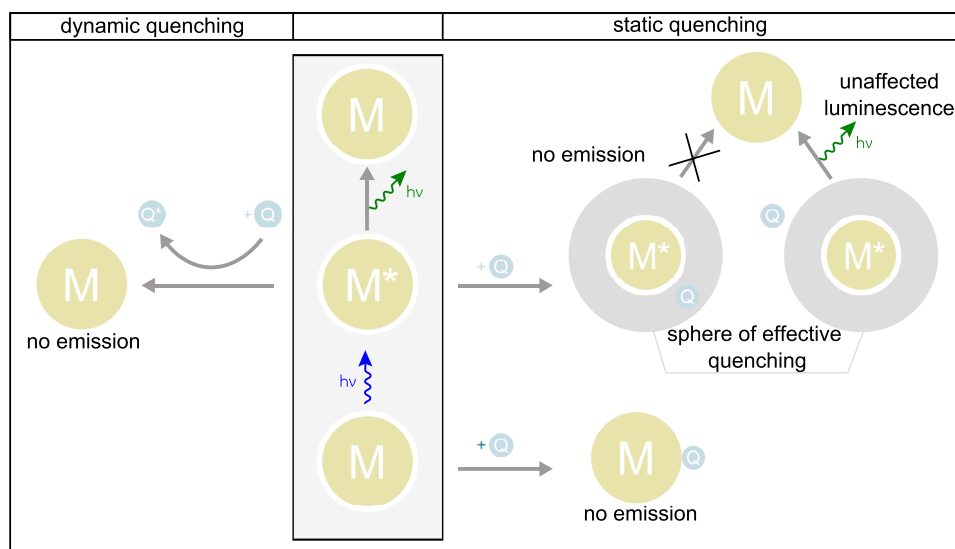
Figure 2.5: Illustration of static and dynamic quenching of a luminescent molecule M.

For the formation of the ground state complex, there is a quantitative description for the luminescence intensities depending on the quencher concentration. It is given by a relationship

similar to the Stern-Volmer equation:

$$\frac{I_0}{I} = 1 + K_S[Q] \tag{2.12}$$

K_S is the stability constant for the complex QM, I_0/I the ratio of intensities without and at a given quencher concentration, respectively and $[Q]$ is the quencher concentration.

Dynamic quenching happens if molecule in the excited state collides with a quencher (Figure 2.5, left). Typical quenchers are dioxygen and halides.[8] This returns the molecule to the ground state without emission. Therefore it is also called collisional quenching. The process is diffusion controlled as it requires the luminophore and quencher to mutually approach/collide within the excited state lifetime. This type of quenching also reduces the decay time, as a collision gets more probable the longer the molecule stays in the excited state. Consequentially, less molecules stay in the excited state for long, the distribution changes to shorter stays in the excited state and hence the decay time is reduced. The intensity I or fluorescence quantum yield Φ and also the decay time τ are described by the Stern-Volmer equation:

$$\frac{\Phi_0}{\Phi} = \frac{I_0}{I} = \frac{\tau_0}{\tau} = 1 + k_q\tau_0[Q] = 1 + K_{SV}[Q] \tag{2.13}$$

k_q is the quenching rate constant and K_{SV} is the Stern-Volmer constant.

Incorporation of luminophores into polymer matrices can introduce a downward curvature into the Stern-Volmer-Plot (I_0/I vs. $[Q]$). This often occurs in microheterogeneous systems. To account for this, the Stern-Volmer relation was modified.[31] The modified relation is usually used with two exponential and is then called two-site model (eq. 2.14), but up to four exponentials can be introduced.

$$\frac{I}{I_0} = \frac{f}{1 + K_{SV}^1[Q]} + \frac{1 - f}{1 + K_{SV}^2[Q]} \tag{2.14}$$

K_{SV}^1 and K_{SV}^2 are the Stern-Volmer constants, f is the fraction of molecules with given Stern-Volmer constant/their contribution to emission in the absence of the quencher. Although some simplifications are made, the relation generally gives valid results.[31]

Bond Formation or Complexation

A bond formation or complexation reaction can alter the color-forming system of an indicator in a way that the change may be measured. A requirement of optical sensors is the reagent independent reversibility of the reaction. Therefore, redox-reactions are not considered here. The reaction of the indicator can result in a spectral change, change of quantum yield, luminescence lifetime or molar absorption coefficient. Alternatively, the reaction can occur at the periphery of the molecule not conjugated to the color-forming system. Here, the change in the receptor part does not affect the color-forming system, but depending on its reaction state can switch on and off other reactions such as photoinduced electron transfer (PET, see section 2.2.6). Also a separate receptor with (partial) conjugation can be used; this results in intramolecular charge transfer (ICT, see section 2.2.6). If both forms of the indicator are luminescent, this allows for ratiometric measurement. Leaching and bleaching are not affecting the measurement as the two forms are in equilibrium and the ratio stays the same even if only one form is leached or bleached faster. In contrast, if only one form is luminescent, this only allows for intensity based measurement or requires a reference dye. Hence, susceptibility to leaching and bleaching is introduced.

Typical examples for bond formation and complexation can be found among indicators for pH and ions. For fluorescein and its derivatives, molar absorption coefficients and fluorescence quantum yields vary significantly between deprotonated and protonated forms.[32,33] For most, the phenolate form is much brighter compared to the phenol form. Also some Ru(II) polypyridyl complexes show pH-dependent properties. A $[Ru(Ph_2phen)_2DCbpy]^{2+}$ (DCbpy = 4,4'-dicarboxy-2,2'-bipyridine) complex was shown to change emission intensity, emission peak and decay time upon protonation.[34] For HPTS, emission is observed only from the deprotonated form (520 nm) upon excitation of both the protonated (405 nm) and deprotonated form (460 nm). The protonated/deprotonated forms display molar absorption coefficients (at their absorption peak) of around 20 000/24 000 M^{-1} cm^{-1} and a quantum yield close to unity for both.[35] Rhodamines and diketopyrrolopyrroles display luminescence changes upon pH-dependent lactam formation.[36,37] For the rhodamine, the spirolactam form is colorless, whereas ring opening upon protonation yields a highly absorbing and fluorescent rhodamine.
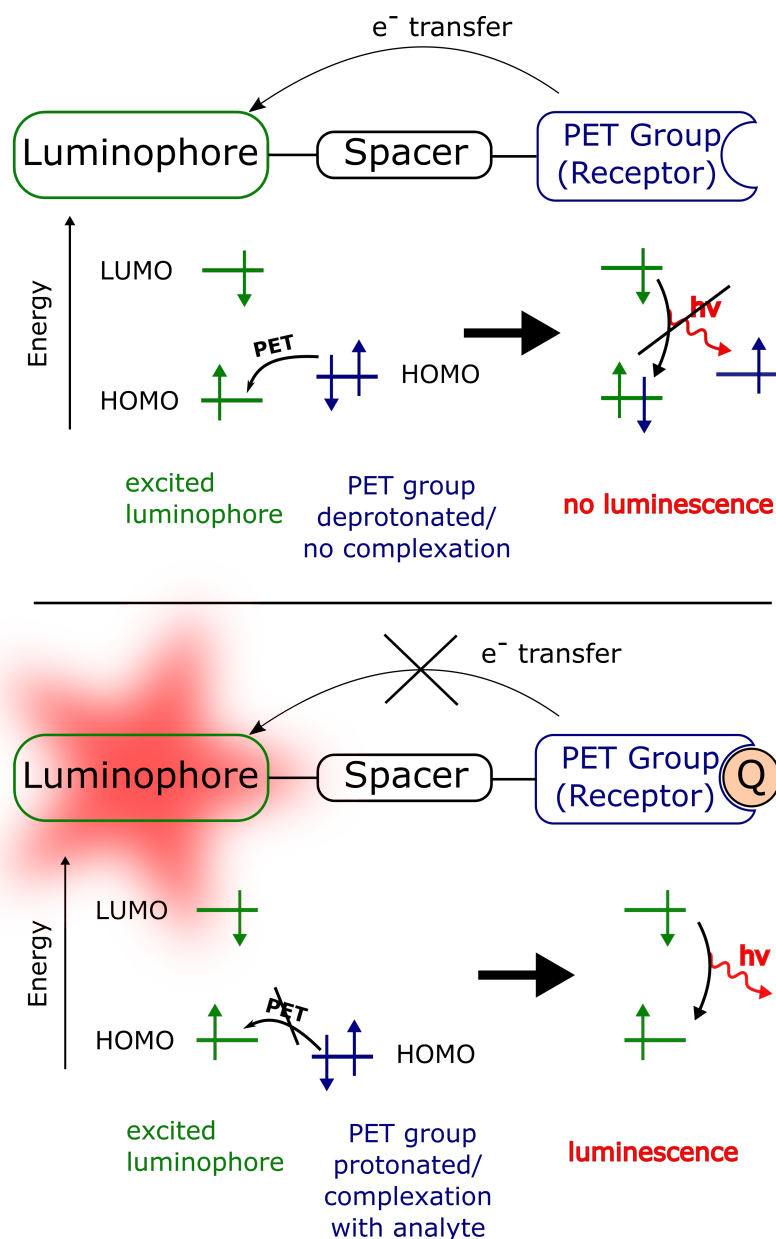
Figure 2.6: Illustration of photoinduced electron transfer (PET) based quenching.

Molecules in the excited state can take part in reversible electron transfer reactions that can quench fluorescence (Figure 2.6). If a molecule is photoexcited, the ground state can take up one more electron from a donor and hence the excited electron cannot return to the ground state via a radiative pathway. No luminescence occurs. This is called reductive photoinduced electron transfer. The donor is usually a phenolate or tertiary amine. An electron from the free electron pairs of these groups can be transferred to the luminophore if the orbital has suitable/matching HOMO/LUMO levels or as another measure, oxidation potentials. The donor groups are

protonable or chelating groups (crown ethers etc.) that upon protonation/coordination change their oxidation potential/HOMO. Then they are no longer able to reduce the fluorophore (Figure 2.6). This effect can be used for sensing.[38] The relative positions of the levels/potentials determine the efficiency of the PET. Not every PET group can quench every luminophore. Other electronic factors can also influence PET. Repulsive local electric fields can inhibit the electron transfer reaction.[39] The receptor groups are connected to the luminophore so that no conjugation takes place. This is done by using a spacer part (CH_2) or induced by steric reasons, e.g. when the receptor group is oriented orthogonally to the luminophore. PET does not influence the absorption spectrum as the receptor group has no influence on the color-forming system. The advantage of PET-based systems is the flexibility they offer. Basically, it is a modular system that simply allows coupling of a chosen luminophore with a desired PET-receptor group.

For intramolecular charge transfer (ICT), the receptor group is conjugated to the color-forming system. Excitation of the luminophore facilitates the electron/charge transfer from a donor group to another part of the molecule. Consequently, the charge distribution in the excited state is significantly different from the ground state. A change in the electronic situation of the receptor (often the donor) perturbs the ICT, which changes the electronic situation (HOMO-LUMO levels) of the luminophore. This induces photophysical changes that can be used for sensing. ICT can lead to a change in spectral properties, decay time, quantum yield or to a quenching of luminescence if the ICT state is a dark state.[40]

Förster Resonance Energy Transfer and other Energy Transfer Reactions

The **Förster resonance energy transfer** (FRET) occurs when two dyes are in close proximity and have overlapping absorption and emission spectra. The excited donor molecule transfers energy radiationless to an acceptor molecule. The transfer occurs via dipole-dipole interactions and it results in a return of the donor to the ground state and an excitation of the acceptor. FRET is a non-radiative process and emission and re-absorption of luminescence does not take place. FRET is highly dependent on the distance between the FRET pair and scales with $1/\mathrm{r}^6$ as can be seen in eq. 2.15 describing the FRET rate constant k_T.

$$k_T = \frac{R_0^6}{\tau_D^0 r^6} \tag{2.15}$$

τ_D^0 is the excited state lifetime of the donor, r the distance between the FRET pair and R_0 the Förster critical radius. This radius is the distance at which FRET and de-excitation of the donor are equally probable. Generally, FRET is used to measure distances on molecular level. For sensing analyte concentrations, FRET can be used either when the analyte changes the absorption/emission of the indicator dye or when a changing analyte concentration changes the distance between two dyes. This can happen either by changing the conformation of carrier molecules or the volume of matrices. For the analyte changing the absorption/emission, typically

two dyes are used and analyte recognition enables or disables FRET because one dye changes absorption/emission for FRET to occur. Various possibilities for read-out schemes have been described.[41,42] FRET between two forms of indicator, e.g. protonated/deprotonated, is called homoFRET. Analyte binding enables FRET from the unbound to the bound form of the dye. This was proposed to enable lifetime based pH-sensing for triangulenium dyes,[43] yet introduces a concentration dependency. The dependency occurs because a decreasing concentration is increasing the average distance between the dye molecules.

The groups using conformational changes of a carrier molecule usually have sharp transition regions for parameters like pH[44–47] or temperature,[48] limiting the detection range but displaying enormous sensitivity in this small range. Conformational changes can also be induced by analyte binding such as hybridization with target DNA or chemical reactivity of the analyte such as cleavage of groups linking the FRET pair (c.f.[41,42]).
Apart from FRET utilized for sensing, it can also unfavorably occur in design of multiparameter sensors, if the indicator dyes are incorporated in the same layer. Generally, this can be avoided by using dye doped/coupled nanoparticles instead of the sole indicator for immobilization.

FRET is the most commonly utilized energy transfer reaction. All other reactions are much less commonly used. Other short range energy transfer reactions are based on intermolecular orbital overlap. This includes Dexter energy transfer, where electrons are exchanged.[49] Surface energy transfer (SET) is observed at metallic surfaces interacting with molecular dipoles.[50] Through-bond energy transfer (TBET) is similar to FRET with regard to the donor and acceptor part of the system. Here, however, the two parts are linked by a conjugated bond and spectral overlap is not necessary.[51]

Dark State Quenching

Dark states are states that do not absorb or emit light. It is argued that during deactivation pathways, these states can be responsible for luminescence quenching that is attributed to PET.[40] For certain structures, PET is often by default attributed to be responsible for quenching, although this is not proven experimentally (detection of radical ions with time-resolved spectroscopies).[40] It is argued that according to quantum mechanical calculations of potential energy surfaces, the unprotonated/uncoordinated (PET receptor) groups can lead to dark states during the deactivation pathways and no electron transfer is involved. From these states, only non-radiative deactivation pathways lead back to the ground state. The differentiation has to be made case by case.

Inner Filter Effect

The inner filter effect describes the attenuation of the relationship between excitation light and luminescence intensity in concentrated solutions compared to the linear relationship in dilute solutions. This can be caused by absorption of the excitation light in the first few "layers" of the sample or by reabsorption of the emitted luminescence. For sensing purposes, it can be used to

22

modulate the luminescence of inert dyes/materials by analyte sensitive absorbing dyes/materials. This is either achieved by using an analyte sensitive absorber that absorbs/reduces the excitation light or the emission of the inert luminophore. This allows design of turn-on, turn-off and ratiometric sensing systems. The modulation of the luminescence is proportional to the analyte concentration. The effect is used to prepare sensors based on bright luminophores, independent of the brightness of the indicator. This allows for high flexibility in sensor design. However, usually high concentrations of indicator have to be used to generate significant signal changes. Since this sensing scheme is solely based on emission and reabsorption, the excited state is not affected and the decay time does not change. As there is no energy transfer involved, it is not dependent on close proximity of the dyes.

Conformational Changes or Swelling

Physical or chemical parameters can induce conformational changes or changes in volume of the sensing chemistry. This is exploited by optical sensors based on changes in refractive index, structural colors (e.g. photonic crystals) or luminescence. The changes in luminescence are typically modulated by FRET or polarity of the sensing chemistries environment. The physical and chemical parameters that change typically are charge, temperature, ionic strength, polarity or pH. pH, charge and ionic strength, however, are interconnected. As mentioned before in the FRET section, pH[44–47] or temperature[48] induce changes that modulate FRET. Temperature induced phase transitions of polymers (such as poly(N-isopropylacrylamide) NIPAM) change the polarity in the microenvironment of the polymer. This can be used for temperature sensing in aqeous systems using solvatochromic dyes.[52] In another approach, a changing volume of the sensor material changed the number of illuminated luminophores. A copolymer of acrylamide and dimethylaminoethyl methacrylate displays pH dependent swelling. Swelling of the material reduces the concentration of the luminophore in the illuminated region and consequentially reduces luminescence intensity.[53]

Polarity

Polarity probes change their optical properties according to the complex interplay of solute-solvent interaction what is commonly termed polarity. This includes nonspecific dielectric solute–solvent interactions originating from permanent dipoles and polarizabilities (dipole–dipole, solute dipole–solvent polarizability, solute polarizability–solvent dipole, polarizability–polarizability) and specific interactions such as hydrogen bonding.[8] These interactions affect the extent to which the ground and excited states are stabilized by its surrounding molecules. Consequentially, a changing environment induces changes in positions, intensities, and shapes of absorption and emission bands. The change is called solvatochromism. For emission, also the lifetime of the excited state can change.[54] An empirical parameter for solvent polarity was proposed by Dimroth und Reichardt, the $E_T(30)$, which is based on the longest-wavelength solvatochromic

absorption band of a pyridinium *N*-phenolate betaine dye.[55] Solvent polarity probes were used in sensors for water content in solvents such as acetone,[56,57] ethanol,[57,58] or acetonitrile.[57]

Thermal Energy

Temperature influences nearly every process or transition related to luminescence. The effects vary according to the nature of the process. According to Boltzmann, the temperature of the environment affects the distribution of the molecules over vibrational energy levels in the electronic states. An increased temperature broadens the spectrum as more energy levels are accessible via thermal energy ($\propto k_B T$ without other interactions). Additionally, increased temperature results in more thermal agitation. Thermal agitation includes collisions with solvent molecules, molecular vibrations, rotations, and etc.[8] In general, all these processes promote non-radiative deactivation and consequentially decrease luminescence quantum yields. Often the decrease/temperature effect is so minor that sensing is not (heavily) affected. Yet, there are indicator dyes that are sensitive enough for temperature measurement[10] and that are solely based on more efficient non-radiative deactivation competing with prompt fluorescence or phosphorescence. Apart from the decrease in luminescence intensity, also the decay time shortens with increasing temperature as k_{nr}^s in eq. 2.1 increases with thermal agitation.

In contrast, the intensity of **thermally activated delayed fluorescence** increases with increasing temperature (see section 2.2.2). Here, thermal energy of the environment is necessary for reverse intersystem crossing from the triplet state. Yet, the decay time of TADF decreases with increasing temperature as the rate constant for reverse intersystem crossing increases.

For molecules with **twisted intramolecular charge transfer states** (TICT), temperature can shift emission peaks. This shift results from changes in the thermal equilibrium between local excited state emission and the TICT excited state emission.[27]

Lanthanides are often used to prepare upconverting nanoparticles (UCNP),[59] phosphors and metal organic frameworks[60] for thermometry. Regarding the UCNPs, the upconversion process is nonlinear and consequentially little information about quantum yields and its temperature dependence is available. However, all these materials often have a ratiometric response on temperature. Their luminescence consists of emission/transitions from several closely spaced energy levels that have different temperature dependencies.[59] The ratio of luminescence intensities from these transitions ($\frac{I_2}{I_1}$) is controlled by the energy gap ΔE between the two energy levels and is described by the following equation:[59]

$$R = \frac{I_2}{I_1} = Ae^{-\frac{\Delta E}{kT}} \tag{2.16}$$

k is the Boltzmann constant, and T is the absolute temperature.

2.3 Indicators

2.3.1 State of the Art Oxygen Indicators

Oxygen sensors exploit quenching of the luminescence of appropriate indicator dyes by molecular oxygen via a radiationless deactivation process which involves the collision of the indicator dye with an oxygen molecule. The collisional quenching has influence on both luminescence intensity and lifetime, with the latter being the preferred parameter. This is because it allows for self-referenced measurement, being independent of leaching, photobleaching and other drawbacks of intensity-based measurement. The most commonly used indicators belong to the classes of Ru(II) polypyridyl complexes, metalloporphyrins, cyclometalated Ir(III) and Pt(II) complexes. Extensive reviews about oxygen indicators, sensing and imaging are available.[6,61]

Ru(II) and Os(II) **polypyridyl complexes** (e.g. Ru(dpp)$_3$ in Figure 2.7) are generally characterized by a large Stokes shift and good photostability, but also by moderate molar absorption coefficients, considerable thermal quenching and rather short lifetimes requiring immobilization into highly oxygen permeable materials.[6,61]

Metalloporphyrins are the most popular class of oxygen indicators and are generally used with Pt(II) and Pd(II) as central atoms. The metalloporphyrins are characterized by strong phosphorescence at room temperature, a large Stokes shift and high molar absorption coefficients.[6,61] The inherently long lifetime of these complexes can be adjusted to ranges in the micro and milliseconds timescale by using the appropriate central atom, Pt(II) for the μs range and Pd(II) up to the ms range, and to a lesser extent via variation of the substitution. The first standard indicators were Pt(II) and Pd(II) octaethylporphyrin (PtOEP, PdOEP), but they later have been replaced by much more photostable, Pt- and Pd tetrakis(pentafluorophenyl)porphyrins (PtTFPP, PdTFPP, Figure 2.7).[6] As NIR indicators, the Pt- and Pd tetraphenyltetrabenzoporphyrins (PtTPTBP, PdTPTBP, Figure 2.7) are popular.[62]
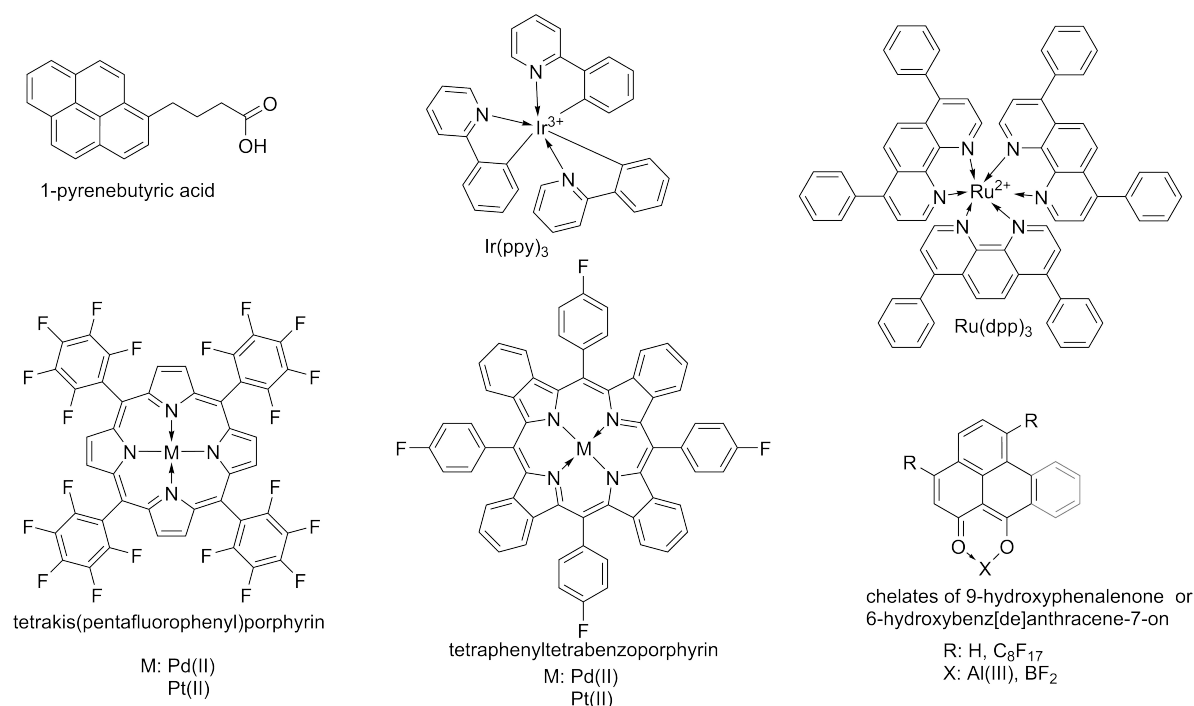
Another possible central atom for metalloporphyrins is Ir(III). Ir(III) porphyrin complexes have two additional axial coordination sites, introducing the possibility to tune the photophysical properties by modification of the axial ligands. The reported Ir(III) octaethylporphyrins, pyridine coordinated Ir-OEP-Py$_2$, n-butyl imidazole coordinated Ir-OEP-n-butIm$_2$, carboxyimidazol coordinated Ir-OEP-CarbIm$_2$, were prepared from a parent complex by ligand exchange.[63]

Another class of indicators are **cyclometalated Ir(III) and Pt(II) complexes.** These complexes exhibit large Stokes shifts, are photostable and possess high quantum yields.[6,61,64] Typical representatives are phenylpyridine based [Ir(ppy)$_3$] (Figure 2.7),[65] thienylpyridine based Pt(thpy)$_2$,[66] and benzoisoquinolinedione as well as acetylacetonato coordinated CNPt(acac) indicators,[67] the latter allowing for the design of a ratiometric sensor using a single molecule. Although a plethora of cyclometalated complexes has been prepared, only few found application in optical sensing. This can be explained by the fact that contrary to metalloporphyrins, the cyclometalated complexes lack high molar absorption coefficients beyond the UV region. This, however, does not impede their application using electrical excitation; cyclometalated

complexes found intense application in organic light emitting diode (OLED) technology.[68–71] Cyclometalated coumarin complexes represent a notable exception, showing very efficient absorption in the blue part of the spectrum and strong phosphorescence.[72] Unfortunately, photostability of these compounds is rather poor.

Indicators based on Eu(III),[73–75] Gd(III),[74,75] Tb(III),[76] Cu(I) and other metal complexes, such as Pd(II) or Pt(II) Schiff base complexes[77] have also been reported and feature some interesting properties (such as narrow-band emission of the Eu(III) complexes) but so far did not find broad applicability in oxygen sensing materials.

Typically, indicators displaying thermally activated delayed fluorescence are susceptible to oxygen quenching. This is due to their long decay times that are caused by the intermediate stay in the triplet state. They, however, are strongly temperature sensitive. This is generally not desirable, but also has been utilized for temperature compensated oxygen sensing. Dual sensing was reported for Pd(II)[78] and Zn(II) electron-deficient tetraphenyltetrabenzoporphyrins.[79] Apart from dual sensing, fullerenes have been successfully used for (ultra) trace oxygen sensing.[4,80,81]

1-pyrenebutyric acid

Ir(ppy)₃

Ru(dpp)₃

tetrakis(pentafluorophenyl)porphyrin

M: Pd(II)
Pt(II)

tetraphenyltetrabenzoporphyrin

M: Pd(II)
Pt(II)

chelates of 9-hydroxyphenalenone or 6-hydroxybenz[de]anthracene-7-on

R: H, C₈F₁₇
X: Al(III), BF₂

Figure 2.7: Chemical structures of various indicators that are used for oxygen sensing based on luminescent materials.

The mentioned groups of indicators already display advanced characteristics with regard to oxygen sensing, but during development of applications, indicator dye choice is often still a compromise. Improved control or an increased number of methods to control the photophysical properties of indicator dyes is of major importance for further advances in optical oxygen sensing. In the following subsections, a few applications for oxygen sensors and their requirements regarding the indicators are discussed.

Oxygen Sensors utilizing Indicators with Short Decay Times - High Pressure or Fast Responding Sensors

Oxygen sensitivity of sensing materials is mainly governed by the luminescence decay time of the indicator, the solubility of oxygen in the polymer matrix and the quenching rate constant, which is related to the diffusion coefficient of oxygen in the polymer.[82] As the solubility of oxygen in various polymers does not vary signficantly, the main parameters are decay time and diffusion coefficient. For high pressure sensors, short decay times and small diffusion coefficients are desired to adjust the sensing range to high oxygen partial pressures. Small diffusion coefficients, however, also slow down diffusion and result in long response times. Faster responding sensors for the same sensing range are produced from combining indicators having short decay times with highly permeable materials or adsorption/coupling of the indicator at the surface of the sensing material. Also decreasing film thickness improves/reduces response times. For surface located indicators even fluorescence can be significantly quenched by oxygen and be used for sensing.[83,84] Among indicators for oxygen sensing, transition metal polypyridyl complexes and polycyclic aromatic hydrocarbons display short luminescence decay times. The phosphorescence decay times τ_0 for ruthenium polypyridyl complexes are in the range of 0.25 to 10 µs.[6] Osmium polypyridyl complexes have even very short decay times in the range of 5 - 15 ns.[6] Polycyclic aromatic hydrocarbons have fluorescence decay times up to 450 ns.[85]

The indicator Ru(dpp)$_3$ (Figure 2.7) was immobilized in sol gels of different porosities[86] and organically modified silicas (ORMOSIL).[87] The sol gels were prepared from different mixtures of tetraethoxysilane and methyltriethoxysilane under different conditions. The porosities of the sol gel films were then correlated with oxygen diffusion. Response times down to 5 ms were reached for 20 nm thick films. Microoptodes produced from mixtures of phenyltrimethoxysilane and trimethylmethoxysilane had response times of around 250 ms. Compared to other sol gels, ORMOSILs avoid penetration of water into the matrix that may change the oxygen permeability.[87]

Very early, a fast responding sensor was reported based on the long fluorescence lifetime of pyrenebutyric acid (Figure 2.7, $\tau \sim$100 ns).[88] The indicator was coupled to activated controlled porous glass and resulted in a response time of below 20 ms. Ter(9,9-diarylfluorene) forms films under vacuum deposition that can be used for oxygen sensing.[84] The films have broad fluorescence emission between 400 and 500 nm when excited at 370 nm. The response times of the 100 nm thick films are below 100 ms. Another fluorescent indicator was used in a sensing material with submillisecond respone time.[83] A free ligand porphyrin was adsorbed on the surface of various silica materials. The response times was as low as 25 µs for one material.

Oxygen Sensors from Indicators with Long Decay Times - Trace Oxygen Sensors

Oxygen trace sensors are required in polymer industry,[89] surface treatment applications,[90] semiconductor industry,[91] food packaging[92] and in biological and medical reasearch of hypoxic and anoxic systems.[93] For trace oxygen sensing, indicators with long decay times and highly

permeable matrix materials are required.[82] The decay times of these indicators start with 1 ms of Pd(II) porphyrins for the moderately low oxygen concentrations and go up to several 100 ms for phosphorescent boron- and aluminium chelates.[94]

Several materials have been reported on the basis of metalloporphyrins. Generally, the decay times of Pd(II) porphyrins are in the range of 300 μs to 1 ms. The representatives with decay times close to 1 ms are suitable for trace sensing when incorporated in highly oxygen permeable materials such as PdOEP in 8F-PEKEK(Ar) films[95] or Pd(II) tetrakispentafluorphenylporphyrin covalently immobilized on silica-gel particles (limit of detection of 0.015 Pa O_2).[96]

An alkylsulfone-substituted Zn(II) tetraphenyltetrabenzoporphyrin was reported with a TADF lifetime of around 7 ms.[79] The material was suitable for oxygen measurement in the range of 0.002 hPa to 6 hPa, although it was immobilized in PSAN, a polymer of low oxygen permeability. The sensing material was proposed for temperature compensated oxygen trace sensing as TADF is highly temperature sensitive.

C_{70} fullerenes have distinctly longer decay times in the range of 15-45 ms and hence have a even higher oxygen sensitivity.[4,80,81] They were used for oxygen sensing down to 160 ppbv when incorporated into ethyl cellulose. ^{13}C enriched C_{70} fullerenes display even higher oxygen sensitivity.[80]

For ultra trace sensing, phosphorescent boron- and aluminium chelates of 9-hydroxyphenalenone or its benzannelated derivative are suitable (Figure 2.7).[94] They display decay times in the range of 250 to 730 ms and were used to measure oxygen down to 7 pM. Additionally, oxygen measurement can be temperature compensated as they also display TADF. The ratio of TADF and phosphorescence solely depends on temperature. The oxygen calibration, however, proves especially challenging.[97] Even high purity commercial gases (nitrogen or argon) have "significant" oxygen impurities regarding the sensitivity of these sensors. However, a standard addition calibration can be performed. The polymer material can have oxygen stored inside that only slowly diffuses out. The long excited states can lead to a non-linear dependency of excitation light intensity. The long stay in the excited state enables a variety of other transitions (e.g. ground state depletion, triplet-triplet annihilation, triplet state absorption) that can influence the oxygen sensing behaviour. Also singlet-oxygen accumulation can occur and influence measurement, if the concentration of indicator molecules becomes higher than the oxygen concentration. Additionally, oxygen photoconsumption can occur. Here, singlet oxygen reacts with unreacted functional groups left in the polymer matrix, impurities or the indicator itself.

2.3.2 State of the Art Temperature Indicators

Although conventional temperature probes (such as resistance thermometers) are very widely used offering good resolution over a broad temperature range, optical temperature probes represent a very interesting alternative for some applications. These include in particular imaging applications including imaging on surfaces (e.g. in multi-component pressure-sensitive paints) and in cells with help of nanoprobes, and microprobes for ultrafast temperature measurement. Moreover, optical thermometers are promising as components in multi-parameter sensors, allowing for temperature compensation with the same spatial and temporal resolution. The most commonly employed classes of materials are purely organic compounds, metal ligand complexes, lanthanide complexes, inorganic phosphors, nanomaterials and proteins.[29] The literature on luminescent thermometry is plentiful.[28,29,59,98–105]
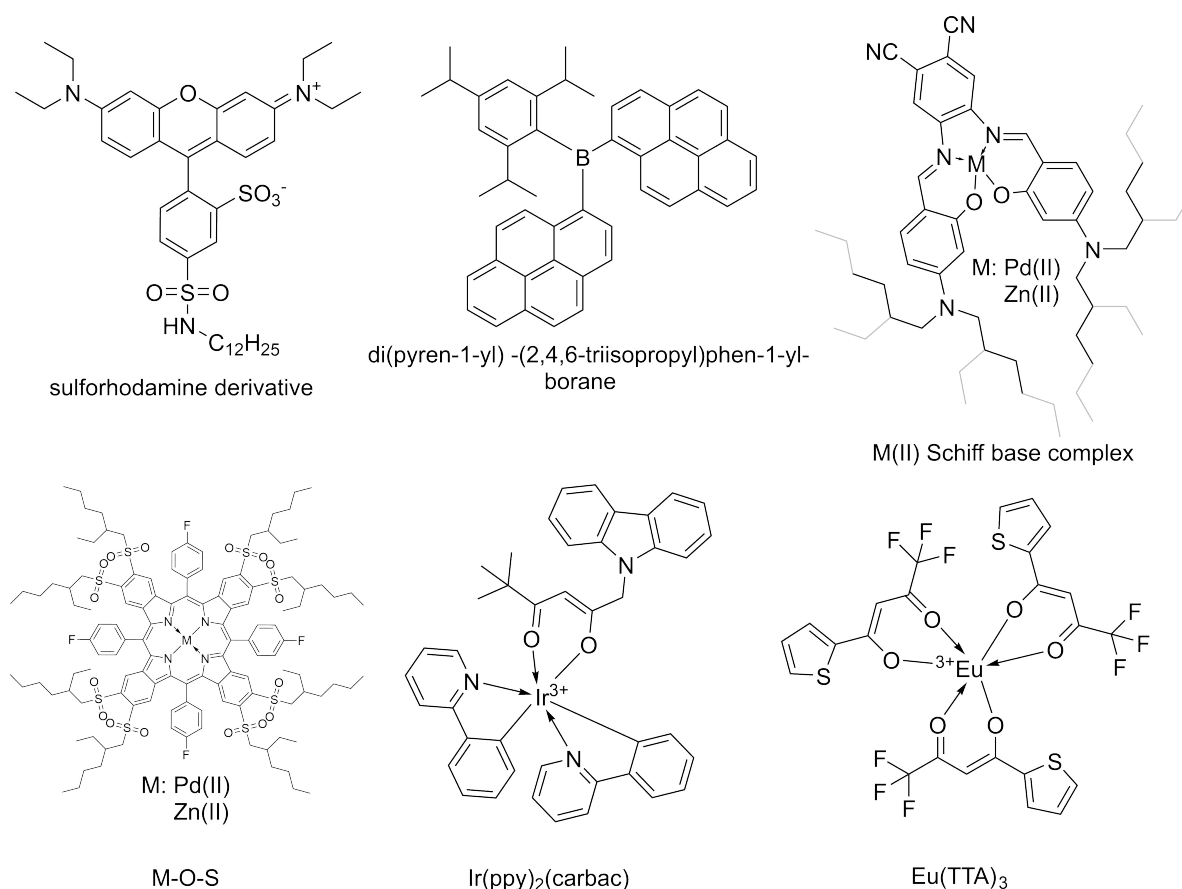
Figure 2.8: Chemical structures of various indicators that are used for temperature sensing based on luminescent materials.

Purely **organic dyes** such as rhodamine and derivatives[106–110] display high brightness and no oxygen cross-talk, but only moderate temperature dependency of both their fluorescence intensity and decay time.[10,111] They enable intracellular temperature measurement as molecular probes via ratiometric measurement[107] or as nanoprobes via fluorescence lifetime imaging

(FLIM) when incorporated into polymers such as Eudragit Rl-100.[10]

Dipyren-1-yl(2,4,6-triisopropylphenyl)borane (Figure 2.8) has a different response to temperature. Upon rising temperature, the complex shows a colorimetric luminescence change that is due to a shift of the thermal equilibrium between a local excited state and a twisted intramolecular charge transfer state.[27] The absorption is not affected by temperature. The probe has a sensitivity of 0.30 nm wavelength shift per °C.

Another response mechanism is the temperature dependent formation of exciplexes or excimers.[112–114] Upon formation, typically a second emission peak occurs. For the pair, perylene and *N*-allyl-*N*-methylaniline, this works even when immobilized in a polystyrene matrix.[112]

Thermally activated delayed fluorescence can be used for optical thermometry as shown by Fister et al.[2] for acridine yellow. For most TADF indicators, long decay times introduce oxygen cross-talk. This is can be addressed by the appropriate choice of immobilization matrix. Baleizão et al.[3] utilized TADF of C_{70} fullerene to prepare optical thermometers by immobilizing the emitter in various oxygen impermeable polymers. Augusto et al.[5] dispersed polystyrene particles doped with C_{70} fullerene in PAN. The material was then treated in a hydraulic heated press. This sensor design exhibits high sensitivity (-0.75 to -1.75 %/°C change of TADF lifetime in the range from 20 to 90 °C) and no oxygen cross-talk. Another approach to eliminate oxygen cross talk was reported by Steinegger and Borisov.[115] Here, a TADF emitting Zn(II) Schiff base (Figure 2.8) chelate complex was immobilized in polystyrene on a glass support. The sensing layer was then covered with an oxygen scavenging OSTE layer (**off**stoichiometry **t**hiol-**e**ne polymer). Subsequently, a layer of poly(vinylidene chloride-*co*-acrylonitrile) was added to reduce the oxygen diffusion into the oxygen scavenging layer. This additional layer increases the long-term stability of the sensor material by prolonging the oxygen-scavenging capability. The material shows high temperature sensitivity (4.1 %°C change of TADF lifetime at 25 °C), a resolution better than 0.03 °C and no oxygen cross-talk.

Some **metal-ligand complexes** are also useful temperature probes. Although they are subject to oxygen quenching due to their long lifetimes, this can be overcome by incorporating the dyes in polymers with low oxygen permeability. For instance, Ru(II) polypyridyl complexes incorporated in polyacrylonitrile or poly(vinylidene chloride-*co*-acrylonitrile) are among the typically used temperature probes.[29] The group of Orellana screened various combinations of Ru(II) polypyridyl complexes and matrix materials for the highest temperature sensitivity. The complex [Ru(phen)$_2$(4-Clp)]$^{2+}$ incorporated into poly(ethyl cyanoacrylate) (PCA) has a relative sensitivity of -1.35%/K change of lifetime at 25°C. The oxygen permeability of PCA is sufficiently low to eliminate the oxygen cross-talk of the complex with a 2.65 μs lifetime.

Pt(II) and Pd(II) Schiff base complexes (Figure 2.8) were reported to have strong temperature dependent luminescence. In contrast to the Zn(II) Schiff bases with TADF, the Pt(II) and Pd(II) Schiff base show strong red room temperature phosphorescence when immobilized in polystyrene. At 25 °C, the materials show sensitivities of -2.1 and and -0.52%τ/K for the Pd(II) and the Pt(II) complex, respectively. Phosphorescent boron- and aluminium chelates allow for

temperature compensated ultra-trace oxygen sensing.[94] Here, the temperature can be accessed via the ratio of TADF and phosphorescence, which is independent of the oxygen concentration.

Also **metalloporphyrins** were found useful for temperature sensing. Platinum(II) octaethylporphyrin immobilized in polystyrene shows a changing ratio of emission peaks with temperature.[116] An electron deficient Pd(II) tetraphenyltetrabenzoporphyrin (Pd-O-S, Figure 2.8) shows a temperature dependent ratio of TADF and phosphorescence.[78] Both luminescence emissions have the same decay time and are subject to oxygen quenching. This allows dual sensing of oxygen and temperature as the TADF/phosphorescence ratio is independent of the oxygen concentration. Interestingly, the type of luminescence emission can be changed to prompt and thermally activated delayed fluorescence by exchanging the central atom of the complex with Zn(II) (Zn-O-S, Figure 2.8). Phase fluorometry now enables dual sensing of oxygen and temperature at a single wavelength. The prompt fluorescence can be considered an internal reference. Temperature and oxygen have different effects on the decay time and intensity ratio of TADF. Via phase fluorometry at two frequencies and a 3D calibration plane both parameters can be determined.

Cyclometalated Pt(II) and Ir(III) complexes were investigated for sensing temperature. Their lifetimes also require incorporation into gas blocking polymers to minimize oxygen crosstalk. As described above, these complexes exhibit large Stokes shifts and possess high quantum yields, molar absorption coefficients are moderate. The complex Ir(ppy)$_2$(carbac) (Figure 2.8) shows good temperature sensitivity (-0.5%τ/K) and brightness but unfortunately is not very photostable. A cyclometalated Pt(II) complex, Pt(Brph-thq)(acac) was found useful as temperature probe in a composite material for dual oxygen and temperature sensing.[117]

Lanthanide chelates belong to another group of commonly used temperature probes. Generally, Eu(III) and Tb(III) ions are combined with various diketonate ligands (c.f. Eu(TTA)$_3$, Figure 2.8) and optionally additional ligands acting as an antenna. Compared to other metal-ligand complexes, their luminescence is not or much less affected by oxygen quenching. This is due to their filled outer s and p orbitals that are protecting the valence electrons in the f orbitals from external electric fields. These complexes are generally characterized by their narrow luminescence bands and high temperature sensitivity but often have only limited stability in polar solvents. The excitation maxima of the Eu(III) complexes generally lies within a range of 350 - 450 nm, and is even shorter for the Tb(III) complexes, which makes this class less favourable for bioanalytical applications.[118]

Phosphors consist of a host material doped with activator atoms. Typically, the luminescence originates from these activator atoms and is dependent on the dopant concentration. Generally, lanthanides (e.g. Er, Yb) or transition metals (e.g. Cr, Mn) are used as activators. Thermographic phosphors represent the only class suitable for wide range and high temperature measurement, as they are thermally stable and not easily oxidized or reduced. These materials are generally characterized by large Stokes/anti-Stokes shifts, band emissions, long luminescence lifetimes, and yet negligible cross sensitivity towards oxygen. However, the absorption of the

phosphors is much less efficient compared to organic and metal-organic dyes. Phosphors suitable for room temperature sensing are Er(III), Mo(III) - doped $Yb_2Ti_2O_7$ featuring upconverted emission[119] Mn(IV)doped magnesium fluorogermanate,[120] ruby,[121] spinel,[122] and Cr(III)-doped yttrium aluminium borate[123] but temperature coefficients for many of them are very moderate in room temperature region (Table 2.1). Cr(III)-doped yttrium aluminium borate, however, has relatively high sensitivity compared to other thermographic phosphors. The material has a relative sensitivity of -1.35%/K change of lifetime at 273 K. In contrast, the luminescence intensity changes only insignificantly with temperature. In general, the region of maximum sensitivity strongly varies for these materials.[124] For Er(III) doped materials, it is often reached only far beyond 400 K. For a few Ho(III) doped representatives, it lies below 100 K.

Beside molecular temperature probes and phosphors, the diverse class of nanomaterials also displays temperature dependent properties enabling their use for preparation of optical temperature sensors. Among this class, **quantum dots** (QD) generally possess high quantum yields, good photostability and strongly temperature dependent luminescence properties.[29,101,102] Their absorption and emission spectra can be tuned by controlling the size of the QD. Drawbacks include toxicity and the notorious blinking that can be as long as 100 s for some QDs.[125] For application, modification of the QD surface is necessary to improve solubility and eliminate quenching. Temperature can be measured using nearly all luminescence properties such as intensity,[126] intensity ratio,[127] decay time[128] and spectral shift.[129]

Up-conversion nanoparticles (UCNPS) are another type of temperature probes. The advantages and drawbacks of up-conversion materials are discussed in section 2.2.4. The temperature sensitivity of UCNPS is rather complex and individual for each system.[59] Often, however, the ratio of two transitions that have different temperature dependencies is measured. The most common host material for UCNPS is $NaYF_4$ and typically lanthanide ions, Yb^{3+}, Er^{3+}, Tm^{3+}, Nb^{3+}, Ho^{3+}, and Nd^{3+}, are incorporated as sensitizer or activator ions. The typical excitation wavelengths is 980 nm that originates from the use of Yb^{3+} as sensitizer. Also 808 nm excitation is possible, when Nd^{3+} is used as sensitizer.[23] For $NaYF_4$:Er^{3+},Yb^{3+} nanoparticles, the ratio of two luminescence bands of the Er^{3+} ions were used to measure temperature in HeLa cells.[130] A Er^{3+}/Yb^{3+} co-doped Gd_2O_3 phosphor is suitable for temperature measurement in the high temperature range from 300 to 900 K.[131] A silica shell coating can increase the thermal stability of UCNPS. Protected by a silica shell, also $NaYF_4$:Er^{3+},Yb^{3+} nanoparticles can be used for temperature measurement up to 900 K compared to 600 K for the uncoated UCNPS.[132] For temperature measurement in tissues, CaF_2:Tm^{3+},Yb^{3+} nanoparticles were found to enable penetration depths as large as 2 mm due their favourable NIR emission (from Tm^{3+} around 800 nm) and NIR excitation.[133]

Ln^{3+}-containing **metal organic frameworks** (MOFs) are promising sensing materials for the biological and cryogenic temperature range. In these MOFs, the lanthanide ions are the light-emitting centers with temperature sensitivity as it is seen in other lanthanide materials. The highest relative temperature sensitivities are found in MOFs with 31%/K in the cryogenic

Table 2.1: Figures of merits for various optical thermometers

Material	T [K]	Ex/Em [nm]	Relative sensitivity, $d\tau/dT$ [%/K]	Relative sensitivity, dI/dT [%/K] or dR/dT [%/K]	τ	T range [°C]	Ref.
Ru(phen)	303	470/580	-0.64	n.d.	3.6 µs	0 - 60	[138]
$[Ru(phen)_2(4\text{-}Clp)]^{2+}$	298	450/590	∼-1.35	-1.81 (273 K)	∼2.65 µs	0 - 40	[139]
$Eu(TTA)_3$	298	350/615	-2.3	-4.28	293 µs	5 - 50	[118]
EuDT	298	400/616	-2.2	-3.1	∼250 µs	10 - 50	[140]
$Ir(ppy)_2carbac$	303	405/519	∼-0.5	n.d.	2.2 µs	1 - 50	[141]
Mn_{4+}-doped magnesium fluorogermanate	274	355/620-683	-0.19	n.d.	3610 µs	25-725	[142]
Ruby	274	520 or 532/694	-0.25	n.d.	3980 µs	15-400	[122]
Spinel	274	520 or 532/690	-0.38	n.d.	9830 µs	15-400	[122]
Cr_{3+}-doped yttrium aluminium borate	274	422 or 600/NIR	-0.97	n.d.	237 µs	-10-70	[123]
$Y_3Al_5O_{12}$:Ce nanophosphor	298	337/700	-0.48	n.d.	25 ns	7-77	[143]
Sulforhodamine derivative	298	540/565-605	-1.3	n.d.	2.8 ns	5-55	[10]
Rhodamine B	301	400/575		-2.3		10-46	[111]
1 nm CdTe quantum dots	298	405/510	-1.7	n.d.	14 ns	20-50	[128]
arylamino-substituted anthraquinone	298	465/610	-3.7	n.d.	677 µs	5-50	[144]
carbazole-substituted anthraquinone	298	470/580	-2.7	n.d.	42 µs	5-50	[144]
carbazole-substituted dicyanobenzene	298	455/530	-2.0	n.d.	11 µs	5-50	[144]
$PS\text{-}C_{70}$/PAN film	293/363	470/700	∼-0.75 /-1.75	∼3.2/0.8	27.2 ms	-75 - 105	[5]
Pd(II) Schiff base complex	298	392/613	-2.1	-2.1	103 µs	5-65	[77]
Zn(II) Schiff base complex - Zn-1	298	456/542	-4.1	n.d.	5.71 ms	5-45	[115]
Zn(II) Schiff base complex - Zn-2	298	456/547	-3.5	n.d.	1.45 ms	5-45	[115]
Pd-O-S	310	470/640 and 772		∼3		20-120	[78]
Zn-O-S	298	490/670	-1.6	n.d.	7.9 ms (PS)	5-45	[79]
Benzofurazan fluorophore in poly(DBD-AE-*co*-NIPAM)	305	430/580	∼80		3-13.5 ns	23-38	[137]
poly(NIPAM-*co*-DBD-AA)	305	275/560	27		4.2 ∼ 14.1 ns	30-35	[136]
$Ca_8BaCe\text{-}(PO_4)_7$:Mn^{2+} phosphor	573	315/375	-5.14	∼2.17		30-300	[145]
LnMOF $Tb_{0.9}Eu_{0.1}$(pia)	300	360/546 and 615		-3.53		100-300	[146]
LnMOF $Tb_{0.957}Eu_{0.043}$(cpda)	300	335/546 and 615		-16		40-300	[134]
LnMOF $Tb_{0.95}Eu_{0.05}$HL	4	325/540 and 615		-31		4-290	[147]
Er-Mo:$Yb_2Ti_2O_7$ UC nanophosphor	300	976/525 and 550		∼0.8		290-610	[119]
Yb/Er: $NaGdF_4$@$NaYF_4$core@shell nanocrystals	300	980/528 and 540		1-1.2		303-333	[148]
ZJU-88 perylene dye MOF composite	293	388/473 and 615		1.3		293-353	[149]
Gd_2O_3:Yb^{3+}/Er^{3+} phosphor	300	980/525 and 555		1.5		298-723	[150]

range ($Tb_{0.95}Eu_{0.05}$HL at 4 K) and 16%/K ($Tb_{0.957}Eu_{0.043}$cpda at 300 K)[134] in the biological range. However, the limited thermal (and sometimes chemical) stability also limits application.

Some optical thermometers are based on temperature dependent **conformational changes**. Here, a polymer chain undergoes a phase-transition. This phase transition can change the average distance between a FRET pair[135] or change the quantum yield of a dye due to a change in environment from hydrophobic to hydrophilic.[136,137] These materials only have a small measurement range (typicall 30-35 °C), but display extremely high sensitivities (c.f. table 2.1).

The reported materials all have their merits and shortcomings and may be already well adapted for specific applications. For future materials, there is still much room for improvement regarding brightness, sensitivity, measurement range, photostability, spectral properties suitable

for biological samples[29] and two photon absorption properties. Hence, the search for alternative methods and concepts making use of other (luminescent) phenomena is still of high interest.

2.4 Cyclometalation

Cyclometalation describes the intramolecular metalation reaction forming a metal-carbon σ-bond between a (transition) metal and an already coordinated ligand resulting in a chelate ring (3-8 membered, 5 most common).[151] Cyclometalated complexes are rather stable and inert due to the chelate effect and the ligating ability of both involved donor atoms. Nearly any transition metal can participate in cyclometalation reactions, but the platinum metal group received most attention.[151]

The **metal precursor** is required to provide a site for coordination of the ligand.[151] This site can be provided by cleaved dimeric species or only loosely coordinated ligands. The metalation is facilitated by strongly basic ligands. These ligands then form products such as HCl, H_2, an alcohol or alkane. Especially, gaseous products that vanish from the reaction mixture are an additional thermodynamic driving force of the reaction.[151]

During the reaction, the **ligand** initially coordinates the metal center before the C-R bond (R is most often a hydrogen atom) is cleaved and the carbon-metal bond is formed. The ligand is usually coordinated via a heteroatom (such as N, O, P, S, Se, and As), but also "carbon-assisted" (ligand coordinated via carbene) cyclometalation has been reported.[151] The ligand needs to appropriately coordinate the metal. Not too strongly, then a second ligand would bind instead of C-R activation, and not too weakly, then the equilibrium would stay on the side of the starting materials.[151] The precoordination affects two aspects of the cyclometalation reaction. It changes the electronic situation at the metal center and it arranges the C-R bond in close proximity to the metal center.[151] The simplest and most often used ligand for these reactions is 2-phenylpyridine. The cyclometalation reaction is further facilitated if the leaving group at the metal center and the activated substituent R in the ligand combine well, such as H (R) and CH_3 (leaving group). This combination results in formation of methane which further drives the cyclometalation reaction forward.

The (anionic) carbon atom acts as a strong σ-donor and the heteroatom-containing group (e.g. pyridyl group) usually are good π-acceptors. This provides a strong ligand field. Importantly for the luminescence properties, the strong ligand-field raises the energy of metal centered d-d excited states. Energetically low d-d excited states promote thermally activated non-radiative deactivation pathways and consequentially deactivate luminescence.[152] Most luminescent complexes are based on Pt(II) or Ir(III) as central metal and they often have β-diketonates as second ligands. The group of Williams, however, also reported dually cyclometalated complexes with highly efficient luminescence.[153–158] The introduction of a second cyclometalated structure leads to red-shifted absorption and emission spectra and increased radiative rate constants.

Cyclometalated complexes have found application, inter alia, in organic light emitting diodes (OLEDs),[19,70] as photosensitizers for singlet oxygen generation,[159] as catalysts for organic reactions,[160] labels,[161,162] and indicators (c.f. section 2.4.2).

2.4.1 Synthesis of Cyclometalated Pt(II) β-diketonate Complexes
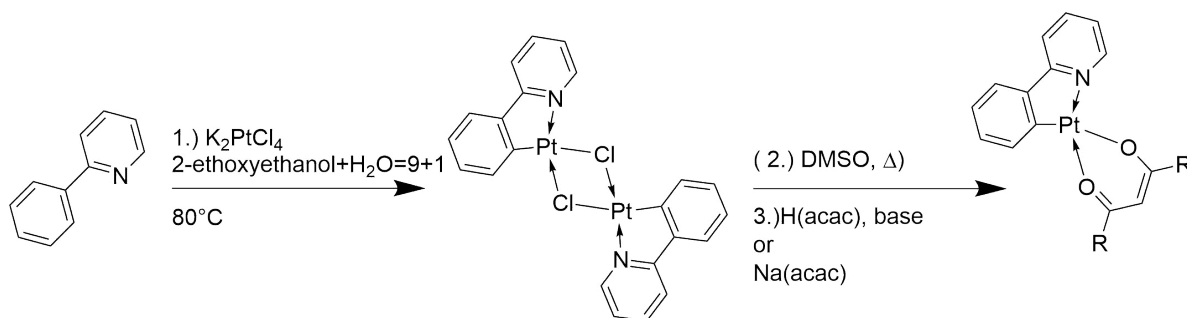
Figure 2.9: A typical reaction scheme for cyclometalation of 2-phenylpyridine via the μ-chloro bridged dimer.

In a typical procedure, K_2PtCl_4 is added to the ligand and the mixture is heated in 2-ethoxyethanol (+water mixtures) or refluxed in acetic acid.[163] This results in the formation of a μ-chloro bridged dimer (Figure 2.9). The dimer is then reacted with sodium β-diketonates or the corresponding diketones in presence of a base. There are variations of this procedure that include an intermediate step. Here, the μ-chloro bridged dimer is refluxed in DMSO to break up the dimer and form the chloro-DMSO coordinated complex.[153] The purification of this complex is easier than that of the β-diketonate complex. Finally, also here the β-diketonate is introduced via ligand exchange. The ligand exchange can be further faciliated by using Tl(I) β-diketonates that drive the reaction by precipitation of insoluble thallium(I) chloride.[164] Alternatively, the β-diketonate and dimer are reacted in the presence of Ag_2O that also facilitates cleavage of the dimer by driving the reaction via precipitation of AgCl.[165]

Other metal precursors that have been used include $PtCl_2(solv)_2$, $PtMe_2(solv)_2$, (solv = SMe_2, DMSO, benzonitrile), $Pt(acac)_2$ and the platinum amide $Pt(cod)Cl(N(SiMe_3)_2)$.[151] Also a one pot procedure at room temperature has been reported using $[PtMe_2(SMe_2)]_2$ as the platinum source/precursor.[166] The ligand is treated with $[PtMe_2(SMe_2)]_2$ giving a cyclometalated $Pt(ligand)Me(SMe_2)$ complex. The reaction is driven by the irreversible loss of CH_4. The complex is then treated with trifluoromethane sulfonic acid (TfOH). Again, CH_4 is lost and a OTf is introduced as a second labile ligand. SMe_2 and OTf are then readily replaced by sodium β-diketonates.

2.4.2 Cyclometalated Indicator Dyes

Cyclometalation was found to produce efficiently phosphorescent $Pt(II)$[152] and $Ir(III)$ complexes.[167] The heavy atoms introduce strong spin-orbit coupling that promotes intersystem crossing and further raise the energy of luminescence deactivating d-d states.[152] Unfortunately, cyclometalated complexes are often poor candidates for optical sensing due to very low molar absorption coefficients in the visible region. On the other hand, they exhibit large Stokes shifts, are photostable and possess high quantum yields. Cyclometalated Pt(II) and Ir(III) complexes

found application as indicators for optical oxygen (section 2.3.1)[6,61,64] and temperature sensing (section 2.3.2).[117] Typical representatives are phenylpyridine based [Ir(ppy)$_3$] (Figure 2.7),[65] thienylpyridine based Pt(thpy)$_2$,[66] and benzoisoquinolinedione as well as acetylacetonato coordinated CŃPt(acac) indicators.[67] Cyclometalated coumarin complexes represent a notable exception regarding poor vis-absorption, showing very efficient absorption in blue part of the spectrum and strong phosphorescence.[72]

2.5 Optical Luminescent Sensors - Considerations

2.5.1 Application to Indicator or Indicator to Application

Application of optical sensors implicates certain requirements for the sensor material. To fulfill these requirements, an appropriate combination of indicator/sensing chemistry, host material, additives/coatings/other components, and referencing is necessary. However, there is often a complex interplay between the components itself and the application that is not expected in the first place. Generally, there is no perfect choice or combination and trade-offs have to be made. Before individual points are addressed, a few questions should be considered and often help to prioritize the pros and cons of certain parts of the material.

- What do I want to measure (parameter, absolute values/relative changes) and for how long? What is state-of-the-art for this type of measurement?

- In which environment/sample is my sensor going to measure and are there specific requirements (response time, resolution, sterilization, stability etc.)? Are environmental parameters (temperature, composition) constant over time?

- What is the approximate (concentration) range of the parameter i want to measure?

- Are there optical inferences?

- Which interferences are expected from other chemical and physical parameters, microorganism (e.g. bioufouling), physical and mechanical stress?

- How small does it need to be?

- How many measurement points do I need?

- Does the sensor need recalibration over time? Can the sensor be accessed for recalibration?

- and etc...

These questions have implications on the various parts of the sensor material. For example, the second question about the environment can completely change sensor design. For an oxygen sensor, aqueous environments allow for use of standard materials for preparation of the oxygen sensor. In contrast, measurement of oxygen in solvents is very problematic. Here, typical issues include solubility of sensor components, swelling and leaching that affect response time, sensitivity, drift, and reproducibility. For pH and ion sensors, especially changes in temperature, ionic strength and specific ion composition can affect sensor characteristics. For pH sensors, temperature affects dissociation constants of indicators, the fraction of water in the host material, and photophysical properties (quantum yield, decay time) of indicators. The effect on the indicator also depends on the pH sensitive group. Phenols posses much lower

temperature coefficients compared to secondary and tertiary amines (in the range of -0.007 and -0.012[168] and -0.013 and -0.020 units/K,[169] respectively).

In the following subsections, a few points that require consideration are mentioned and addressed. This section, however, is by no means comprehensive.

2.5.2 Indicator
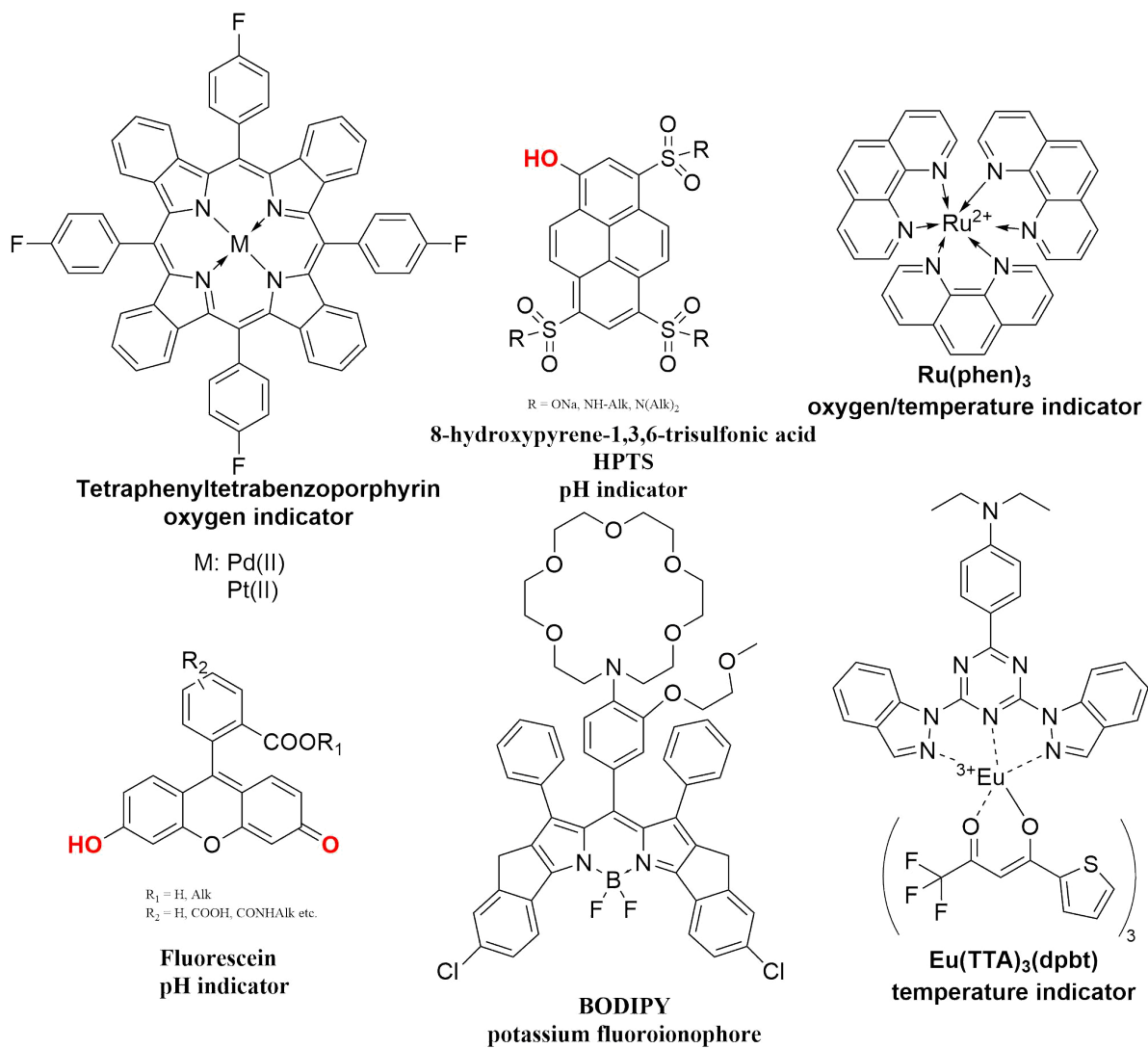
Figure 2.10: Chemical structures of indicator dyes used in optical sensors for oxygen, temperature, pH and ions.

The most obvious requirement for the indicator dye is to be **analyte sensitive**. In general, absorption, emission wavelength, quantum yield and decay time can be affected and used for measurement. Regarding the measurement setup, the chosen read-out parameter defines the requirements for instrumentation. A change in emission wavelength requires either multi-wavelength read-out or a spectrometer. In the most basic setup, a change in emission intensity

(induced from changes in quantum yield or absorption) only requires an LED and a photodiode. An analyte sensitive decay time can enable self-referenced measurement but generally has high instrumental requirements.

Ideally, the indicator is analyte/parameter **specific** . This, however, is hardly ever the case. Every indicator is, to a varying extent, sensitive towards temperature. Relatively long decay times introduce oxygen (cross-) sensitivity for temperature indicators such as $Ru(phen)_3$ (in Figure 2.10). From another perspective, $Ru(phen)_3$ is also used as an oxygen indicator with large temperature cross-sensitivity. Oxygen quenching, however, was also reported for pH indicators with decay times in the nano-second range such as HPTS (Figure 2.10).[11] Fluoroionophores based on ICT or PET effect have cross-sensitivities to ions of similar size or can be protonated (BODIPY, 2.10).

There are specific properties of the indicator dyes that define **sensitivity** and/or measurement range. For oxygen indicators based on quenching (Figure 2.10, porphyrin and ruthenium complex), the luminescence decay time defines the sensitivity towards oxygen. For fluoroionophores, the binding or stability constant is the equilibrium constant for the binding/complex formation reaction of the ion with the ionophore ((BODIPY, 2.10). This constant describes the affinity of the receptor to the analyte. The analogous constant for pH indicators is the K_a value, the acid dissociation constant, or its negative decadic logarithm, the pK_a. The pK_a can be seen as the center of the pH range ($\pm$ 1.5 pH units) over which the change of the indicators optical properties are useful for optical sensing.

The photophysical properties define how easily the analyte specific luminescence changes can be measured. The brightness is defined as the product of the molar absorption coefficient and the quantum yield. In other words, it is a measure for how much luminescence is emitted after excitation with light of a given wavelength. However, a high brightness can not always be fully utilized in practice. The Stokes shift is the difference in wavelength between absorbed and emitted photons. If absorption and emission maxima are close to each other (small Stokes shift), the separation of excitation and emission light becomes more challenging. This includes the choice of applied excitation and collected emission wavelengths. Often they are shifted to regions far from the maxima. Hence, the utilized brightness is reduced. Consequentially, also the Stokes shift is a crucial parameter for application.

Depending on the magnitude of the decay time, **instrumental requirements** significantly vary. Short nanosecond decay times require expensive instruments for measurement whereas microsecond decay times are accessible with cheaper instruments. Longer decays enable reduction of optical interferences. Background fluorescence and fading of excitation light sources can be cut off during measurements.

The location of absorption and emission wavelength controls the amount of scattering and background fluorescence caused in the sample (of biological origin) and the penetration depth of excitation light.

The overall and longterm performance is also affected by dye migration or leaching, aggre-

gation and properties such as photostability and chemical stability. Fluorescein displays poor photostability that result in severe bleaching during microscopy experiments. Metal ligand complexes such as $Eu(TTA)_3(dpbt)$ (Figure 2.10) often are prone to ligand exchange reactions with the environment, in given case with polar solvents. All this terms/effects result in a changing indicator concentration that significantly affects all but self-referenced measurement types.

The structure of the indicator dye also controls the possibilities for immobilization. There can be functional groups that allow for covalent immobilization (R_2 of the fluorescein in Figure 2.10). Appropriate substitution can also improve solubility and consequentially reduce/eliminate leaching and aggregation (alkyl groups on HPTS, Figure 2.10).

2.5.3 Host Material
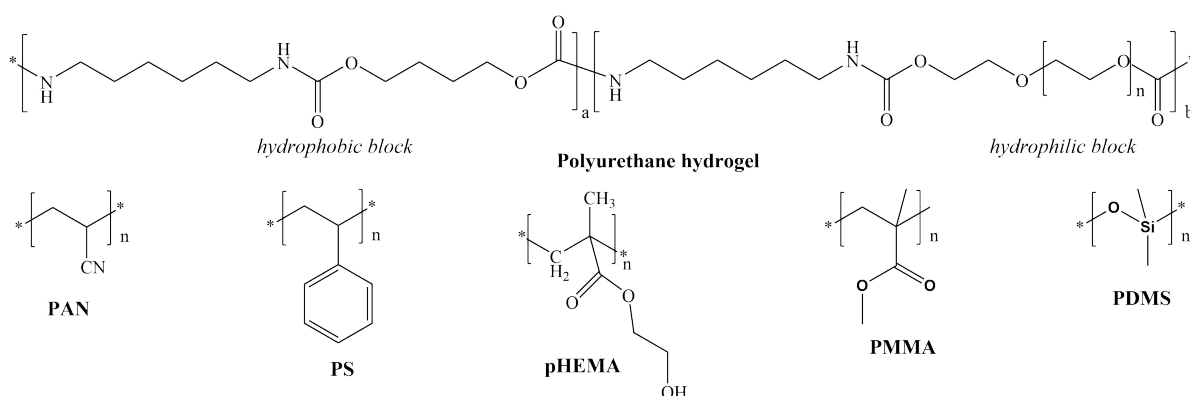
Figure 2.11: Chemical structures of polymers used as host materials in optical sensors.

The host material is of significant importance for the performance of optical luminescent sensors. The host material is used to immobilize the sensing chemistry in fixed/known environment and to separate it from the sample. This is due to the fact that the properties of the sensing chemistry change in dependence of the environment and that the sample can be contaminated by the sensing chemistry. Generally, outside the matrix the indicators can be diluted/washed away, aggregate, change their quantum yield or spectral properties or be quenched by unknown components of the sample. A basic requirement is that the host material needs to dissolve the indicator dye or allow covalent coupling to the surface and be permeable for the analyte.

For **immobilization**, there are various possibilities available (Figure 2.11), but not all methods may be suitable for every indicator and host combination. Typical methods include immobilization by physical means (adsorption, electrostatic, physical entrapment) or covalent immobilization where the indicator is chemically bonded to the host. The type of immobilization controls how well the indicator is retained inside the host material. For covalently immobilized indicators, the dye concentration does not change due to diffusion out of the matrix. For physically immobilized dyes, it depends on the solubility of the dye in the matrix and in the sample, charge of dye and host material, size of the dye and pore size of the host material

and other parameters. In heterogeneous polymers (e.g. polyurethane hydrogels, Figure 2.11), physically immobilized indicators, however, can also migrate into other domains that have different properties. Here, the indicators can aggregate, change properties or leach faster.

The host material influences/controls the **diffusion of the analyte** to the indicator dye. This directly affects the response time and sensitivity, but also specificity if other chemical species or interferents are blocked from interacting with the indicator (*c.f.* barrier layers in section 2.5.4). For oxygen sensing, the sensitivity is controlled by choice of the luminescence lifetime of the indicator and the oxygen permeability of the host material (*c.f.* section 2.3.1). For temperature sensing, there are indicators that are oxygen cross-sensitive (section 2.3.2). These indicators, however, can be immobilized in oxygen impermeable matrices such as PAN (Figure 2.11). The diffusion of solvent molecules, ions or other into the host material can lead to swelling or turbidity of the sensing material, which subsequently changes the sensor characteristics.

During (prolonged) storage of the sensing materials, some host materials display **aging effects**. Especially sol gels continuously react and become more cross-linked and hence denser. These structural changes affect the sensor characteristics and are the source of a continuous drift. The aging, however, depends on the conditions during storage. Storage in air resulted in significant aging effects for aminofluorescein/TEOS films, whereas storage in aqueous media left the sensor characteristics unaffected.[170] For plasticized PVC films, the plasticizer can be washed out over long term use. This affects analyte diffusion and stability of the sensor film. Chemical stability is important for oxygen sensors and measurement in harsh environmental conditions. Host materials are oxidized/photodegraded to a varying extent, among the less stable are e.g. poly[1-(trimethylsilyl)-1-propyne],[171] (especially long term) and PMMA (Figure 2.11).[172] Also rather stable materials such as polystyrene (Figure 2.11) are oxidized to some degree when singlet oxygen is involved. Highly reactive singlet oxygen is produced during oxygen sensing due to the mechanism of luminescence quenching. The oxidation of the host material by singlet oxygen, however, can have unwanted side effects. In oxygen trace measurements, reactions with the host material can significantly alter the oxygen concentration.[97] Hence, it is crucial that the host material does not consume oxygen, whereas this can be neglected for standard range oxygen sensors.

The host material also affects the **photobleaching** of the indicator. The photodegradation of polymers and dyes on its own is well known. The immobilization of dyes in host materials, however, affects the photodegradation of both components. For (oxygen) sensing films, the produced singlet oxygen is trapped in close proximity to the dye as the host material hinders diffusion. Also, reaction products from singlet oxygen with the host material can start free-radical reactions that photodegrade the dye.[173]

For measurements in the environment or biological media, longer measurements can be impaired by **biofouling**. Here, (micro)organism or plants grow on the sensing material. This can destroy the sensing material, produce local analyte concentrations that are different from the

environment, restrict diffusion of the analyte or lead to optical interferences from fluorescence of the organism.

Mechanical stability and adherence of the sensing film to support material is important for practical application of the sensing material and the durability. The adherence of the sensing layer to the support material can be improved by surface (pre-)treatment of the support material. The treatment changes the (functional) groups on the surface of the material. This can either change the polarity of the surface to match the polarity of the sensing layer or introduce functional groups that allow covalent coupling. Among possible treatments are plasma treatment (more hydrophilic surface), silanization (allows a wide range of possible surface modifications), or diazotisation (functional group for covalent coupling).

When **detergents** are present in the sample, they can diffuse into the sensing membrane and accumulate there. This can occur because detergents have analogous properties to plasticizers.

2.5.4 Additives, Coatings and other Components
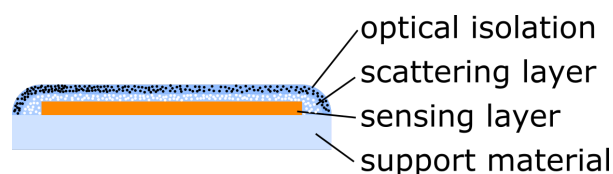
Figure 2.12: Cross section of a planar optode with additional layers for light scattering and optical isolation.

Barrier layer: Barrier layers prevent diffusion of certain components from the sample into the sensing layer that would normally diffuse through the host material. This prevents/reduces interferences and enhances selectivity. For excluding solvents and ions, a porous teflon layer can be used. This keeps interfering species out, but can also be used to keep the sensing chemistry inside. In ammonia sensing based on an internal buffer reaction, a teflon layer is used to block (water and other) ions from entering the sensing layer and the internal buffer solution is prevented from leaching out.[174]

Plasticizer: Plasticizers enable or improve diffusion of ions or ion carriers in otherwise hydrophobic materials, such as PVC. They are typically used in carrier-based ion-selective optodes that are based on the ion exchange mechanism and pH indicators. For the sensing material, the plasticizer affects the selectivity and measuring range.[175]

Scattering layer: scattering particles are used to enhance signal emission intensity by increasing the optical path of excitation light in the sensor materials. From materials with high refractive index, nanoparticles or microparticles are prepared and dispersed in the sensing layer or as an additional layer. Possible materials are titanium dioxide, diamond powder, cubic zirconia, zinc oxide and barium sulfate.

Optical isolation layer: optical isolations are used to separate/protect the sensing layer from optical interferences/light from the environment or sample background luminescence. The

isolation is usually just an opaque layer that is placed as last layer over scattering and sensing layers (Figure 2.12). Possible materials are lamp black, ferric oxide, barium sulfate or titanium dioxide.

A few aspects have to be considered when **additional layers** are coated over the sensing layer (Figure 2.12). For non-covalently immobilized indicators, there is the risk of indicator migration into the coating layers that may change sensor characteristics. Also, additional layers increase the distance between the sensing layer and the sample. Hence, they increase the distance for analyte diffusion. This slows down the response of the sensor.

Oxygen scavenger: oxygen scavengers can be used to control the oxygen concentration in a sensing material or microfluidic chips with integrated optical sensors. Various temperature indicators possess long luminescence lifetimes that introduce oxygen cross-sensitivity. To reduce oxygen cross-sensitivty, they can be immobilized in oxygen impermeable matrices (e.g. PAN)[5] or the sensing layer can be coated with an oxygen scavenging material (e.g. off-stoichiometry thiol-ene polymers (OSTE)).[115]

Photostabilizer: photodegradation is often caused by singlet oxygen. Singlet oxygen is produced by many indicator dyes. Photodegradation is especially problematic for longterm measurements, measurements with strong light sources or under continuous illumination. To prevent degradation, light intensities and measurement frequency may be reduced. Also more photostable indicator dyes can be chosen (e.g. fluorinated dyes, or dyes with protective functional groups such as tert. amino groups). As another strategy, additives can be used to reduce photodegradation for a given sensor material.[172] These additives are called photostabilizers and quench the highly reactive singlet oxygen. A typical representative is DABCO (Diazabicyclo[2.2.2]octane).[172]

Support material: for planar optodes, most sensing layers alone would not be mechanically stable enough for measurement. Support materials are used as a substrate onto which the sensing layer is coated. To ensure proper performance, the support material should be transparent to excitation and emission light, be chemically stable, and should not luminesce itself. Typical substrates, are poly(ethylene terephthalates) (PET), and glass. The substrates can be surface modified for better adhesion of the sensing layer. For fiber optic sensors, the fiber itself fulfills the function of a support material.

3 Purely Organic Dyes with Thermally Activated Delayed Fluorescence - A Versatile Class of Indicators for Optical Temperature Sensing
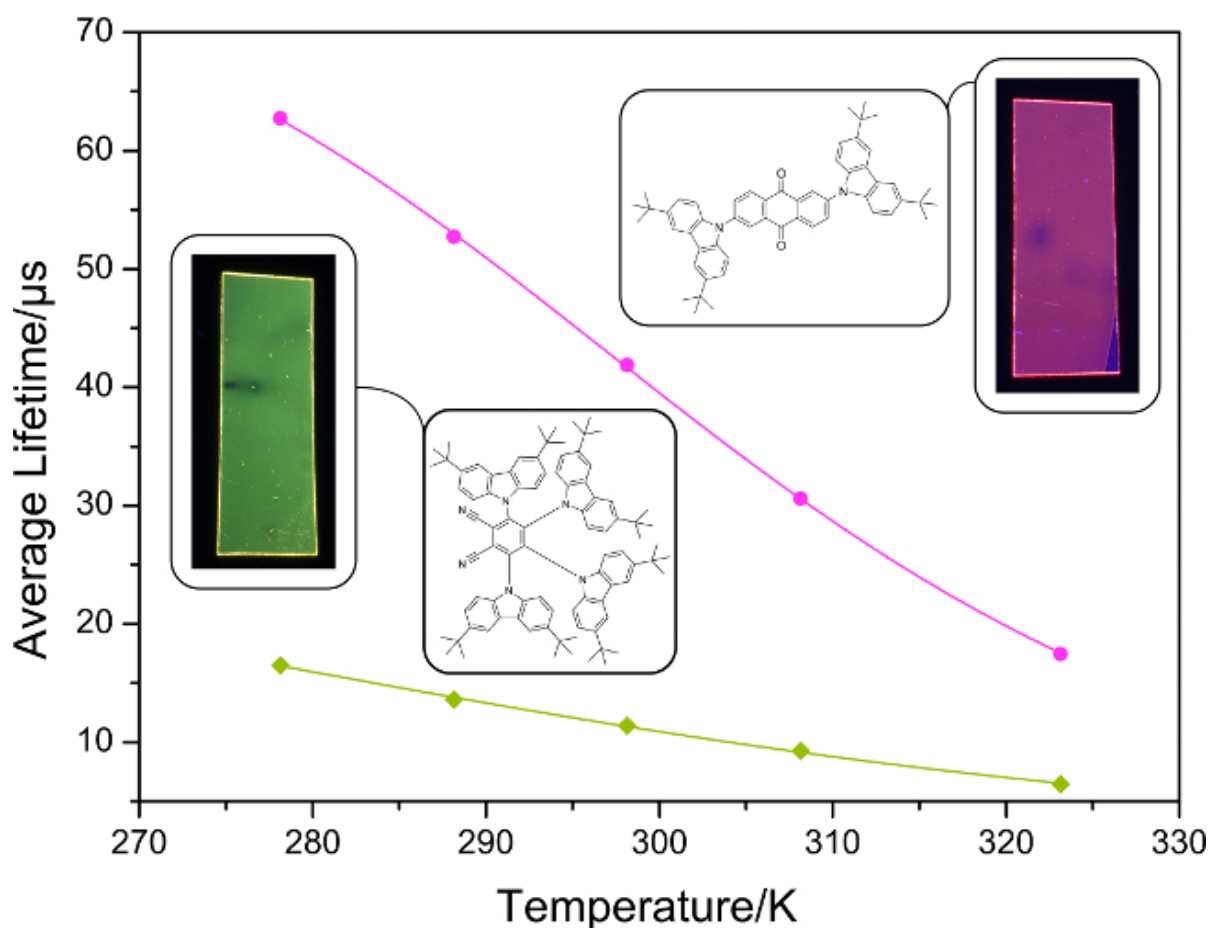
Preface to Chapter 3

This manuscript was published as *Full Paper* in *Advanced Optical Materials* and presents the study on two classes of TADF emitters and their applicability in optical oxygen and temperature sensing.

Many TADF emitters were reported in the last few years that were developed for organic light emitting diode (OLED) technology. Only some of the reported emitters fulfill the requirements for application in optical sensors: (i) absorption in the vis-region, (ii) adequate brightness, (iii) stability (chemical, photostability), (iv) possibilities for immobilization - compatibility with common host materials.

Two classes of TADF emitters were chosen that were potentially suitable for optical sensing applications according to reported photophysical properties. The two classes were carbazole-substituted dicyanobenzenes and anthraquinone based intramolecular charge-transfer dyes. Apart from literature known representatives, different modifications (substitution) were chosen to systematically investigate the influence of (a) the size of the conjugated π-system, (b) the rigidity of the donor unit, and (c) the introduction of heavy atoms. The classes showed excellent tunability of photophysical properties. Especially, the TADF lifetimes of the anthraquinone-based emitters could be controlled in the range 11-583 µs in toluene.

Regarding application, the TADF emitters do not offer any improvement for oxygen sensing compared to the state-of-the-art probes. The high temperature dependency of the TADF decay times, however, enables highly sensitive optical thermometry. The new temperature indicators display excellent sensitivity from -1.4 to -3.7% change of TADF lifetime per K. Oxygen cross-sensitivity was minimized by incorporation into virtually gas impermeable poly(vinylidene chloride-*co*-acrylonitrile).

We also demonstrated potential applicability of the new systems for imaging applications in biology and medicine. The indicators were incorporated into cell penetrating polymeric nanoparticles (RL-100). Also in the nanoparticles, the indicators display excellent temperature sensitivity.

Manuscript

Purely Organic Dyes with Thermally Activated Delayed Fluorescence - A Versatile Class of Indicators for Optical Temperature Sensing

Authors: A. Steinegger, I. Klimant, and S. M. Borisov*

Graz University of Technology, Institute of Analytical Chemistry and Food Chemistry, Stremayrgasse 9, 8010 Graz, Austria

E-mail: sergey.borisov@tugraz.at

Abstract: Carbazole-substituted dicyanobenzenes and anthraquinone based intramolecular charge-transfer dyes, two classes of organic thermally activated delayed fluorescence (TADF) emitters developed for organic lightemitting diode (OLED) technology, are prepared and investigated for their suitability for optical oxygen and temperature sensing. The new materials do not offer any improvement compared to the state-of-the-art probes in respect to oxygen sensing. In contrast, due to very high temperature dependency of the TADF decay times, the new dyes are particularly advantageous for optical thermometry. Contrary to many state-of-the-art optical thermometers, the dyes show only moderate decrease of TADF intensity at increased temperatures. The dyes immobilized into a nearly oxygen impermeable poly(vinylidene chloride-*co*-acrylonitrile) matrix feature excellent temperature sensitivity in the investigated temperature range (278-323 K) with 1.4-3.7% K^{-1} change of TADF lifetime at 298 K. Indicator-loaded cell penetrating cationic nanoparticles are prepared for biological applications and feature sensitivities from 2.2 to 2.8% K^{-1} change of TADF lifetime at 298 K. Moreover, fiber-optic minisensors enable fast monitoring of temperature fluctuations in small sample volumes. The outcome of our work demonstrates the high potential of organic TADF emitters for optical temperature sensing and imaging.

3.1 Introduction

Optical sensors have become an integral part of analytical chemistry. Sensors for pH,[176,177] ions,[175,176,178,179] oxygen,[6,61] carbon dioxide,[180,181] and other analytes based on luminescent materials have been well established and offer some distinct advantages over conventional sensing schemes. They are inexpensive, miniaturizable, noninvasive, allow contactless measurement and online monitoring, are suitable for imaging[182] and their properties can be optimized for almost any desired application.

State-of-the-art oxygen indicators mostly rely on complexes of platinum group metals; the most common representatives are platinum(II) and palladium(II) porphyrins, ruthenium(II) polypyridyls and Ir(III) cyclometallated dyes.[6,61] Although, these complexes display superior characteristics with regard to oxygen sensing, they are economically and ecologically less favorable for applications requiring large indicator amounts, such as food packaging and pressuresensitive paints.[183–185] Additionally, conventional oxygen indicators are often prepared in multistep synthesis which further increases the cost of the optical sensors. Therefore, easily accessible purely organic dyes with long lifetimes would be highly desirable for oxygen sensing.

Another field of particular interest, but still in need for more advanced probes, is optical thermometry based on luminescent materials.[29,101,102] Temperature, as a key parameter to numerous physical, chemical, and biological processes, can be measured by a variety of methods (e.g., liquid-in-glass, dilatation, bimetallic, Seebeck effect based, etc.[186]), with only a few reaching spatial resolution smaller than 10 µm[14] (e.g. thermocouple for intracellular measurement[187] and carbon nanotube-based nanothermometers[102]). These traditional methods do not address applications, especially in medical and biological research, requiring high spatial resolution and high temperature coefficients combined with noninvasive read-out. Optical luminescent thermometry is highly suitable for these applications as it enables sensing on cellular level, features instant response and enables continuous measurement, providing the basis for investigation of temperature changes upon cellular activity as demonstrated, e.g., for in vivo temperature sensing in Zebrafish larva.[188] Common optical probes include inorganic phosphors,[124,189] metal ligand and lanthanide complexes,[118] organic dyes,[2,3,10,113,190] polymers (e.g., PNIPAM or PNNPAM),[188,191] nanomaterials,[192,193] and proteins.[194] Major drawbacks that limit applications can be poor stability, UV excitation, poor quantum yields, moderate temperature resolution, and toxicity.

Metal-free organic dyes featuring thermally activated delayed fluorescence (TADF) have been intensively investigated in recent years[195–208] due to their high potential for Organic Light Emitting Diode (OLED) industry.[13,209–213] However, application of TADF outside of OLED technology is still very rare. Particularly, applicability of TADF emitters for time-resolved imaging has been proposed[1] and application of acridine yellow[2] and C_{70}-fullerenes[3] for optical temperature sensing has been demonstrated. Since TADF relies on reverse intersystem crossing, it shows strongly temperature-dependent behavior and has high potential for optical temperature sensing. The inherently long lifetimes of TADF render the dyes also susceptible to oxygen quenching, and therefore may make them promising for oxygen sensing. Therefore, further research in this direction is definitely of high interest.

In this contribution, we apply two different classes of organic TADF emitters (carbazole-substituted dicyanobenzenes[209] and anthraquinone based intramolecular chargetransfer dyes[214]) for optical oxygen and temperature sensing and demonstrate their high potential due to simple synthesis, good tunability of the photophysical properties, high photostability, and large Stokes shifts. The temperature sensitivity in the physiological range is among the highest in literature[29]

and the new dyes valuably extend the present library of temperature probes.

3.2 Results and Discussion

3.2.1 Choice of Materials

Although many TADF chromophores were reported in the last few years, those potentially suitable for optical sensing applications should fulfill the following requirements: (i) be excitable in the visible part of the spectrum; (ii) possess good brightness which is defined as a product of molar absorption coefficient ε and luminescence quantum yield; (iii) have good photostability; and (iv) show adequate solubility in polymers to avoid aggregation after immobilization. Evidently, only some of the reported TADF emitters fulfill these requirements, since high molar absorption coefficients in the visible part of the electromagnetic spectrum are not relevant for OLED applications. Therefore, we choose two different chromophore classes based on anthraquinone and dicyanobenzenes (Figure 3.1), which were reported to absorb in the visible part of the spectrum and emit orange and green TADF, respectively.[209,214]

The individual substituents for the anthraquinone based dyes were chosen to systematically investigate the influence of (a) the size of the conjugated π-system (a1 and a3, a8, a9), (b) the rigidity of the donor unit (a1 and a7), and (c) the introduction of heavy atoms (a2 and a5). In the dicyanobenzene series, the influence of the substitution pattern on the sensing properties is of particular interest. Finally, highly conjugated compound e extends the donor–acceptor–donor (D-A-D) architecture of the anthraquinone dyes a1-a9 to D-A-D-A-D structure.

3.2.2 Synthesis

The anthraquinone based dyes a1–a9 were synthesized from 2,6-dibromoanthraquinone and *N,N*-diarylamines via a Buchwald–Hartwig amination adapting a literature procedure.[214] Yields were moderate to good (from 18% for a7 to 68% for a6). Moderate solubility of some representatives (such as a2, a5, and a7) negatively affected the yields due to more laborious purification. It should be emphasized that the dyes a1, a4, a6–a9 can be prepared via a single step in multigram quantities.

Two dyes a1 and a4 were further brominated by Lewis acid catalyzed electrophilic aromatic substitution giving a2 and a5, respectively, with intention to increase spin orbit coupling and to introduce a functionality for further modification via Suzuki coupling (a3).

The dicyanobenzene dyes b, c, and d1 were prepared adapting the literature procedure[209] starting from different isomers of tetrafluorodicyanobenzene and carbazole via an aromatic nucleophilic substitution. 3,6-Di-*tert*-butyl-9*H*-carbazole was used for synthesis of d2 with intention to increase the moderate solubility of d1.

Finally, oligomeric e was synthesized via Suzuki coupling of 9,9-diheptylfluorene-2,7-diboronic acid and 2,6-dibromoanthraquinone and subsequent Buchwald–Hartwig amination.
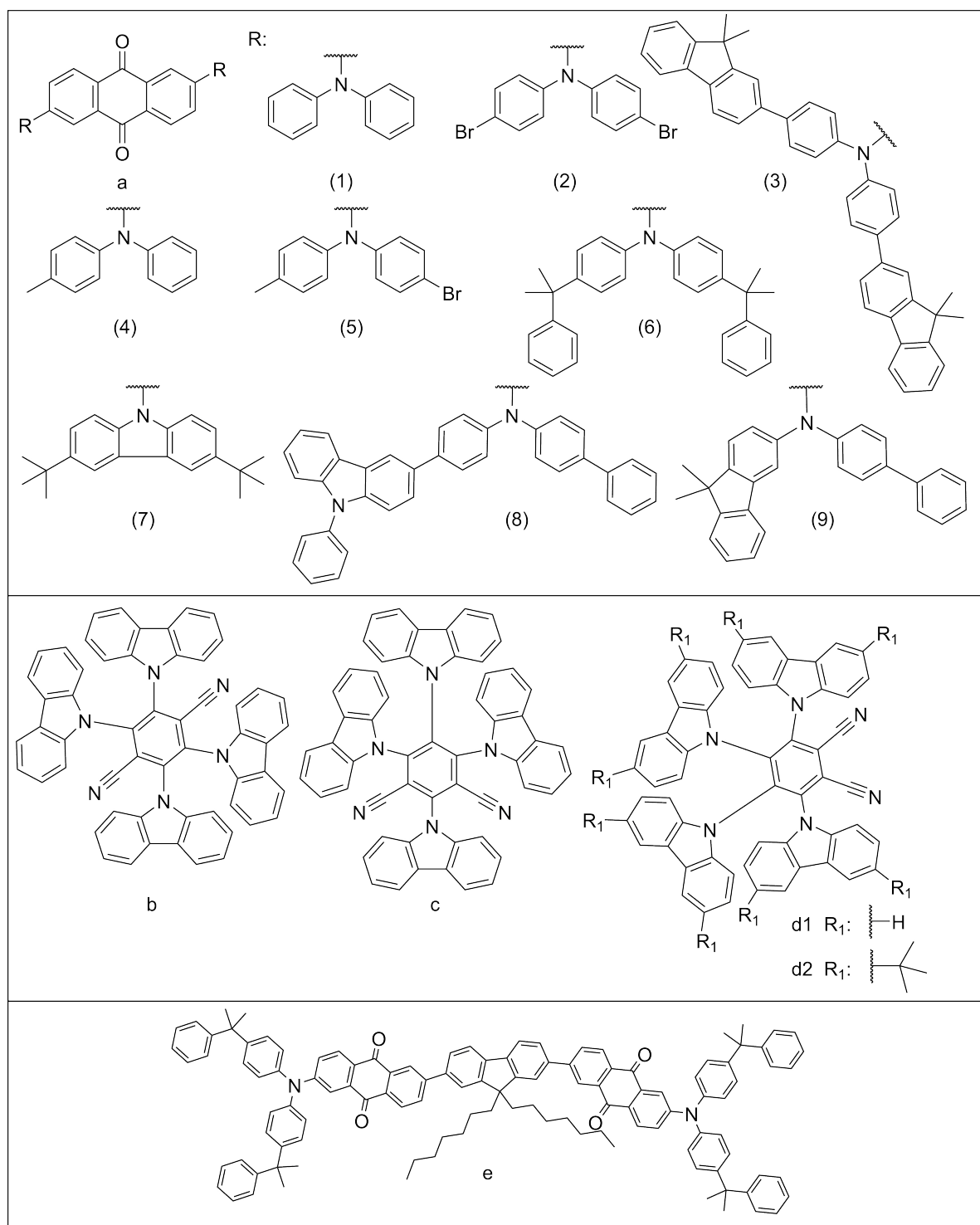
Figure 3.1: Chemical structures of the investigated TADF emitters.

3.2.3 Photophysical Properties

The absorption and emission spectra in toluene of several representatives of the dyes are shown in Figure 3.2a and Figures S3.1–S3.3 of the Supporting Information. The dyes feature absorption in the violet to green region of the spectrum and broad emission peaks in the green (dicyanobenzene-based dyes b, c, d1, and d2) or in the orange-red part of the spectrum (anthraquinone-based dyes a1-a9 and e), cf. Table 3.1. The molar absorption coefficients are moderate and are generally significantly higher for the anthraquinone derivatives ($\varepsilon \approx 20\ 000$ $m^{-1}\ cm^{-1}$ in the visible part of the spectrum except for a7) compared to the dicyanobenzene derivatives.

The Stokes shifts for both dye classes are very large (from 80 nm for b to 205 nm for a8). Such properties are particularly valuable for sensing applications since the emission can be efficiently separated from the excitation light. The emission peaks are increasingly bathochromically shifted with increasing size of the π-system (λmax 618 nm for the diphenyl-amine-substituted a1 and 667, 676, and 678 nm for larger substituents in a9, a8, and a3, respectively). Electron-donating alkyl groups introduced into the diphenyl-amino part also bathochromically shift the emission wavelength (λmax 631 and 651 nm for a4 and a6, respectively, compared to λmax 618 nm for a1). Bromination of compounds a1 and a4, giving a2 and a5, respectively, shifts the emission peaks hypsochromically by 2-3 nm per added bromine.

The dicyanobenzene based dyes are characterized by high quantum yields (0.61-0.78) in toluene with already large shares of TADF. In contrast, the anthraquinone based dyes show low quantum yields in solution, a2 being the highest with 0.15, most others with values below 0.10. All dyes apart from c display a single-exponential TADF decay in toluene, ranging from 5 to 15 µs within the dicyanobenzene based series and varying over a very wide range, from 11 to 583 µs, within the anthraquinone based series. Notably, the rigid carbazole-substituted derivative a7 shows the shortest decay time among the anthraquinone dyes (a1-a9 and e, cf. Table 3.1).

As expected, bromination results in a decrease of the TADF lifetime (334 and 123 µs for a2 and a5, respectively, compared to 581 and 245 µs for a1 and a4, respectively) due to the heavy atom effect which is also manifested by increase in quantum yields of the TADF compared to prompt fluorescence. The size of the substituents in the anthraquinone-based dyes also seems to affect the TADF decay times (shorter decay time for larger substituents) which may be due to more efficient nonradiative deactivation. However, the decay time for the largest molecule, conjugated oligomer e, is almost identical to that of a1.

At 77 K time-resolved spectra of two dyes (a2, d1) were measured in a mixture of tetrahydrofuran (THF)/toluene (6/4, v/v), which at this temperature forms a frozen solvent glass, to investigate the presence of phosphorescence. TADF was expected to disappear at low temperature, since the reverse intersystem crossing is a highly temperature dependent process. For a2 this proves true and is accompanied by the appearance of a small share of phosphorescence which is visible in the time-resolved spectra (Figure S3.4a, Supporting Information). For the dicyanobenzene dye d1, however, even at low temperatures efficient TADF occurs (Figure S3.4b,

Supporting Information) with drastically increased decay times ($\approx$1 s), the decay being visible with a naked eye.
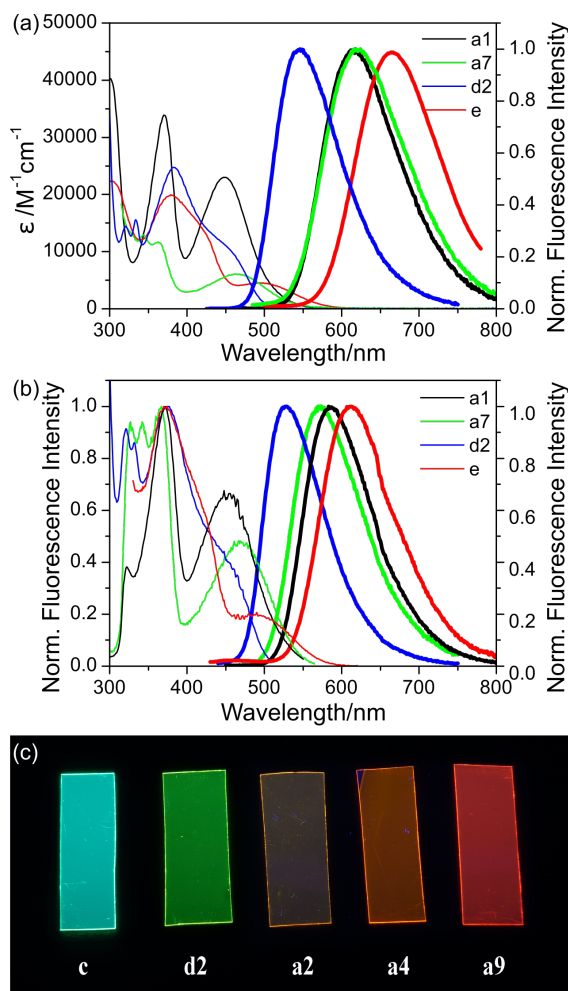
Figure 3.2: (a) absorption and emission spectra of the selected representatives in toluene at 25 °C, (b) excitation and emission spectra of the same dyes immobilized in polystyrene at 25 °C, (c) photographic images of the dyes immobilized in polystyrene under UV-excitation.

3.2.4 Photophysical Properties of Immobilized Dyes

Immobilization of dyes in polymers is essential for their application in materials for optical oxygen/temperature sensing. Therefore, we choose moderately oxygen-permeable polystyrene (P_{O2} = 2 × 10^{-13} cm^3 (STP) cm cm^{-2} s^{-1} Pa^{-1}[15]) and virtually gas-impermeable poly(vinylidene chloride-*co*-acrylonitrile) (P_{O2} = 0.0031 × 10^{-13} cm^3 (STP) cm cm^{-2} s^{-1} Pa^{-1}[16]) for preparation of oxygen-sensitive and temperature-sensitive materials, respectively. The incorporation of the indicator dyes into rigid polymer induced a hypsochromic shift of the emission peaks (cf. Figure 3.2a,b; Figures S3.1-S3.3 and S3.5-S3.7, Supporting Information; Tables 3.1 and 3.2). This shift can be explained by the lacking stabilization of the highly polar ^{1}CT excited

Table 3.1: Photophysical properties of the dyes in toluene solution at 25 °C.

Dye	$\lambda_{abs,max}$ [nm]/ε[M^{-1}cm^{-1}]	$\lambda_{em,max}$ [nm]	τ_{TADF} [μs]	ϕ_F/ϕ_{TADF} [%]	Dye	$\lambda_{abs,max}$ [nm]/ε[M^{-1}cm^{-1}]	$\lambda_{em,max}$ [nm]	τ_{TADF} [μs]	ϕ_F/ϕ_{TADF} [%]
a1	370/34000, 448/23000	618	581	7/3	a8	327/92500, 380/37500, 470/23500	676	n.d.[a]	0.1/0
a2	372/30000, 448/20000	609	334	6/9	a9	334/73000, 383/37000, 473/25000	667	57	1/0.2
a3	345/62000, 472/13000	678	47	1/0.1	b	322/13000, 335/12000, 460/1200	537	2.9 (73), 19 (27)[b]	23/50
a4	373/27000, 453/19000	631	245	5/2	c	326/14000, 377/1500, 445$^{(sh)}$	506	5	23/56
a5	373/26500, 452/18000	625	123	5/3	d1	326/15000, 371/16000, 430$^{(sh)}$	528	16	11/57
a6	375/30000, 457/21000	651	140	4/1	d2	383/24500, 450$^{(sh)}$	546	8	11/50
a7	342/13000, 463/6000	617	11	3/3	e	379/20000, 492/4500	669	583	3/0.4

[a] signal too low for decay time measurement,

[b] bi-exponential fit (relative amplitudes),

$^{(sh)}$ shoulder

state by reorganization of surrounding molecules that occurs in solution.[214] Nevertheless, similarly to toluene solutions, the dyes with extended π-conjugation in the diarylamino-unit show bathochromically shifted absorption ($\approx$20 nm) and emission ($\approx$30 nm) spectra compared to the diphenlyamino-substituted anthraquinone and its brominated derivative indicating possibility of fine-tuning of the spectral properties.

The decay curves cease to be single-exponential and now adopt a biexponential form. From the two components average lifetimes were calculated and are listed in Table 3.2. According to Zhang et al.[214] the rigid matrix prevents the dyes from rotation, entrapping at least two different rotamers. Immobilization of the anthraquinone-based dyes into rigid polystyrene matrix also results in a drastic increase of TADF lifetimes and quantum yields (cf. Tables 3.1 and 3.2). This can be explained by prevention of collisions with surrounding molecules, which decreases the efficiency of nonradiative deexcitation pathways. All the anthraquinone-based dyes show moderate to high quantum yields of TADF. π-extension of the diarylamino group appears to decrease the ratio of TADF/prompt fluorescence (dyes a3, a8, a9). Interestingly, the TADF quantum yields and decay times of the brominated analogues in polystyrene are very similar to the nonbrominated dyes, which is in contrast to the behavior in solutions. Despite comparable quantum yields, the TADF decay time of the carbazole-substituted anthraquinone a7 is 1-2 orders of magnitude shorter than for the other emitters is the series.

Carbazole-substituted dicyanobenzene emitters preserve relatively short TADF decay time in polystyrene. Interestingly, the decay time is the longest for the *o*-dicyanobenzene derivatives, followed by *p*-dicyanobenzene and finally by the *m*-substituted isomer. It should also be noted that *para*-substituted dyes show higher percentage of TADF in the overall emission, whereas prompt fluorescence is stronger than the delayed fluorescence for b and c.

Photostability of the dyes is an essential parameter for their practical applications. Due to pronounced change of photophysical properties upon immobilization into polymers, the photodegradation studies were performed for the polystyrene foils. The foils were continuously illuminated with high power 465 nm light emitting diode (LED) array (average irradiance 141.5 mW cm^{-2}). Measured absorbance reflects the amount of the remaining dye. As can be seen in

Table 3.2: Photophysical properties of the dyes immobilized in polystyrene (25 °C, anoxic conditions).

dye	$\lambda_{abs,max}$ [nm]	$\lambda_{em,max}$ [nm]	τTADF [µs](a)	ϕ_F/ϕ_{TADF} [%]	pd. [%][b]	dye	$\lambda_{abs,max}$ [nm]	$\lambda_{em,max}$ [nm]	τTADF [µs][a]	ϕ_F/ϕ_{TADF} [%]	pd. [%][b]
a1	372, 455	583	5560	8/38	5	a8	329, 466	614	973	11/15	2
a2	371, 448	577	4820	7/41	8	a9	336, 466	612	1200	11/21	2
a3	346, 466	608	1370	11/18	3	b	333, 455[sh]	531	17	38/21	1
a4	372, 455	594	2830	8/27	6	c	365, 450[sh]	493	9	58/38	1
a5	371, 448	589	2920	7/28	6	d1	366, 440[sh]	516	40	33/54	2
a6	373, 460	598	2840	8/26	7	d2	375, 455[sh]	528	21	40/53	<1
a7	367, 470	577	42	15/28	n.d.	e	370, 490[sh]	611	2820	21/5	<1

[a] average decay times,

[b] amount of degraded dye after 60 min irradiation,

[sh] shoulder

Figure S3.8 in the Supporting Information and Table 3.2, the dicyanobenzene based dyes (b–d2) are remarkably photostable showing less than 2% bleaching after 1 h of continuous irradiation. The, anthraquinone based dyes (a1–a9) degraded about 2–5 folds faster, however they can still be considered as very photostable compounds. Interestingly, the anthraquinone dyes with piextended donor substituents (a3, a8, and a9) appear to be more photostable than the other representatives. Since the photobleaching experiments were conducted under air saturated conditions, reaction of singlet oxygen with the dye may be an important photobleaching pathway. The dyes a3, a8, and a9 have lower share of TADF and therefore possibly lower singlet oxygen quantum yields. Additionally, shorter TADF lifetimes of these representatives may be beneficial if singlet oxygen predominantly reacts with the dyes in their (more reactive) triplet excited state.

3.2.5 Oxygen Sensing Materials

Oxygen sensing materials were prepared by incorporating the dyes into polystyrene matrix, which is a commonly used material with good chemical stability and moderate oxygen permeability. Oxygen sensing properties were evaluated in the intensity based measurement (Figure 3.3). Corresponding to the wide range of covered TADF lifetimes (42 µs to 5.5 ms), the sensitivity of the sensors spans from low (b, c, d1, d2) to remarkably high (a1, a2, a4–a6) (Figure 3.3a,b). The Stern–Volmer plots are not linear which can be explained by the residual prompt fluorescence which is not quenched by oxygen. Similarly to oxygen sensors based on state-of-the-art indicators, which lack the unquenchable luminescent component, existence of less oxygen-permeable domains in the polymer may be responsible for additional nonlinearity of the curves. Nevertheless, not being physically meaningful as applied to our systems, the equation

from the two site model can be used to fit the calibrations almost ideally (Equation (3.1))[31]

$$\frac{I}{I_0} = \frac{f}{1 + K_{SV}^1 pO_2} + \frac{1 - f}{1 + K_{SV}^2 pO_2} \tag{3.1}$$

where K_{SV}^1 is the Stern–Volmer constant for the quenchable component and f is share of this emissive component.

The calculated fit parameters are listed in Table S3.1 (Supporting Information). As can be seen, the sensitivity of the sensors spans over the three orders of magnitude ($K_{SV}^1 = 1.15$ and 0.0017 hPa^{-1} for a1 and c, respectively). It should be mentioned that more and less sensitive sensors can easily be prepared by immobilizing the same dyes into polymers with higher (e.g., ethylcellulose, organically modified silica, etc.) or lower (e.g., poly(styrene-*co*-acrylonitrile) oxygen permeabilities. The bimolecular quenching constants $k_q = K_{SV}^1/\tau_0$ are similar to the common phosphorescent oxygen indicators embedded into polystyrene such as platinum(II) pentafluorophenylporphyrin (k_q 3.29 Pa^{-1} s^{-1}),[72] platinum(II) tetraphenyltetrabenzoporpyhrin (k_q 2.98 Pa^{-1} s^{-1})[217] or ruthenium(II)-tris-4,7-diphenyl-1,10-phenanthroline (k_q 4.22 Pa^{-1} s^{-1}).[72] Interestingly, the k_q constants appear to be lower for the anthraquinone dyes bearing largest conjugated diarylamino-substituents (a9, a8, and particularly a3).

As temperature is known to affect the calibration of all optical sensors to a certain extent, the temperature cross-sensitivities of the sensors were investigated and are depicted in Figures S3.9–S3.11 (Supporting Information). Aware of the temperature dependent reverse intersystem crossing involved in TADF, comparably high cross-talk was expected. However, the temperature cross-sensitivity of the sensors was found to be too large for them to be of high potential for oxygen sensing (Supporting Information), particularly considering that many good probes already exist.[6,61] On the other hand, high temperature sensitivity suggested application of the new dyes as molecular thermometers.

3.2.6 Planar Optodes for Temperature Sensing

Since no or low crosstalk of molecular thermometers to oxygen is highly desirable, we selected the dyes with comparably short lifetimes and incorporated them into a polymer matrix with very low oxygen permeability, namely poly(vinylidene chloride-*co*-acrylonitrile) (P(VDC-co-AN)) ($P_{O2} > 0.0031 \times 10^{-13}$ cm^3 (STP) $\times$ cm cm^{-2} s^{-1} Pa^{-1216}). Similar to the polystyrene foils, the dyes embedded into P(VDC-*co*-AN) can be excited at 450–470 nm which is a distinct advantage compared to many optical temperature probes such as Eu(III) complexes, Tb(III) complexes or Ir(III) complexes. They, therefore, show excellent compatibility with bright blue 455 and 465 nm LEDs. The change of the matrix from polystyrene (PS) to P(VDC-*co*-AN) induces a small red shift for both dye classes probably due to higher polarity of P(VDC-*co*-AN). For the anthraquinone based dyes, the shift is more pronounced with 20-30 nm; for the dicyanobenzene dyes, the shifts are all below 12 nm (cf. Table S3.2, Supporting Information). Furthermore, both lifetimes and quantum yields are reduced, with the effects being much more pronounced
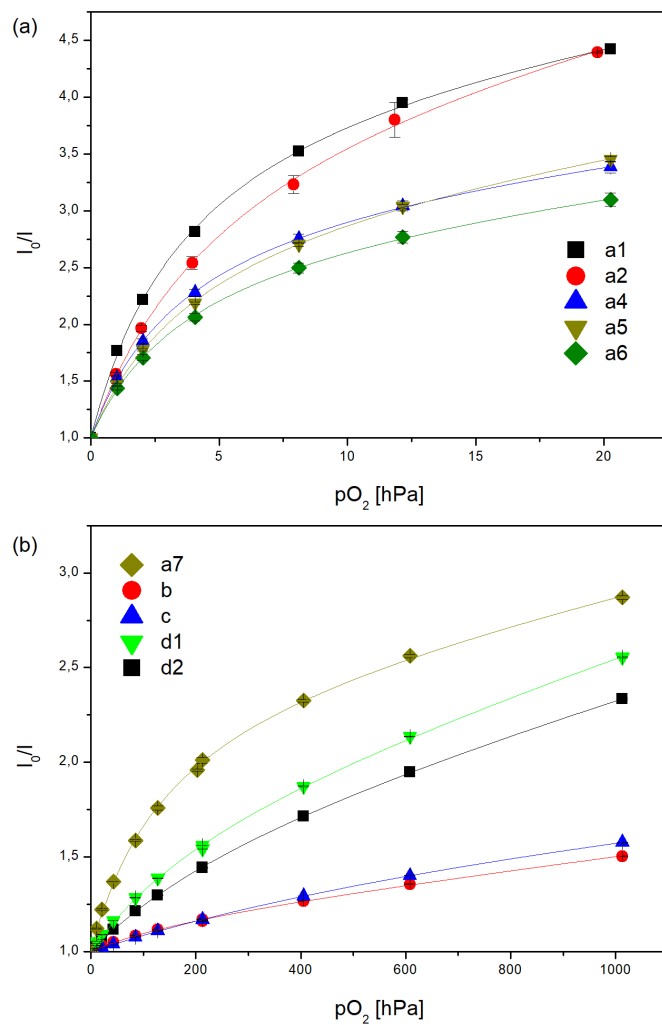
Figure 3.3: Stern-Volmer plots for the dyes immobilized in polystyrene (25 °C)

New Indicators for Optical Sensing by Manipulating the Intersystem Crossing in Luminescent Dyes

for the anthraquinone based dyes. Figure 3.4a,b shows that crosstalk of the sensing materials to oxygen is indeed very small since the calibrations obtained under deoxygenated conditions and at air saturation are virtually identical. Only minimal oxygen cross sensitivity for the dyes with longer lifetimes of about 1 ms (a3, a7, a8, a9) is observed. Such crosstalk is not critical, since extreme changes in oxygen content are not expected for most applications. It should be mentioned that polyacrylonitrile features even lower oxygen permeability, but high boiling DMF has to be used as solvent which is significantly less convenient for sensor preparation.

Temperature calibrations in the lifetime mode (average lifetimes obtained in the time domain measurement) reveal very high sensitivity of all the materials (Figure 3.4a,b). Linear regression almost ideally fits the experimental data ($r^2 > 0.99$), however a physically more meaningful Arrhenius type model[218] (Equation (3.2)) can also be used, with the latter one performing even better

$$\tau = (k_0 + k_1 e^{\frac{-\Delta E}{k_B T}})^{-1} \tag{3.2}$$

where k_0 is the temperature-independent decay rate for the excited-state deactivation, k_1 is a pre-exponential factor, k_B the Boltzmann constant, ΔE the energy necessary for the reverse Intersystem Crossing (ISC), and T the absolute temperature.

However, it has to be noted, that the uncertainty of the set temperature originating from the measurement setup (water bath, Peltier element, cuvette) contributes to deviations of the experimental data from the calibration model. The relative sensitivities of the sensors in % change of τ per K at 298 and 310 K are listed in Table 3.3. They vary from -1.4 to -3.7% K^{-1} at 298 K and are even higher at 310 K. These values exceed those of the highly sensitive state-of-the-art optical thermometers such as Eu(III) chelates,[118] Ru(II) tris-phenanthroline[218] or Cr^{3+}-doped yttrium aluminium borate[123] showing values between -0.64 and -2.3% lifetime change per K (Table 3.4). Notably, lifetime sensitivity of other useful optical thermometers is even smaller, e.g., Mn^{4+}-doped magnesium fluorogermanate,[120] ruby,[121] and spinel[122] (Table 3.4).

In contrast to the very high sensitivity of the TADF lifetime to temperature, the decrease in intensities with increasing temperature is much less pronounced. As estimated from the timeresolved measurements of TADF and the steady state experiments, the TADF intensity of the sensing materials decreased by less than 2 folds over the measured temperature range (278-323 K). Such behavior is highly advantageous since temperature does not significantly affect the signal to noise ratio. It should be mentioned that the situation is opposite for most of the phosphorescent and fluorescent lifetime-based temperature probes for which the decrease of the intensity is at least comparable and in most cases more pronounced than the lifetime changes.

Table 3.3: Relative sensitivities of the dyes immobilized in poly(vinylidene chloride-*co*-acrylonitrile) (anoxic conditions).

dye	dt/dT [%/K] at 298 K	t [µs] at 298 K	dt/dT [%/K] at 308 K	t [µs] at 308 K	dye	dt/dT [%/K] at 298 K	t [µs] at 298 K	dt/dT [%/K] at 308 K	t [µs] at 308 K
a3	-3.7	677	-4.2	540	b	-1.4	11.5	-1.5	9.9
a7	-2.7	42	-3.3	31	c	-1.7	7.3	-1.7	6.3
a8	-3.1	598	-3.5	459	d1	-2.0	21.9	-2.2	18.0
a9	-3.3	659	-3.5	496	d2	-2.0	11.4	-2.1	9.4
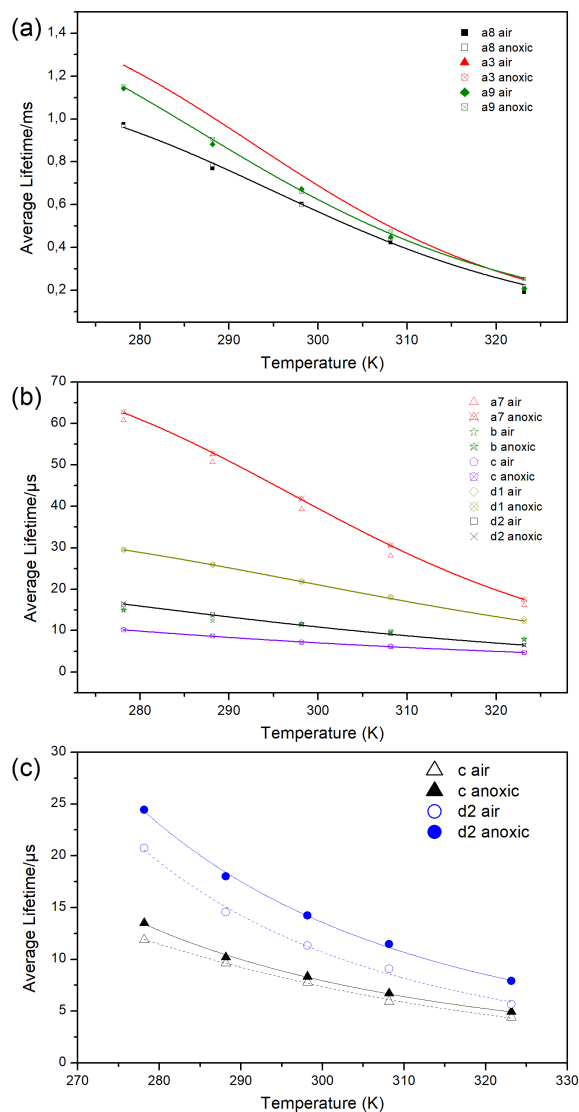
Figure 3.4: (a, b) Temperature dependence of the average luminescence decay times of the dyes immobilized in poly(vinylidene chloride-*co*-acrylonitrile) (c) Temperature dependence of the average luminescence decay times of two dyes incorporated into RL100 nanoparticles.

Table 3.4: Properties of common probes for optical thermometry based on the luminescence lifetime read-out.

Material	Temperature [K]	dt/dT [%/K]	τ	Reference
Ru(phen)/PAN	303	-0.64	3.6 µs	[138]
Eu(TTA)$_3$/FIB (fluoroacrylic polymer)	298	-2.3	293 µs	[118]
EuDT/(BTD-PMMA)-silica nanoparticles	298	-2.2	∼250 µs	[140]
Mg$_4$FGeO$_6$:Mn(IV)	274	-0.19	3610 µs	[120]
Ruby	274	-0.25	3980 µs	[121,122]
Spinel	274	-0.38	9830 µs	[122]
YAl$_3$(BO$_3$)$_4$:Cr(III)	274	-0.97	237 µs	[123]
Y$_3$Al$_5$O$_{12}$:Ce nanophosphor	280	-0.65	18.5 µs	[143]
Sulforhodamine derivative/RL100	298	-1.3	2.8 ns	[10]
1 nm CdTe quantum dots	298	-1.7	14 ns	[128]
a3/(P(VDC-*co*-AN))	298	-3.7	677 µs	This work
a7/(P(VDC-*co*-AN))	298	-2.7	42 µs	This work
d2/(P(VDC-*co*-AN))	298	-2.0	11 µs	This work

3.2.7 Fiber-Optic Temperature Minisensor

In order to underline the practical applicability of the new materials, we prepared a fiber-optic minisensor by coating the distal end of the glass optical fiber (Figure 3.5b) with the temperature-sensitive composition based on d2 immobilized into poly(vinylidene chloride-*co*-acrylonitrile). An additional optical isolation layer (carbon black in silicone rubber) was coated over the fiber tip in order to completely eliminate the potential interferences associated with autofluorescence of the probe or light scattering. The fiber-optic sensor is interrogated with a compact USB-powered phase fluorometer from PyroScience (Figure 3.5b). Although the current optical set-up (Figure 3.5a) shows only very limited compatibility with the spectral properties of the indicator dye (less efficient excitation with a blue 465 nm LED and only partial collection of the emission with help of OG 590 long-pass filter), high resolution self-referenced measurement (phase shift) is clearly possible (Figure 3.5c) even with this set-up. In fact, the response of the sensor to temperature changes is fully reversible. However, the most remarkable feature of the new sensor is its very fast dynamic response which is well below 0.5 s. It should be mentioned here that not only the optical set-up can be significantly improved in future via modification with a better matching LED (405, 435, or 455 nm) and filters but also even smaller microsensors (tapered 430 µm or 230 µm fibers with tip diameter of 40-60 µm) can be easily manufactured in a similar way and are expected to enable even faster measurements in smaller probe volumes.

(a)

dichroic filter
Linos DT cyan

blue LED 465 nm

filter deep golden amber

filter OG 590
photodiode

fiber

sensor layer

(b)

sensor layer with
optical isolation
(carbon black layer)

(c)

22°C

37°C

dphi/°

Time/s

dphi /°

Time/s
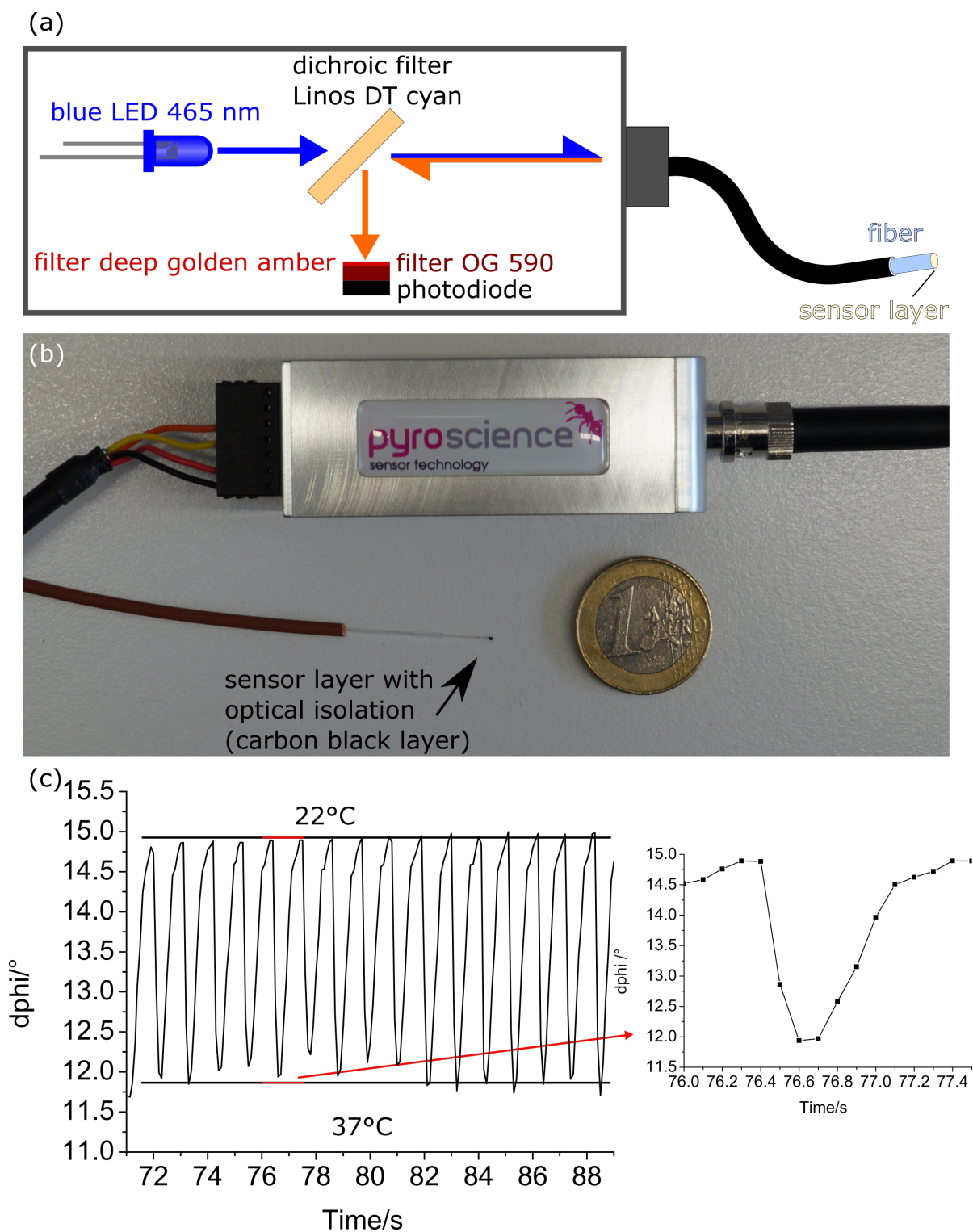
Figure 3.5: a) Schematic representation of the optical set-up of Firesting-mini phase fluorom-
eter from PyroScience. b) Photographic image of the phase fluorometer with the connected
fiber-optic temperature sensor. c) Response of the sensor to temperature changes obtained by
repeatable sensor transfer between two water-filled beakers (T = 22 and 37 °C, respectively).

3.2.8 Temperature Sensitive Nanoparticles

To show possible application in biology, two dyes were incorporated into cationic Eudragit RL100 nanoparticles as a model system for imaging at cellular level. Intracellular measurements play a crucial part in understanding cellular mechanism relevant to biology and medicine. Nanoparticles from RL100 are cell penetrating and have been used previously for intracellular oxygen and temperature measurements.[10,219] Since RL100 is a poly(methyl methacrylate)-based polymer and therefore moderately oxygen-permeable, dyes from the dicyanobenzene series (c and d2) have been incorporated into the beads to minimize the oxygen crosstalk. The temperature dependency of the TADF lifetime was investigated under air-saturated and deoxygenated conditions (2 wt% aq. Na_2SO_3). Figure 3.4c shows that the dyes immobilized into the nanoparticles preserve their high sensitivity of the TADF lifetime to temperature. Arrhenius type model fitting reveals relative sensitivities of -2.2 and -2.8% change of TADF lifetime per K at 298 K for c and d2, respectively, underlining potential application of the new material for intracellular nanothermometry. It should be mentioned that in case of d2/RL 100 nanoparticles, large fluctuations in oxygen concentration may impair temperature measurement. For instance, for the unknown oxygen concentration which varies between air saturation and anoxic conditions, the error in temperature determination at 25 °C is ±4 K. The oxygen crosstalk of RL 100 particles doped with dye c, is much less pronounced, showing the error of ±1.5 K in the same conditions. Although much smaller fluctuations in oxygen concentration are expected for most applications, further minimization of the oxygen cross-talk is highly desirable. Our current work is focused on preparation of cell penetrable nanoparticles based on gas-blocking polymers (such as polyacrylonitrile) which would allow complete elimination of the oxygen crosstalk. It should be noted that although dye-doped polyacrylonitrile nanoparticles were reported,[220] they lack charged groups which enable cell penetration and improve stability.

3.2.9 Temperature Imaging

Temperature imaging represents one of the very important applications of the optical thermometers. Importantly, the new materials can be used for temperature imaging in the self-referenced lifetime mode. Although in this work the imaging of TADF decay times was performed with a gated CCD camera (Sensicam) and so called rapid lifetime determination (RLD) method[26,221] was used, other hardware is of course possible. The luminophore is excited by a short light pulse. After a delay to cut of excitation light, the emitted luminescence is then quantitatively detected during two gates. From the emission during the two gates, A1 and A2, and the starting times of the gates, t1 and t2, the lifetime can be calculated by

$$\tau = \frac{t_2 - t_1}{ln(\frac{A_1}{A_2})} \tag{3.3}$$

Figure 3.6b,c,e,f shows temperature imaging with planar optodes and with dispersion of nanoparticles, respectively. Since RL100 particles are cell penetrating, intracellular temperature

mapping with phosphorescence lifetime imaging equipment can be of high interest.
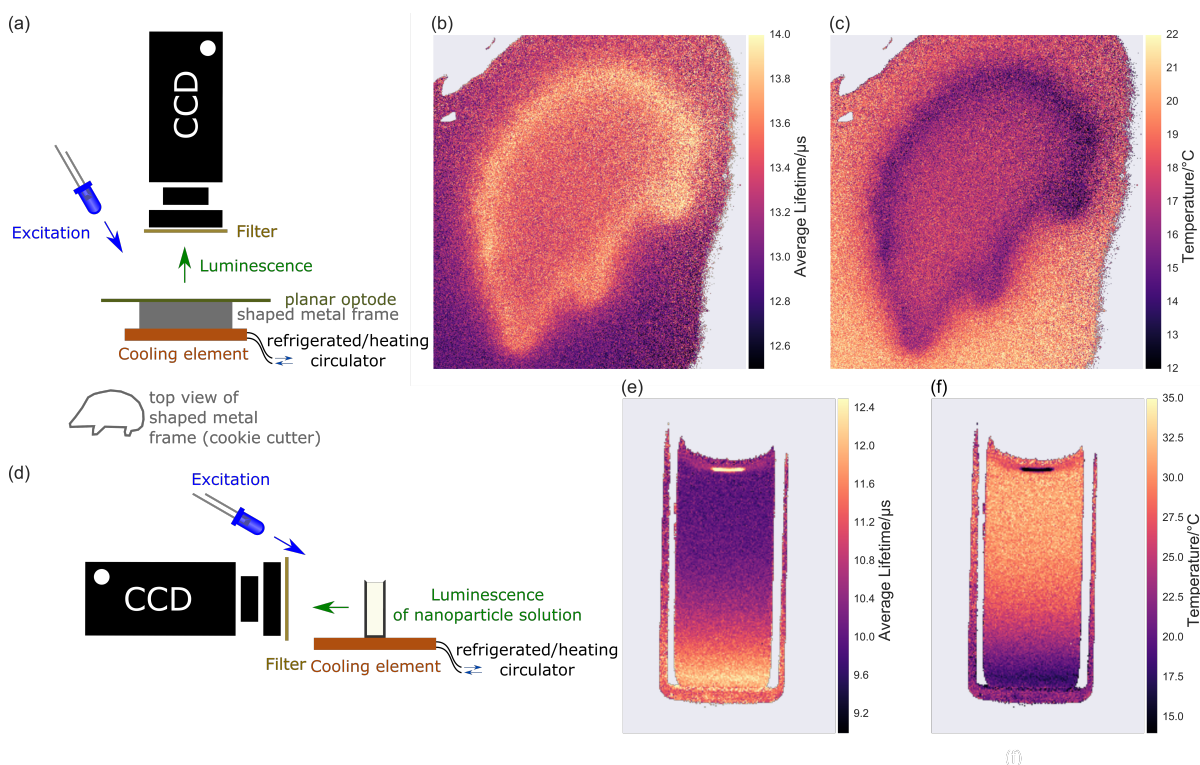
Figure 3.6: Temperature imaging with a planar optode in contact with a hedgehog shaped metal frame (cookie cutter), which was placed on a cooling element set to 5 °C (a, b) and with dispersion of nanoparticles in a cuvette which was first heated to 40 °C and then placed onto a cooling element at 5 °C (d, e). Lifetime distribution (a, d) and calculated temperature distribution (b, e). Illustration of experimental setup with a planar optode (c) and dispersion of nanoparticles (f).

3.3 Conclusions

In this work, dyes belonging to two promising classes of organic TADF emitters have been prepared and investigated for their applicability in optical sensing materials. Simple and low-cost synthesis from commercially available precursors and excellent tunability of photophysical properties are highly advantageous for practical applications. Particularly, the anthraquinone-based emitters show TADF lifetimes tunable over a very broad range (11–583 µs in toluene). The dyes incorporated into polystyrene show moderate to very high oxygen sensitivity corresponding to the average TADF lifetimes varying from 17 µs to 5.5 ms. Although the dyes are in principle applicable for oxygen sensing, the temperature cross-sensitivity is very high which makes many state-of-the-art oxygen probes more advantageous over the new dyes. However, high temperature dependency of the TADF lifetime was found to be very useful for designing advanced optical temperature probes. Oxygen cross-talk is eliminated by incorporating the dyes

into virtually gas impermeable poly(vinylidene chloride-*co*-acrylonitrile). The new temperature sensors demonstrate excellent sensitivity from -1.4 to -3.7% change of TADF lifetime per K which favorably compares even to the highly sensitive optical thermometers reported in the literature. Moreover, the new TADF probes show only moderate decrease of brightness at higher temperature, in contrast to much stronger decrease of luminescence intensity observed for most of the state-of-the-art lifetime temperature probes. To demonstrate potential applicability of the new systems in biology and medicine, the new dyes have been successfully incorporated into cell penetrating polymeric nanoparticles, where they retain their excellent temperature-sensitive properties albeit showing some crosstalk to oxygen. Moreover, we manufactured novel fiber-optic temperature minisensors which enable ultrafast high resolution temperature measurements.

Overall, our work paves the way to a new generation of highly sensitive optical thermometers which will benefit from the great versatility of TADF dye classes and possible structural modifications particularly regarding intense work conducted in context of their application in OLED technology. Preparation of new TADF dyes with bathochromically shifted absorption and emission spectra is of particular interest since they would enable even broader range of applications including in vivo sensing and imaging.

3.4 Experimental

Materials: Chemicals were purchased from various commercial providers (TCI, Frontier Scientific, Fluka, Sigma Aldrich, Acros Organics, Roth, ABCR), solvents were purchased from VWR and both were used as received. Eudragit RL-100 copolymer (poly-(ethylacrylate-comethylmethacrylate-*co*-trimethyl-aminoethyl methacrylate), average MW ≈ 150 000 Da, 8.85-11.96 wt % trimethyl-aminoethyl methacrylate units on dry substance) was from Degussa (www.evonik.com), PS, average MW ≈ 260 000 Da, was from Acros Organics, P(VDC-*co*-AN), 20 wt% acrylonitrile content, average Mn ≈ 80 000 Da, average MW ≈ 125 000 Da, was from Scientific Polymer (scientificpolymer.com). $PdCl_2(amphos)_2$ and PEPPSI-IPr catalysts were from Acros Organics and Aldrich, respectively.

Measurements: NMR spectra were recorded on a Bruker AVANCE III spectrometer equipped with an autosampler (300.36 MHz ^{1}H-NMR, 75.53 MHz ^{13}C-NMR). Mass spectrometry was performed in a positive reflector on a Micromass TofSpec 2E time-of-flight (TOF) mass spectrometer or on a Matrix-Assisted Laser Desorption/ Ionization (MALDI)-TOF/TOF spectrometer (Bruker UltrafleXtreme). UV–vis spectra were recorded on a VARIAN CARY 50 conc, UV–vis spectrophotometer or on Agilent Cary 60 UV-VIS using Hellma Analytics (www.hellma-analytics.com) optical glass 10 mm precision cuvettes. Luminescence spectra were recorded on FluoroLog 3 spectrofluorometer from Horiba Scientific equipped with a R2658 photomultiplier from Hamamatsu (www.hamamatsu.com). Screw-capped quartz precision cuvettes from Hellma Analytics were used for measurement under anoxic conditions. Deoxygenation was performed by bubbling high purity argon (99.999% purity) through the solution for 10 min. Luminescence decays were obtained via time correlated single photon counting on a FluoroLog 3 spectrofluorometer equipped with a DeltaHub module controlling a SpectraLED-390 ($\lambda =$ 392 nm) and using DAS-6 Analysis software for data analysis. Data were fitted using a mono- or biexponential decay model. Average lifetimes were calculated from equation

$$\tau_{av} = \frac{\sum_{i=1}^n B_i T_i^2}{\sum_{i=1}^n B_i T_i} \tag{3.4}$$

with B values from a pre-exponential function and T for the individual lifetimes. Absolute quantum yields were determined using a Quanta-φ integrating sphere-based set-up on a FluoroLog 3 spectrofluorometer, both from Horiba Scientific.

Oxygen calibrations of the sensor films were done on a Hitachi-F-7000 spectrofluorometer in a home-made flow-through cell at a constant temperature of 298 K adjusted by a Julabo F12-ED refrigerated/heating circulator (www.julabo.com). A gas-mixing device based on two massflow controllers, Voegtlin red-y smart series (www.voegtlin.com) and a custom built software were used to adjust oxygen partial pressure for the calibration. Nitrogen (99.999% purity), oxygen (99.999% purity), compressed air and test gas (1.95% O_2 in N_2) were purchased from Linde Gas. For temperature dependency measurements constant temperature was adjusted with a Cary SPV – 1 × 0 Single Cell Peltier Accessory peltier element from Varian in combination

with a refrigerated/heating circulator.

Temperature measurements with the fiber-optic probe were performed using a modified Firesting-mini phase fluorometer from Pyro Science (www.pyro-science.com). The device was equipped with a 465 nm excitation LED, Linos DT-cyan dichroic mirror and the Schott OG 590 long-pass filter used in combination with a Deep Golden Amber plastic filter from Lee filters (www.leefilters.com). The modulation frequency of 12 kHz was used. The fiber-optic probe was rapidly transferred between two water-filled beakers kept at 22 and 37 °C. For the photostability tests, the sensor films, diagonally placed in Hellma Analytics 100-OS 10 mm precision cuvettes, were exposed to the irradiation of a three LED array (at 11.5 V, P = 18 W, λmax em = 465 nm) equipped with a focusing lens producing an average photon flux of 5500 µmol s^{-1}m^{-2} (141.5 mW cm^{-2}) as determined by a LI-250A Light Meter from LI-COR Biosciences (www.licor.com).

Imaging experiments were performed using a modular lifetime imaging system[221] based on an electrically cooled CCD-camera, PCO SensiCam from PCO Computer Optics (www.pco.de), equipped with a Pentax TV Lens 12 mm 1:1.2 lens and a gated, high power LED array (λmax em = 455 nm) as excitation source. A combination of a Schott GG 495 and a LEE 767 Oklahoma Yellow (www.leefilters.com) filters was used in front of the camera.

Sensor Preparation—Planar Sensors: The prepared dye "cocktails" were knife coated onto 125 µm biaxially oriented polyethylene terephthalate (PET) foils (MELINEX 506) supplied by Pütz GmbH + Co. Folien KG (www.puetz-folien.com). Polystyrene foils: Dye "cocktails" with ≈1 wtdye with respect to the amount of PS (7 wt% PS in CHCl$_3$) were knife coated (25 µm thick wet film) on dust-free PET support foils. After evaporation of the solvent (30 min), the foils were dried at 60 °C in an oven for 24 h. Poly(vinylidene chloride-co-acrylonitrile): Dye "cocktails" with ≈1 wt% dye with respect to the amount of poly(vinylidene chloride-*co*-acrylonitrile) (10 wt% P(VDC-*co*-AN) in dry tetrahydrofuran) were knife coated (75 µm thick wet film) on dust-free PET support foils under inert conditions (glove box). After evaporation of the solvent (1 h), the foils were retrieved from the glove box and dried in an oven at 60 °C for another 24 h.

Sensor Preparation—Fiber-Optic Sensors: A commercially available 430 µm optical fiber (Industrial Fiber Optics Inc.) was flat broken and the tip was melted to produce a hemispherical shape. The P(VDCco-AN) dye "cocktail" was prepared as described for the sensor foils and was then used to dip coat the fiber. After evaporation of the solvent, an optical isolation layer (8 wt% carbon black, 32 wt% silicone E43, 60 wt% dry hexane) was coated over the fiber tip. The fiber-optic sensors were then stored at room temperature for 24 h for the silicone layer to polymerize.

RL100 Particles: ≈ 100 mg Eudragit RL100 were dissolved in 50 mL acetone, and 1 wt% dye with respect to the amount of RL100 was added. 250 mL distilled water were added under vigorous stirring over a time span of 3 s; acetone was removed under reduced pressure and the particle dispersion was concentrated to a volume of 50 mL.

Synthesis-**a1**: A flame-dried and Argon-flushed 25 mL Schlenk tube was charged with 2,6-

dibromoanthraquinone (250.4 mg, 684 µmol, 1 eq), potassium *tert*-butoxide (191.8 mg, 1.71 mmol, 2.50 eq), diphenylamine (241.2 mg, 1.43 mmol, 2.08 eq), and PEPPSI-IPr catalyst (22.9 mg, 34 µmol, 0.05 eq) under Ar counterflow. Then the Schlenk-tube was evacuated and Ar-flushed (5× cycles). Dry toluene (8 mL), deoxygenated by purging with Ar for 15 min, was added to the reagents. After stirring for 1 min the reaction mixture was placed in a preheated oil bath and was stirred at 100 °C for 2 h taking on a brown color. After quantitative conversion monitored by thin layer chromatography (TLC) (cyclohexane (CH)/ethyl acetate (EA) = 5 + 1, Rf(Anq) = 0.66), the reaction mixture was allowed to cool to R.T. and precipitated from a mixture of methanol (MeOH)/H_2O = 9 + 1 (v/v) (50 mL). After centrifugation, the red precipitate was collected and dried at 60 °C overnight. The crude product was purified by flash column chromatography on silica gel (CH/dichloromethane (DCM) = 3 + 1 (v/v), detection by TLC CH/EA = 5 + 1 (v/v), Rf = 0.51).

Yield: 142 mg (38%), red solid.

$C_{38}H_{26}N_2O_2$ [542.64 g mol^{-1}]

^{1}H-NMR (300.36 MHz, CDCl$_3$): 8.02 (d, ^{3} J^{HH} = 8.7 Hz, 2H, Anq), 7.76 (d, $^4J_{HH}$ = 2.6 Hz, 2H, Anq), 7.41-7.29 (m, 8H, Ph), 7.23-7.13 (m, 14H, Ph + Anq) ppm.

APT-NMR (75.53 MHz, CDCl$_3$): 182.08 (C_q^{Ar}, C=O, Anq), 153.17 (C_q^{Ar}, Anq-N), 146.06 (C_q^{Ar}, Ph-N), 135.64 (C_q^{Ar}, Anq), 130.00 (C_t^{Ar}, Ph), 129.15 (C_t^{Ar}, Anq), 126.46 (C_t^{Ar}, Ph), 126.15 (C_q, Anq), 125.51 (C_t^{Ar}, Ph), 123.38 (C_t^{Ar}, Anq), 116.64 (C_t^{Ar}, Anq) ppm.
Analytical data are in accordance with those reported.[214]

Synthesis—**a2**: In a 25 mL round-bottom flask, **a1** (35.5 mg, 65 µmol, 1 eq) was dissolved in CHCl$_3$ (8 mL) and a catalytic amount of FeCl$_3$ was added. Then a Br$_2$ solution in CHCl$_3$ (1 mL, 0.254 m, 254 µmol, 3.88 eq) was added dropwise via syringe to the solution. The solution was stirred for 30 min and the reaction mixture was quenched with 2 wt% Na$_2$SO$_3$ aqueous solution (5 mL). After phase separation, the organic layer was filtered through silica gel using DCM and the solvent was removed under reduced pressure. The crude product was purified by flash column chromatography on silica gel (gradient starting with CH/DCM = 3 + 1 (v/v), detection by TLC CH/EA = 5 + 1 (v/v), Rf = 0.64).

Yield: 31 mg (55%), red solid.

$C_{38}H_{22}Br_4N_2O_2$ [858.22 g mol^{-1}]

^{1}HNMR (300.36 MHz, CD$_2$Cl$_2$): 8.04 (d, $^3J_{HH}$ = 8.7 Hz, 2H), 7.71 (d, $^4J_{HH}$ = 2.5 Hz, 2H), 7.55-7.44 (m, 8H), 7.23 (dd, $^3J_{HH}$ = 8.7, $^4J_{HH}$ = 2.5 Hz, 2H), 7.10–7.03 (m, 8H) ppm.

APT-NMR (75.53 MHz, CD_2Cl_2): 181.97 (C_q^{Ar}, C=O, Anq), 171.54 (C_q), 145.43 (C_q), 139.02 (C_q), 138.62 (C_q), 133.59 (C_t^{Ar}, Ph), 129.58 (C_t^{Ar}, Anq, 128.17 (C_t^{Ar}, Ph), 124.89 (C_t^{Ar}, Anq), 118.90 (C_q^{Ar}, Ph-Br), 117.80 (C_t^{Ar}, Anq) ppm.

MALDI-TOF: m/z: [M$^+$] calc.: 857.84, found: 857.84.

Synthesis-**a3**: **a2** (34 mg, 40 µmol, 1 eq), potassium carbonate (33.9 mg, 239 µmol, 6.03 eq) and (9,9-dimethyl-9H-fluoren-2-yl) boronic acid (43.7 mg, 184 µmol, 4.63 eq) were placed in a flame-dried and Ar-flushed 25 mL Schlenk tube. Then a mixture of toluene/THF/ H_2O = 2 + 2 + 1 (v/v/v) (5 mL) was added and the suspension was degassed by purging with Ar for 15 min. Subsequently, the Schlenk tube was placed in a preheated oil bath at 80 °C and after 2 min of stirring, Pd(PPh$_3$)$_4$ (5 mg, 4 µmol, 0.11 eq) was added under Ar counterflow. The reaction mixture was kept stirring at 80 °C for 24 h and then allowed to cool down to R.T. before it was filtered through silica gel using DCM. The solvent was then removed under reduced pressure to give a red solid. The crude product was then purified by flash column chromatography on silica gel (CH/EA = 19 + 1, v/v, Rf = 0.19).

Yield: 10 mg (19%), red solid.

$C_{98}H_{74}N_2O_2$ [1311.68 g mol^{-1}]

^{1}H-NMR (300.36 MHz, CDCl$_3$): 8.12 (d, ^{3}J$_{HH}$ = 8.7 Hz, 2H, Anq), 7.95 (d, ^{4}J$_{HH}$ = 2.5 Hz, 2H, Anq), 7.80 (d, ^{3}J$_{HH}$ = 7.9 Hz, 4H, Fl), 7.78-7.74 (m, 4H, Fl), 7.68 (m, 12H,Ph(8H) + Fl(4H)), 7.60 (dd, ^{3}J$_{HH}$ = 8.0, ^{4}J$_{HH}$ = 1.8 Hz, 4H, Fl), 7.48-7.44 (m, 4H, Fl), 7.40-7.29 (m, 18H, Fl + Ph(8H)), 1.56 (s, 24H, CH$_3$) ppm.

APT-NMR (75.53 MHz, CDCl$_3$): 182.11, 154.50, 154.03, 152.99, 145.07, 139.59, 138.97,138.78, 138.71, 135.78, 129.32, 128.73, 127.45, 127.20, 126.55, 126.46, 126.12, 123.96,122.78, 121.39, 120.50, 120.23, 117.24, 47.13, 27.4 ppm.

MALDI TOF: m/z: [M$^+$] calc.: 1311.58, found: 1311.58.

Synthesis—**a4**: It was prepared analogously to the procedure used for **a1**, but 4-methyl-N-phenylaniline (1.7 mmol, 2.5 eq) was used instead of diphenylamine. Purification was done by flash column chromatography on silica gel (CH/DCM = 3 + 1, v/v, Rf = 0.1).

Yield: 196 mg (50%), red solid.

$C_{40}H_{30}N_2O_2$ [570.69 g mol^{-1}]

^{1}H-NMR (300.36 MHz, CDCl$_3$): 8.00 (d, ^{3}J$_{HH}$ = 8.7 Hz, 2H, Anq), 7.72 (d, ^{4}J$_{HH}$ = 2.6 Hz, 2H, Anq), 7.39-7.29 (m, 4H, Ph), 7.22-7.13 (m, 12H, Ph + Anq), 7.11-7.03(m, 4H, Ph), 2.36 (s, 6H, CH$_3$) ppm.

APT-NMR (75.53 MHz, CDCl$_3$): 182.13 (C$_q$, C=O, Anq), 153.30 (C$_q$, Anq-N), 146.08 (C$_q$, Ph-N), 143.38 (C$_q$, CH$_3$- Ph-N), 135.66 (C$_q^{Ar}$), 135.61 (C$_q^{Ar}$), 130.70 (C$_t^{Ar}$, Ph), 129.92 (C$_t^{Ar}$,Ph), 129.11 (C$_t^{Ar}$, Anq), 126.72 (C$_t^{Ar}$, Ph), 126.23 (C$_t^{Ar}$, Ph), 125.82 (C$_q^{Ar}$, Anq), 125.32 (C$_t^{Ar}$, Ph), 122.78 (C$_t^{Ar}$, Anq), 116.13 (C$_t^{Ar}$, Anq), 21.15 (CH$_3$) ppm.

MALDI TOF: m/z: [M$^+$] calc.: 570.23, found: 570.24.

Synthesis—**a5**: It was prepared analogously to the procedure used for **a2**, but **a4** (277 µmol) was used instead of **a1**. The product was not further purified.

Yield: 192 mg (95%), red solid.

C$_{40}$H$_{28}$Br$_2$N$_2$O$_2$ [728.48 g mol^{-1}]

^{1}H-NMR (300.36 MHz, CDCl$_3$): 8.02 (d, ^{3}J$_{HH}$ = 8.7 Hz, 2H, Anq), 7.72 (d, ^{4}J$_{HH}$ = 2.5 Hz, 2H, Anq), 7.48-7.40 (m, 4H, Ph), 7.21– 7.13 (m, 6H, Ph + Anq), 7.09-7.01 (m, 8H, Ph), 2.36 (s, 6H, CH$_3$) ppm.

APT-NMR (75.53 MHz, CDCl$_3$): 181.95 (C$_q^{Ar}$, C=O, Anq), 152.88 (C$_q^{Ar}$, Anq-N), 145.26 (C$_q$, Ph-N), 143.00 (C$_q$, CH$_3$-Ph-N), 136.01 (C$_q^{Ar}$), 135.63 (C$_q^{Ar}$), 132.99 (C$_t^{Ar}$, Ph),130.86 (C$_t^{Ar}$, Ph), 129.24 (C$_t^{Ar}$, Anq), 127.38 (C$_t^{Ar}$, Ph), 126.67 (C$_t^{Ar}$, Ph), 126.26 (C$_q^{Ar}$, Anq), 123.36 (C$_t^{Ar}$, Anq), 118.02 (C$_q^{Ar}$, Ph-Br), 116.61 (C$_t^{Ar}$, Anq), 21.16 (CH$_3$) ppm.

MALDI TOF: m/z: [M$^+$] calc.: 728.05, found: 782.05.

Synthesis—**a6**: It was prepared analogously to the procedure used for **a1**, but bis(4-(2-phenylpropan-2-yl)phenyl)amine (660 µmol, 2.2 eq) was used instead of diphenylamine. Purification was done by flash column chromatography on silica gel (CH/DCM = 1+1, v/v, Rf = 0.2).

Yield: 206 mg (68%), intense orange solid.

C$_{74}$H$_{66}$N$_2$O$_2$ [1015.35 g mol^{-1}]

^{1}H-NMR (300 MHz, CD$_2$Cl$_2$): 7.96 (d, ^{3}J$_{HH}$ = 8.7 Hz, 2H, Anq), 7.64 (d, ^{4}J$_{HH}$ = 2.5 Hz, 2H, Anq), 7.33-7.04 (m, 38H, Ph + 2Anq), 1.70 (s, 24H, CH$_3$) ppm.

^{13}C NMR (76 MHz, CD$_2$Cl$_2$): 182.21, 153.68, 150.99, 148.65, 136.03, 129.26, 128.72, 128.61,

127.31, 126.41, 126.24, 126.13, 123.06, 116.03, 43.23, 31.04 ppm.

MALDI TOF: m/z: [M$^+$] calc.: 1014.51 found: 1014.51.

Synthesis—**a7**: It was prepared analogously to the procedure used for **a1**, but 3,6-di-*tert*-butyl-9*H*-carbazole (433 µmol, 2.1 eq) was used instead of diphenylamine. Purification was done via vacuum sublimation.

Yield: 28 mg (18%), red solid.

C$_{54}$H$_{54}$N$_2$O$_2$ [763.04 g mol^{-1}]

^{1}H-NMR (300.36 MHz, CDCl$_3$): 8.62 (d, ^{4}J$_{HH}$ = 2.2 Hz, 2H, Anq), 8.58 (d, ^{3}J$_{HH}$ = 8.3 Hz, 2H, Anq), 8.18-8.14 (m, 4H, Carb), 8.08 (dd, ^{3}J$_{HH}$ = 8.2, ^{4}J$_{HH}$ = 2.2 Hz, 2H, Anq), 7.56-7.50 (m, 8H), 1.49 (s, 36H) ppm.
Analytical data are in accordance with those reported.[214]

Synthesis—**a8**: It was prepared analogously to the procedure used for a1, but *N*-[4-(9-phenyl-9*H*-carbazol-3-yl)phenyl]-[1,1´-biphenyl]-4-amine (302 µmol, 2.2 eq) was used instead of diphenylamine. Purification was done by flash column chromatography on silica gel (CH/DCM = 3 + 2, v/v, Rf = 0.17).

Yield: 50 mg (31%), dark purple solid.

C$_{86}$H$_{56}$N$_4$O$_2$ [1177.42 g mol^{-1}]

^{1}H-NMR (300.36 MHz, CDCl$_3$): 8.38 (d, ^{4}J$_{HH}$ = 1.8 Hz, 2H), 8.20 (d, ^{3}J$_{HH}$ = 7.7 Hz, 2H), 8.12 (d, ^{3}J$_{HH}$ = 8.7 Hz, 2H, Anq), 7.94 (d, ^{4}J$_{HH}$ = 2.5 Hz, 2H, Anq), 7.78-7.55 (m, 22H), 7.53–7.28 (m, 26H) ppm.

APT-NMR (75.53 MHz, CDCl$_3$): 182.1 (C$_q^{Ar}$, C=O, Anq), 153.1, 145.30, 144.5, 141.5, 140.6, 140.5, 139.4, 138.2, 137.8, 135.8, 132.7, 130.4, 129.3, 129.0, 128.8, 128.7, 127.7, 127.5, 127.2, 127.1, 126.8, 126.5, 126.4, 126.3, 125.4, 124.1, 123.9, 123.6, 120.5, 120.2, 118.8, 117.1, 110.3, 110.1 ppm.

MALDI TOF: m/z: [M$^+$] calc.: 1176.44, found: 1176.43.

Synthesis—**a9**: It was prepared analogously to the procedure used for **a1**, but *N*-([1,1´-biphenyl]-4-yl)-9,9-dimethyl-9*H*-fluoren-3-amine (660 µmol, 2.2 eq) was used instead of diphenylamine. Purification was done by flash column chromatography on silica gel (CH/DCM = 1 + 1, v/v, Rf = 0.14).

Yield: 80 mg (29%), red solid.

$C_{68}H_{50}N_2O_2$ [927.14 g mol^{-1}]

^{1}H NMR (300 MHz, CDCl$_3$): 8.08 (d, $^3J_{HH}$ = 8.7 Hz, 2H), 7.92 (d, $^4J_{HH}$ = 2.0 Hz, 2H), 7.74-7.65 (m, 4H), 7.65-7.55 (m, 8H), 7.49-7.28 (m, 20H), 7.18 (dd, $^3J_{HH}$ = 8.1, $^4J_{HH}$ = 2.0 Hz, 2H), 1.46 (s, $^3J_{HH}$ = 9.1 Hz, 12H) ppm.

MALDI-TOF: m/z: [M$^+$] calc.: 926.39 found: 926.39.

Synthesis—**b**: It was prepared by a procedure according to literature[209] from tetrafluoroterephthalonitrile (1 mmol, 1 eq) and carbazole (5 mmol, 5 eq).

Yield: 450 mg (57%), intense orange powder.

^{1}H NMR (300 MHz, CDCl$_3$): 8.11–8.06 (m, 8H), 7.52–7.36 (m, 16H), 7.25–7.20 (m, 8H) ppm.
Analytical data are in accordance with those reported.

Synthesis—**c**: It was prepared by a procedure according to literature[209] from tetrafluoroisophthalonitrile (1 mmol, 1 eq) and carbazole (5 mmol, 5 eq).

Yield: 256 mg (32%), yellow powder.

^{1}H NMR (300 MHz, CDCl$_3$): 8.22 (d, $^3J_{HH}$ = 7.8 Hz, 2H), 7.77-7.63 (m, 8H), 7.55-7.42 (m, 2H), 7.37-7.30 (m, 2H), 7.24-7.18 (m, 4H), 7.13-7.02 (m, 8H), 6.82 (t, $^3J_{HH}$ = 7.5 Hz, 4H), 6.63 (t, $^3J_{HH}$ = 7.6 Hz, 2H) ppm.
Analytical data are in accordance with those reported.

Synthesis—d1: It was prepared by a procedure according to literature from tetrafluorophthalonitrile (1 mmol, 1 eq) and carbazole (5 mmol, 5 eq).[209]

Yield: 119 mg (15%), orange powder with 14 wt% carbazole contamination.

^{1}H NMR (300 MHz, CDCl$_3$): 7.74 (d,$^3J_{HH}$ = 7.5 Hz, 4H), 7.30 (d, $^3J_{HH}$ = 7.7 Hz, 4H), 7.20 (d, $^3J_{HH}$ = 8.0 Hz, 4H), 7.08 (m, 8H), 6.87 (d, $^3J_{HH}$ = 8.2 Hz, 4H), 6.77 (t, $^3J_{HH}$ = 7.4 Hz, 4H), 6.56 (t, $^3J_{HH}$ = 7.7 Hz, 4H) ppm.
Analytical data are in accordance with those reported.

Synthesis—d2: It was prepared analogously to the procedure used for d1 but 3,6-di-*tert*-butyl-9*H*-carbazole (369 μmol, 5 eq) was used instead of carbazole. Purification was done by flash column chromatography on silica gel (CH/EA = 95 + 5, v/v, Rf = 0.46) and vacuum sublimation.

Yield: 30 mg (33%), intense yellow solid.

$C_{88}H_{96}N_6$ [1237.78 g mol^{-1}]

^{1}H-NMR (300.36 MHz, CDCl$_3$): 7.59 (d, $^4J_{HH}$ = 2.0 Hz, 4H), 7.23 (d, $^4J_{HH}$ = 2.0 Hz, 4H), 6.94 (dd, $^3J_{HH}$ = 8.5, $^4J_{HH}$ = 2.0 Hz, 4H), 6.80 (d, $^3J_{HH}$ = 8.5 Hz, 4H), 6.72 (d, $^3J_{HH}$ = 8.5 Hz, 4H), 6.57 (dd, $^3J_{HH}$ = 8.5, $^4J_{HH}$ = 2.0 Hz, 4H), 1.37 (s, 36H, *tert*-butyl), 1.20 (s, 36H, *tert*-butyl) ppm.

APT-NMR (75.53 MHz, CDCl$_3$): 144.26 (CArq -Carb), 143.89 (CArq -Carb), 141.44 (CArq -core), 139.77 (CArq -core), 136.91 (CArq -N), 136.32 (CArq -N), 124.85 (CArq -Carb), 124.53 (CArq -Carb), 123.10 (CArt -Carb), 122.71 123.10 (CArt -Carb), 115.99 (CArt -Carb), 115.43 (CArt -Carb), 113.39 (Cq, CN), 109.80 (CArt -Carb), 109.55 (CArt -Carb), 100.13 (CArq -CN), 34.72 (Cq, *tert*-Bu), 34.47 (Cq, *tert*-Bu), 32.04 (CH$_3$), 31.84 (CH$_3$) ppm.

MALDI-TOF: m/z: [M$^+$] calc.: 1237.77, found: 1237.76.

Synthesis—e: It was prepared in two steps. In a flame-dried and Ar-flushed 25 mL Schlenk tube, a mixture of toluene/THF/ H$_2$O = 7 + 2 + 1 (v/v/v) (10 mL) was degassed by purging with Ar for 10 min. Then (9,9-diheptyl-9*H*-fluorene-2,7-diyl)diboronic acid (34.4 mg, 76 µmol, 1 eq), 2,6-dibromoanthraquinone (85.4 mg, 233 µmol, 3.05 eq) and K$_2$CO$_3$ (47.1 mg, 341 µmol, 4.46 eq) were added under Ar counterflow. After purging the yellow suspension for another 10 min with Ar, the Schlenk was placed in a preheated oil bath at 80 °C and stirred for 10 min. Then PdCl$_2$(amphos)$_2$ (5 mg, 4 µmol, 0.06 eq) was added under Ar counterflow. The reaction mixture was stirred at 80 °C for 17 h until quantitative conversion of the fluorene was detected by TLC (DCM/MeOH = 4 + 1, v/v, Rf(fluorene) = 0.40). Then the flask was allowed to cool down to room temperature. Afterward the mixture was diluted with H$_2$O (5 mL) and EA (15 mL). After phase separation, the organic layer was filtered through silica gel using DCM/ MeOH = 4 + 1 (v/v). The product mixture was then purified by flash column chromatography on silica gel (gradient starting with CH/DCM = 2 + 1 (v/v), detection by TLC CH/DCM = 1 + 1 (v/v), Rf = 0.53) and vacuum sublimation to remove residual anthraquinone.

Yield: 7 mg (10%), yellow solid.

$C_{55}H_{48}Br_2O_4$ [932.79 g mol^{-1}]

^{1}H-NMR (300.36 MHz, CDCl$_3$): 8.63 (d, $^4J_{HH}$ = 2.0 Hz, 2H), 8.48 (d, $^4J_{HH}$ = 2.0 Hz, 2H), 8.42 (d, $^3J_{HH}$ = 8.1 Hz, 2H), 8.23 (d, $^3J_{HH}$ = 8.3 Hz, 2H), 8.13 (dd, $^3J_{HH}$ = 8.1, $^4J_{HH}$ = 2.0 Hz, 2H), 7.95 (dd, $^3J_{HH}$ = 8.3, $^4J_{HH}$ = 2.0 Hz, 2H), 7.90(d, $^3J_{HH}$ = 7.9 Hz, 2H), 7.77 (dd, $^3J_{HH}$ = 7.8, $^4J_{H}$H = 1.7 Hz, 2H), 7.72 (d, $^4J_{HH}$ = 1.7 Hz, 2H), 2.19–2.06 (m, 4H), 1.19–0.98

(m, 16H, CH$_2$), 0.75 (t, ^{3}J$_{HH}$ = 6.9 Hz, 6H, CH$_3$), 0.72–0.62 (m, 4H, CH$_2$) ppm.

In the second step, a flame-dried and Ar-flushed 10 mL Schlenk tube was charged with the product from the previous step (7 mg, 8 µmol, 1 eq), potassium *tert*-butoxide (3 mg, 27 µmol, 3.35 eq), bis(4-(2-phenylpropan-2-yl)phenyl)amine (8 mg, 20 µmol, 2.47 eq) and PEPPSI-IPr catalyst (2.3 mg, 3 µmol, 0.42 eq) under inert conditions. Then the Schlenk tube was evacuated and Ar flushed (5 cycles). Dry toluene (2 mL), deoxygenated by purging with Ar for 10 min, was added to the reagents. After stirring the reaction mixture for 1 min, the Schlenk flask was placed in a preheated oil bath at 100 °C and the intense red solution was kept stirring for 1 h. The reaction mixture was allowed to cool down to R.T. and was then precipitated from a mixture of MeOH/H$_2$O = 9 + 1 (v/v) (10 mL). The precipitate was collected after centrifugation and then the crude product was purified by flash column chromatography on silica gel (CH/DCM = 1 + 1 (v/v), Rf = 0.49).

Yield: 3 mg (24%), red solid.

C$_{115}$H$_{108}$N$_2$O$_4$ [1582.14 g mol^{-1}]

^{1}H-NMR (300.36 MHz, CDCl$_3$): 8.61 (d, ^{4}J$_{HH}$ = 2.0 Hz, 2H), 8.33 (d, ^{3}J$_{HH}$ = 8.1 Hz, 2H), 8.15 (d, ^{3}J$_{HH}$ = 8.7 Hz, 2H), 8.04 (d, ^{3}J$_{HH}$ = 8.0 Hz, ^{4}J$_{HH}$ = 2.0 Hz, 2H), 7.87 (d, ^{3}J$_{HH}$ = 7.8 Hz, 2H), 7.81 (d, ^{4}J$_{HH}$ = 2.4 Hz, 2H), 7.76 (dd, ^{3}J$_{HH}$ = 7.8 Hz, ^{4}J$_{HH}$ = 1.7 Hz, 2H), 7.72 (d, ^{4}J$_{HH}$ = 1.7 Hz, 2H), 7.37-7.27 (m, 16H, Ph), 7.22 (m, 12H, Ph + Anq), 7.08 (d, ^{3}J$_{HH}$ = 8.6 Hz, 8H, Ph), 2.11 (m, 4H), 1.72 (s, 24H), 1.16-1.04 (m, 16H), 0.75 (t, ^{3}J$_{HH}$ = 6.9 Hz, 6H), 0.71–0.60 (m, 4H) ppm.

MALDI-TOF: m/z: [M$^+$] calc.: 1581.83, found: 1581.83.

3.5 Acknowledgments

3.6 Supporting Information
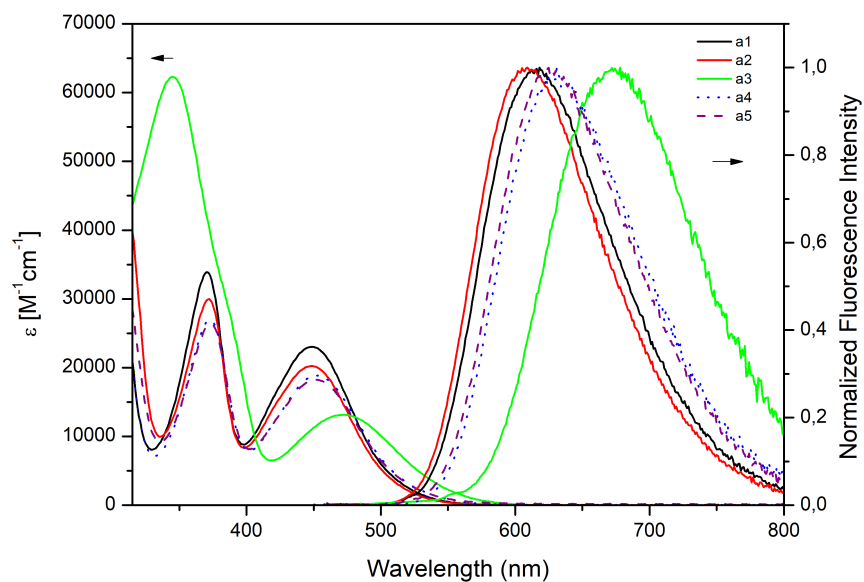
Figure S3.1: Absorption and emission spectra of the anthraquinone dyes a1-a5 in toluene at 25 °C.

Table S3.1: Fit parameters (equation 1) and bimolecular quenching constants for the dyes immobilized in polystyrene (25 °C).

dye	KSV_1 [hPa^{-1}]	f	m	k_q [Pa^{-1} s^{-1}]	dye	KSV_1 [hPa^{-1}]	f	m	k_q [Pa^{-1} s^{-1}]
a1	1.15	0.781	5.64E-03	2.07	a8	0.163	0.512	2.60E-03	1.68
a2	0.817	0.785	1.16E-02	1.70	a9	0.214	0.598	1.99E-03	1.78
a3	0.128	0.408	2.30E-03	0.93	b	0.00553	0.181	5.12E-02	3.22
a4	0.895	0.709	7.05E-03	3.16	c	0.00169	0.514	5.44E-02	1.96
a5	0.765	0.709	1.16E-02	2.62	d1	0.00724	0.529	5.99E-02	1.81
a6	0.763	0.674	1.02E-02	2.69	d2	0.00528	0.511	7.58E-02	2.53
a7	0.0175	0.612	1.31E-02	4.17	e	0.583	0.160	2.19E-04	2.07
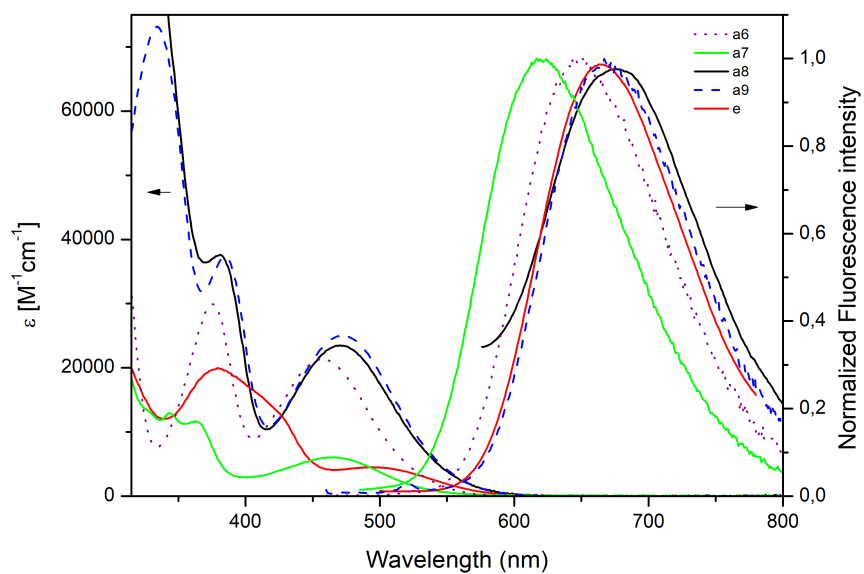
Figure S3.2: Absorption and emission spectra of the anthraquinone dyes a6-a9 and oligomeric e in toluene at 25 °C.
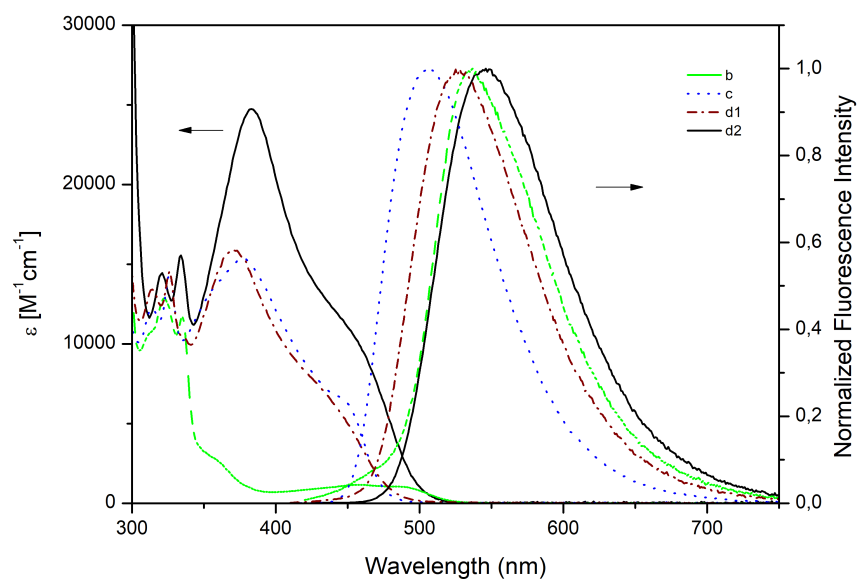
Figure S3.3: Absorption and emission spectra of the dicyanobenzene dyes b-d2 in toluene at 25 °C.
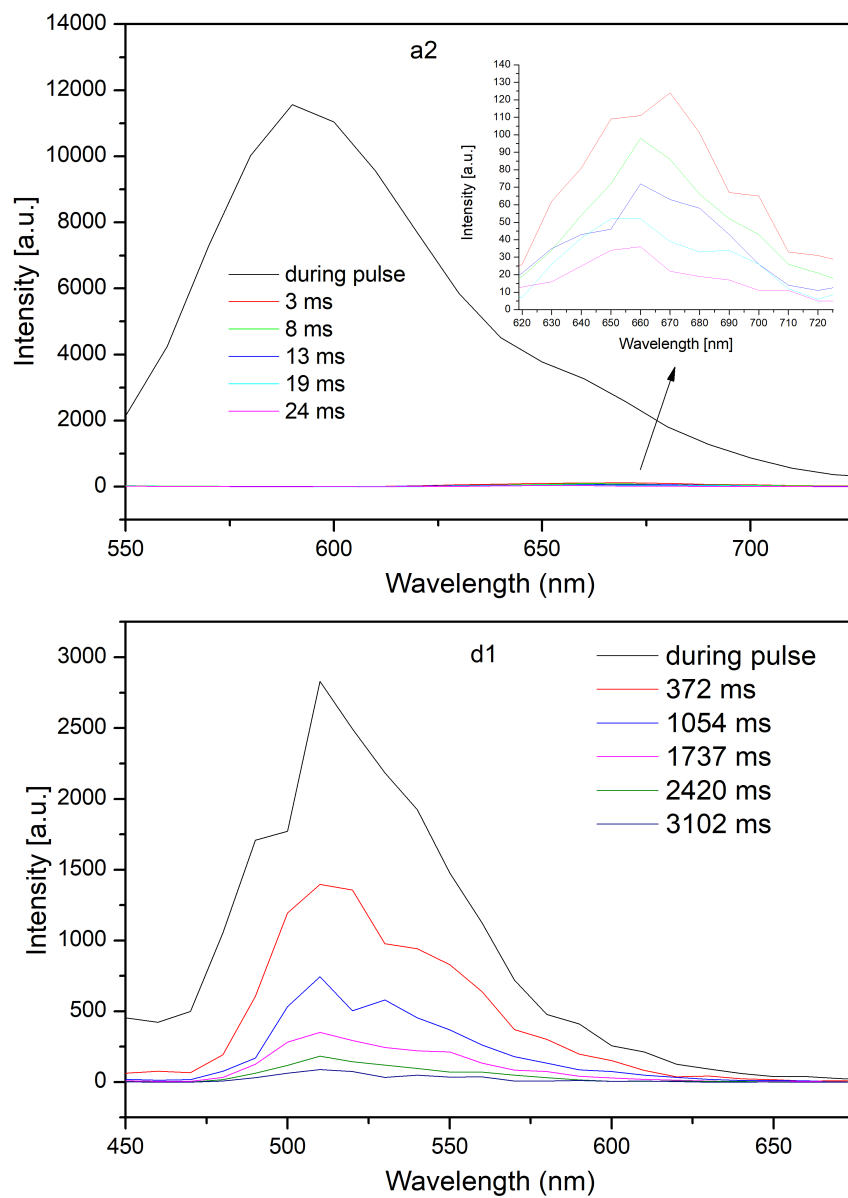
Figure S3.4: Time-resolved luminescence spectra of a2 and d1 in a frozen solvent glass (THF/Toluene=6+4 v/v) at 77K
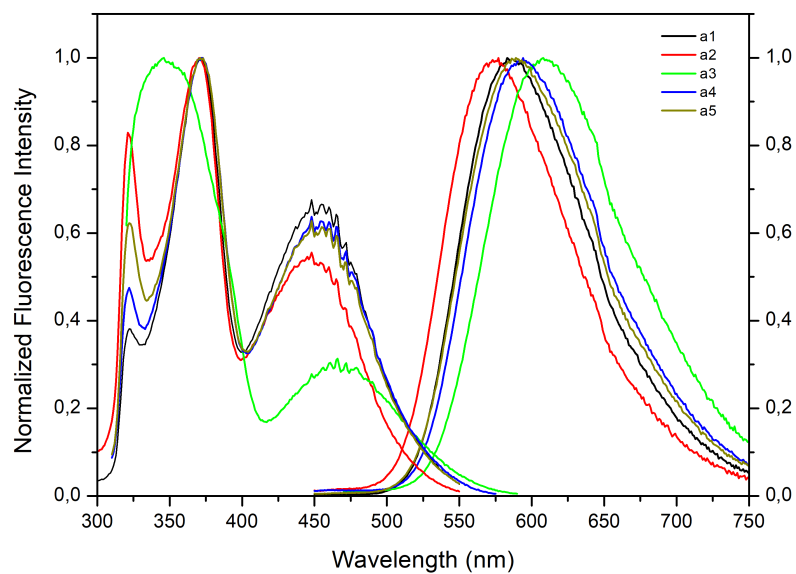
Figure S3.5: Excitation and emission spectra of the anthraquinone dyes a1-a5 immobilized in polystyrene at 25 °C.
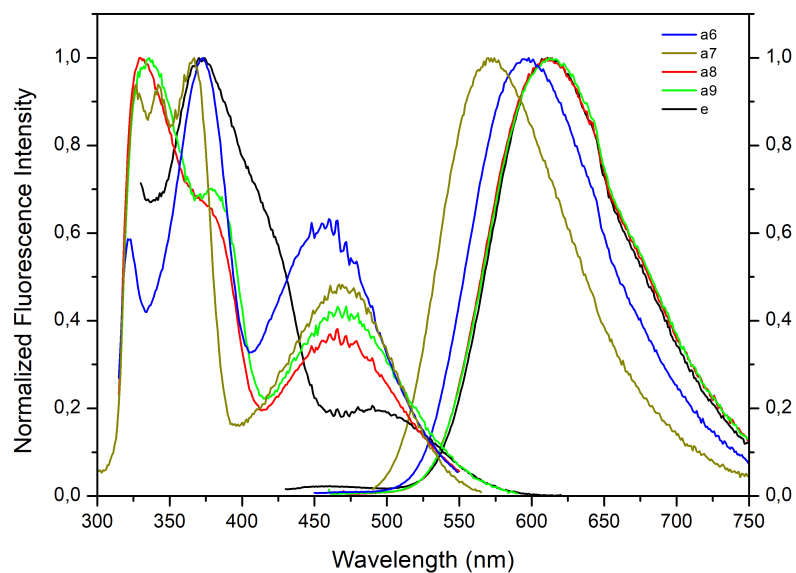
Figure S3.6: Excitation and emission spectra of the anthraquinone dyes a6-a9 and oligomeric e immobilized in polystyrene at 25 °C
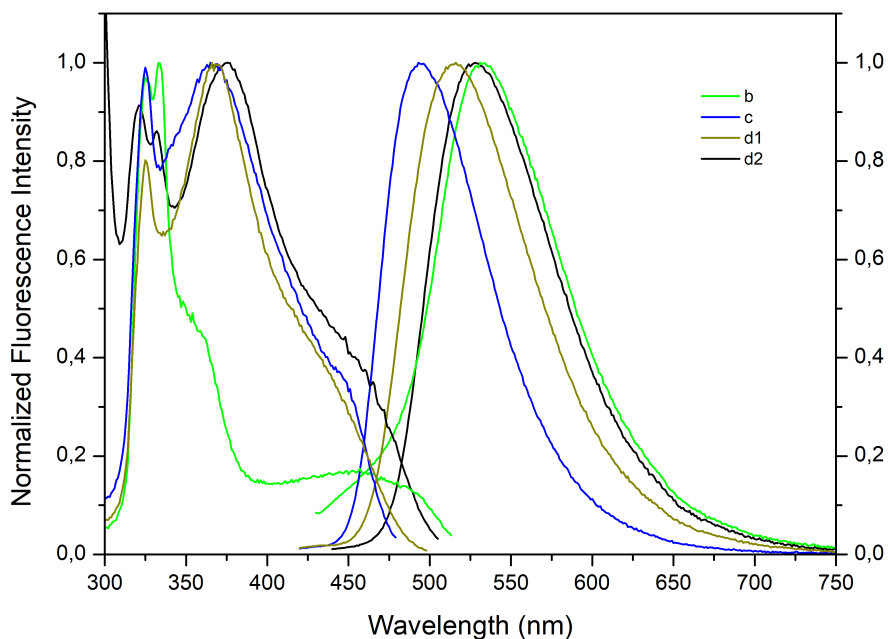
Figure S3.7: Excitation and emission spectra of the dicyanobenzene dyes b-d2 immobilized in polystyrene at 25 °C

Table S3.2: Comparison of the photophysical properties of the dyes immobilized in PS and P(VDC-*co*-AN).

	PS			P(VDC-*co*-AN)		
	$\lambda_{em,max}$ (nm)	τ [s]	ϕ [%]	$\lambda_{em,max}$ (nm)	τ [s]	ϕ [%]
a3	608	1.37E-03	29	630	8.26E-04	5
a7	577	4.20E-05	42	597	4.19E-05	6
a8	614	9.73E-04	26	639	5.98E-04	4
a9	612	1.20E-03	33	644	6.59E-04	5
b	531	1.72E-05	58	531	1.15E-05	30
c	493	8.63E-06	96	498	7.23E-06	72
d1	516	3.99E-05	87	522	2.22E-05	53
d2	528	2.09E-05	93	539	1.14E-05	47
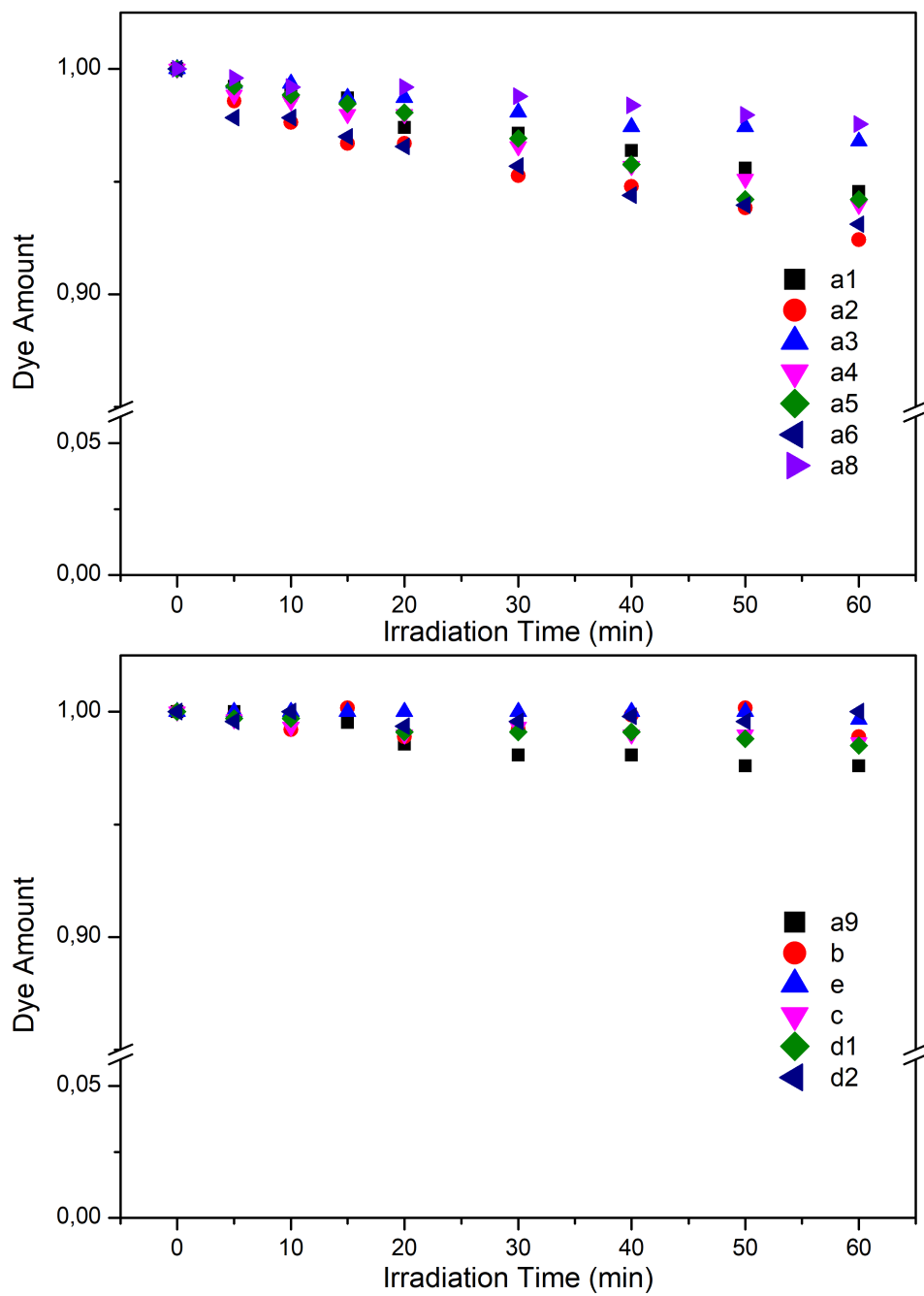
Figure S3.8: Photostability of the polystyrene-immobilized dyes(25°C, ambient air)
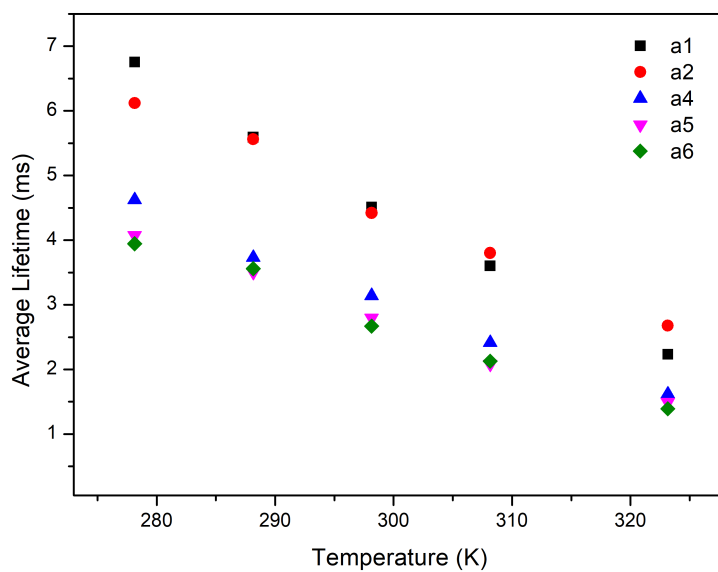
Figure S3.9: Temperature dependency of τ_0 (anoxic conditions) for anthraquinone dyes a1, a2, a4, a5 and a6 immobilized in polystyrene.
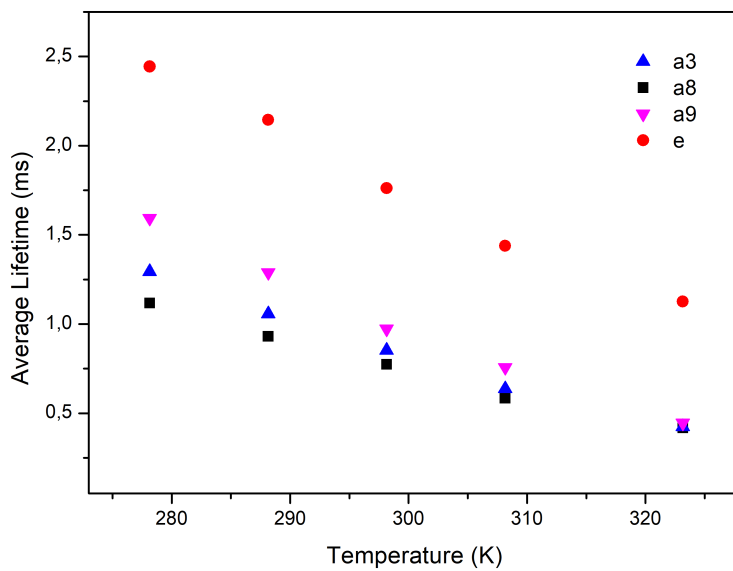
Figure S3.10: Temperature dependency of τ_0 (anoxic conditions) for anthraquinone dyes a3, a8, a9 and oligomeric e immobilized in polystyrene.
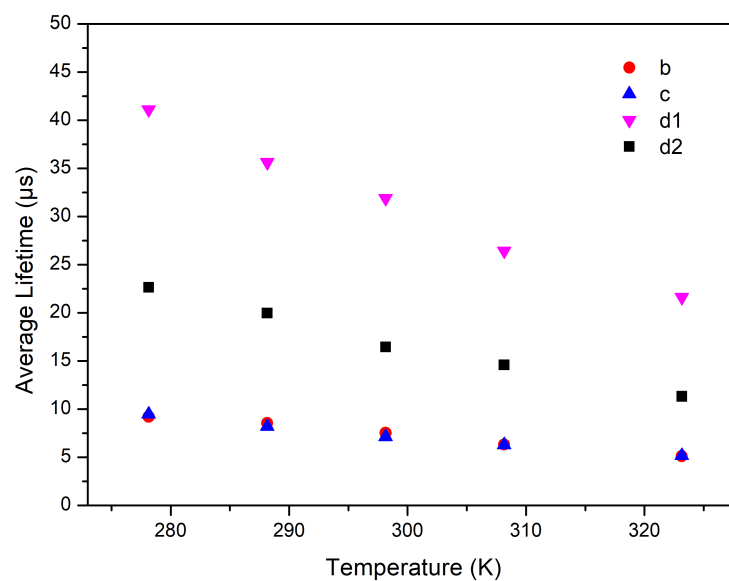
Figure S3.11: Temperature dependency of τ_0 (anoxic conditions) for dicyanobenzene dyes b-d2 immobilized in polystyrene.
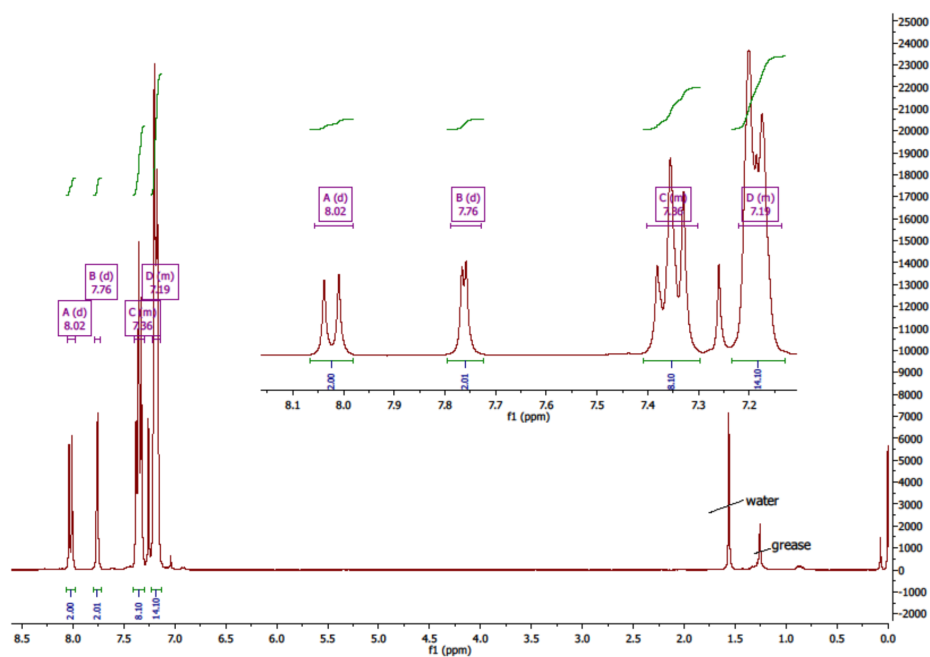
Figure S3.12: ^{1}H NMR spectrum (CDCl$_3$) of a1.
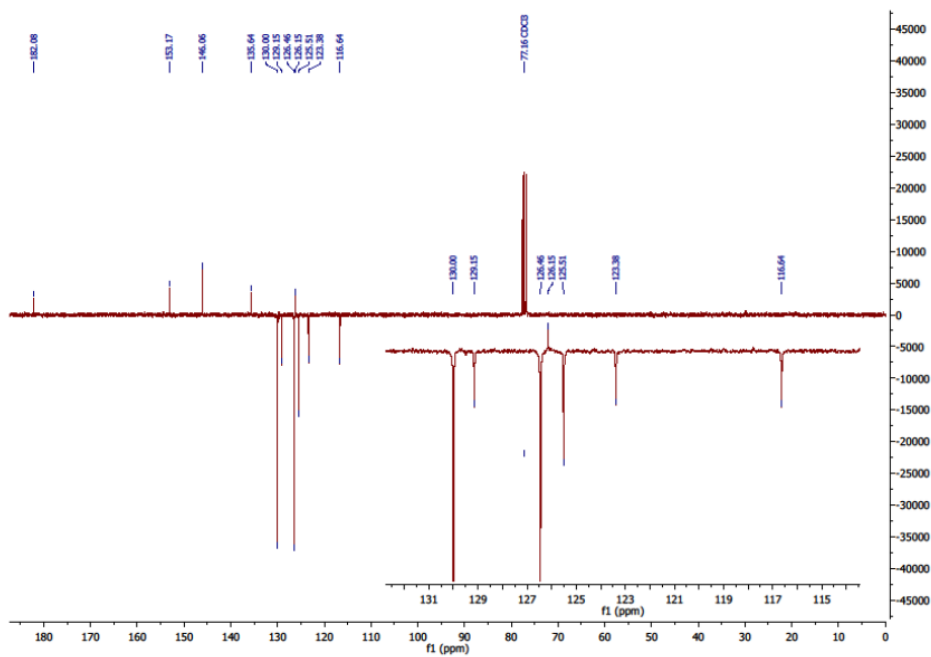
Figure S3.13: APT NMR spectrum (CDCl$_3$) of a1.
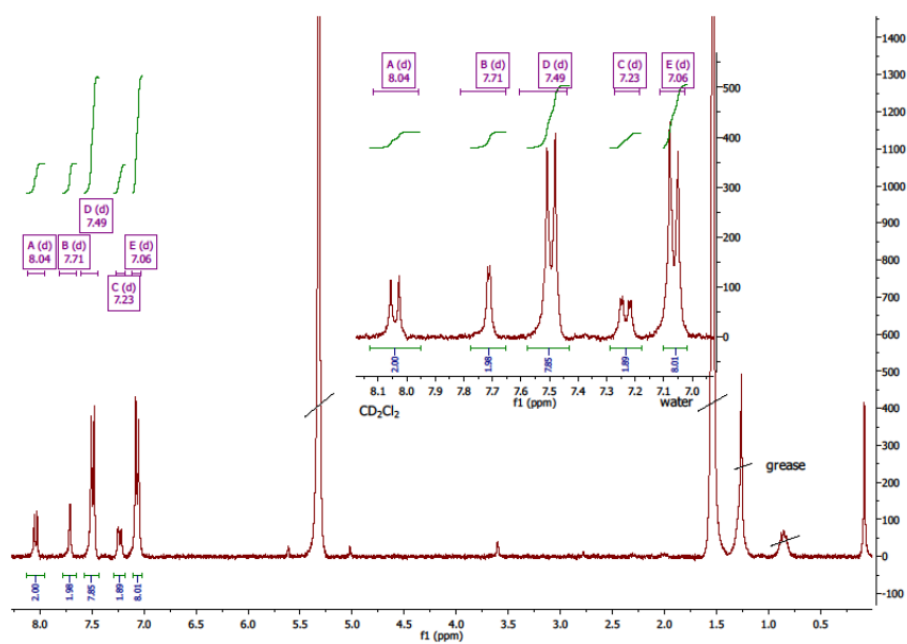
Figure S3.14: ^{1}H NMR spectrum (CD$_2$Cl$_2$) of a2.

Figure S3.15: APT NMR spectrum (CD$_2$Cl$_2$) of a2.

Figure S3.16: ^{1}H NMR spectrum (CDCl$_3$) of a3.
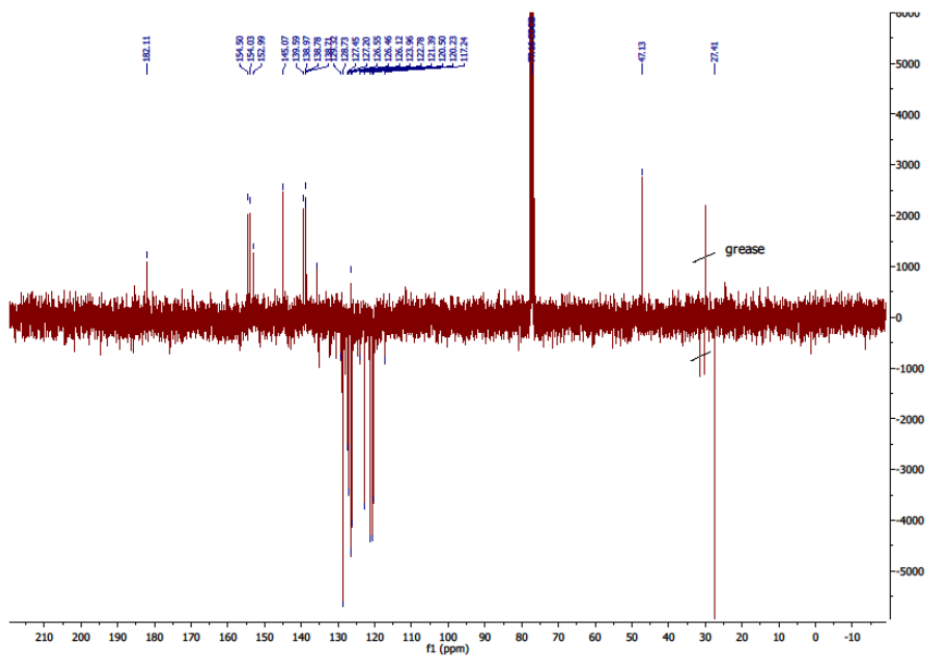
Figure S3.17: APT NMR spectrum (CDCl$_3$) of a3.
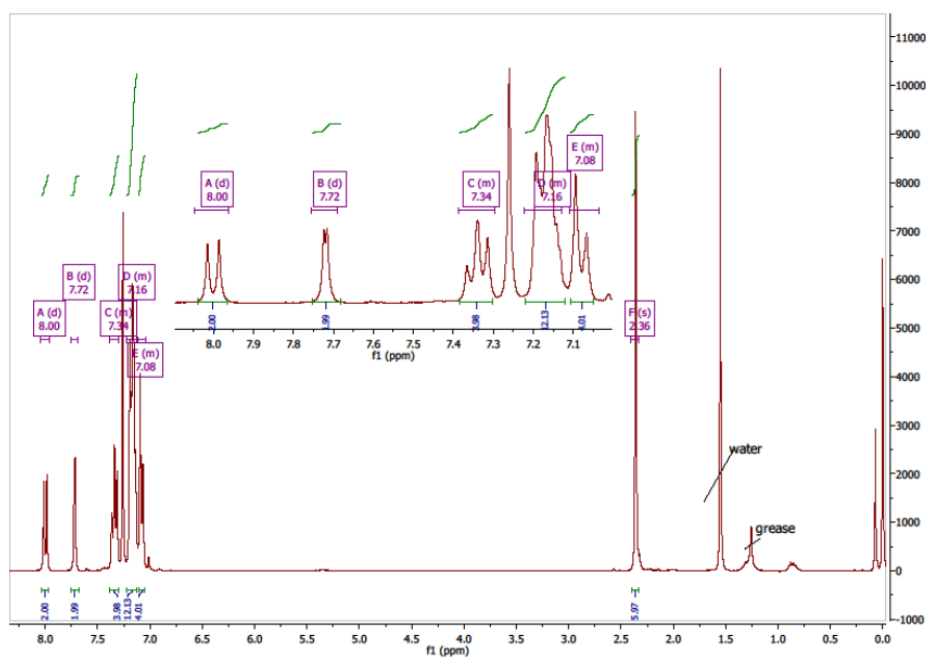
Figure S3.18: ^{1}H NMR spectrum (CDCl$_3$) of a4.
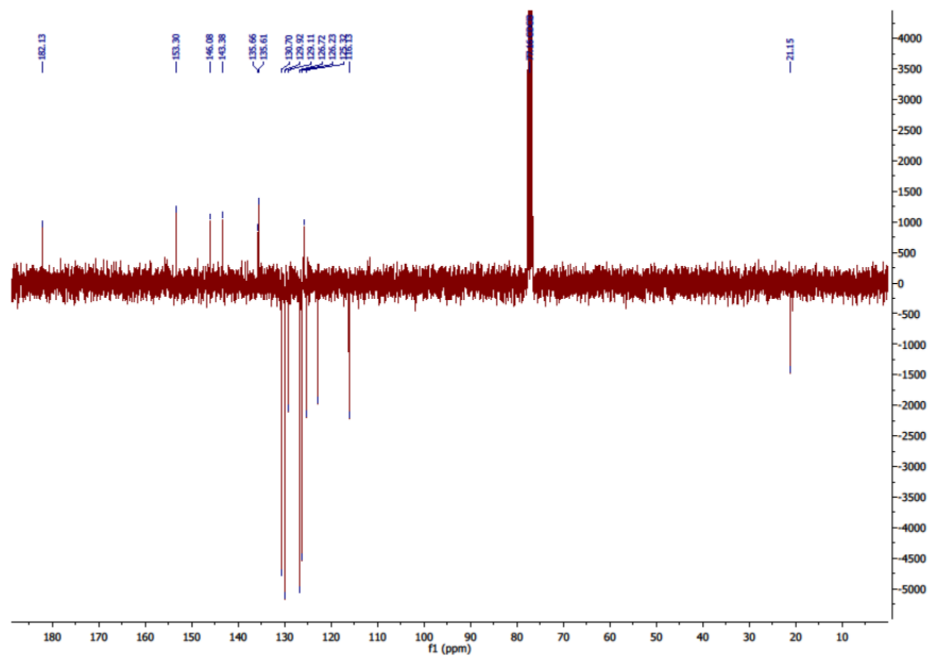
Figure S3.19: APT NMR spectrum (CDCl$_3$) of a4.
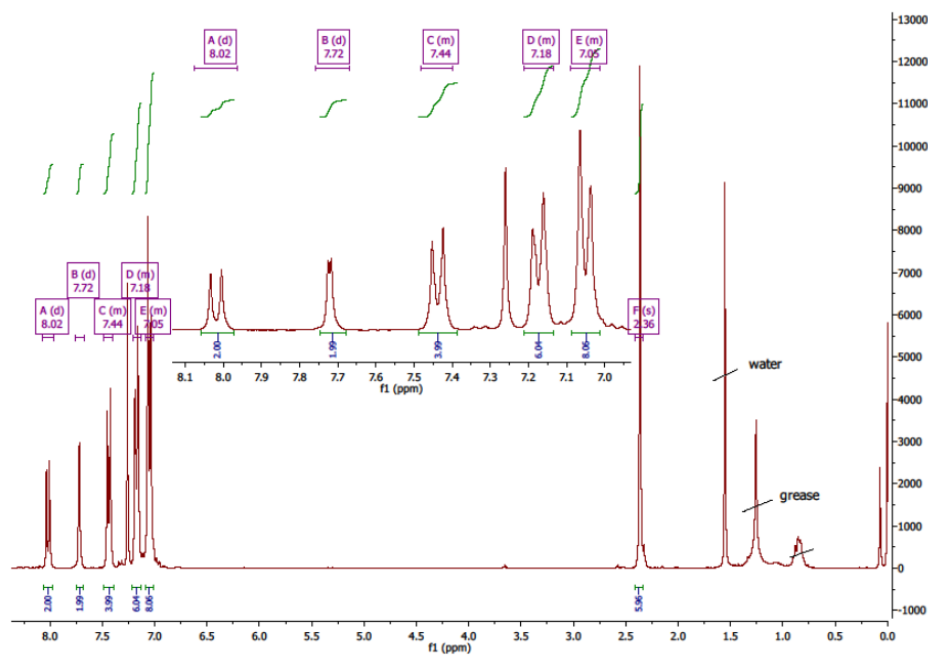
Figure S3.20: ^{1}H NMR spectrum (CDCl$_3$) of a5.

New Indicators for Optical Sensing by Manipulating the Intersystem Crossing in Luminescent Dyes
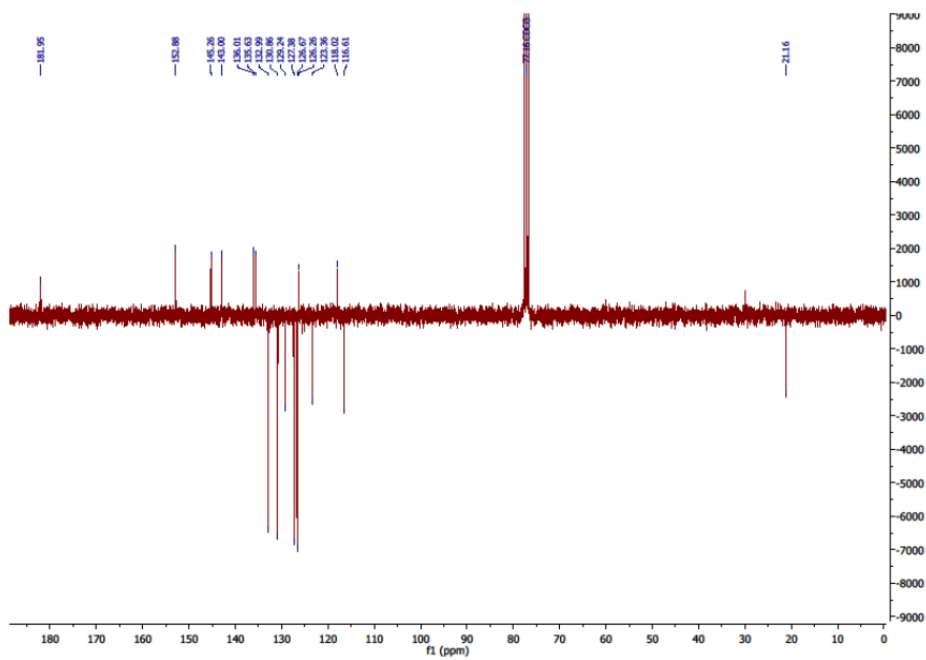
Figure S3.21: APT NMR spectrum (CDCl$_3$) of a5.
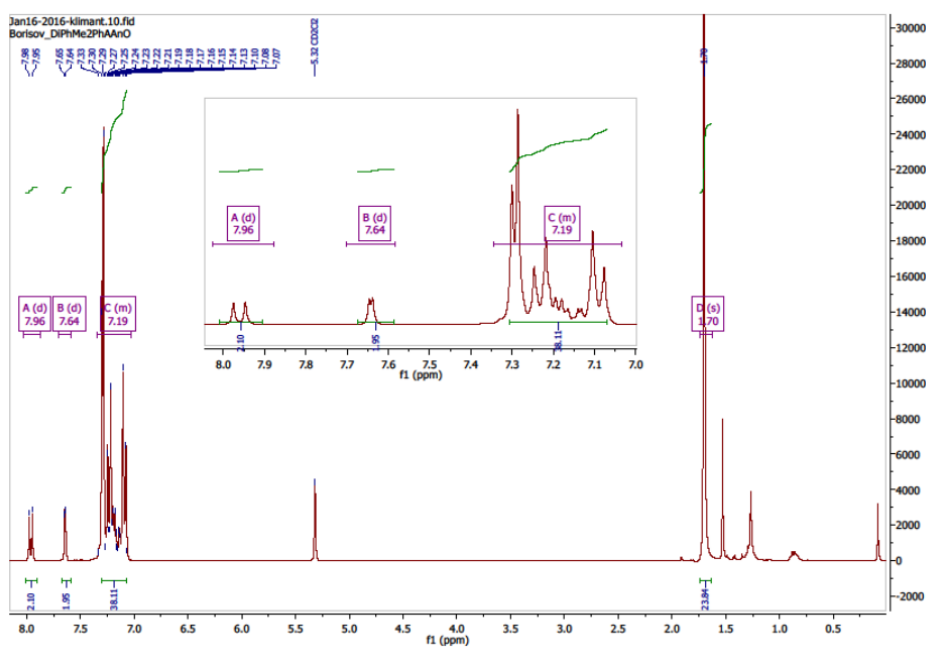
Figure S3.22: ^{1}H NMR spectrum (CD$_2$Cl$_2$) of a6.
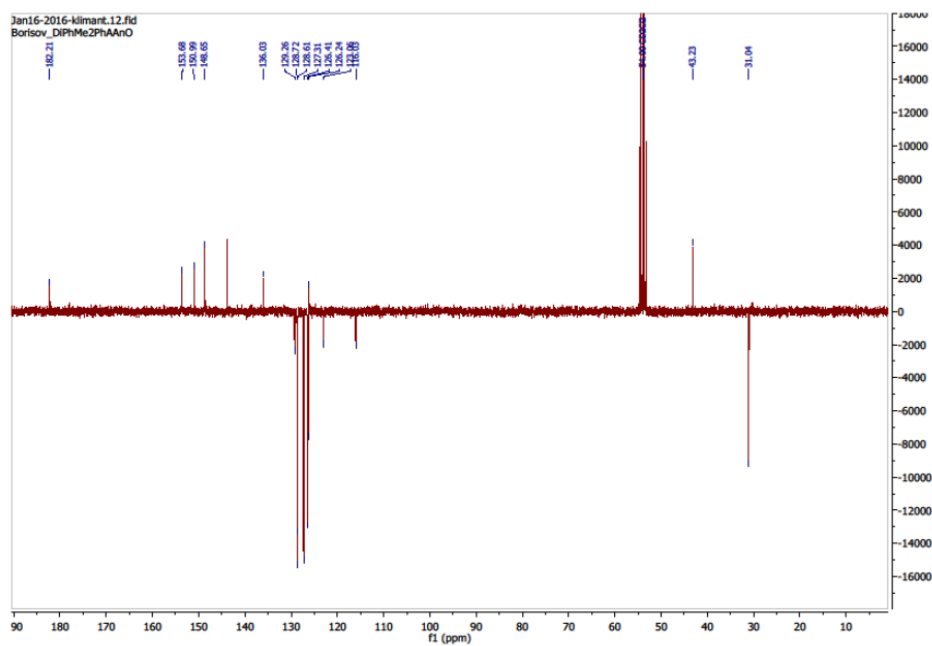
Figure S3.23: APT NMR spectrum (CD_2Cl_2) of a6.
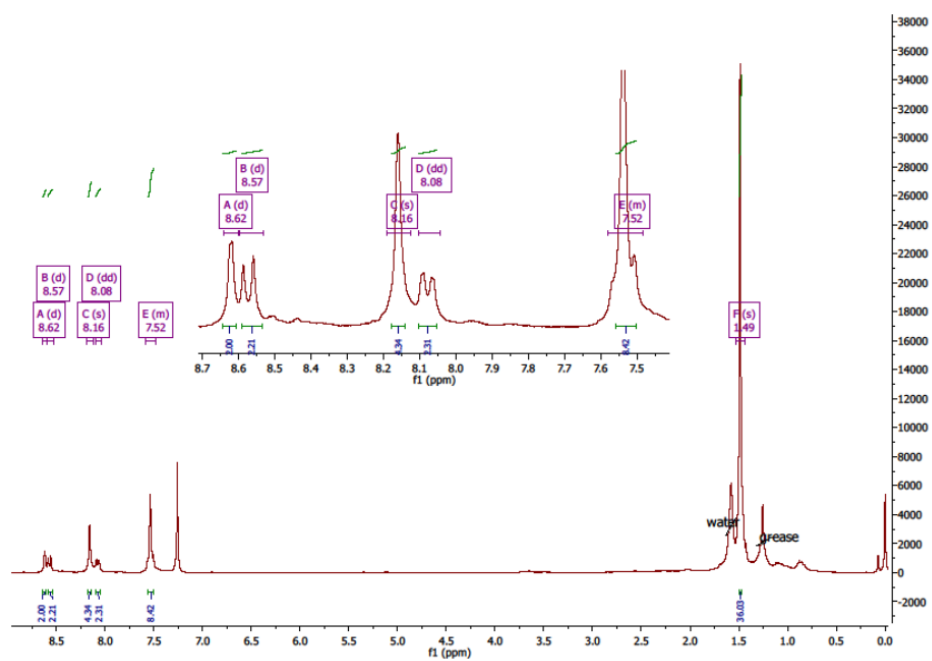
Figure S3.24: ^{1}H NMR spectrum ($CDCl_3$) of a7.

New Indicators for Optical Sensing by Manipulating the Intersystem Crossing in Luminescent Dyes
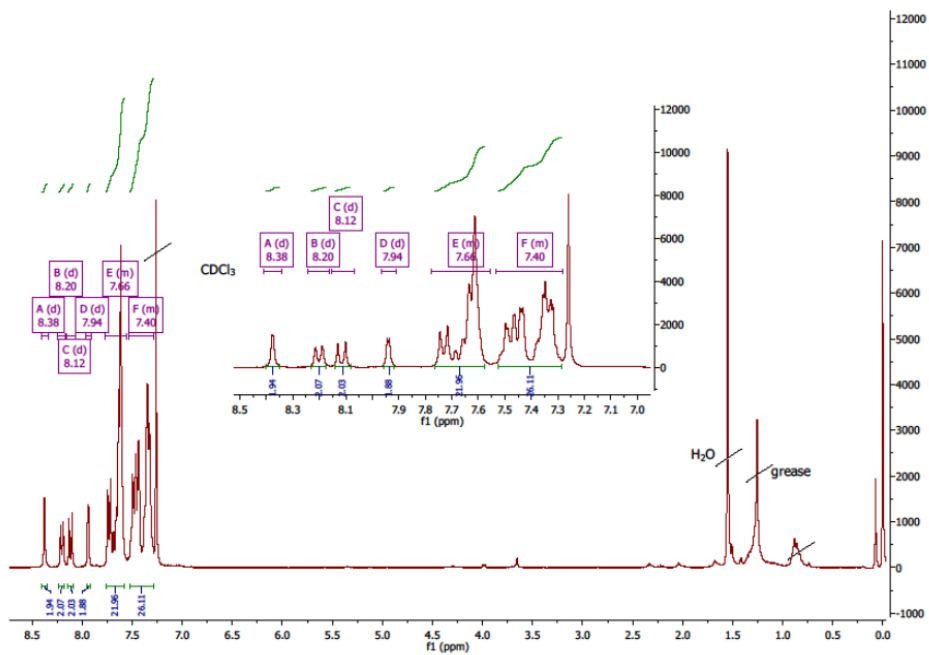
Figure S3.25: ^{1}H NMR spectrum (CDCl$_3$) of a8.
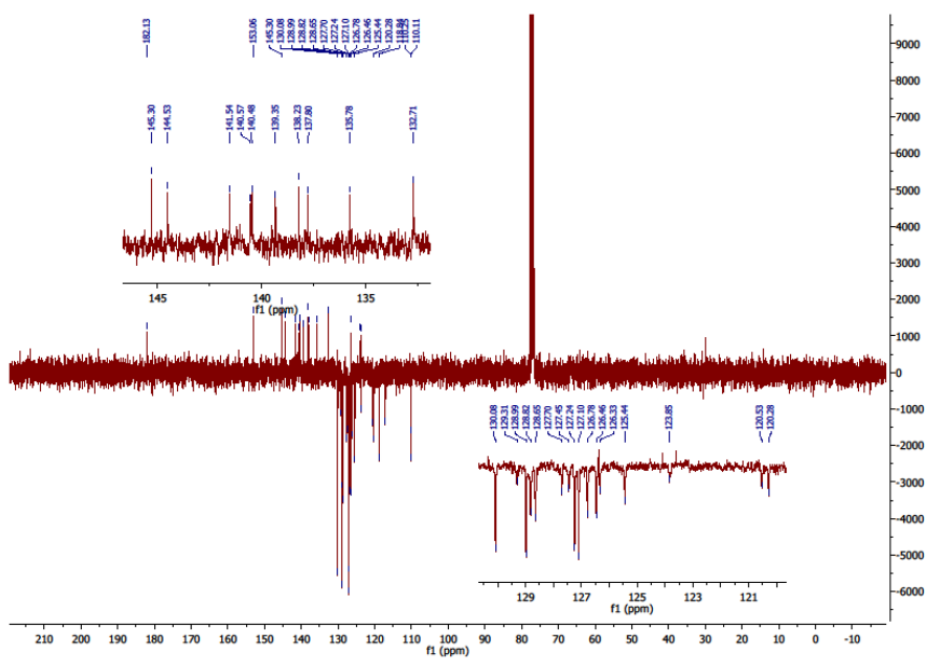
Figure S3.26: APT NMR spectrum (CDCl$_3$) of a8.

Figure S3.27: ^{1}H NMR spectrum (CDCl$_3$) of a9.

Figure S3.28: APT NMR spectrum (CDCl$_3$) of a9.

New Indicators for Optical Sensing by Manipulating the Intersystem Crossing in Luminescent Dyes
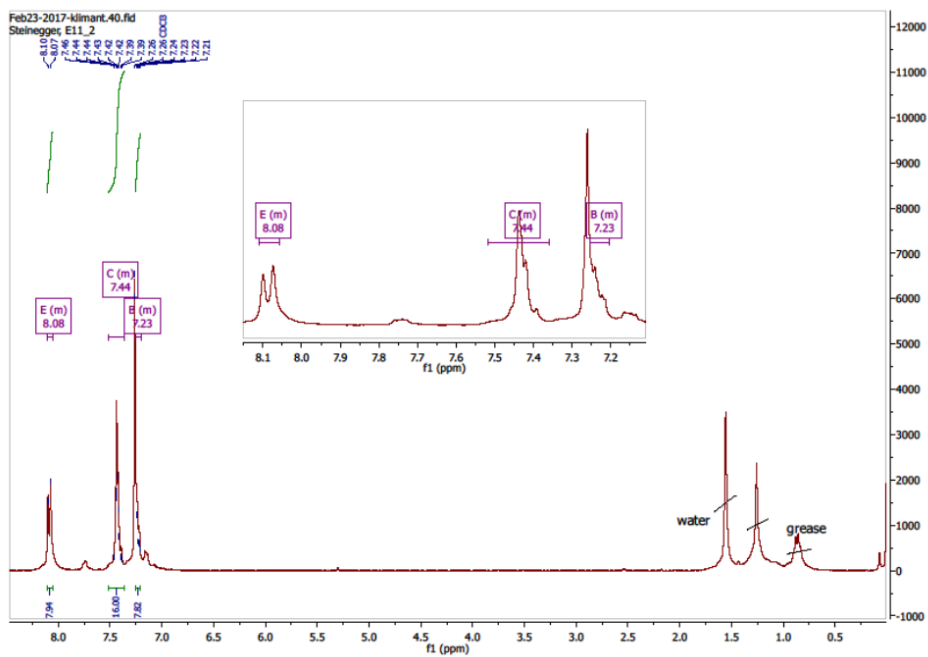
Figure S3.29: ^{1}H NMR spectrum (CDCl$_3$) of b.
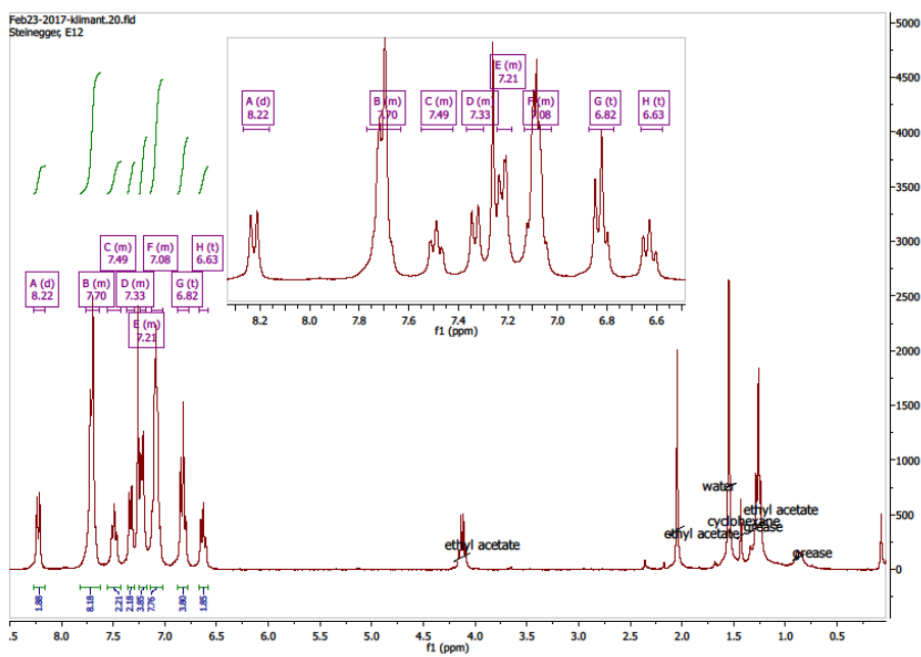
Figure S3.30: ^{1}H NMR spectrum (CDCl$_3$) of c.
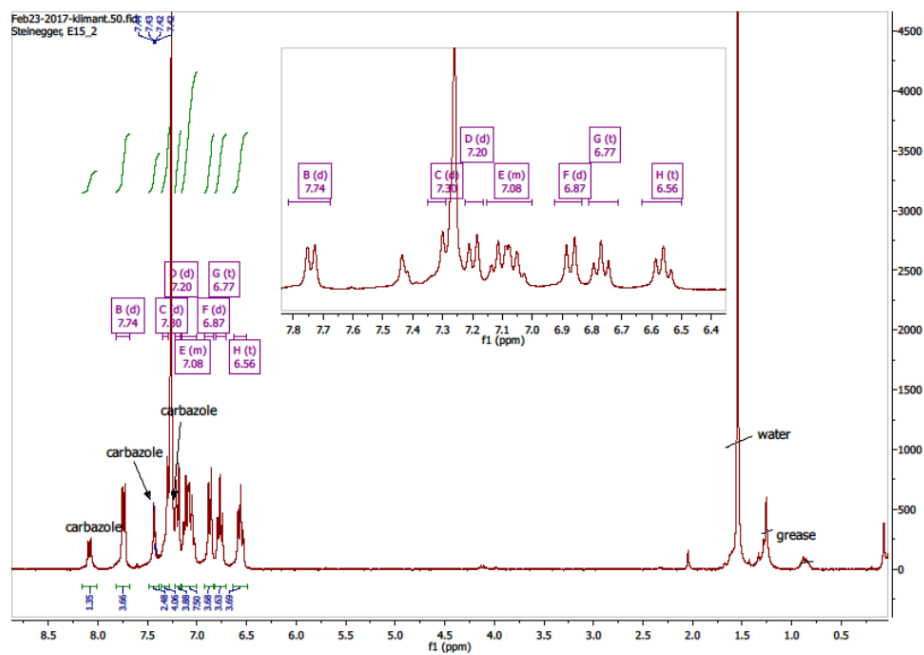
Figure S3.31: ^{1}H NMR spectrum (CDCl$_3$) of d1.
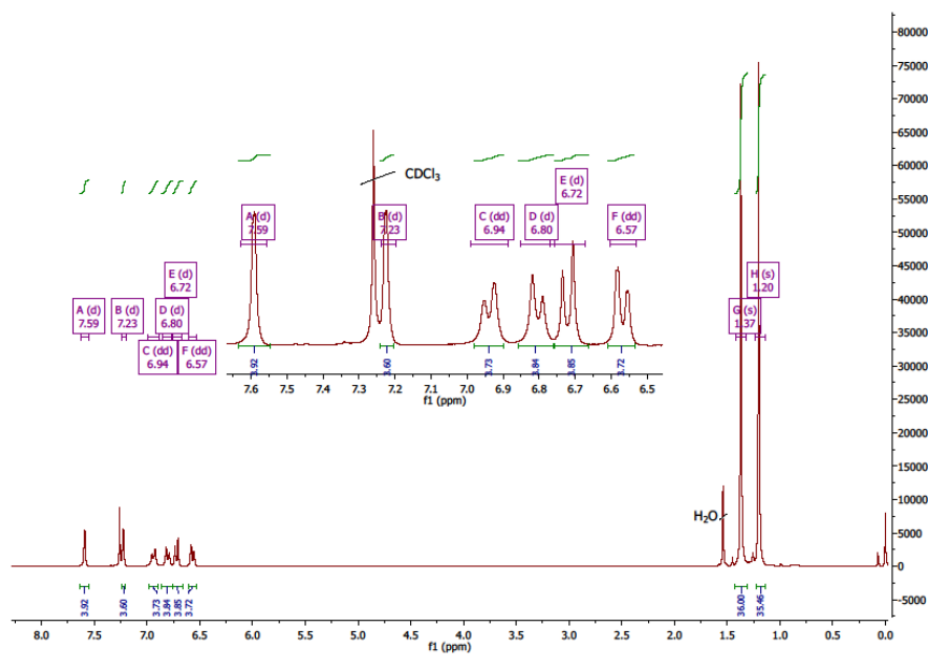
Figure S3.32: ^{1}H NMR spectrum (CDCl$_3$) of d2.

New Indicators for Optical Sensing by Manipulating the Intersystem Crossing in Luminescent Dyes

Figure S3.33: APT NMR spectrum (CDCl₃) of c.

Figure S3.34: ¹H NMR spectrum (CDCl₃) of e.

4 Zn(II) Schiff Bases: Bright TADF Emitters for Self-referenced Decay Time-Based Optical Temperature Sensing
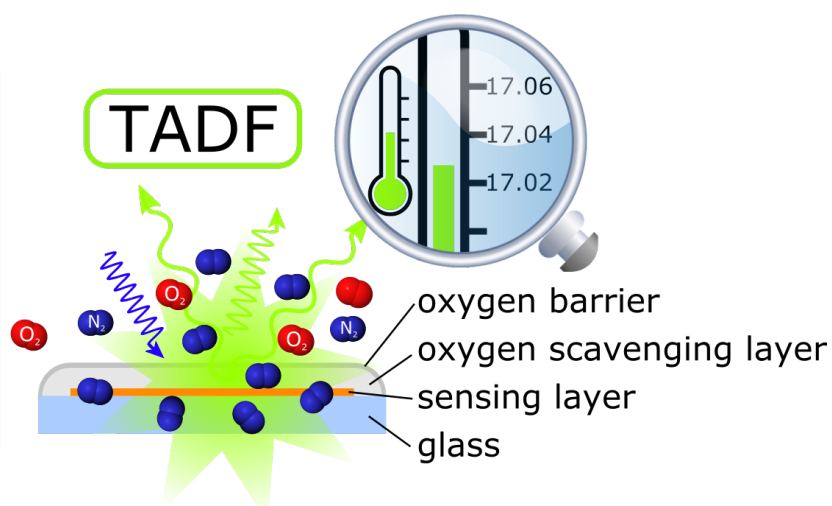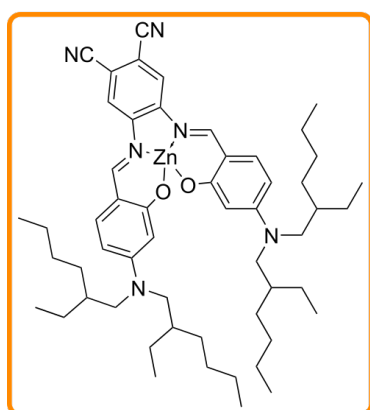
Preface to Chapter 4

This manuscript was published as *Full Paper* in *ACS Omega* and presents a new class of TADF emitters, Zn(II) Schiff base complexes, that possess excellent brightness and high temperature sensitivity and their application in temperature sensing materials.

Previously, a series of metal (Pd(II), Pt(II), Zn(II)) complexes with a donor-acceptor Schiff base were reported.[77] The Pd(II) and Pt(II) complexes were phosphorescent, the Zn(II) chelate displays prompt fluorescence and TADF. Despite good brightness, the Zn(II) complex was only poorly soluble in solvents and typical host materials for optical chemical sensors. In order to address this limitation, we prepared an analogous dye that was substituted with 2-ethylhexyl chains ensuring excellent solubility in apolar media. Additionally, another Zn(II) Schiff base complex was prepared to investigate the possibility of reducing the TADF lifetime and hence oxygen cross-sensitivity of the dye. To reduce the lifetime, a stronger donor in the donor-acceptor structure of the dye was used. The dye showed reduced TADF lifetime and exceptionally high TADF quantum yield when immobilized in a polymer matrix but suffered from poor solubility.

This new class of TADF emitters display high temperature sensitivity of the decay time at ambient temperature (4.1%/K change of TADF lifetime at 25 °C), while enabling a resolution better than 0.03 °C. For preparation of temperature sensing materials, the oxygen cross-talk was eliminated by covering the sensing layer with an off-stoichiometry thiol-ene polymer that acts as an oxygen-consuming layer, and a poly(vinylidene chloride-*co*-acrylonitrile) layer serving as an oxygen barrier. The sensing material was stable after more than 2 months of storage at ambient air.

The new materials benefit from the self-referenced character of the decay time read-out and are attractive candidates for high-resolution optical temperature sensing and imaging at ambient conditions.

Manuscript

Zn(II) Schiff Bases: Bright TADF Emitters for Self-referenced Decay Time-Based Optical Temperature Sensing

Authors: A. Steinegger and S. M. Borisov*

Graz University of Technology, Institute of Analytical Chemistry and Food Chemistry, Stremayrgasse 9, 8010 Graz, Austria

E-mail: sergey.borisov@tugraz.at

Abstract: Thermally activated delayed fluorescence (TADF) is a highly temperature-dependent process and can be used in optical thermometry. TADF-based optical thermometers reported so far show fairly hightemperature sensitivity but have poor brightness and significant oxygen crosstalk. A new class of TADF emitters, Zn(II) Schiff base complexes, possess excellent brightness and high temperature sensitivity of the decay time at ambient temperature (4.1%/K change of TADF lifetime at 25 °C), enabling a resolution better than 0.03 °C. Oxygen cross-sensitivity is eliminated by covering the sensing layer (luminophore in polystyrene) with an off-stoichiometry thiol-ene polymer as an oxygen-consuming layer, and a poly(vinylidene chloride-*co*-acrylonitrile) layer as an oxygen barrier. The material is stable after more than 2 months of storage at ambient air, which enables long-term temperature monitoring.

4.1 Introduction

Temperature is a fundamental parameter that is measured by a variety of methods. Although conventional temperature probes such as resistance temperature sensors are widely used offering good resolution over a broad temperature range, luminescent temperature probes represent an interesting alternative for some applications. Similar to IR thermometers, sensors based on luminescent probes offer advantages such as contactless measurement, minimal invasiveness, the possibility of imaging, and the absence of interference from electromagnetic fields.[29] Moreover, they can be combined with optical probes for other analytes,[222,223] enabling compensation of temperature cross-talk in situ, and be used on a nanoscale for studies in small objects such as microfluidic devices and cells.[29,108,137,224–227] Luminescent probes with analytically useful temperature-dependent behavior[29,102,104] include complexes of transition-metals[4,77,117,138,139,141,218,228–230] and lanthanides,[140,231–235] inorganic phosphors,[122–124,142,143] polymers,[188,191] nanomaterials,[100,126,128,192,193,236–238] proteins,[194] and organic dyes.[2,3,5,10,106,108,113,144,190] Transitionmetal complexes (most prominently Ru(II)

polypyridyls) are subject to oxygen quenching because of their long lifetimes and typically feature moderate brightness. The luminescence of lanthanide chelates[234,239–242] is much less affected by oxygen, but these complexes often suffer from low chemical stability (especially in polar solvents) and short-wavelength excitation which spans from the UV to blue part of the spectrum.22 In contrast, inorganic phosphors show much better chemical, thermal, and photochemical stability but their brightness is significantly lower than that for (metal)organic dyes. Moreover, the temperature coefficients are typically below 1%/K, particularly in the case of the decay time read-out.[119,121–123,142] Quantum dots generally possess high quantum yields, good photostability, and strongly temperature-dependent luminescence properties[101,102] but toxicity has been a concern. Fluorescent organic dyes such as rhodamine and derivatives display high brightness and no oxygen cross-talk but moderate temperature sensitivity. Because all the above probes show some limitations, search for alternative concepts utilizing other luminescent phenomena is still of high interest.

Thermally activated delayed fluorescence (TADF) is a highly temperature-dependent process that so far has only scarcely been used in optical thermometry.[2,3,5,78,144] The reported TADF dyes show high temperature sensitivity which makes them attractive emitters for potential applications such as molecular thermometers. On the other hand, fluorescence brightness, a crucial parameter for sensing and imaging applications, is moderate to poor because of low molar absorption coefficients.

In this contribution, we will show that a new class of TADF emitters, Zn(II) complexes with Schiff bases, combine high fluorescence brightness with highly temperature-dependent luminescence decay time and are, therefore, excellent indicators for luminescence thermometry. We will also demonstrate a simple approach to eliminate the intrinsic cross-sensitivity of such materials to oxygen by covering the sensing layer with an oxygen consuming offstoichiometry thiol-ene polymer (OSTE) layer and, subsequently, with an gas-impermeable poly(vinylidene chloride-*co*-acrylonitrile) layer. The resulting material has a 4.1 %K^{-1} change of the TADF lifetime at 25 °C and a resolution exceeding 0.03 °C.

4.2 Results and Discussion

4.2.1 TADF Indicators

TADF Indicators. Dyes with TADF have strongly temperature- sensitive luminescence that can be used for optical thermometry.[2,3,5,78,144] This dependency is manifested in TADF intensity that is enhanced with the temperature and the TADF decay time that is decreased with temperature. Whereas the fluorescence intensity depends on numerous parameters like the intensity of the excitation light or sensitivity of the photodetector and so forth, the luminescence decay time is a self-referenced parameter free of these interferences. TADF dyes have been reported to show strong temperature dependency of the decay time varying from -2.0 to -3.7%/ K for anthraquinone and dicyanobenzene emitters. Unfortunately, typical TADF emitters
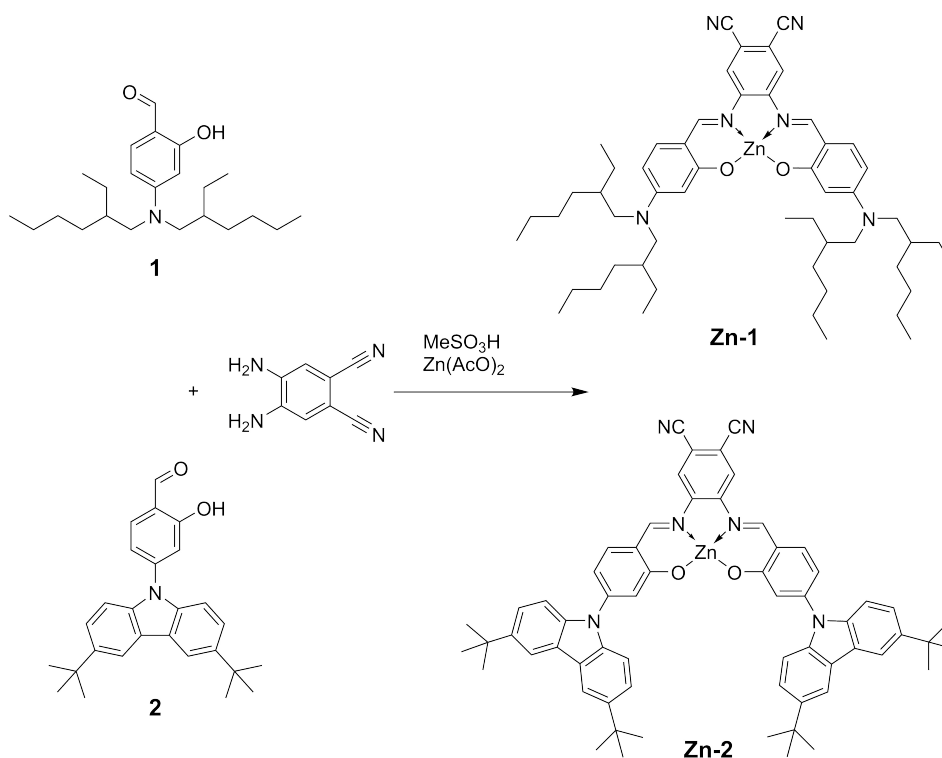
Figure 4.1: Synthesis and chemical structures of Zn(II) Schiff base complexes.

possess moderate to poor brightness[144] because of low molar absorption coefficients. Another challenge to overcome is strong oxygen cross-talk because of long decay times.[3]

Previously, we reported a series of metal complexes with a donor-acceptor Schiff base.[77] Whereas Pd(II) and Pt(II) complexes were phosphorescent, a Zn(II) chelate possessed prompt fluorescence and TADF. Despite rather high molar absorption coefficients, the solubility of the Zn(II) complex in organic solvents and polymers was poor which prevented potential applications of the dye in sensing materials. In order to address this issue, we prepared an analogous dye **Zn-1** (Figure 4.1) that is equipped with four 2-ethylhexyl chains ensuring excellent solubility of the dye in apolar media. The dye can be conveniently prepared in several steps (Figures S4.1 and S4.2). In order to investigate the possibility of reducing the TADF lifetime by using a stronger donor in the donor- acceptor structure of the dye,[15] we also synthesized dye **Zn-2** (Figure 4.1). The dye bears 3,6-di-*tert*-butylcarbazole that is a stronger electron donor compared to *N,N*-dialkylaniline. Four tert-butyl groups were expected to ensure sufficient solubility of the Zn(II) complex.

4.2.2 Photophysical Properties of the Indicators

Absorption and emission spectra of the Zn(II) complexes are shown in Figure 4.2 and the photophysical properties are summarized in Table 4.1. Both dyes absorb in the violet to blue region of the electromagnetic spectrum. **Zn-1** features a molar absorption coefficient of 75,000
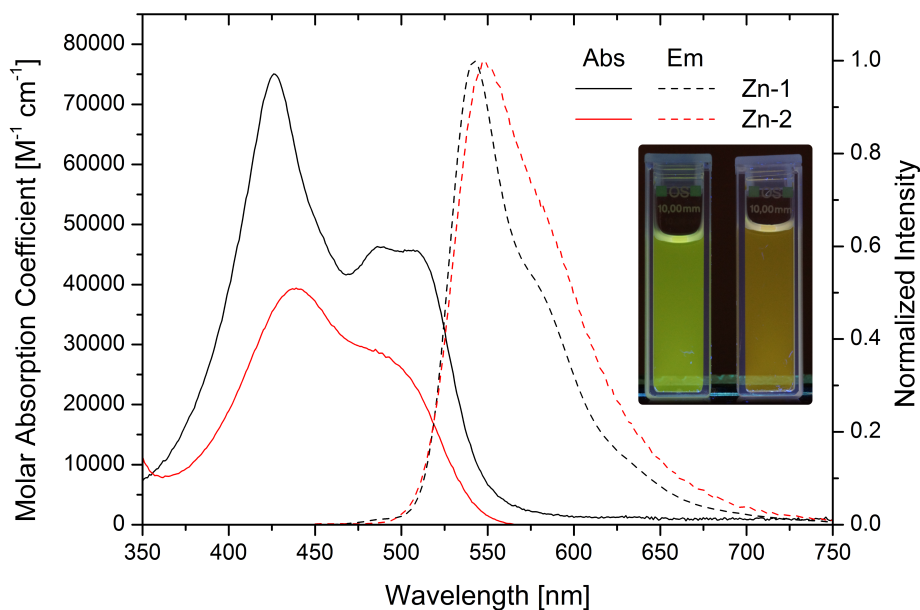
Figure 4.2: Absorption and emission spectra of **Zn-1** and **Zn-2** in toluene and photographic images of the solutions under UV-excitation (**Zn-1** left, **Zn-2** right).

M^{-1} cm^{-1} at 426 nm. The value is similar to the one reported for the dibutyl-substituted Zn(II) Schiff base complex.[77] This is several times higher than for typical TADF emitters, for instance dicyanobenzenes ($\varepsilon < 15{,}000$ M^{-1} cm^{-1}) and 2,6-diarylaminoanthraquinones ($\varepsilon < 25{,}000$ M^{-1} cm^{-1}).[144] The dye also shows efficient absorption at around 500 nm ($\varepsilon \approx 45{,}000$ M^{-1} cm^{-1}). Such spectral properties enable excitation with a bright palette of blue and green LEDs. **Zn-2** has a lower molar absorption coefficient of 39,000 M^{-1} cm^{-1} at 435 nm.

The dyes show bright green to orange emissions (Figure 4.2) that are attributed to a combination of prompt and delayed fluorescence. The latter is completely quenched by molecular oxygen in air-saturated solutions. In the case of **Zn-2** at 25 °C, the quantum yield of delayed fluorescence was estimated to be 14%, which is about 30% of the overall emission quantum yield (Table 4.1). For **Zn-1**, the quantum yield ϕ of prompt fluorescence determined under air-saturation was very similar to **Zn-2** (26 and 27%, respectively). Precise determination of the contribution of TADF is difficult in these conditions because of long decay times of the delayed fluorescence (>2.1 ms) and therefore very high efficiency of oxygen quenching. Estimation with the help of oxygen-scavenging Na_2SO_3 solution showed that ϕ DF is at least 5% for Zn-1, however, some degree of quenching by molecular oxygen cannot be excluded. As expected, increase in the donor strength resulted in a significant decrease of the TADF lifetime (435 µs and >2.1 ms for **Zn-2** and **Zn-1**), respectively. The decay curves have a mono-exponential form. Measurement at 77 K in a frozen glass (toluene/THF (4 + 6), v/v) reveal red phosphorescence with 625 and 630 nm, for **Zn-1** and **Zn-2**, respectively. The singlet-triplet energy gap was estimated (i) from temperature dependency of the DF decay time using an Arrhenius type

model[218] that is analogous to eq 35 from ref[12] and (ii) from the emission spectra. For **Zn-1**, the singlet-triplet energy gap was estimated to be 2725 cm^{-1} from the temperature calibration and 2515 cm^{-1} from the emission spectra. For **Zn-2**, the values are 2450 and 2280 cm^{-1}, respectively.

Table 4.1: Photophysical Properties of Zn(II) Schiff Bass Complexes in Toluene at 25 °C

Dye	$\lambda_{max,abs}$ [nm]	ε [M^{-1}cm^{-1}]	$\lambda_{max,em}$ [nm](a)	ϕ_{PF} [%]	ϕ_{DF} [%]$^{(b)}$	τ_{PF}[ns]	τ_{DF} [µs]$^{(b)}$
Zn-1	426, 486	75,000±1,700; 46,000±1,200	542	26±2	≥5	1.6±0.1	≥2.1 x 10^3
Zn-2	435, 490^a	39,000±600	547	27±2	14±2	1.8±0.1	435±1

$^{(a)}$ shoulder,

$^{(b)}$ anoxic conditions

4.2.3 Optical Temperature Sensors

In order to utilize TADF in optical temperature sensing, the emitters have to be immobilized into a polymeric or inorganic host. A common strategy to minimize oxygen cross-talk is immobilization into polymers with very low oxygen permeability such as poly(acrylonitrile)[4,5,138,141,218,243] or poly(vinylidene chloride-*co*-acrylontrile).[77] This strategy usually works well for the dyes with moderate decay times (∼1-100 µs) but cannot ensure complete elimination of the cross-talk in the case of **Zn-2** and particularly **Zn-1**. Moreover, we observed strong quenching of the TADF component upon immobilization of the Zn(II) Schiff base complexes into polyacrylonitrile (PAN). In fact, the TADF component for PAN-immobilized **Zn-2** constituted only approximately 2.5% of the overall fluorescence intensity. Therefore, PAN was not used for further investigations. Augusto et al.[5] reported a sensor design, where C$_{70}$-PS particles were dispersed in PAN by applying a pressure of 178 ton/m^2 for 1 h, at 120 °C. The system shows high sensitivity and no oxygen cross-talk, but requires a hydraulic heated press. Here, we present another straightforward strategy to eliminate oxygen cross-talk by covering the sensing layer with an oxygen-consuming OSTE layer (off stoichiometry thiol-ene polymer)[244] and, subsequently, with a gas-blocking poly(vinylidene chloride-*co*-acrylonitrile) (PVDCcoAN) layer used to reduce the oxygen diffusion into the OSTE layer, and hence prolong the oxygen-scavenging capability (Figure 4.3A). The OSTE resin is cured via a UV-initiated thiol-ene click reaction and then is subjected to further thermal curing. This step is needed to ensure attachment of the gas-blocking layer, although the oxygen-scavenging properties of the OSTE layer would be better with no thermal curing.[244] Nevertheless, the cured resin contains an excess of unreacted thiol groups responsible for the oxygen-scavenging properties of the material so that the sensing layer underneath can be deoxygenated completely. The glass support material is completely impermeable to oxygen and shields the sensing layer from one side.

This strategy provides the possibility to use virtually any polymer as a matrix for immo-
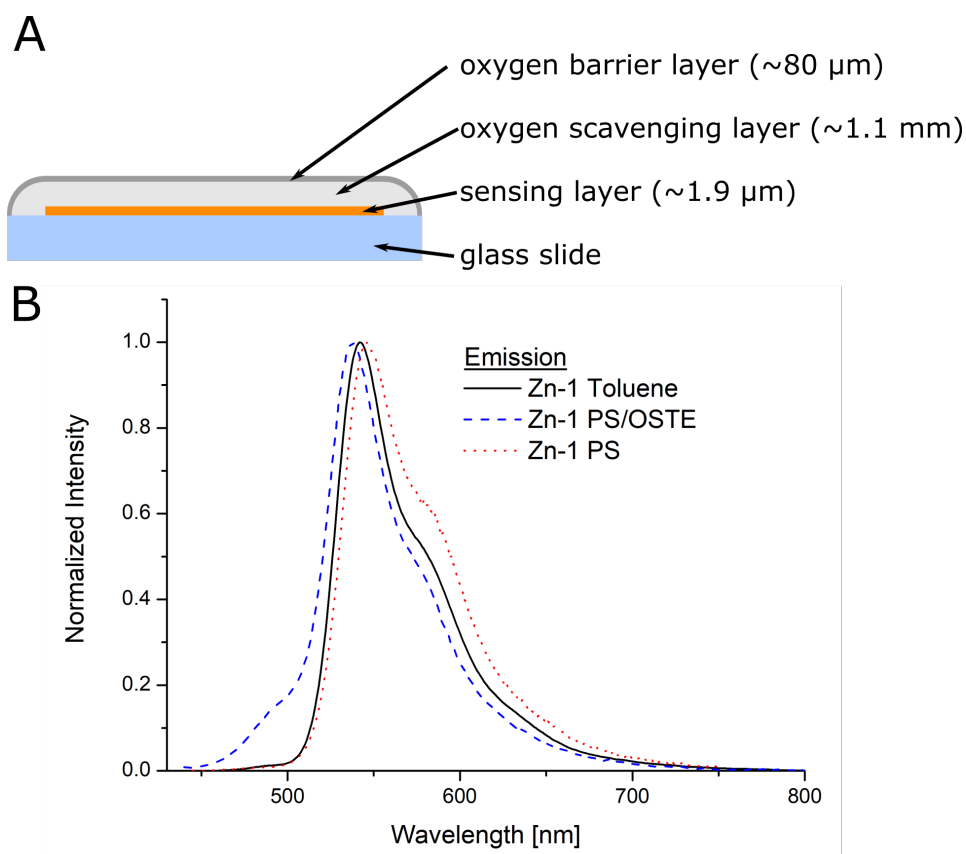
Figure 4.3: (A) Schematic of the optical thermometer utilizing a Zn-Schiff base complex as an indicator and OSTE layer as an oxygen scavenger. (B) Emission spectra of **Zn-1** in different environments.

bilization of the TADF emitter. Polystyrene (PS) was chosen for its high chemical stability, excellent optical properties, and good compatibility with the Zn(II) complexes. As can be seen (Table 4.2) the dyes show both prompt and delayed fluorescence in PS, and the photophysical properties of the immobilized are generally similar to those in toluene (Figure 4.3B). However, the quantum yield of TADF is strongly enhanced compared to toluene, particularly for **Zn-2**. Moreover, the TADF decay time increased several fold compared to toluene (Tables 4.1 and 4.2), which may be due to the more rigid environment in the polymer. Additionally, the decay curves now adopt a biexponential form (Figure 4.4A). Hence, the delayed fluorescence decays in PS were fitted with a bi-exponential model and average decay times were calculated. Because the delayed fluorescence is almost completely quenched in air, temperature dependency of the photophysical properties of PS foil was studied under anoxic conditions. The overall fluorescence intensity remains roughly constant. The intensity of the TADF component slightly increases with temperature. Such behavior is advantageous compared to molecular thermometers based on phosphorescent dyes and the majority of thermographic phosphors that show a decrease of luminescence intensity with temperature and thus decrease in the S/N ratio.

The temperature dependency of the TADF lifetime of the PS-immobilized complexes is shown in Figure 4.4. As can be seen, both dyes show extremely strong temperature dependency of the TADF lifetime. In fact, the decay time decreases by about twofold on going from 5 to 25 °C (Table 4.2). At 25 °C, the temperature sensitivity was 3.7 and 3.5% K^{-1} of the TADF lifetime change for **Zn-1** and **Zn-2** in PS, respectively.

Although both Zn(II) complexes are suitable for optical temperature sensing, **Zn-1** was selected for further investigation because of its significantly better solubility in PS and higher temperature coefficient. Application of additional layers of OSTE and PVDCcoAN was found to only slightly affect the TADF lifetime (Figure 4.4B). A minor effect is likely to be caused by some interaction between the indicator and the reaction products/quenchers that are formed during the curing steps which also maybe the reason for a shoulder in the emission spectrum at 490 nm (Figure 4.3B).

The response curve shown in Figure 4.4 represents the average from five measurement cycles, three of which were performed in air saturated water and two in the anoxic aqueous solution. Evidently, no influence of oxygen is visible. A long equilibration (4 h) in air-saturated and anoxic water also revealed no difference in the lifetimes in these conditions within the standard deviation from the calibration.

At 25 °C, the temperature sensitivity of the **Zn-1**-based sensor was calculated to be 4.1% K^{-1} of the TADF lifetime change. To the best of our knowledge, these values are the highest reported up to date for temperature probes utilizing decay time read-out including TADF emitters,[5,144] phosphorescent dyes,[77,138,139] and inorganic phosphors[121–123,142] (cf. Table 4.3). The poly(N-isopropylacrylamide)-based probes represent a notable exception showing very high sensitivity (10-27% K^{-1}) in a very narrow range (30-35 °C).[136,137] Although, the tested temperature range for most of the (metal)organic probes is typically limited to about 0-50

°C (Table 4.3), these probes are likely to be useful in a broader range. As can be seen from Figure 4.4B, the TADF-based sensor is expected to operate well below 5 °C and above 45 °C. Particularly, at elevated temperatures TADF appears to be advantageous over phosphorescence. In fact, whereas the S/N ratio for TADF probes is nearly constant or even initially improves with temperature, the phosphorescent probes show intensity decrease at elevated temperatures. Clearly, the (metal)organic probes are inferior to inorganic phosphors in respect to the temperature range. The latter feature high stability at temperatures well above 100 °C but the temperature coefficients and luminescence brightness are typically much lower than those for the (metal)organic probes.

The resolution of the sensing material at 21.5 °C was estimated using a frequency domain measurement of the luminescence phase shift with the help of a lock-in amplifier and optical fiber. To do so, the $3\times$ standard deviation (obtained from 100 measurement points) was divided by the sensitivity at the same temperature (Figure 4.5). The resolution calculated for the PS/OSTE/PVDCcoAN-sensing material is 0.03 °C. It should be considered that the resolution may be higher in reality because minor temperature fluctuations during the measurement cannot be excluded. Unfortunately, the resolution of a PT-100 resistance thermometer used as a reference is only 0.02 °C according to the specifications of the manufacturer.

The long-term stability of the **Zn-1**/PS/OSTE/PVDCco- AN-sensing material was assessed via decay time measurements at 25 °C during storage at ambient air (Figure 4.6). The decay time is expected to decrease after the oxygen-scavenging capabilities of the OSTE layer are exhausted.

As can be seen, no change in the decay time could be observed over 62 days. It should be noted that the thickness of the oxygen-scavenging layer is rather high (1.1 mm) but the concept is expected to be efficient also for thinner scavenging layers. The ability to completely eliminate oxygen quenching could also be useful for the design of reference materials for optical sensors based on phosphorescent dyes.

Table 4.2: Photophysical Properties of Zn(II) Schiff Base Complexes in PS

Dye	$\lambda_{max,abs}$ [nm]	$\lambda_{max,em}$ [nm]	τ_0 DF at 5 °C [ms]	τ_0 DF at 25 °C [ms]	ϕ_{PF} at 25 °C [%]	ϕ_{DF} at 25 °C [%]
Zn-1	438	542	14.4±0.5	7.41±0.03	19±4	11±4
Zn-2	446	547	2.91±0.11	1.45±0.01	18±2	47±6
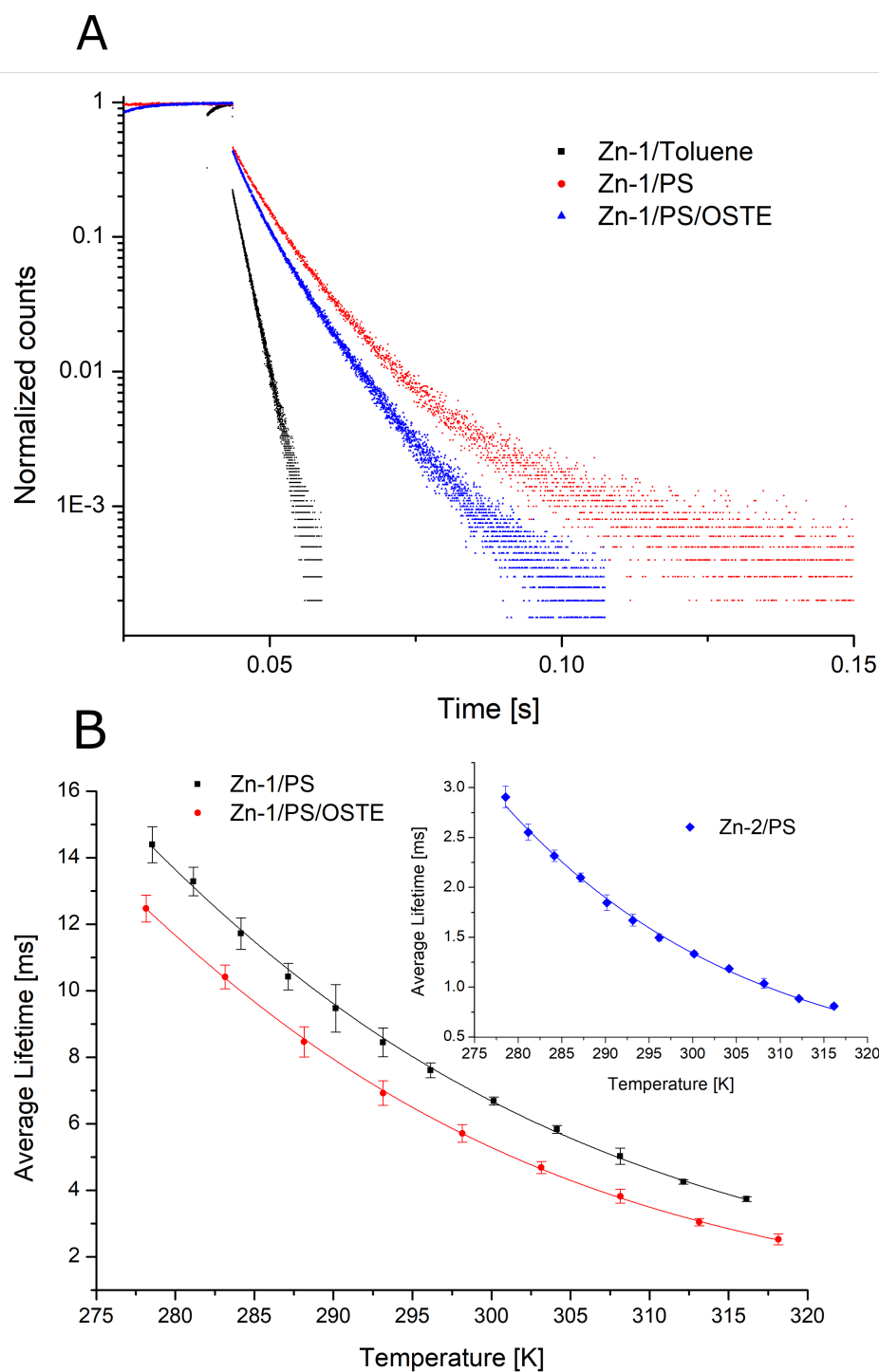
Figure 4.4: (A) TADF decay of **Zn-1** in different environments at 25 °C. (B) Temperature dependency of the average TADF decay time for the Zn(II) complexes embedded in PS. The decay times were measured under anoxic conditions in the case of PS foil (2 wt % aq Na_2SO_3 solution). For PS/OSTE/PVDCcoAN, the decay times are average values from measurements under air (2 times) and in deoxygenated conditions (3 times).

New Indicators for Optical Sensing by Manipulating the Intersystem Crossing in Luminescent Dyes

Table 4.3: Figures of Merits for Optical Thermometers Based on Decay Time Read-out

Material	T [K]	Ex/Em [nm]	Relative sensitivity, $d\tau/dT$ [%/K]	τ	T range [°C]	Ref.
Ru(phen)	303	470/580	-0.64	3.6 µs	0-60	[138]
$[Ru(phen)_2(4\text{-}Clp)]^{2+}$	298	450/590	$\sim$-1.35	$\sim$2.65 µs	0-40	[139]
Eu(TTA)3	298	350/615	-2.3	293 µs	5-50	[118]
EuDT	298	400/616	-2.2	$\sim$250 µs	10-50	[140]
Ir(ppy)$_2$carbac	303	405/519	$\sim$-0.5	2.2 µs	1-50	[141]
Mn^{4+}-doped magnesium fluorogermanate	274	355/620-683	-0.19	3610 µs	25-725	[142]
Ruby	274	520 or 532/694	-0.25	3980 µs	15-400	[122]
Spinel	274	520 or 532/690	-0.38	9830 µs	15-400	[122]
Cr^{3+}-doped yttrium aluminium borate	274	422 or 600/NIR	-0.97	237 µs	-10-70	[123]
Y$_3$Al$_5$O$_{12}$:Ce nanophosphor	298	337/700	-0.48	25 ns	7-77	[143]
Sulforhodamine derivative	298	540/565-605	-1.3	2.8 ns	5-55	[10]
1 nm CdTe quantum dots	298	405/510	-1.7	14 ns	20-50	[128]
arylamino-substituted anthraquinone	298	465/610	-3.7	677 µs	5-50	[144]
carbazole-substituted anthraquinone	298	470/580	-2.7	42 µs	5-50	[144]
carbazole-substituted dicyanobenzene	298	455/530	-2.0	11 µs	5-50	[144]
PS-C$_{70}$/PAN film	293	470/700	$\sim$-0.75	27.2 ms	-75-105	[5]
Pd(II) Schiff base complex	298	392/613	-2.1	103 µs	5-65	[77]
Zn-1	298	456/542	-3.7 (PS) -4.1 (PS/OSTE)	7.41(PS) ms 5.71 (PS/OSTE) ms	5-45	This work
Zn-2	298	456/547	-3.5	1.45 ms	5-45	This work
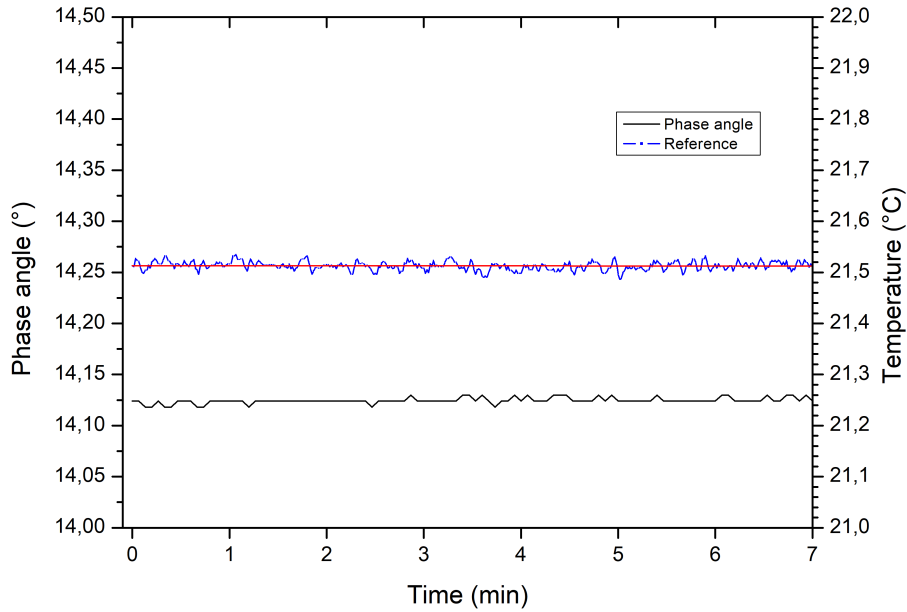
Figure 4.5: Time trace of the luminescence signal from the **Zn-1**/PS/OSTE/PVDCcoAN sensor (modulation frequency 32 Hz; black line) and the temperature as measured by a PT-100 resistance thermometer (blue line).
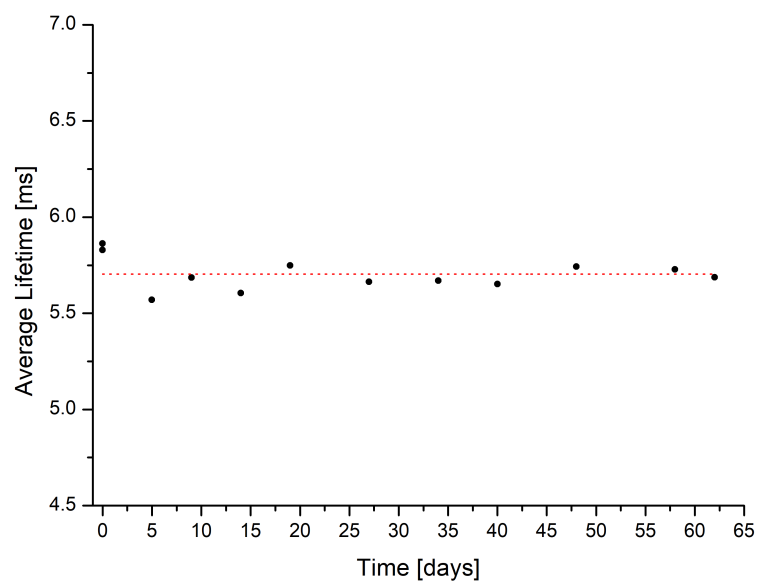
Figure 4.6: Long-term stability of the **Zn-1**/PS/OSTE/PVDCcoAN sensing material assessed via decay time measurements at 25 °C. The material was stored under ambient conditions between the measurements.

4.3 Conclusion

We presented highly sensitive materials for optical temperature monitoring based on the TADF-emitting Zn(II) Schiff base complexes. In contrast to common TADF emitters, the new dye class is characterized by high molar absorption coefficients resulting in excellent brightness under photoexcitation. The complexes feature unusually high temperature sensitivity of TADF lifetime exceeding 3.5%/K at 25 °C, enabling a resolution of at least 0.03 °C and benefitting from self-referenced character of the decay time read-out. Although, the carbazole-based derivative shows poor solubility in organic solvents and polymer matrices, it features about fourfold shorter decay times and higher TADF quantum yield compared to the *N,N*-dialkylamino derivative, which can be attractive for measurements in the frequency domain because of the higher modulation frequencies required.

Oxygen cross-talk is an intrinsic property of molecular emitters with long luminescence decay times. Above, we demonstrated a simple and efficient method to completely eliminate this cross-talk by adding a layer of the oxygen-scavenging OSTE polymer combined with a gas barrier made of PVDCcoAN. The OSTE layer retains its oxygen-scavenging capabilities for more than 60 days during storage under ambient air ensuring suitability of the new sensor for long-term temperature monitoring. The new materials are expected to be attractive for high-resolution optical temperature sensing and imaging at ambient conditions. Moreover, Zn(II) complexes with Schiff bases do not contain precious metals but abundant zinc and thus may be interesting for further investigation for potential applications in OLED technology. **Zn-2** shows exceptionally high TADF quantum yield when immobilized in a polymer matrix but the energy gap is still too high. Synthetic modifications that reduce the energy gap (stronger donor and acceptor groups) and improve solubility in polymers appear to be necessary here and they also are expected to be beneficial for the application of the dye as a molecular thermometer.

4.4 Experimental Section

4.4.1 Materials

Silica gel (0.04-0.063 mm) was purchased from Acros Organics (www.acros.com); anhydrous sodium sulfate and sodium hydrogen carbonate from VWR (www.vwr.com); chloro(trimethyl)-silane, $Zn(OAc)_2 \cdot 2H_2O$, $POCl_3$, and $BBr_3 \cdot SMe_2$ from Aldrich (www.sigmaaldrich.com); and methanesulfonic acid from abcr (https://www.abcr.de/). Solvents were purchased from VWR [cyclohexane (CH), ethyl acetate (EE), tetrahydrofurane (THF), all deuterated solvents], Fisher Scientific [dichloromethane (DCM)], Acros Organics (1,2- dichloroethane) and Roth [chloroform, *N,N*-dimethylformamide (DMF), toluene]. PS, av. MW ≈ 260,000 Da, was purchased from Acros Organics, PVDCcoAN, 20 wt % acrylonitrile content, av. Mn ≈ 80,000 Da, av. MW ≈ 125,000 Da, was from Scientific Polymer (scientificpolymer.com). Ostemer 322 Crystal Clear (OSTE) was purchased from Mercene Labs AB (https://www.ostemers.com/). Biaxially

oriented polyethylene terephthalate (PET) foils (125 µm) (MELINEX 506) were supplied by Pütz GmbH Co. Folien KG (www.puetz-folien.com).

4.4.2 Synthesis

3-(Bis(2-ethylhexyl)amino)phenol (**P1**)[245] and 4-(3,6-di-*tert*-butyl-9*H*-carbazol-9-yl)-2-methoxy-benzaldehyde (**P2**)[246] were prepared according to literature procedures (Figures S4.1 and S4.2).

4-(Bis(2-ethylhexyl)amino)-2-hydroxybenzaldehyde (**1**). In a flame-dried and Ar-flushed Schlenk tube, 447 mg (1.34 mmol, 1 equiv) of **P1** were dissolved in 13.4 mL of dry DMF. The slightly yellow solution was cooled to -50 °C and 650 µL (6.7 mmol, 5 equiv) of $POCl_3$ were added under stirring. The green reaction mixture was stirred for 30 min at -50 °C and was then allowed to warm up to room temperature. After quantitative conversion monitored by TLC, the solution was poured onto 40 mL of ice water. The product was extracted with 100 mL of DCM. Subsequently, the organic phase was washed with sat. $NaHCO_3$ (1 × 40 mL) and distilled water (2 × 40 mL). After drying over Na_2SO_4, the solvent was removed under reduced pressure. The crude product was further used without any purification.

Yield: 333 mg (69%), yellow oil.

^{1}H NMR (300 MHz, $CDCl_3$): δ 11.61 (s, 1H, -OH), 9.48 (s, 1H, O=C-H), 7.25 (d, $^3J_{HH}$ = 8.9 Hz, 1H), 6.27 (dd, $^3J_{HH}$ = 9.0, $^4J_{HH}$ = 2.4 Hz, 1H), 6.06 (d, $^4J_{HH}$ = 2.2 Hz, 1H), 3.38- 3.17 (m, 4H, 2× CH_2), 1.81 (m/hept, 2H, C-H), 1.41-1.14 (m, 16H, 8× CH2), 0.89 (m, 12H, 4× CH_3).

^{13}C-APT NMR (76 MHz, $CDCl_3$): δ 191.95 (O=C), 164.16 (C_q, C-OH), 154.95 (C_q, C-NR_2), 135.05 (C_t, ortho-C O=C), 111.41 (C_q, C-C=O), 105.47 (C_t), 97.88 (C_t), 56.41 (C_s, C-N), 37.21 (C_t), 30.60 (C_s), 28.65 (C_s), 23.91 (C_s), 23.20 (C_s), 14.12 (C^p), 10.73 (C_p).

MS (APCI): calcd for $C_{23}H_{39}NO_2$ [MH]$^+$, 362.3; found, 362.1.

4-(3,6-Di-tert-butyl-9H-carbazol-9-yl)-2-hydroxybenzaldehyde (**2**). In a flame dried and Ar flushed 50 mL Schlenktube, 600 mg (1.45 mmol, 1 equiv) of **P2** were dissolved in 25 mL of dry 1,2-dichloroethane under Ar. Boron tribromide dimethyl sulfide complex (693 mg, 2.18 mmol, 1.5 equiv) were added to the yellow solution. The intensivly purple solution was heated to 90 °C and stirred for 2 h. After full conversion monitored by TLC (CH + DCM = 1 + 1, dinitrophenylhydrazine staining), the reaction mixture was allowed to cool to room temperature and was washed with water (3 × 30 mL). The organic fraction was dried over Na_2SO_4 and the solvent was removed under reduced pressure. The crude product was purified by flash column chromatography on silica gel (CH + DCM = 1 + 1).

Yield: 441 mg (71%), pale white crystals.

^{1}H NMR (300 MHz, CDCl$_3$): δ 11.35 (s, 1H), 9.92 (s, 1H), 8.12 (s, 2H), 7.73 (d, $^3J_{HH}$ = 8.2 Hz, 1H), 7.58-7.43 (m, 4H), 7.33-7.21 (m, 2H), 1.46 (s, 18H). NMR data are consistent with the literature.[245]

MS (APCI): calcd for C$_{27}$H$_{29}$NO$_2$ [MH]$^+$, 400.2; found, 400.2.

Zn-1. In a 10 mL Schlenk tube, 50 mg (138 µmol, 4 equiv) of compound **1**, 5.5 mg (35 µmol, 1 equiv) of 4,5- diaminophthalonitrile, and 12 mg (52 µmol, 1.5 equiv) of zinc(II) acetate dihydrate were suspended in 4 mL of MeOH under Ar. Then, 20 µL of a methanesulfonic acid solution in MeOH (1 + 9, v/v) were added under Ar counterflow. The reaction mixture was heated to 40 °C and stirred for 2 h. After quantitative conversion, water was added to the reaction mixture and the precipitate was isolated via centrifugation and washed with water. The crude product was purified via precipitation from DCM with a MeOH/H$_2$O mixture (4 + 1, v/v), the precipitation was repeated five times.

Yield: 16 mg (51%), dark red solid.

^{1}H NMR (300 MHz, DMSO-d$_6$): δ 8.77 (s, 2H), 8.35 (s, 2H), 7.11 (d, $^3J_{HH}$ = 9.1 Hz, 2H), 6.21 (d, $^3J_{HH}$ = 8.4 Hz, 2H), 5.82 (s, 2H), 3.32-3.23 (m, 8H), 1.89-1.67 (m, 4H), 1.43- 1.13 (m, 32H), 0.86 (t, J = 6.5 Hz, 24H).

^{13}C NMR (76 MHz, DMSO-d$_6$): δ 174.67, 160.23, 154.56, 143.47, 137.86, 120.01, 116.85, 112.04, 108.21, 104.25, 102.03, 55.12, 36.95, 29.81, 28.07, 23.25, 22.57, 13.88, 10.58.

MALDI-TOF m/z: calcd for C$_{54}$H$_{78}$N$_6$O$_2$Zn [MH]$^+$, 907.5556; found, 907.4702.

Zn-2. In a 10 mL Schlenk tube, 88 mg (220 µmol, 4 equiv) of compound 2, 8.7 mg (55 µmol, 1 equiv) of 4,5- diaminophthalonitrile, and 18 mg (83 µmol, 1.5 equiv) of zinc(II) acetate dihydrate were suspended in 4 mL of MeOH under Ar. Then, 50 µL of a methanesulfonic acid solution in MeOH (1 + 9, v/v) were added under Ar counterflow. The reaction mixture was heated to 40 °C and stirred for 2 h. After quantitative conversion, the precipitate was isolated via centrifugation and washed with MeOH (3 × 3 mL) and CH (2 × 3 mL). The crude product was purified via precipitation from DCM with methanol/water mixture (4 + 1, v/v), repeated five times. Yield: 19 mg (35%), dark red solid. ^{1}H NMR (300 MHz, DMSO-d$_6$): δ 9.28 (s, 2H), 8.72 (s, 2H), 8.29 (s, 4H), 7.68 (d, J = 8.4 Hz, 2H), 7.54 (m, 8H), 6.89 (m, 4H), 1.42 (s, 36H).

MALDI-TOF m/z: calcd C$_{62}$H$_{58}$N$_6$O$_2$Zn [MH]$^+$ for, 983.3991; found, 983.4188.

4.4.3 Sensor Preparation

Silanization of Glass Slides. Microscopy glass slides were thoroughly washed with acetone and dried for 30 min at 110 °C. The slides were then immersed in a 10 wt % solution of chloro(trimethyl)silane in dry THF for 30 min. After drying at ambient air, the slides were further dried at 120 °C for 1 h. After silanization, the slides were broken to diagonally fit into 10 mm cuvettes.

PS Sensor Foil. Dye (1 wt % with respect to PS) and PS were dissolved in chloroform (7.5 wt % of PS in chloroform) and this "cocktail" was knife-coated (25 µm thick wet film) onto dust-free PET support foil. After evaporation of the solvent, the sensor foil was dried at 60 °C for 24 h.

OSTE Sensor Slides and Spots. Preparation of the sensing layer was performed as described above but dust-free trimethylsilyl-modified glass slides or spots (Ø8 mm, www. hilgenberg-gmbh.de) were used as a support instead of PET. The slides or spots were then covered with an approximately 1 mm thick layer (exact thickness of 1.14 ± 0.02 mm as determined with an "Inductive Dial Comparator 2000 Extramess" from Mahr, https://www.mahr.com/) of OSTE (from two components according to instructions) and UV cured for 2 min (365 nm, 8 W, UV-handheld lamp from Herolab supplied by Carl Roth GmbH). Subsequently, the slides were thermally cured at 150 °C for 7 min. Finally, the OSTE layer was covered with a (PVDCcoAN) solution in THF (10 wt %) in a dry atmosphere (glove box) and dried for 24 h. The thickness of the PVDCcoAN layer was 79 ± 2 µm.

4.4.4 Characterization

NMR spectra were recorded on a Bruker AVANCE III spectrometer equipped with an autosampler (300.36 MHz ^{1}H NMR, 75.53 MHz ^{13}C NMR). MS: mass spectrometric measurements of **Zn-1** and **Zn-2** were performed on a matrix-assisted laser desorption/ionization (MALDI)-TOF/TOF (time of flight) spectrometer from Bruker (www.bruker.com).

Mass spectrometry of the precursors was performed on an Advion expression CMS with atmospheric pressure chemical ionization (APCI).

UV-vis spectra were recorded on a VARIAN CARY 50 conc. using Hellma Analytics (www.hellma-analytics.com) optical glass 10 mm precision cuvettes.

Luminescence spectra were recorded on a Fluorolog 3 spectrofluorometer from HORIBA Scientific equipped with a R2658 photomultiplier from Hamamatsu (www.hamamatsu.com). Screw-capped quartz precision cuvettes from Hellma Analytics were used for measurement under anoxic conditions. Deoxygenation of toluene solutions was performed by bubbling high purity argon (99.999% purity) through the solution for 10 min and subsequent addition of 2 wt % aq Na_2SO_3 solution.

Luminescence decays were obtained via time-correlated single photon counting on a Fluorolog 3 spectrofluorometer equipped with a DeltaHub module controlling a SpectraLED-460 (456 nm)

or NanoLED (456 nm) laser diode and using DAS-6 Analysis software for data analysis. Data were fitted using a mono or biexponential decay model. Average lifetimes, τ, were calculated from the relative amplitudes (B1, B2) and lifetimes (τ_1, τ_2) of the individual components from the biexponential model using the equation $\tau = (B1 \times \tau_1 + B2 \times \tau_2)$. A "Quanta-$\varphi$" integrating sphere-based set-up on a Fluorolog 3 spectrofluorometer (HORIBA Scientific) was used to determine absolute quantum yields.

Fiber Optic Setup. The luminescence phase shifts were measured with a lock-in amplifier (SR830 DSP, Standford Research, www.thinksrs.com). The excitation of the sensor material was performed with a 440 nm LED from Roithner (www.roithner-laser.com). The LED was filtered through a combination of a BG12 glass filter and a "Lagoon-blue" plastic filter obtained from bk Interferenzoptik (www.interferenzoptik. de) and from LEE Filters (www.lee-filters.com), respectively. A fiber bundle was used to guide the excitation light to the indicator spot and to transfer the emitted luminescence to the photomultiplier detector. A combination of an OG550 longpass filter obtained from bk Interferenzoptik and a plastic filter "Oklahoma Yellow" from LEE filters was installed in front of the photomultiplier. The phase shift was measured at a modulation frequency of 32 Hz and the 0-phase adjustment was performed with a solution of fluorescent dye Lumogen orange (Kremer Pigmente) in toluene.

For *temperature calibrations*, the temperature was adjusted with a Cary SPV-1X0 Single Cell Peltier Accessory Peltier element from Varian in combination with a cryostat from Avantor, model 1150S (us.vwr.com). The PS sensor foil or the PS/OSTE/PVDCcoAN sensor slides were placed diagonally in Hellma Analytics optical glass 10 mm precision cuvettes. The cuvettes were filled with air-saturated water (OSTE sensors) or aqueous 2 wt % Na_2SO_3 solution (PS and OSTE sensors). After temperature adjustment, the cuvettes were thermally equilibrated for 10 min. The temperature was adjusted between 5 and 45 °C. Five decay time measurements were made at each temperature. The calibration cycle was repeated three times.

Determination of the Resolution with the Fiber Optic Setup. The fiber was immersed in a cryostat from Avantor, model 1150S (us.vwr.com). The temperature was adjusted to 15 and 35 °C. The calibration cycle was repeated three times at a modulation frequency of 32 Hz. The average phase shifts were used to determine the sensitivity of the sensor. To determine the noise, the sensor fiber was immersed in a 5 L beaker that was thermally equilibrated at room temperature and the phase shift of 100 measurement points was recorded. The resolution was calculated by dividing three times the standard deviation obtained for 100 measurements by the sensitivity. The temperature was logged with a PT-100 resistance thermometer (resolution of 0.02 °C) connected to a commercially available FireStingO2 oxygen meter (from PyroScience, www.pyroscience.com).

Long-Term Stability. For the long-term stability tests, the sensor material was stored at ambient conditions (air; temperature 22 °C), but shielded from light. For measurements, the PS/OSTE/PVDCcoAN sensor slides were placed diagonally in cuvettes filled with air-saturated water. The temperature was adjusted to 25 °C with the same setup used for temperature

calibration. The cuvettes were thermally equilibrated for 10 min and then five decay time measurements were made.

4.4.5 Data Analysis

An Arrhenius type model[218] (eq 4.1) was used to fit the average decay times from the temperature calibrations

$$\tau = (k_0 + k_1 e^{\frac{-\Delta E}{k_B T}})^{-1} \tag{4.1}$$

where k_0 is the temperature-independent decay rate for the excited-state deactivation, k_1 is a pre-exponential factor, k_B is the Boltzmann constant, ΔE is the energy necessary for the reverse ISC (corresponds to the singlet-triplet energy gap), and T is the absolute temperature.

4.5 Acknowledgements

4.6 Supporting Information
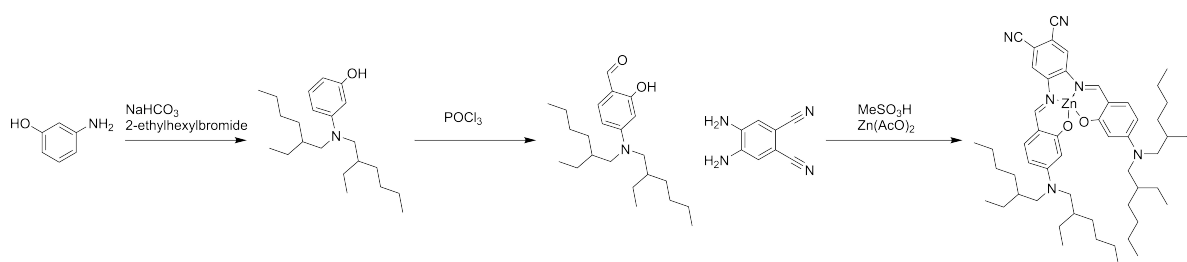
Figure S4.1: Synthesis of **Zn-1**. The first step according to literature.[245]
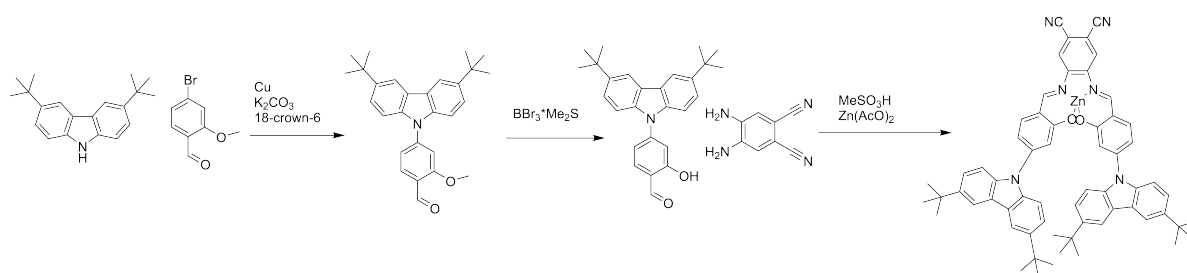
Figure S4.2: Synthesis of **Zn-2**. The first step according to literature.[246]
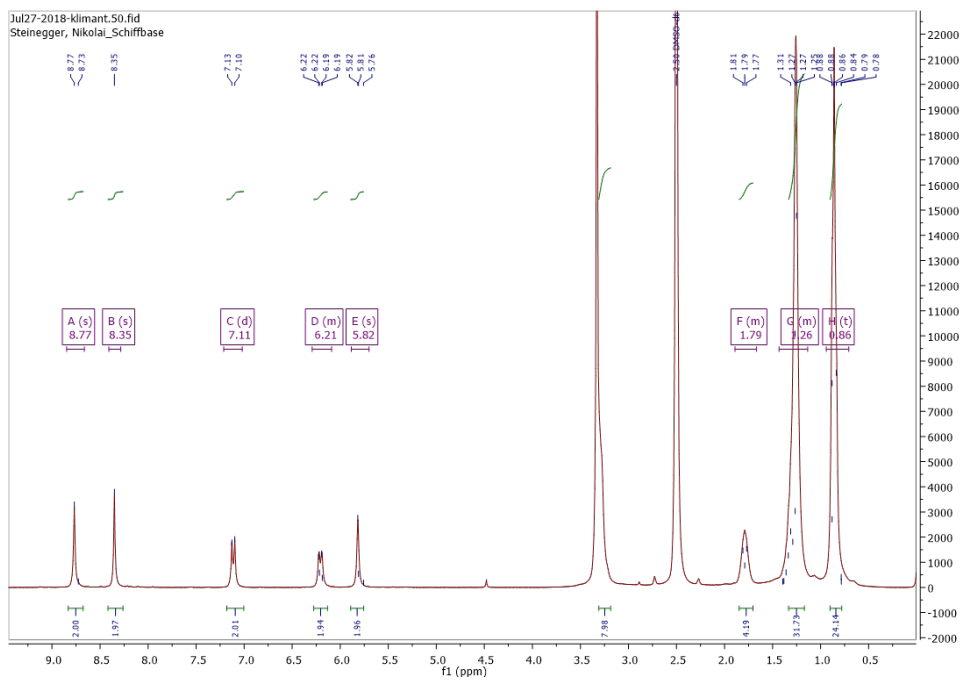
Figure S4.3: ^{1}H-NMR spectrum of **Zn-1** in DMSO-d$_6$.
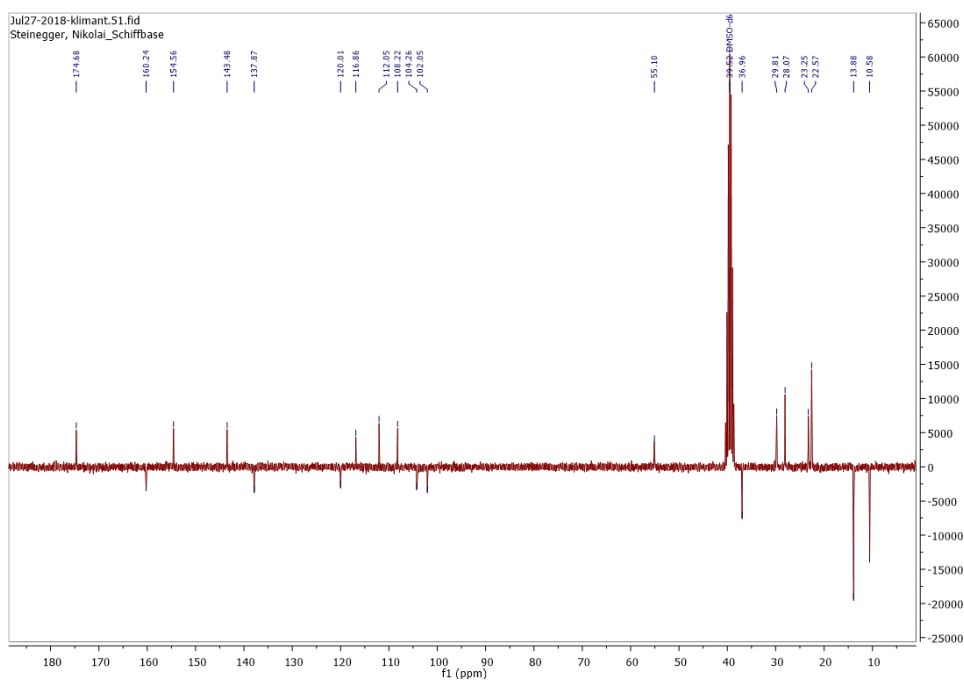
Figure S4.4: APT-NMR spectrum of **Zn-1** in DMSO-d$_6$.

New Indicators for Optical Sensing by Manipulating the Intersystem Crossing in Luminescent Dyes
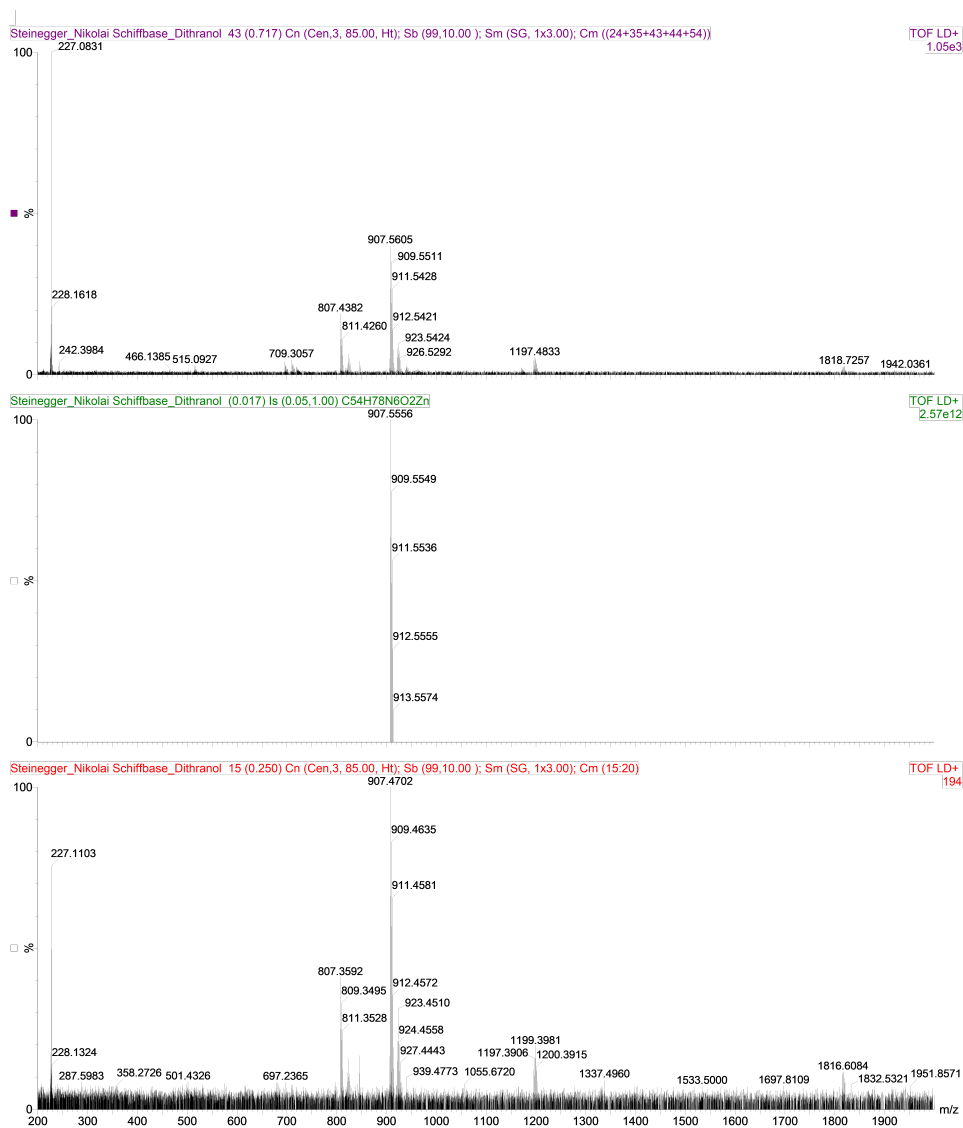
Figure S4.5: MS spectrum of **Zn-1**.

Figure S4.6: Isotope pattern from the MS spectrum of **Zn-1**.
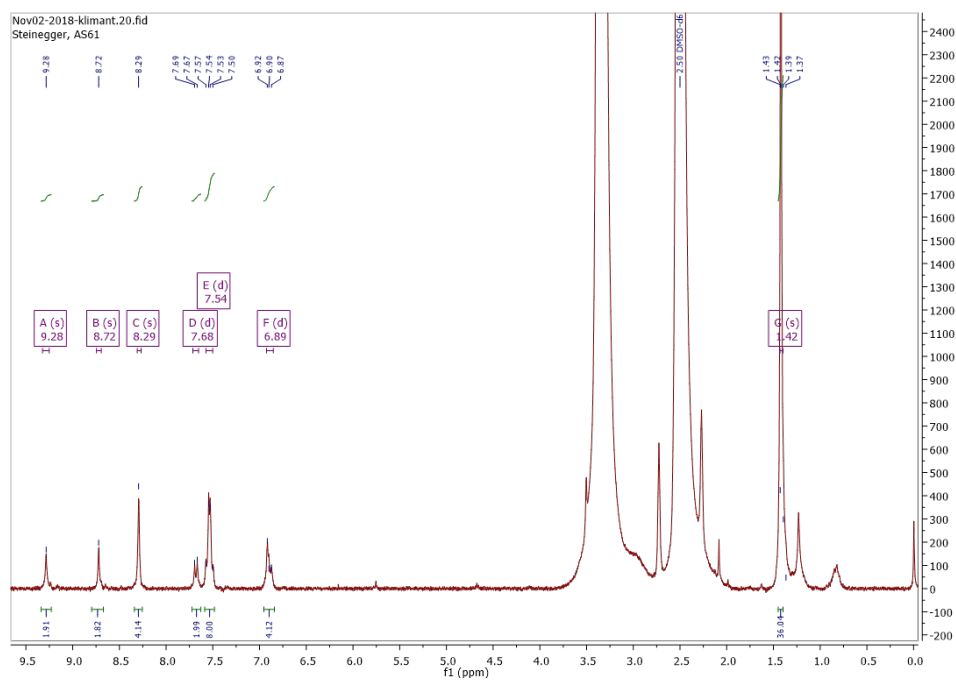
Figure S4.7: ^{1}H-NMR spectrum of **Zn-2** in DMSO-d$_6$.
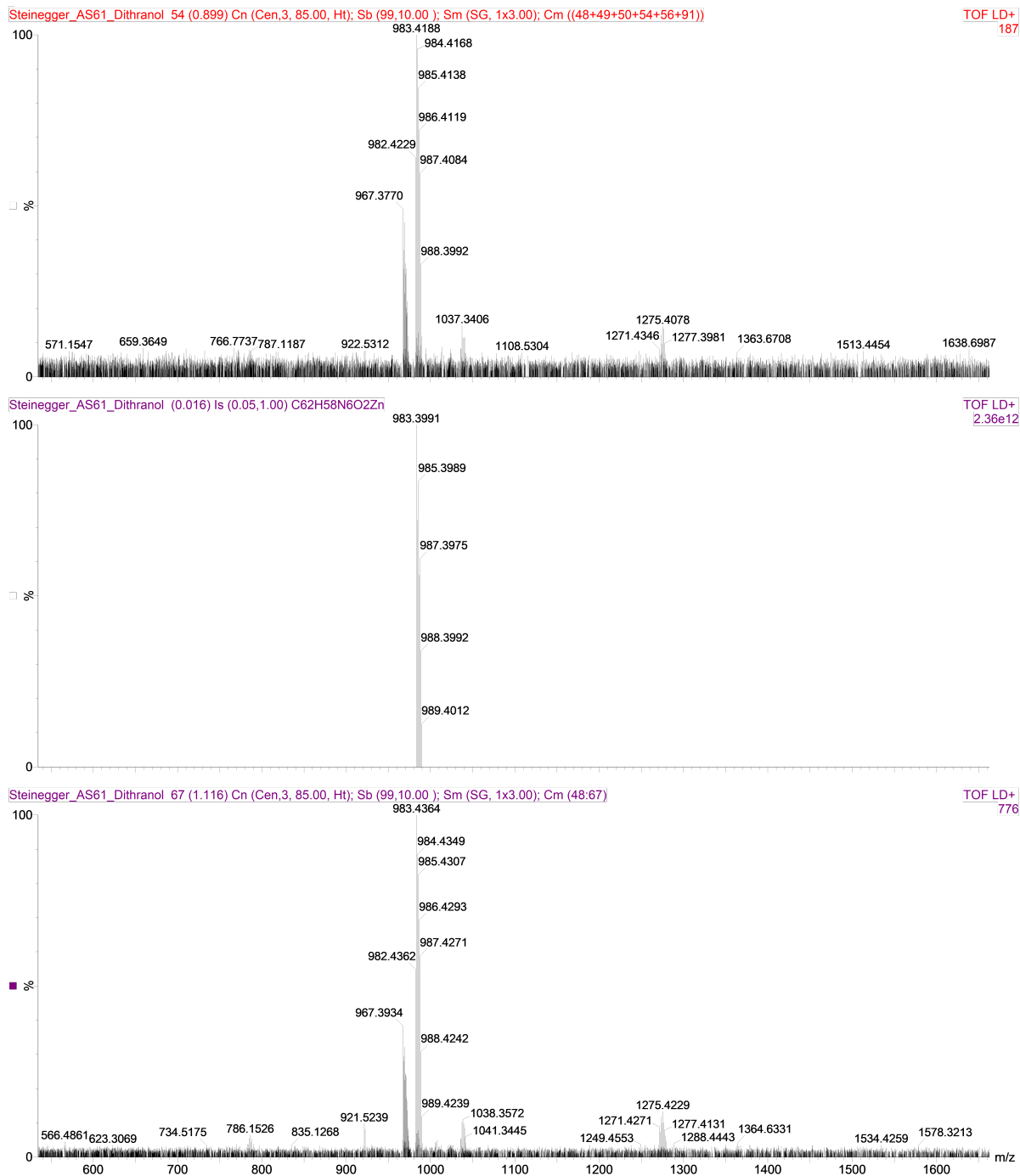
Figure S4.8: MS spectrum of **Zn-2**.

New Indicators for Optical Sensing by Manipulating the Intersystem Crossing in Luminescent Dyes
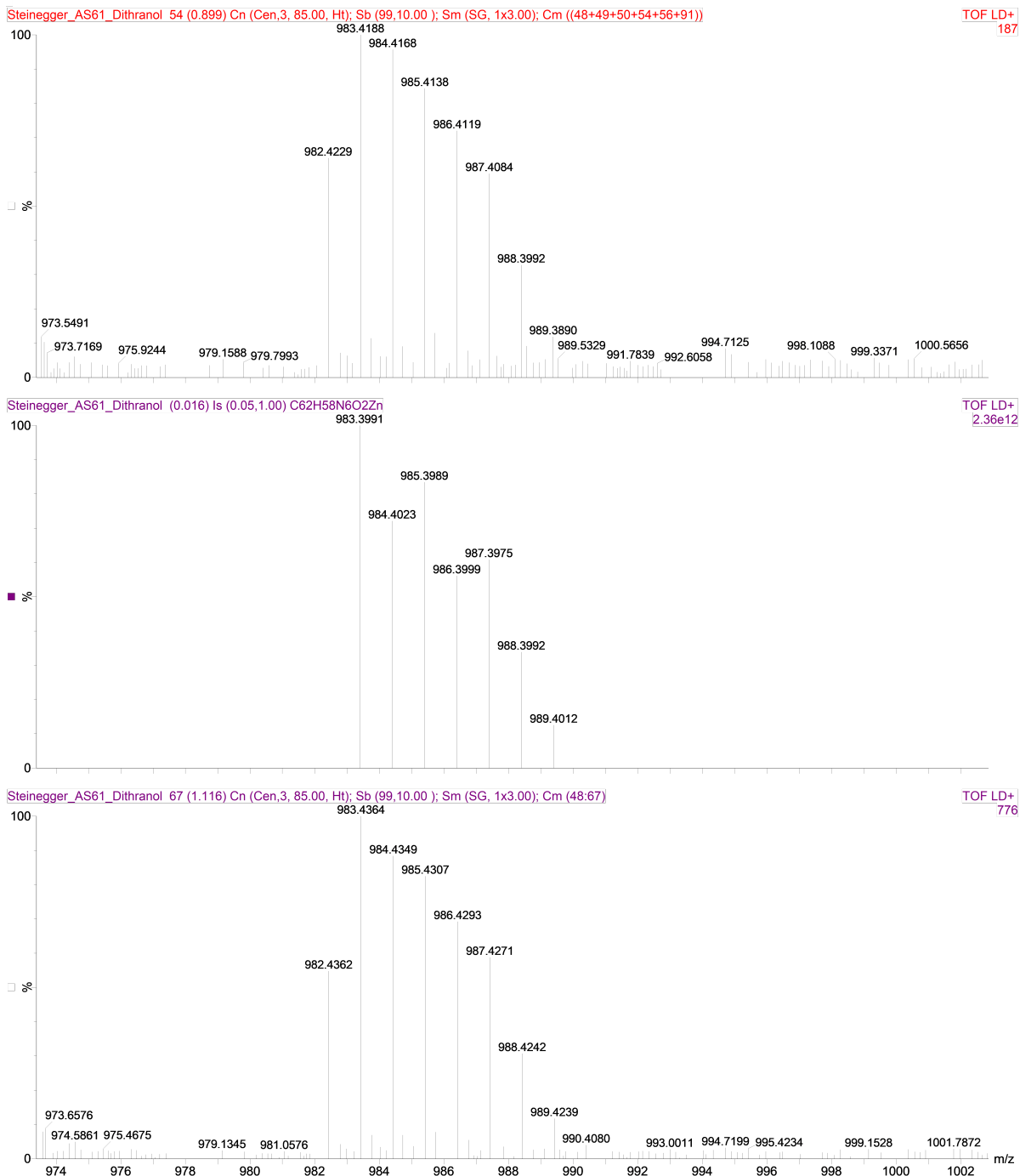
Figure S4.9: Isotope pattern from the MS spectrum of **Zn-2**.

5 TADF-Emitting Zn(II)-Benzoporphyrin: An Indicator for Simultaneous Sensing of Oxygen and Temperature
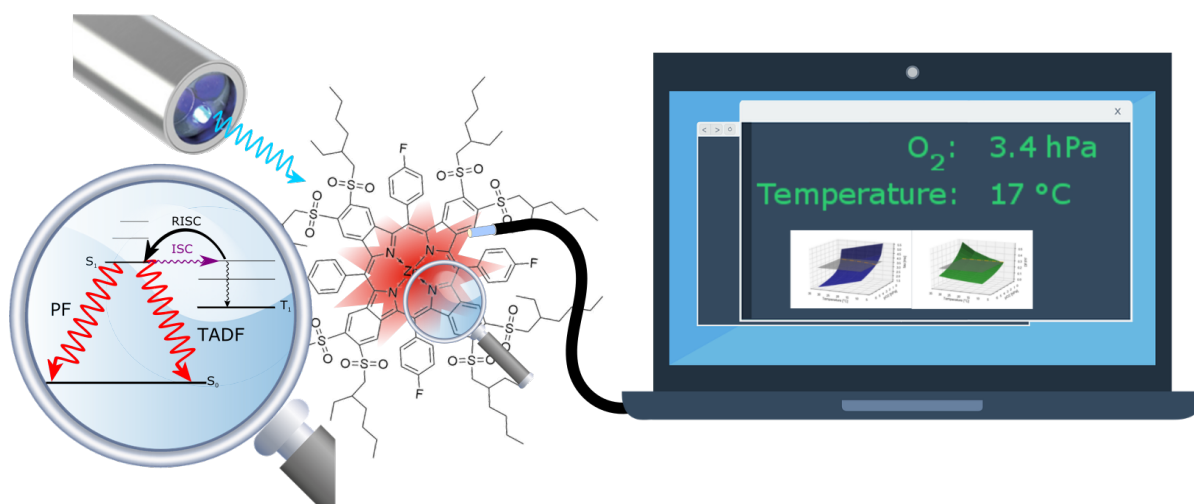
Preface to Chapter 5

This manuscript was published as *Full Paper* in *ACS Sensors* and presents a luminescent indicator that enables simultaneous measurement of oxygen and temperature at a single wavelength by using a multifrequency phase fluorometry method.

The temperature cross-talk of optical oxygen sensors can be corrected if temperature is measured simultaneously. This usually achieved by using a multiprobe approach. This, however, includes certain disadvantages such as drifts because of different leaching and photobleaching rates, and complex optical setups. The limitations can be overcome by finding a single indicator which can give spectrally or temporally distinct responses on temperature and on oxygen. Thermally activated delayed fluorescence emitters are usually sensitive both towards oxygen and temperature.

Previously, electron deficient Pt(II) and Pd(II)-benzoporphyrins simultaneously were reported to display delayed fluorescence and phosphorescence.[78] Favorably for optical sensing, they possess high molar absorption coefficients, NIR emission, and good stability (chemical, photostability). The luminescence of these complexes is responsive both to oxygen (change in decay time) and temperature (ratio of delayed fluorescence to phosphorescence) and enables determination of both parameters via two-wavelength read-out. We envisioned that by modification of those benzoporphyrins to display prompt and delayed fluorescence (spectrally identical) the same information could be collected via single-wavelength read-out. In order to change the type of the emission in the electron deficient Pt(II) and Pd(II)-benzoporphyrins, we used Zn(II) as a central atom instead of Pt(II) or Pd(II) due to a strongly reduced heavy atom effect. The Zn(II) benzoporphyrins, however, retains the samll- singlet-triplet energy gap and consequentially displays delayed fluorescence.

The combination of prompt and delayed fluorescence allows simultaneous determination of oxygen and temperature using a multifrequency phase fluorometry method. The prompt fluorescence acts as an intrinsic reference as it is neither significantly affected by oxygen nor temperature. Delayed fluorescence is differently affected by oxygen and temperature. Oxygen quenching decreases the decay time and intensity of delayed fluorescence. On the other hand, temperature decreases the decay time but increases the intensity.

Planar optodes made from poly(styrene-*co*-acrylonitrile) and the indicator dye, were presented to allow temperature-compensated trace oxygen sensing (0.002-6 hPa pO_2) at ambient conditions. Importantly, the setup only requires this single indicator and single-wavelength readout.

Manuscript

TADF-Emitting Zn(II)-Benzoporphyrin: An Indicator for Simultaneous Sensing of Oxygen and Temperature

Authors: Silvia E. Zieger,[§1,2] Andreas Steinegger,[§1] Ingo Klimant,[1] and Sergey M. Borisov*[1]

[§] S.E.Z. and A.S. contributed equally. [1]Graz University of Technology, Institute of Analytical Chemistry and Food Chemistry, Stremayrgasse 9, 8010 Graz, Austria

[2]Department of Biology, Aarhus University Centre for Water Technology (WATEC), 8000 Aarhus C, Denmark

E-mail: sergey.borisov@tugraz.at

Keywords: optical oxygen sensing, dual sensor, temperature compensation, molecular thermometer, fluorescence

Abstract: A new luminescent indicator is presented that enables simultaneous measurement of oxygen and temperature at a single wavelength. The indicator, an alkylsulfone-substituted Zn(II)-*meso*-tetraphenyltetrabenzoporphyrin, emits prompt and thermally activated delayed fluorescence (TADF). TADF is sensitive toward oxygen and temperature and is referenced against prompt fluorescence (PF) that is not affected by oxygen. The information on both parameters is accessed from the decay time of TADF and the temperature-dependent ratio of TADF and PF. Sensor foils, made from poly(styrene-*co*-acrylonitrile) and the indicator dye, enable temperature-compensated trace oxygen sensing (0.002-6 hPa pO$_2$) at ambient conditions. Compared to the previously reported dual sensors based on two emitters, the new sensor significantly simplifies the experimental setup and eliminates risks of different leaching or photobleaching rates by utilizing only one indicator dye and operating at a single wavelength.

5.1 Introduction

Optical oxygen sensors utilize luminescent indicators such as metalloporphyrins[138,234,237,239,240,243,247–250] or Ru(II)-polypyridyl complexes[241,251] and others[252,253] embedded in oxygen-permeable matrices.[6,61] Like any chemosensor, optical oxygen sensors are always affected by temperature.[6,61] This crosstalk, however, can be corrected if temperature is measured. This can be done with help of a conventional thermometer or using an optical temperature probe.[2–4,10,29,100,106,108,113,117,118,124,126,128,138,140,141,188–194,218,229,230,232–238,253–258] The latter rely on oxygen insensitive luminophores such as inorganic phosphors,[247,249,251] quantum dots,[237,259] or metal-organic indicators such as Eu(III)- β-diketonate complexes.[234,239–242] Temperature indicators with pronounced cross-talk to oxygen such as Ru(II)-polypyridyl

complexes[138,243,250] have to be incorporated in gas-impermeable matrices such as polyacrylonitrile.[253]

Dual sensors for oxygen and temperature[117,138,234,237,239–243,247–251,259,260] are particularly interesting because they allow compensation of the temperature effects at exactly the same place. This is essential in systems with strong temperature gradients. Moreover, this is the only format suitable for simultaneous imaging of both parameters, for example, for application as pressure-sensitive paints.[141,234,251,253] In all these systems, the signal from the temperature probe has to be separated from the oxygen signal either spectrally or temporally. Although systems based on two indicators with largely different decay times have been reported,[239,251] spectral separation is by far the most popular strategy.[237,240,242,243,248,250,253,259,260] Mostly combinations of metalloporphyrins or Ru(II)-polypyridyl complexes[241,251] with temperature probes, including inorganic phosphors,[247,249,251] quantum dots,[237,259] or metal-organic indicators such as Eu(III)-β- diketonate complexes[234,239–242] have been explored. The main disadvantages of the multiprobe approach include higher complexity in material chemistry, drifts because of different leaching and photobleaching rates, and complex optical setups. As one possibility, the complexity of such systems can be reduced by finding a single indicator, which can give spectrally or temporally distinct responses on temperature and on oxygen. Unfortunately, indicators with such properties are extremely rare.

In particular, indicators based on thermally activated delayed fluorescence (further referred to as DF), can be promising for the temperature-compensated determination of oxygen because DF is inherently sensitive toward temperature.[2,3,78,144] A plethora of DF emitters have emerged in research for the organic light-emitting diode industry.[13,14,212] Most of these dyes, however, have photophysical properties unsuitable for optical sensing. They usually have poor molar absorption coefficients resulting in reduced brightness and absorb in the UV to blue parts of the electromagnetic spectrum. We have previously shown that some electrondeficient Pt(II) and Pd(II)-benzoporphyrins simultaneously display fairly bright DF and phosphorescence.[78] The singlet- triplet energy gap decreased and the DF quantum yield increased with increasing electron withdrawing character of substituents in the β-position of the porphyrin. The emission of these complexes is dually responsive to oxygen (decay time change) and temperature (a ratio of DF to phosphorescence) and allows determination of both parameters via two-wavelength read-out. We thus envisioned that similar benzoporphyrins could be used to collect the same information via single-wavelength read-out providing that they simultaneously emit prompt fluorescence (PF) and DF because these two emission types are spectrally identical. By using a multifrequency phase fluorometry method, both temperature and oxygen can be determined from the DF with the PF serving as an intrinsic reference.

Herein, we present a dually sensitive material relying on a red-emitting Zn(II)-benzoporphyrin that features both PF and DF. The new material enables simultaneous sensing of oxygen and temperature with a simple optical setup (one emission channel) with frequency domain read-out at two different modulation frequencies.

5.2 Experimental Section

Details about materials, instrumentation, NMR, and MS spectra are provided in the Supporting Information.

5.2.1 Preparation of the Indicator Dye Zn-OS

The ligand *meso*-tetra(4-fluorophenyl)-tetra(4,5-bis(2-ethylhexylsulfonyl))-benzoporphyrin (H$_2$-OS) was prepared according to the literature.[78] Zn(II) *meso*-tetra(4-fluorophenyl)-tetra(4,5-bis(2-ethylhexylsulfonyl))- benzoporphyrin (Zn-OS): 30 mg (13 µmol, 1 eq) of the ligand H$_2$-OS was dissolved in a mixture of dichloromethane and methanol (10 mL, CH$_2$Cl$_2$/MeOH 4:1 v/v). In total, 573 mg of zinc acetate dihydrate (2.61 mmol, 200 equiv) and 21 mg of sodium acetate (261 µmol, 20 equiv) were added to the reaction mixture, and the solution was stirred for 5 min. Turnover was monitored via UV-vis spectroscopy. After quantitative conversion, the reaction mixture was washed with distilled water (4 × 20 mL). The organic layer was dried over Na$_2$SO$_4$, and the solvent was removed under reduced pressure resulting in dark green powder (24 mg, yield 80%).

UV-vis: $\lambda_{max}/\varepsilon$ (nm/M^{-1} cm^{-1}) in toluene: 490/386.000, 623/28.000, 664/ 79.000.

^{1}H NMR (300 MHz, CDCl$_3$) δ in ppm: 8.16 (s, 16H), 7.68 (m, 8H), 3.47 (m, 16H), 1.95 (m, 8H), 1.48-1.34 (m, 32H), 1.28-1.21 (m, 32H), 0.84 (m, 48H).

^{13}C NMR (76 MHz, CDCl$_3$) δ in ppm: 166.69, 163.34, 144.27, 140.52, 137.21, 136.28, 134.81, 130.29, 119.28, 117.59, 117.30, 60.35, 34.56, 32.72, 28.22, 26.03, 22.87, 14.15, 10.32.

HRMS (MALDI-TOF): calcd for C$_{124}$H$_{160}$F$_4$N$_4$O$_{16}$S$_8$Zn [M + H]$^+$, 2358.884; found, 2358.905.

5.2.2 Sensor Preparation

Poly(styrene-*co*-acrylonitrile) [PSAN, acrylonitrile 30 wt %, Aldrich, MW = 185.00 (GPC)] and dye Zn-OS (1 wt % with respect to PSAN) were dissolved in chloroform (7.5 wt % dye + PSAN in chloroform), and the solution was knife-coated (a 25 µm thick wet film) onto dust-free poly(ethylene terephthalate) (PET) support foils [125 µm biaxially oriented PET foils (MELINEX 506) supplied by Pütz GmbH Co. Folien KG (www.puetz-folien.com)]. After evaporation of the solvent, the sensor foils were dried at 60 °C for 24 h.

5.2.3 Measurements

Luminescence measurements were conducted in the gas phase at different temperatures (10-41 °C). A sensor spot, prepared by punching the planar foil, was incorporated into a glass capillary, which was then deployed into a cryostat from Avantor [model 1150S (us.vwr.com)]

for temperature control. Inlets and outlets of the capillary were connected to stainless steel gas pipes using a Tygon R-3603 tube, and the gas pipes were also placed into the cryostat. The inlet of the gas pipe was further connected to a gasmixing device based on two mass flow controllers (Voegtlin red-y smart series; www.voegtlin.com). A custom-made software was used to adjust the oxygen partial pressure for calibration by mixing nitrogen (99.999% purity) and a test gas (2.00 vol % in nitrogen), obtained from Linde (www.linde-gas.at). The gas flow was 200 mL/min. The overall luminescence phase shifts and overall luminescence amplitudes (from PF and DF, c.f. Supporting Information section Data Analysis) were measured with a lock-in amplifier (SR830 DSP, Stanford Research, www.thinksrs.com). The excitation of the sensor material was performed with a 490 nm light-emitting diode (LED) from Roithner (www.roithner-laser.com). The LED light was filtered through a combination of a BG 12 glass filter and a "Lagoon-blue" plastic filter obtained from bk Interferenzoptik (www.interferenzoptik.de) and LEE Filters (www.lee-filters.com), respectively. A bifurcated fiber bundle was used to guide the excitation light to the sensor spot and to transfer the emitted luminescence to the detector (photomultiplier H9306-02 from Hamamatsu, www.sales.hamamatsu.com). A combination of a RG 645 long-pass filter obtained from bk Interferenzoptik and a plastic filter "Primary Red" from LEE Filters was used in front of the photomultiplier. A solution of fluorescent Lumogen orange (Kremer Pigmente, www.kremer-pigmente.com) was used as a 0 phase standard. For calibration cycles, pO_2 was adjusted between 0 and 6 hPa at one temperature and at one modulation frequency (19 or 61 Hz). After the measurement at the second modulation frequency, the whole cycle was completed two more times. This was done for each temperature. Additionally, the luminescence decay times and intensities were measured for the sensor foil submerged in the anoxic aqueous solution of sodium sulphite (2% wt) containing catalytic amounts of $CoCl_2$. Discrepancy between the values obtained in the sodium sulfite solution and in the gas phase with nominal pO_2 of 0 hPa indicated contamination of the gas phase with traces of oxygen. It was corrected, as described in detail in the Supporting Information. The limit of detection (LOD) was estimated using the blank value method (blank value + 3 ×standard deviation).

5.2.4 Data Analysis

The evaluation of the luminescence phase shift was done based on the variation of the dual lifetime reference technique using the following equation:[261]

$$\tau = \frac{f_1^2 - f_2^2 \pm \sqrt{(f_2^2 - f_1^2)^2 - 4(f_1^2 f_2 cot(\Phi_2) - f_1 f_2^2 cot(\Phi_1))(f_2 cot(\Phi_2) - f_1 cot(\Phi_1))}}{4\pi(f_1^2 f_2 cot(\Phi_2) - f_1 f_2^2 cot(\Phi_1))} \tag{5.1}$$

where Φ_1 and Φ_2 are the overall luminescence phase shifts at the modulation frequencies $f_1 = 19$ Hz and $f_2 = 61$ Hz, respectively. The calculated luminescence lifetime τ has to be interpreted as an apparent lifetime, which deviates from the lifetime determined by other methods (time domain) as some assumptions seem to be violated when using phase-fluorometry.[25] However, the

system is still intrinsically referenced and can be recalibrated for each measurement adjustment with four calibration points.[262] The intensity ratio of PF and DF was calculated according to the following equation:

$$\frac{I_{PF}}{I_{DF}} = \frac{\omega\tau - tan(\Phi)}{(1 + (\omega\tau)^2)tan(\Phi)}, \omega = 2\pi f \quad (5.2)$$

where Φ is the overall luminescence phase shift at the corresponding modulation frequencies f_1 or f_2, and τ is the apparent lifetime of the indicator at given temperature and oxygen partial pressure, respectively. For further explanations and the derivation of eq 5.2, please refer to the Supporting Information. As the chosen modulation frequencies are low, the measurement of luminescence phase shifts can suffer from electromagnetic interferences. The estimation of the error propagation is crucial for appropriate data evaluation. Thus, an outlier test was applied to the measurement data before processing the fitting, and each time, the average value and the standard deviation were determined for both the apparent lifetime and the intensity ratio. The fitting of the apparent lifetime was performed in two dimensions. The Stern-Volmer two-site model[31,141,263] was used to fit the dual response of the lifetime because of oxygen quenching, whereas a linear regression was used for temperature dependency. The final fit model for the apparent lifetime can be summarized as

$$\frac{\tau}{\tau_0(T)} = \frac{f(T)}{1 + K_{SV,1}(T)pO_2} + \frac{1 - f(T)}{1 + K_{SV,2}(T)pO_2} \quad (5.3)$$

where τ and $\tau_0(T)$ are the apparent lifetimes in the presence and absence of oxygen, respectively, $f(T)$ and $(1 - f(T))$ represent the quenchable and the less-quenchable parts of the luminescence, respectively, and $K_{sv,1}(T)$ and $K_{sv,2}(T)$ are the Stern-Volmer constants for the quenchable and less-quenchable parts of luminescence, respectively. Each of the parameters is given at a certain temperature. In contrast to the fitting of the apparent lifetime, the fit model for the intensity ratio is based on empirical studies and was selected according to the minimal chi-square value χ^2. The best result with a chi-square χ^2 of 1.73×10^{-3} was obtained using a reciprocal quadratic function for the oxygen response combined with a linear regression for the temperature response. The overall fit function is shown below.

$$\frac{I_{DF}}{I_{PF}} = \frac{1}{a(T)pO_2^2 + b(T)pO_2 + c(T)} \quad (5.4)$$

where a, b, and c are numerical coefficients. Based on these fitting models, the sensor can be recalibrated using two calibration points for both parameters.
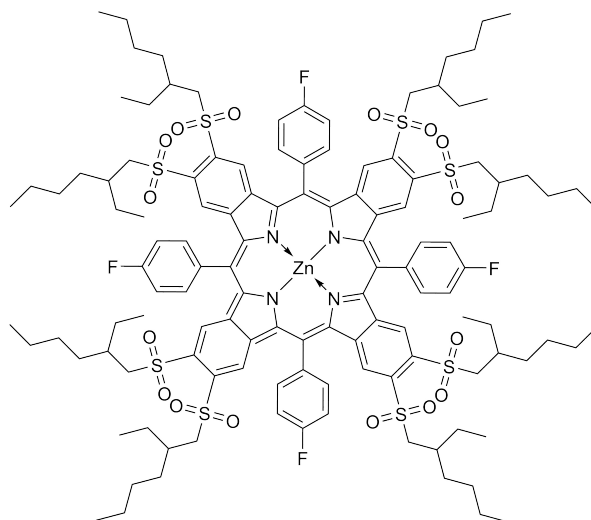
Figure 5.1: Chemical structure of Zn-OS.

5.3 Results and Discussion

5.3.1 Indicator Dye

Pt(II) and Pd(II)-tetrabenzoporphyrins are popular phosphorescent oxygen indicators. They display high molar absorption coefficients, NIR emission, and good stability. Alkylsulfone-substituted Pt(II) and Pd(II) *meso*-tetraphenyltetrabenzoporphyrins have comparably efficient DF in addition to the typical phosphorescence of Pt(II) and Pd(II) porphyrins.[78] DF is a strongly temperature-dependent process. In contrast to PF and phosphorescence that are quenched at higher temperatures because of the more efficient nonradiative deactivation, the intensity of DF initially increases with temperature. Consequently, this effect can be used for temperature measurement. For the simultaneous determination of temperature and oxygen, the indicator is required to have spectrally or temporally distinct responses on temperature and on oxygen. For the alkylsulfone-substituted Pt(II) and Pd(II) meso-tetraphenyltetrabenzoporphyrins, the temperature can be accessed via the ratio of DF and phosphorescence. Additionally, the oxygen concentration can be determined via the luminescent decay time of either phosphorescence or DF because the excited triplet state of the dye is efficiently quenched by molecular oxygen. For this system, temperature measurement requires two-wavelength read-out.

Compared to ratiometric measurement, single-wavelength read-out can further reduce the complexity of the measurement setup. In contrast to DF and phosphorescence, DF and PF emit at the same wavelength and hence would allow singlewavelength read-out. The Pt(II) and Pd(II) *meso*-tetraphenyltetrabenzoporphyrins are therefore unsuitable for this readout because a strong heavy atom effect results in the very efficient population of the triplet state, thus leading to the absence of PF. Therefore, in order to change the type of the emission in the alkylsulfone-substituted *meso*-tetraphenyltetrabenzoporphyrin complexes, we

used Zn(II) as a central atom instead of Pt(II) or Pd(II). The Zn(II)-alkylsulfonesubstituted *meso*-tetraphenyltetrabenzoporphyrin (Zn-OS, Figure 5.1), however, retains the small singlet-triplet energy gap that enables DF. The singlet-triplet energy gap estimated from temperature dependency of the DF decay time using an Arrhenius type model is 1646 cm^{-1} (Supporting Information, Figure S5.6 and eq S5.12).[218]

5.3.2 Photophysical Properties of the Indicator Dye
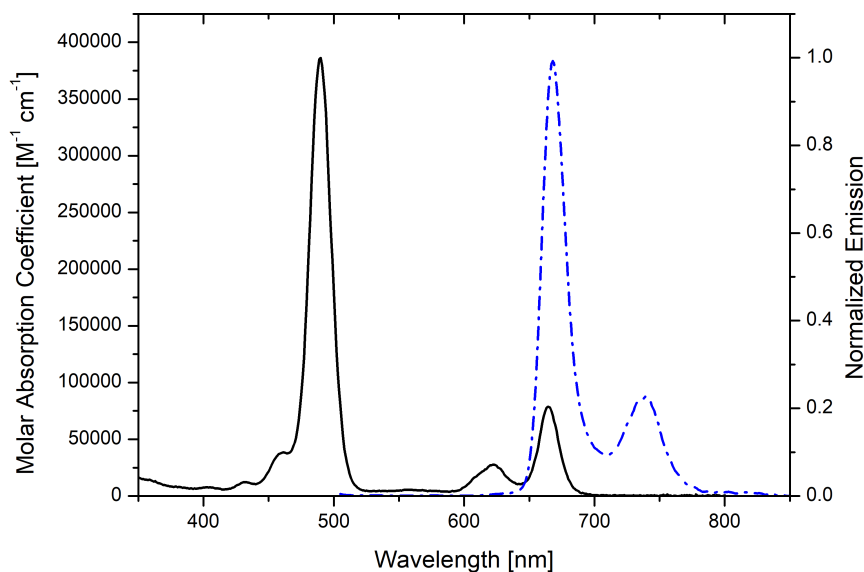
Figure 5.2: Absorption (solid black line) and emission (dashed blue line) spectra of Zn-OS in toluene at 25 °C.

The dye efficiently absorbs in the blue to green (porphyrin Soret band, 490 nm) and red part (Q bands, 623 and 664 nm) of the spectrum (Figure 5.2). The molar absorption coefficients are exceptionally high (Table 5.1), particularly for the Soret band. The emission is located in the red to far-red region (λ_{max} 667 nm). Although the Stokes shift (λ_{max} in the Q band-λ_{max}em) is very small (3 nm), excitation in the Soret band (λ_{max} 490 nm) allows excellent separation of the emission from the excitation ($\Delta\lambda = 177$ nm) which is highly valuable for sensing applications.

The emission can be attributed to the combination of PF and DF; no phosphorescence is observed for the Zn(II) porphyrin. For the dye in toluene solution, ensuring complete deoxygenation of solutions is very challenging; hence, it was not possible to reliably determine the overall quantum yield and DF lifetime. In fact, DF lifetime exceeds 1 ms, which results in extremely efficient quenching by molecular oxygen. On the other hand, for the dye immobilized in PSAN, anoxic conditions can easily be achieved by immersing the foil into the aqueous sodium sulphite solution.

At 25 °C, the overall quantum yield is moderate (3.3%) with roughly 30% contribution of DF and 70% of PF (Table 5.1). Yet, the brightness is acceptably high because of the high molar absorption coefficient. At room temperature, the DF decay time is around 8 ms making the indicator suitable for oxygen trace sensors.

Table 5.1: Photophysical Properties of Zn-OS Dissolved in Toluene and Immobilized in PSAN at 25 °C[b]

matrix	λ_{abs} max [nm]/ε [M^{-1} cm^{-1}]	λ_{em} max [nm]	τ_{DF} [ms]	ϕ [%]
toluene	490/386.000, 623/28.000, 664/79.000	667	≥ 1	n.d.
PSAN	495, 628, 671	675	7.87[a]	2.4 PF 0.9 DF[a]

[a] Under anoxic conditions (2 wt % aqueous sodium sulphite solution),

[b] n.d. - not determined.

5.3.3 Sensing Materials

The choice of the polymer is an essential part in preparation of sensing materials based on immobilized indicators. The long luminescent lifetime of Zn- OS requires polymers with moderate to low oxygen permeability even for trace oxygen sensors. Therefore, a copolymer of moderately oxygen-permeable polystyrene and virtually gas-impermeable poly(acrylonitrile) was selected. PSAN containing 30 wt % acrylonitrile was used. PSAN with 39 wt % acrylonitrile has an oxygen permeability coefficient (P) of 0.35 $\times 10_{-13}$ cm^3 (STP) cm cm^{-2} s^{-1} Pa^{-1},[215] which is significantly lower than for polystyrene [P = 2.0 $\times 10^{-13}$ cm^3 (STP) cm cm^{-2} s^{-1} Pa^{-1}].[215] Because the material based on combination of Zn-OS and PSAN is still highly sensitive to oxygen, its response was studied in the range from 0 to 6 hPa pO$_2$.

5.3.4 Response of Zn-OS/PSAN to Oxygen and Temperature

Oxygen and temperature affect the photophysical properties of Zn-OS but in a different way, making possible simultaneous sensing of the two parameters with a single indicator. Importantly, the intensity of PF (I$_{PF}$) is neither significantly affected by temperature nor by molecular oxygen and thus can be utilized as an intrinsic reference. Dynamic quenching by oxygen results in decrease of the DF decay time (increase of τ_0/τ) and the intensity I$_{DF}$ (Figure 5.3B,D). As expected from the long decay time of the DF, the quenching is very efficient. The LOD at 26 °C was estimated to be 0.002 hPa.

In agreement with the behavior of most optical oxygen sensors, dynamic quenching becomes more efficient as the temperature is increased (Figure S5.7). On the other hand, whereas the DF lifetime decreases with temperature as well (Figure 5.3A), DF is enhanced with increasing temperature (Figure 5.3C) because more molecules have the necessary energy for the reverse
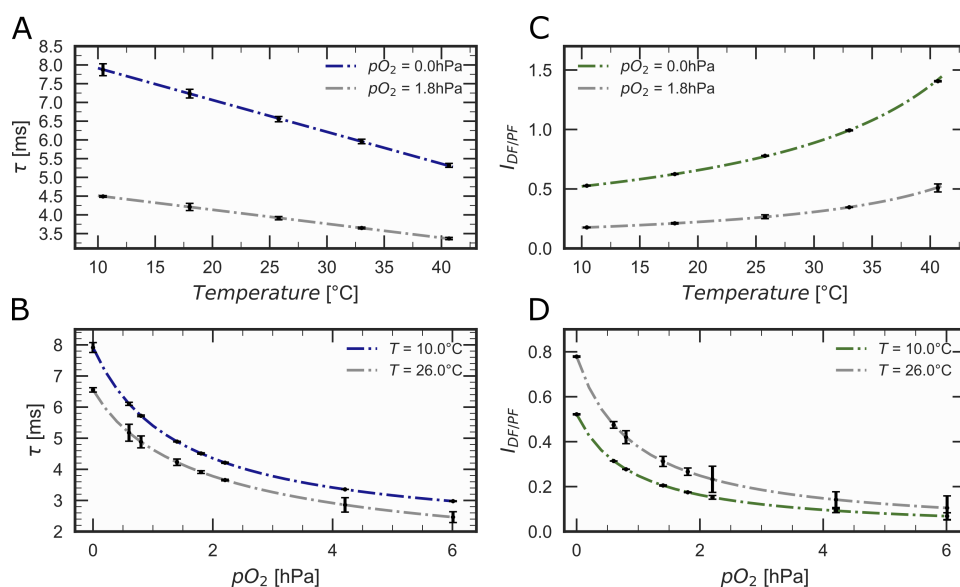
Figure 5.3: Response of the apparent luminescence decay time τ (A,B) and the intensity ratio ($I_{DF/PF}$) (C,D) for the dual sensor to temperature (A,C) and oxygen (B,D). The response is exemplified for two different temperatures and oxygen partial pressures. The fit (indicated by dash-dot lines) is performed according to eqs 5.3 and 5.4.

intersystem crossing. The temperature and oxygen effects on luminescent properties of the Zn-OS are summarized in Table 5.2.

The influence of temperature and oxygen on the luminescence decay curves is shown in Figures S5.8 and S5.8. In these graphs, the intensity at the plateau is the sum of PF and DF. The first point of the decay represents the intensity of the DF. The ratio $I_{DF/PF}$ changes the relative positions of the plateau and the first point of the decay curve. Changes in decay time are manifested in different slopes of the decay curves.

Table 5.2: Summary of the Effects of Oxygen and Temperature on Luminescence Properties of Zn-OS

Parameter	Oxygen ↑	Temperature ↑
I_{PF}	No effect	No pronounced effect
I_{DF}	↓	↑
τ_{DF}	↓	↓

5.3.5 Dual Sensing of Oxygen and Temperature

For the isolation of both parameters (τ and $I_{DF/PF}$) from singlewavelength read-out, a multifrequency phase fluorometry method was used (Data Analysis section). The experimental data form calibration planes (Figure 5.4A,B) that can be fitted according to eqs 5.3 and 5.4 for both the apparent lifetime (τ or τ_0/τ) and the intensity ratio ($I_{DF/PF}$). In each case, the fitting reveals a continuous and monotonous calibration plane, which is the basic prerequisite for
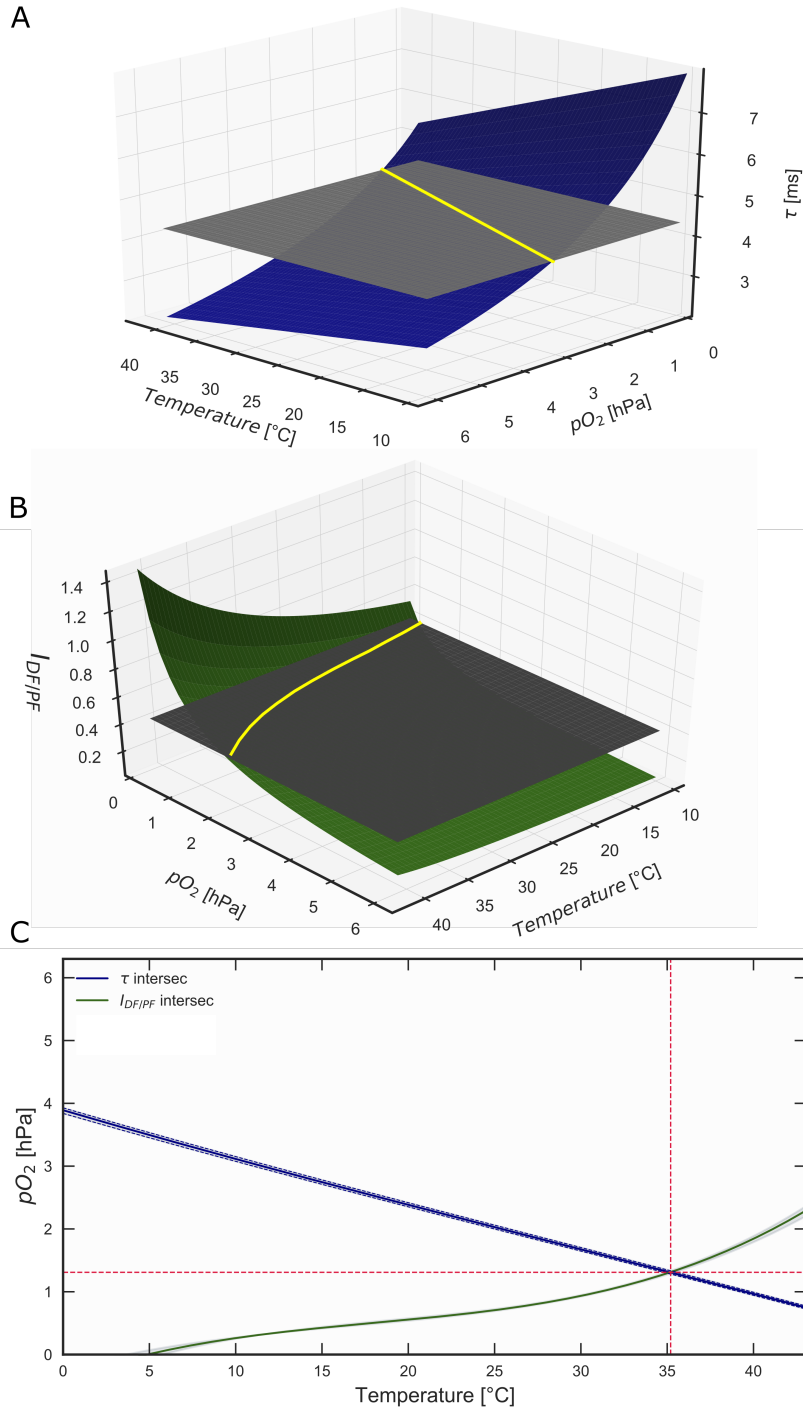
Figure 5.4: Luminescence response of the Zn-OS/PSAN material to temperature and oxygen and illustration of the data analysis using analytical geometry. (A,B) Calibration planes (colored surfaces representing the mean values at each point) for the apparent luminescence decay time and the intensity ratio (delayed I_{DF} vs prompt I_{PF} luminescence). Horizontal gray planes exemplify the τ and $I_{DF/PF}$ obtained at given conditions. Curves resulting from the intersection of the calibration planes and horizontal gray planes are shown in yellow color. (C) Intersection curves (A,B) with the intercept point indicating the unique pair of temperature and pO$_2$ values.

definite analysis of the sample data. The analysis of the sample data is then conducted in the Euclidean space using analytical geometry. Upon determination of the current parameters (τ or τ_0/τ and $I_{DF/PF}$) according to eqs 5.1 and 5.2, a horizontal sample plane is generated for each parameter (gray planes, as shown in Figure 5.4A,B). The horizontal plane is then crossed with the calibration plane for the given parameter to determine the intersection curves (yellow lines, as shown in Figure 5.4A,B). The intersection curves consist of pairs of temperature and oxygen that result in the given parameter (Figure 5.4C). Subsequently, the intercept of the intersection curves reveals the actual temperature and the oxygen partial pressure of the sample, which are clearly defined because of a continuous and monotonous calibration plane (Figure 5.4C).

5.4 Conclusion

We have presented an alkylsulfone-substituted Zn(II)-*meso*-tetraphenyltetrabenzoporphyrin that simultaneously exhibits PF and DF. Although the luminescence quantum yields are moderate, the overall brightness is good because of very high molar absorption coefficients. Additionally, the excitation and the emission are well separated, as the excitation is performed in the Soret band of the indicator. This allows the utilization of the full emission peak/brightness of the indicator. The combination of PF and DF enables simultaneous determination of oxygen and temperature using a multifrequency phase fluorometry method. Importantly, this is done using a single indicator and a single-wavelength readout. This simplifies the experimental setup and does not bear risks of different leaching or photobleaching rates that may compromise the performance of the mutiparameter sensors based on combination of two indicators.

5.5 Acknowledgments

5.6 Supporting Information

5.6.1 Experimental Section

Materials: Chemicals were purchased from various commercial suppliers (Fluka, Sigma Aldrich, Acros Organics, Roth, ABCR), solvents were purchased from VWR. Polystyrene (PSAN), av. MW $\approx$185.000 Da, was purchased from Acros Organics.

Instrumentation: NMR spectra were recorded on a Bruker AVANCE III spectrometer equipped with an autosampler (300.36 MHz ^{1}H-NMR, 75.53 MHz ^{13}C-NMR).

MS: Mass spectrometry was performed in a positive reflector on a Micromass TofSpec 2E time-of-flight (TOF) mass spectrometer or on a Matrix-Assisted Laser Desorption/ Ionization (MALDI)-TOF/TOF spectrometer (Bruker UltrafleXtreme).

Photophysical Properties: UV–vis spectra were recorded on a VARIAN CARY 50 conc using Hellma Analytics (www.hellma-analytics.com) optical glass 10 mm precision cuvettes. Luminescence spectra were recorded on FluoroLog 3 spectrofluorometer from Horiba Scientific equipped with a R2658 photomultiplier from Hamamatsu (www.hamamatsu.com). Luminescence decays were obtained via time correlated single photon counting on a FluoroLog 3 spectrofluorometer equipped with a DeltaHub module controlling a SpectraLED-460 (456 nm) and using DAS-6 Analysis software for data analysis. Data were fitted using a biexponential decay model. Average lifetimes τ were calculated from the relative amplitudes (B1, B2) and lifetimes (T1, T2) of the individual components from the biexponential model using the equation tau=(B1*T1+B2*T2). A "Quanta-φ" integrating sphere-based set-up on a FluoroLog 3 spectrofluorometer (Horiba Scientific) was used to determine absolute quantum yields.

NMR and MS spectra of the indicator dye Zn-OS
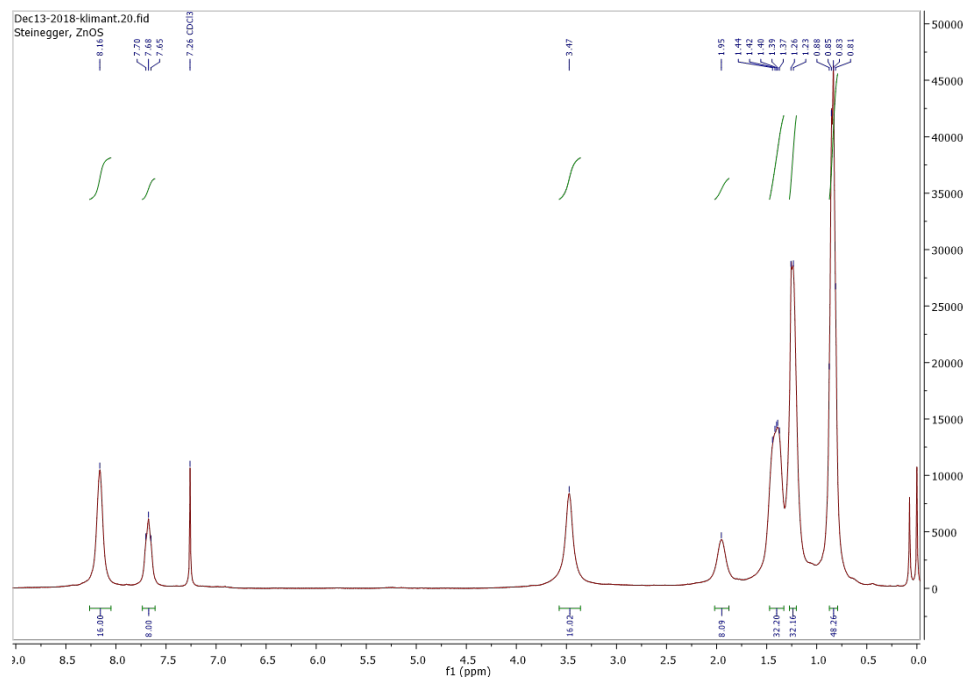
Figure S5.1: ^{1}H-NMR spectrum of Zn-OS in CDCl$_3$.
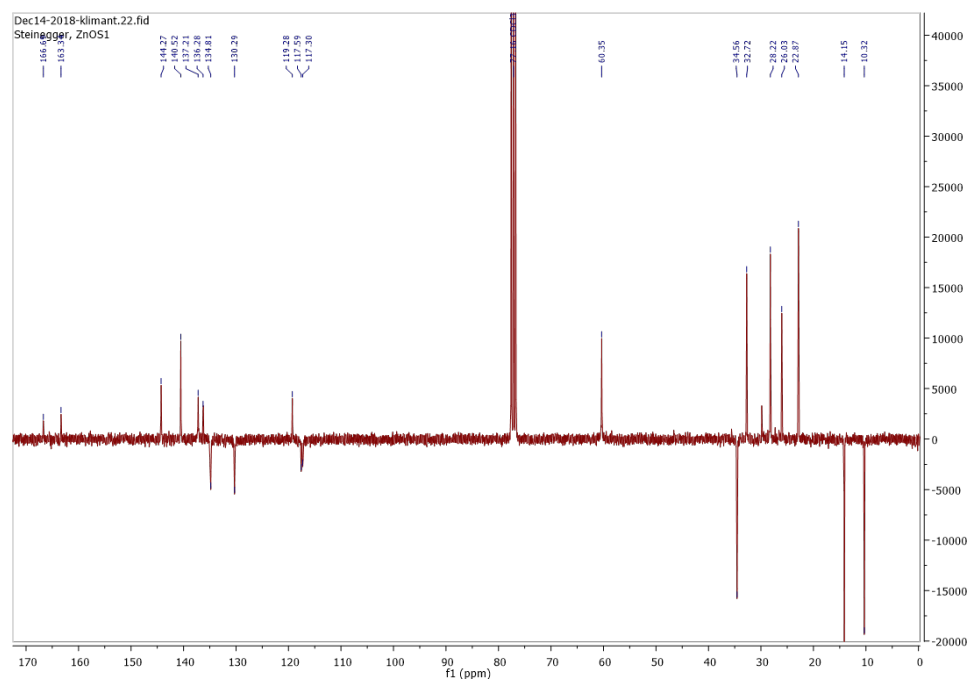
Figure S5.2: APT-NMR spectrum of Zn-OS in CDCl$_3$.

New Indicators for Optical Sensing by Manipulating the Intersystem Crossing in Luminescent Dyes
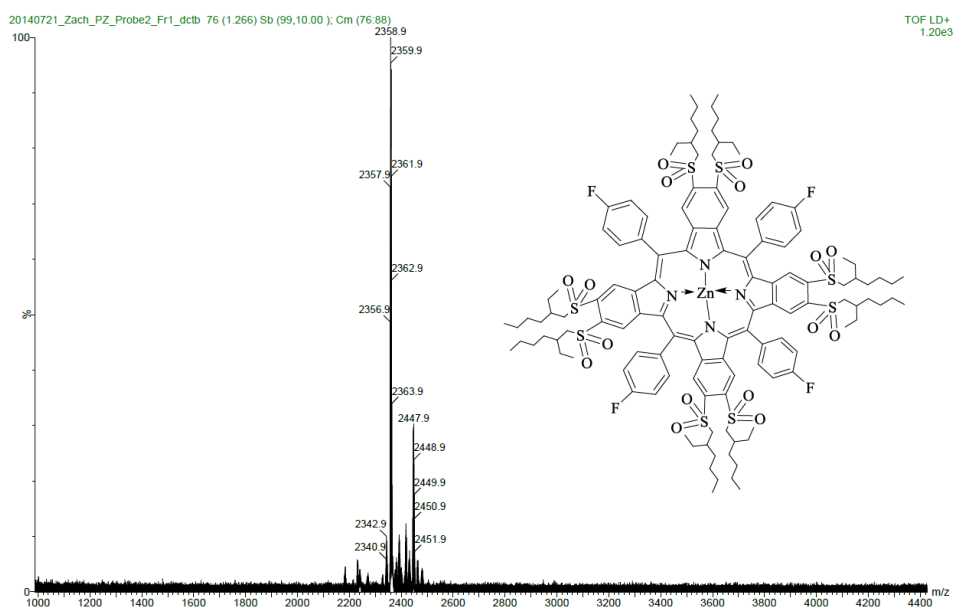
Figure S5.3: MS spectrum of Zn-OS
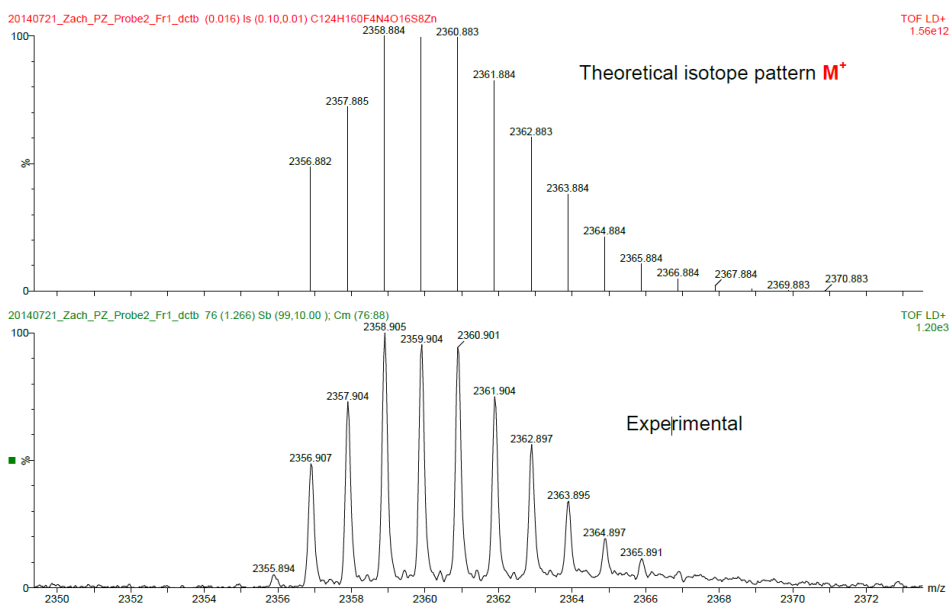
Figure S5.4: Isotope pattern from the MS spectrum of Zn-OS.

5.6.2 Data Analysis

Mathematical derivation of the modified dual lifetime referencing (m-DLR) method

In the frequency domain spectroscopy, a dual optical sensor is described as a superposition of two single sine wave functions. As a result, the phase angle and the amplitude obtained at a single modulation frequency are determined by the decay time and the ratio of the intensity of both luminophores.[24] In order to determine all four parameters of the dual optical sensor and to identify the single unique solution, a set of four linear and independent equations has to be set up or some assumptions must be made to simplify the mathematical system.

The overall phase angle and the overall amplitude obtained at a single modulation frequency can be described by the general interference equation for two wave functions (cf. S5.1 and S5.2).

$$A = \sqrt{a_{PF}^2 + a_{DF}^2 + 2a_{PF}^2 a_{DF}^2 cos(\varphi_{PF} - \varphi_{DF})} \qquad (S5.1)$$

$$tan(\Phi) = \frac{a_{PF}sin(\varphi_{PF}) + a_{DF}sin(\varphi_{DF})}{a_{PF}cos(\varphi_{PF}) + a_{DF}cos(\varphi_{DF})} \qquad (S5.2)$$

where a_{PF}, a_{DF} are the amplitudes of the prompt and delayed fluorescent indicator; $\varphi_{PF}, \varphi_{DF}$ are the corresponding phase shifts. A is the superimposed amplitude and Φ is the corresponding superimposed phase shift at a certain modulation frequency.

At low modulation frequencies, meaning in the kHz range, the dye with prompt fluorescent causes no phase shift ($\varphi_{PF} \approx 0$),[24] which simplifies the previous equations (S5.1 and S5.2) as follows:

$$A = \sqrt{a_{PF}^2 + a_{DF}^2 + 2a_{PF}^2 a_{DF}^2 cos(\varphi_{DF})} \qquad (S5.3)$$

$$tan(\Phi) = \frac{a_{DF}sin(\varphi_{DF})}{a_{PF} + a_{DF}cos(\varphi_{DF})} \qquad (S5.4)$$

In order to simplify the linear equation system further, the amplitude is converted into the intensity using the demodulation factor. This transformation is crucial, since the intensity is independent of the modulation frequency in the kHz range. A general description is shown in equation S5.5.

$$I = \frac{a}{dm} = const. \qquad (S5.5)$$

where a is the amplitude and "dm" is the demodulation factor of the luminophore at a certain modulation frequency. Since the individual intensity of the luminophore is independent of the modulation frequency, also the ratio of both intensities is constant (see S5.6). Equation S5.6 can hereby further simplified, as in the kHz range, the amplitude demodulation of the fast

New Indicators for Optical Sensing by Manipulating the Intersystem Crossing in Luminescent Dyes

fluorophore is very close to unity.

$$\frac{I_{PF}}{I_{DF}} = \frac{a_{PF}dm_{DF}}{a_{DF}dm_{PF}} \approx \frac{a_{PF}}{a_{DF}}dm_{DF}, \quad dm_{DF} = \frac{1}{\sqrt{1+(2\pi f\tau)^2}} \quad \text{(S5.6)}$$

The demodulation of the delayed fluorophore is thereby determined by the modulation frequency and the luminescence decay time of the fluorophore.

To simplify the linear equation system further, equation S4 is solved for the amplitude of the fast luminophore and inserted into equation S5.6.

$$\frac{I_{PF}}{I_{DF}} = \frac{a_{PF}}{a_{DF}}dm_{DF} = [\frac{sin(\varphi_{DF})}{tan(\Phi)} - cos(\varphi_{DF})]dm_{DF} = [\frac{sin(\varphi_{DF})}{tan(\Phi)} - cos(\varphi_{DF})]\frac{1}{\sqrt{1+(2\pi f\tau)^2}}$$
$$\text{(S5.7)}$$

Both trigonomic functions can be converted using trigonomic identities as they are described in equation S5.8 and S5.9.

$$cos(\varphi_{DF}) = cos(arctan(2\pi f\tau)) = \frac{1}{\sqrt{1+(2\pi f\tau)^2}} \quad \text{(S5.8)}$$

$$sin(\varphi_{DF}) = sin(arctan(2\pi f\tau)) = \frac{2\pi f\tau)}{\sqrt{1+(2\pi f\tau)^2}} \quad \text{(S5.9)}$$

After applying the trigonometric identities to equation S5.7, the reduced expression for the intensity ratio is obtained (see equation S5.10):

$$\frac{I_{PF}}{I_{DF}} = [\frac{2\pi f\tau}{tan(\Phi)\sqrt{1+(2\pi f\tau)^2}} - \frac{1}{\sqrt{1+(2\pi f\tau)^2}}]\frac{1}{\sqrt{1+(2\pi f\tau)^2}} = \frac{\omega\tau-tan(\Phi)}{(1+(\omega\tau)^2)+tan(\Phi)}, \quad \omega = 2\pi f$$
$$\text{(S5.10)}$$

The intensity ratio of the fast fluorophore and the delayed fluorophore is constant for different modulation frequencies and only dependent of the overall phase shift Φ and the decay time τ of the delayed fluorophore. The decay time of the fluorophore with delayed fluorescence is determined by the dual lifetime reference (DLR) technique published by Klimant et al.[24] as it is described in the main part (see equation 5.1). The linear equation set is therefore unique and the solution of the dual optical system can be identified.

Correction of the oxygen partial pressures in the gas phase

To check the τ_0 (τ at 0 hPa O_2) values for correctness, Zn-OS in PSAN sensor spot were placed at the bottom of 3 mL Supelco vials filled with 2wt% Na_2SO_3 aq. solution with cat. $CoCl_2$. After 1 day, overall luminescence phase shifts and overall luminescence amplitudes at both modulation frequencies were measured with a lock-in amplifier as described for the gas phase calibrations. Measurements were conducted at different temperatures (10 – 41 °C).

When comparing the measurement data for 0 hPa O_2 in the gas phase to deoxygenated aqueous sodium sulfite solution, it became apparent that the 0 hPa O_2 concentration during

gas phase calibration were not completely oxygen-free. To correct the oxygen concentrations, the values measured in sodium sulphite solution were added to the calibration data and the oxygen concentration are adjusted. This is done according to following procedure. The oxygen partial pressure in the Stern-Volmer equation (5.3) is substituted by:

$$pO_2 = x * 18.942 hPa + (1 - x) * c + c \tag{S5.11}$$

where x is the fraction of the test gas (2.00 vol% in nitrogen) in nitrogen (used by the gas mixing device for adjusting the oxygen partial pressure), 18.942 hPa is the oxygen partial pressure in the test gas adjusted for the altitude, c is the error in oxygen concentration. The oxygen error can be constant if it appears after the gas-mixing device or can be variable if it depends on the fraction of nitrogen (if the nitrogen gas is the source of oxygen error). It was assumed that the oxygen error originates to 50% from both sources. From the measurement in sodium sulfite solution, the new τ_0 values are used to calculate τ_0/τ values. Then, the dependency at 25 °C is fitted according to the Stern-Volmer equation (Figure S5.5) and gives c of 0.195 hPa. Finally, the corrected oxygen partial pressures are calculated according to eq. S5.11.
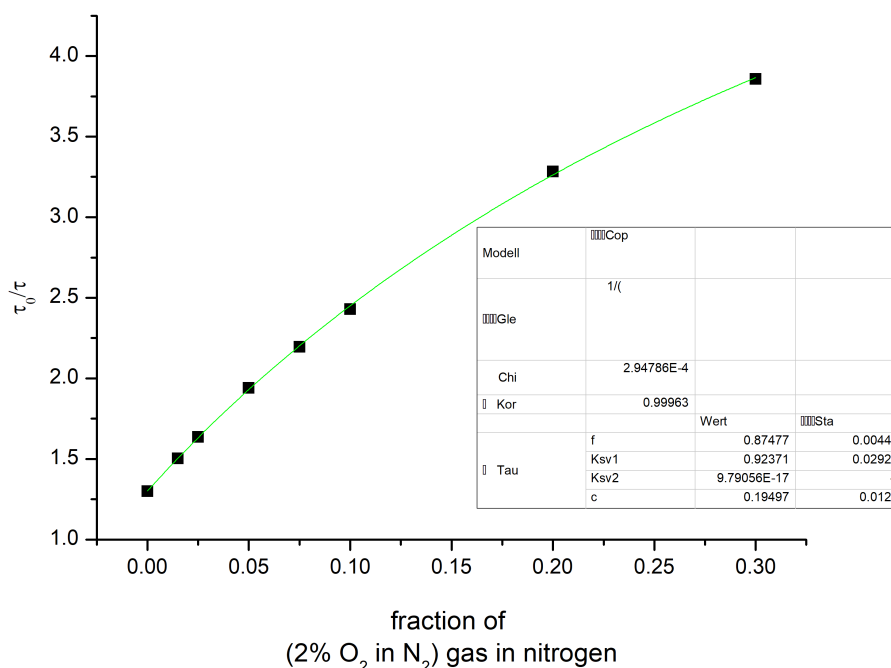
Figure S5.5: The Stern-Volmer fit used to correct the pO$_2$ values for oxygen impurity in the calibration gas and the measurement set-up (T=25°C).

Estimation of the singlet-triplet energy gap

For temperature calibrations, temperature was adjusted with a Cary SPV - 1X0 Single Cell Peltier Accessory Peltier element from Varian in combination with a cryostat from Avantor,

Model 1150S (us.vwr.com). The PSAN sensor foil was placed diagonally in Hellma Analytics optical glass 10 mm precision cuvettes. The cuvettes were filled with aqueous 2wt% Na_2SO_3 solution. After temperature adjustment, the cuvettes were thermally equilibrated for 10 min. Temperature was adjusted between 5 and 45 °C. The TADF lifetime was measured at each temperature with the same setup as for the photophysical characterization. The calibration cycle was repeated three times.

Experimental data (Figure S5.6) was fitted with an Arrhenius type model:[218]

$$\tau = (k_0 + k_1 e^{\frac{-\Delta E}{k_B T}})^{-1} \tag{S5.12}$$

where k_0 is the temperature-independent decay rate for the excited-state deactivation, k_1 is a pre-exponential factor, k_B the ΔE the energy necessary for the reverse Intersystem Crossing (ISC), and T the absolute temperature. ΔE corresponds to the singlet-triplet energy gap. From the fit, ΔE was estimated to be 3.27×10^{-20} J or 1646 cm^{-1}.
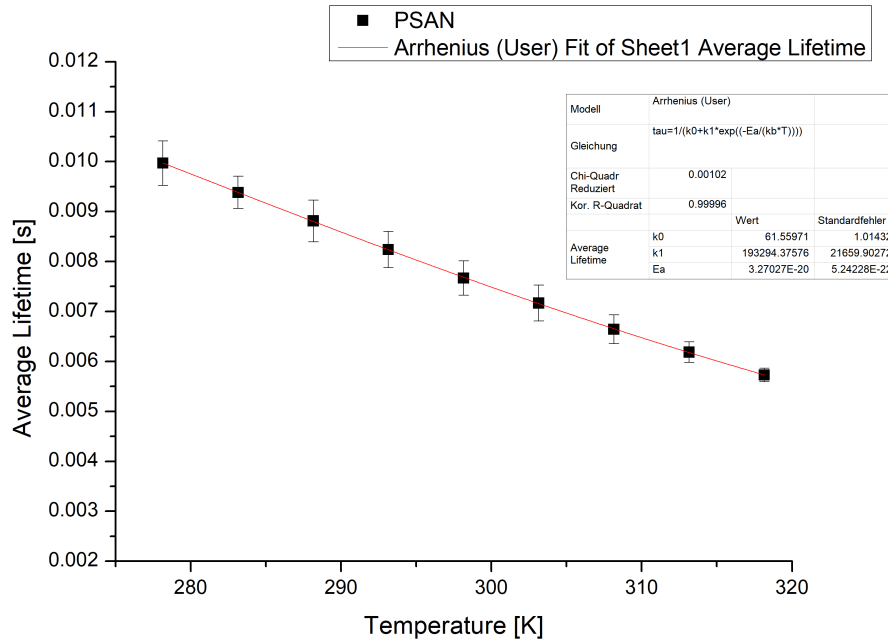
Figure S5.6: Temperature dependence of the average luminescence decay times of ZnOS immobilized in PSAN.

5.6.3 Results and Discussion
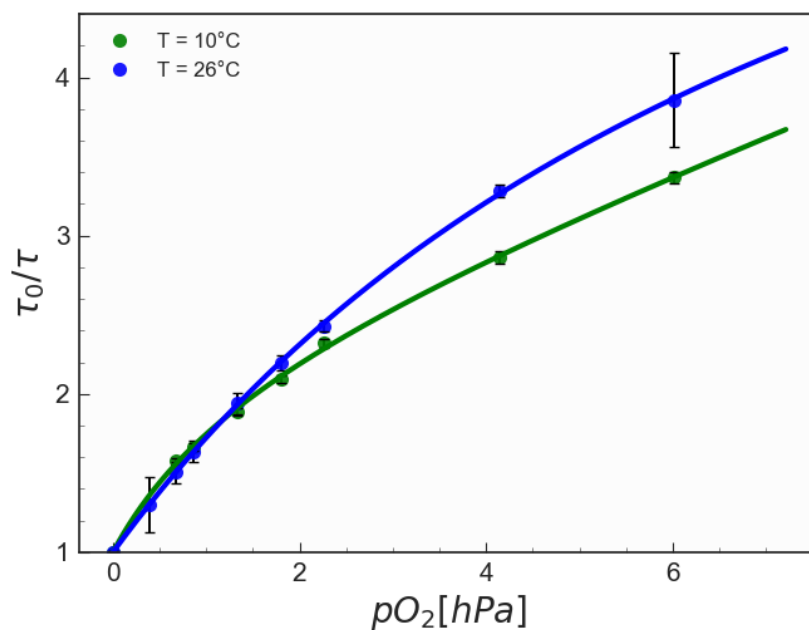
Figure S5.7: Response of the dual sensor (Zn-OS in PSAN) to oxygen exemplified for two temperatures.
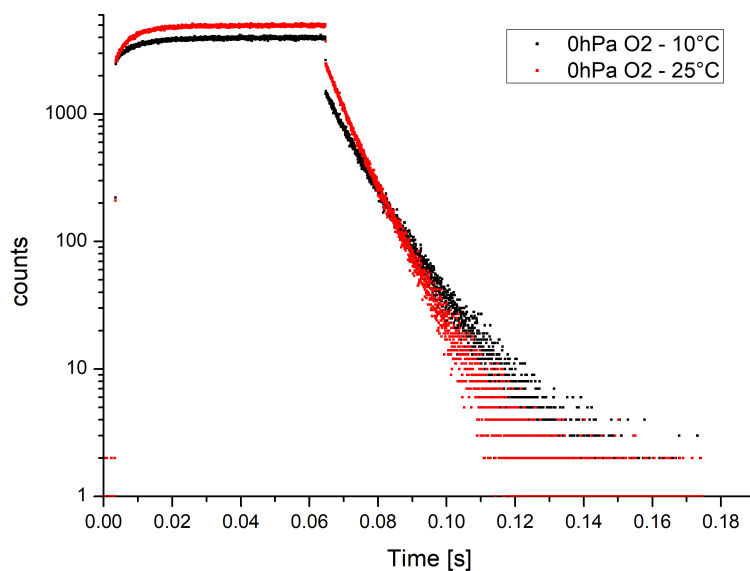
Figure S5.8: Influence of temperature at a constant oxygen concentration on the decay curve of the sensor foil (1 wt% Zn-OS incorporated in PVC).

New Indicators for Optical Sensing by Manipulating the Intersystem Crossing in Luminescent Dyes
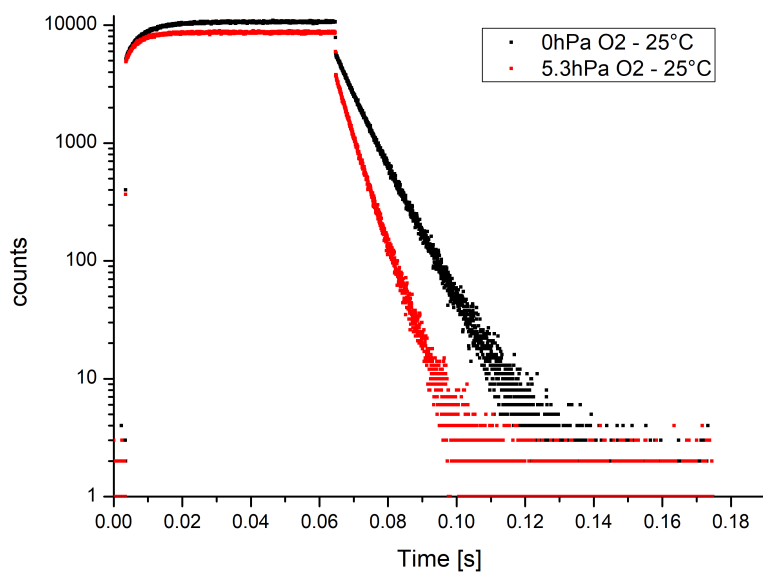
Figure S5.9: Influence of oxygen concentration at a constant temperature on the decay curve of the sensor foil (1 wt% Zn-OS incorporated in PVC).

6 Marrying metalloporphyrins with cyclometalated complexes – a luminous pair?

φ: 5.1%
τ: 698 μs
φ $^1O_2$: 70%

φ: 0.4%
τ: 15 μs
φ $^1O_2$: 85%

Cyclometalation

Wavelength
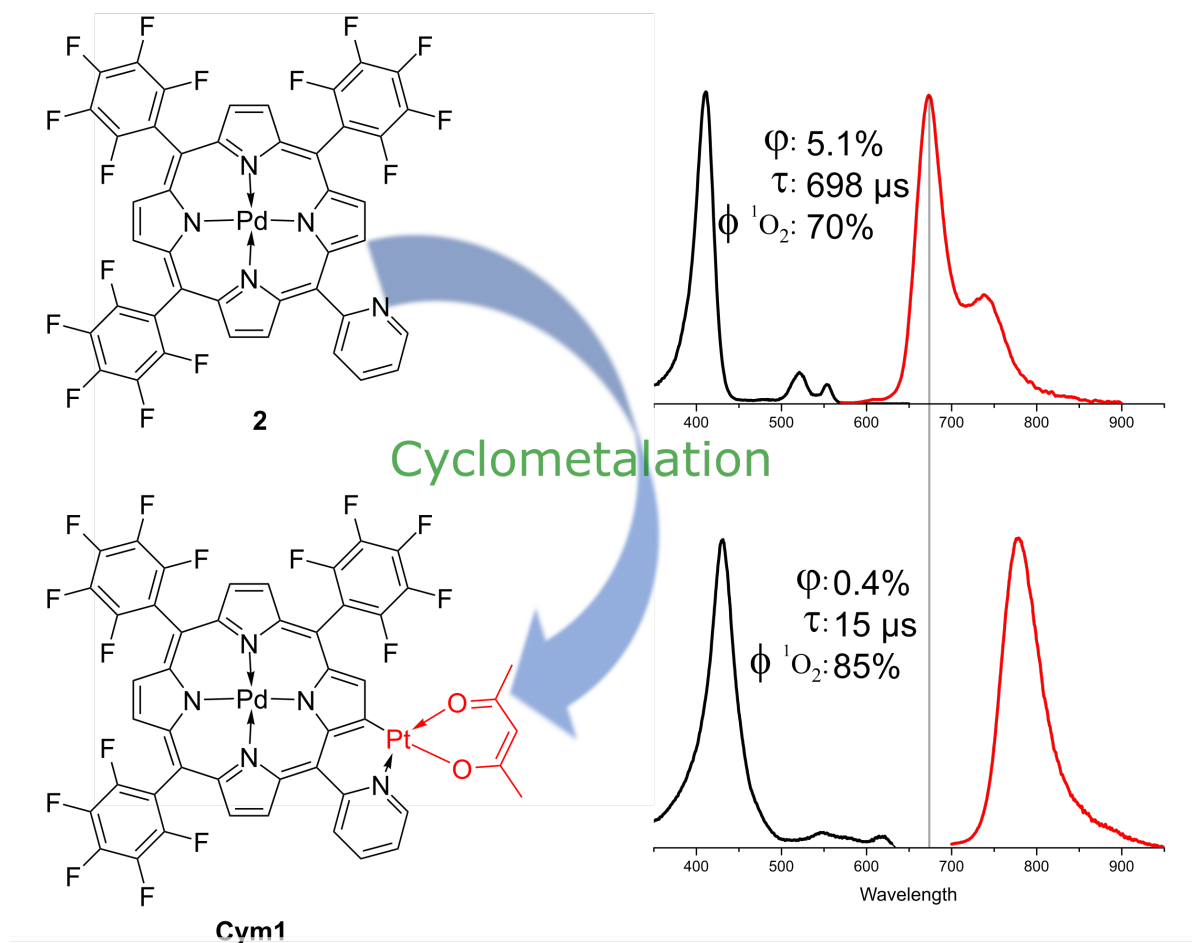
Preface to Chapter 6

This manuscript was submitted as *Full Paper* to *Journal of Photochemistry & Photobiology, A: Chemistry* and currently is in revision. The paper presents the synthesis and characterization of cyclometalated Pd(II) (benzo-)porphyrins.

The performance of metalloporphyrins as triplet photosensitizers and oxygen indicators is to a large extent determined by their photophysical properties. Therefore, it is of significant interest to investigate methods to manipulate the luminescence properties of indicator dyes.

Cyclometalation is known to give efficiently phosphorescent Pt(II) and Ir(III) complexes. The heavy atoms induce strong spin-orbit coupling that promotes intersystem crossing and further raise the energy of luminescence-deactivating d-d states. More efficient intersystem crossing can reduce emissive lifetimes and enhance phosphorescence quantum yields.

Motifs for cyclometalation with Pt(II) were integrated into three Pd(II) porphyrin complexes and the effects on their photophysical properties were investigated. The cyclometalation only minorly affects the photophysical properties if the cyclometalated motif is not in plane with the porphyrin macrocycle but can introduce strong bathochromic shift if the structure is rigidized after the cyclometalation.

The integration of 2-phenylpyridyl in the *meso*-position only affects the luminescence decay time (about 2-fold decrease) in solution. In contrast, decay time remains unchanged for the dyes in frozen glass at 77K or immobilized into a rigid polymeric matrix.

Cyclometalation based on a 2-pyridyl unit in *meso*-position with C-H activation of β-H of the porphyrin results in about 100 nm large bathochromic shift of absorption and emission spectra. Additionally, the phosphorescence decay time drastically decreases (about 20-fold). Unfortunately, also the phosphorescence quantum yield decreases significantly. For this structure, cyclometalation, however, is accompanied by an increase of singlet oxygen quantum yield to 85%. This makes the new dye a powerful red-light excitable $^1O_2$ photosensitizer.

Manuscript

Marrying metalloporphyrins with cyclometalated complexes – a luminous pair?

Authors: Andreas Steinegger,[1] Yvonne Moritz,[1,2] and Sergey M. Borisov*[1]

[1]Graz University of Technology, Institute of Analytical Chemistry and Food Chemistry, Stremayrgasse 9, 8010 Graz, Austria

[2]present address: Christian Doppler Laboratory for Advanced Coated Cutting Tools at the Department of Materials Science, Montanuniversität Leoben, Franz-Josef-Strasse 18, 8700 Leoben, Austria

E-mail: sergey.borisov@tugraz.at

Abstract: Cyclometalation is investigated as a method to modulate the photophysical properties of phosphorescent (benzo)porphyrins. The cyclometalated motif with Pt(II) core was integrated into three Pd(II) porphyrin complexes. Integration of the freely rotating 2-phenylpyridyl based motif in the meso-position does not lead to notable spectral changes and only affects the luminescence decay time (about 2-fold decrease) in solution at room temperature but not for the dyes in frozen glass at 77K or immobilized into rigid polystyrene matrix. In contrast, cyclometalation involving a pyridine unit in the meso-position and β-H of the porphyrin results in about 100 nm large bathochromic shift of absorption and emission spectra and drastic (about 20-fold) decrease of the phosphorescence lifetime. Cyclometalation is also accompanied by increase of singlet oxygen quantum yield to 85 % making the new dye a powerful red-light excitable $^1O_2$ photosensitizer.

6.1 Introduction

Phosphorescence is a type of luminescence with properties interesting for a wide range of applications. Dyes displaying phosphorescence[16] are intensively researched for application in OLEDs,[70,71,264] optical sensing and imaging,[265–267] and as triplet photosensitizers[268] for photodynamic therapy,[269–271] photocatalytic reactions[271–273] and photon upconversion.[274] A general method to promote phosphorescence is to utilize the heavy atom effect. Most phosphorescent molecules contain halides (Br, I) or platinum group metals (Pd, Pt, Ir etc.). Among these, metalloporphyrins are exciting representatives with widespread application in oxygen sensing and as triplet photosensitizers. The performance of metalloporphyrins as triplet photosensitizers and oxygen indicators is to a large extent determined by their photophysical properties. For the former applications, near unity quantum yield of intersystem crossing is highly desirable. The sensitivity of optical oxygen sensors is guided both by the luminescence decay time of the indicator and the oxygen permeability of the matrix in which the indicator is immobilized. A plethora of matrix materials with a wide range of gas permeabilities is available and further modification (e.g. addition of plasticizers) can be used to fine control the properties. On the other hand, porphyrin-based oxygen indicators are mostly limited to Pd(II) and Pt(II) complexes,[6] and only a few indicators with different central metals have been reported, such as Ir(III)[63] and Gd(III)[275,276] complexes. Typically, Pt(II) and Pd(II) porphyrins possess phosphorescence decay times of about 20-70 and 300-1000 microseconds, respectively, that only minor depend on substitution.[6] Combination of these dyes with highly oxygen-permeable matrices results in sensors for trace oxygen, since quenching at ambient O_2 levels is too efficient. Providing that other photophysical properties (luminescence quantum yield, photostability) remain similar to the state-of-the-art metalloporphyrin indicators, new compounds with significantly lower phosphorescence decay times would provide the possibility to design ultra-fast responding sensors for ambient oxygen concentrations by immobilization of such dyes in the matrices with high oxygen permeability. Moreover, metalloporphyrins with shorter decay-times also may enable lifetime-based or time resolved pH or ion sensing and utilization of the dyes as advanced bioanalytical labels,[267] the applications currently compromised by too efficient quenching of phosphorescence by molecular oxygen. Therefore, it is of significant interest to investigate methods to manipulate the luminescence properties of indicator dyes.

Cyclometalation is well known to give efficiently phosphorescent Pt(II) and Ir(III) complexes.[69,277] The heavy atoms induce strong spin-orbit coupling that promotes intersystem crossing and further raise the energy of luminescence-deactivating d-d states.[152] More efficient intersystem crossing can reduce emissive lifetimes and enhance phosphorescence quantum yields. 2-Phenylpyridine or 1,3-di-(2'-pyridyl)benzene structures are known to readily react in cyclometalation reactions. These building blocks can therefore be promising for the introduction of cyclometalated structures into molecules. Unfortunately, typical cyclometalated complexes are poor candidates for sensing and imaging due to very low molar absorption coefficients in the visible region. Williams and co-workers,[153–158] however, reported that the introduction

of further cyclometalated blocks in the dye structure resulted in red-shifted absorption and emission spectra and enhanced molar absorption coefficients. Additionally, the radiative rate constants and hence the quantum yields increased. Since porphyrins typically used for optical sensing already contain Pt(II) or Pd(II) as central atoms, introduction of cyclometalated motifs into the structure may have similar effects on photophysical properties. In this work, we investigate the effects of cyclometalation with Pt(II) on the photophysical properties of Pd(II) porphyrins. It will be demonstrated that such modification only minor affects the photophysical properties if the cyclometalated motif is not in plane with the porphyrin macrocycle but can introduce strong bathochromic shift if the structure is rigidized after the cyclometalation. It will also be shown that such molecular hybrids are powerful photosynthesizers of singlet oxygen.

6.2 Results and Discussion

6.2.1 Choice of Materials

Among the limited number of compounds exhibiting room temperature phosphorescence,[16,266,278] platinum(II) and palladium(II) porphyrins are particularly popular luminophores, due to their moderately high quantum yields, large Stokes shift and high molar absorption coefficients.[6,61] Their inherently long lifetimes enable decay time read-out with compact and cheap phase fluorometers or, alternatively, in the time domain providing the possibility of simple discrimination of the signal from autofluorescence. To study the effect of cyclometalation on the photophysical properties of the metalloporphyrins we chose Pd(II) complexes that are accessible from corresponding free-base porphyrins via milder reaction conditions and in higher yields compared to the respective Pt(II) analogues. Two types of porphyrin macrocycle were selected (Figure 1): (i) "classical" tetraphenylporphyrin-based chromophore that features absorption in the violet-green part of the electromagnetic spectrum and red emission (Cym1 and Cym2) and (ii) π-extended benzoporphyrin derivative which Q-bands are located in the red part of electromagnetic spectrum with the emission in the near-infrared (NIR) optical window (Cym 3). Among the three macrocycles, Cym2 and Cym3 possess the cyclometalating motif in the *meso*-position which can freely rotate before and after cyclometalation. In contrast, in Cym1 cyclometalation reaction involves the pyrrole carbon of the macrocycle and results in rigidization of the system bringing the meso-positioned 2-pyridyl substituent in plane with the porphyrin core (Figure 6.1). In all the compounds, the two remaining coordination positions of the Pt(II) are saturated with the acetylacetonate (acac) ligand.

6.2.2 Synthesis

Figure 6.2 presents the synthetic routes to cyclometalated porphyrins Cym1 and Cym2. For the porphyrin ligand 1, two routes were compared with regard to latter upscaling. The classical Adler-Longo method (depicted in Figure 6.2) gives a statistical product mixture
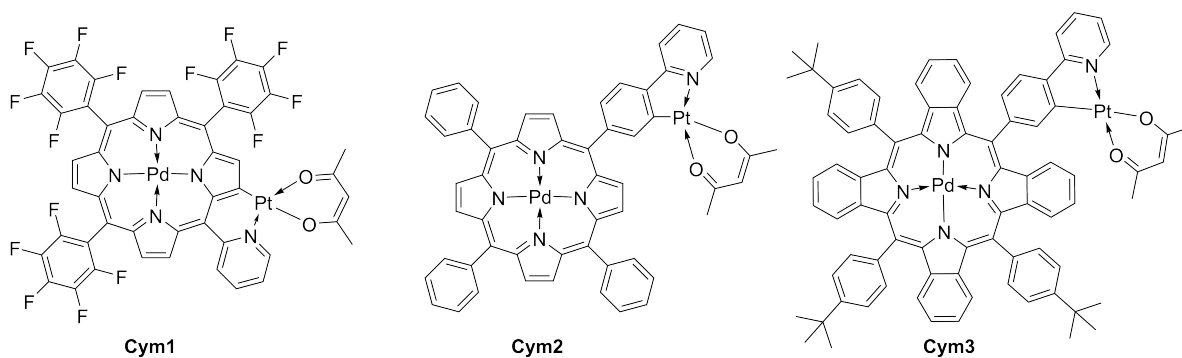
Figure 6.1: Chemical structures of the cyclometalated Pd(II) (tetrabenzo)porphyrins.
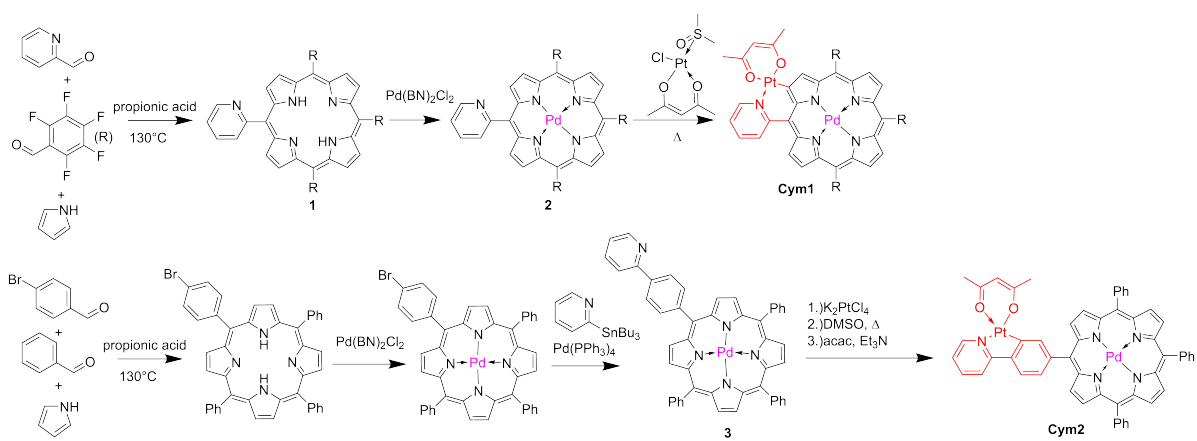
Figure 6.2: Synthesis of the cyclometalated Pd(II) porphyrins.

regarding the meso-substitution pattern. The rational route using dipyrromethanes and 1,9-diacyldipyrromethanes (c.f.[279]) gives one single product but requires 4 reactions steps. Both reactions gave a similar overall yield (∼4 %), but the Adler-Longo method is far less time consuming.

The cyclometalation of 2 proved challenging. The product was expected to have a bathochromic shift of the absorption due to the alignment of the pyridyl substituent with the plane of the porphyrin macrocycle. No significant spectral changes were observed upon reaction of 2 with K$_2$PtCl$_4$ and further ligand exchange reactions (refluxing in DMSO and afterwards treatment with acac under basic conditions). This indicates that either the cyclometalation reaction did not work at all or the produced chloro-bridged dimer intermediate could not be split by DMSO/acac and remained insoluble. Reactions with Pt(PhCN)$_2$Cl$_2$ and [PtMe2(SMe$_2$)]$_2$[166] were accompanied by a bathochromic shift of the absorption spectra, however the reaction products could not isolated/purified. On the other hand, reaction of 2 with [Pt(acac)Cl(DMSO)], a precursor that already contains coordinated acetylacetone, proved to be successful allowing isolation of Cym1 from the reaction mixtures. In addition to Pd(II)-based Cym1, we also attempted synthesis of the corresponding cyclometalated Zn(II) and Pt(II) metalloporphyrins. The reaction with the Zn(II) porphyrin gave product mixtures, where no cyclometalated product could be isolated. The synthesis of the Pt(II) porphyrin proved difficult. The platination of 1 requires harsh reaction conditions that also lead to cyclometalation (concluded from spectral shift) and extremely complex product mixtures.

Synthesis of 3 was straight-forward. Note that compared to 2 the *meso*-substituents of the porphyrin were changed from pentafluorphenyl groups to phenyl groups due higher yields and simpler purification with these substituents. Here, the Adler-Longo method gives a product mixture with varying bromophenyl substitution. The individual products of this mixture behave similarly during purification so the isolation of the desired product at this step was not chosen. The simplest opportunity was to isolate the product after the Stille coupling with the pyridine building block that drastically changes the behavior during chromatography compared to the other products of the reaction mixture. For cyclometalation, a different procedure was used.[153] After reaction with K$_2$PtCl$_4$, the chloro-bridged dimer is refluxed in DMSO to give an intermediate DMSO complex. The purification of this complex is simpler compared to the final acac complex as the DMSO complex gives one distinct band during chromatography. The purified intermediate is then treated with acac and triethylamine in toluene to give Cym2.

Figure 6.3 shows the synthesis of cyclometalated Pd(II)-tetrabenzoporphyrin Cym3. The benzoporphyrin intermediate 4 is obtained in a modified template method[280] via condensation of phthalonitrile with 4-bromophenylacetic acid and 4-*tert*-butylphenylacetic acid in presence of Zn(II) at 280 °C. Zinc is removed with a strong acid and palladium is introduced as a central atom. Again, the product mixture (porphyrins with varying number of bromophenyl and *tert*-butylphenyl groups in *meso*-positions) is not separated until the pyridyl unit is coupled to the benzoporphyrin. In the final step, Cym3 was obtained from 7 in the cyclometalation

procedure established for Cym2.
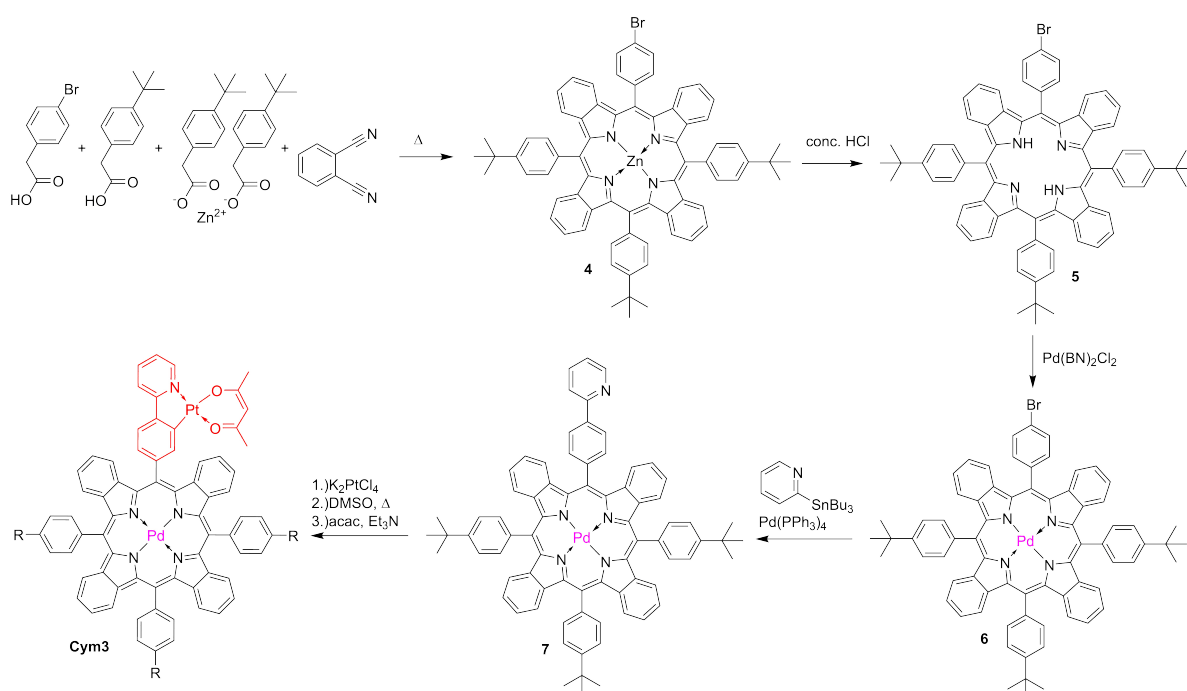
Figure 6.3: Synthesis of the cyclometalated Pd(II) tetrabenzoporphyrin.

6.2.3 Photophysical Properties in Solution at Room Temperature

Figure 6.4 shows excitation and emission spectra of the cyclometalated porphyrins in comparison with the spectra of the corresponding Pt(II)-free Pd(II) metalloporphyrin complexes. The absorption spectra of all dyes are shown in Figure S1 of the supporting information and are virtually identical to the excitation spectra. For Cym2 and Cym3, excitation and emission spectra are virtually not affected by the substitution (Figure 6.4, Table 6.1). In contrast, Cym1 shows a strong bathochromic shift of both absorption/excitation and emission spectra compared to 2 (Figure 6.4). This can be explained by the extension of the conjugated π-system with the pyridyl meso-substituent. Pt(II) with its square planar coordination sphere forces the pyridyl substituent in a coplanar orientation to the porphyrin system.

As expected, the cyclometalated structures showed a decrease in luminescence lifetime compared to the parent Pd(II) porphyrins. The decay times of Cym2 and Cym3 decreased by about 2-fold (Figure 6.5 and Table 6.1). For Cym1, drastic decrease by about 70-fold was observed. Unfortunately, also the phosphorescence quantum yield was strongly affected by cyclometalation decreasing from ~5% for 2 to ~0.5% for Cym1. This value is too low to enable practical applicability of the dye as a phosphorescence emitter.
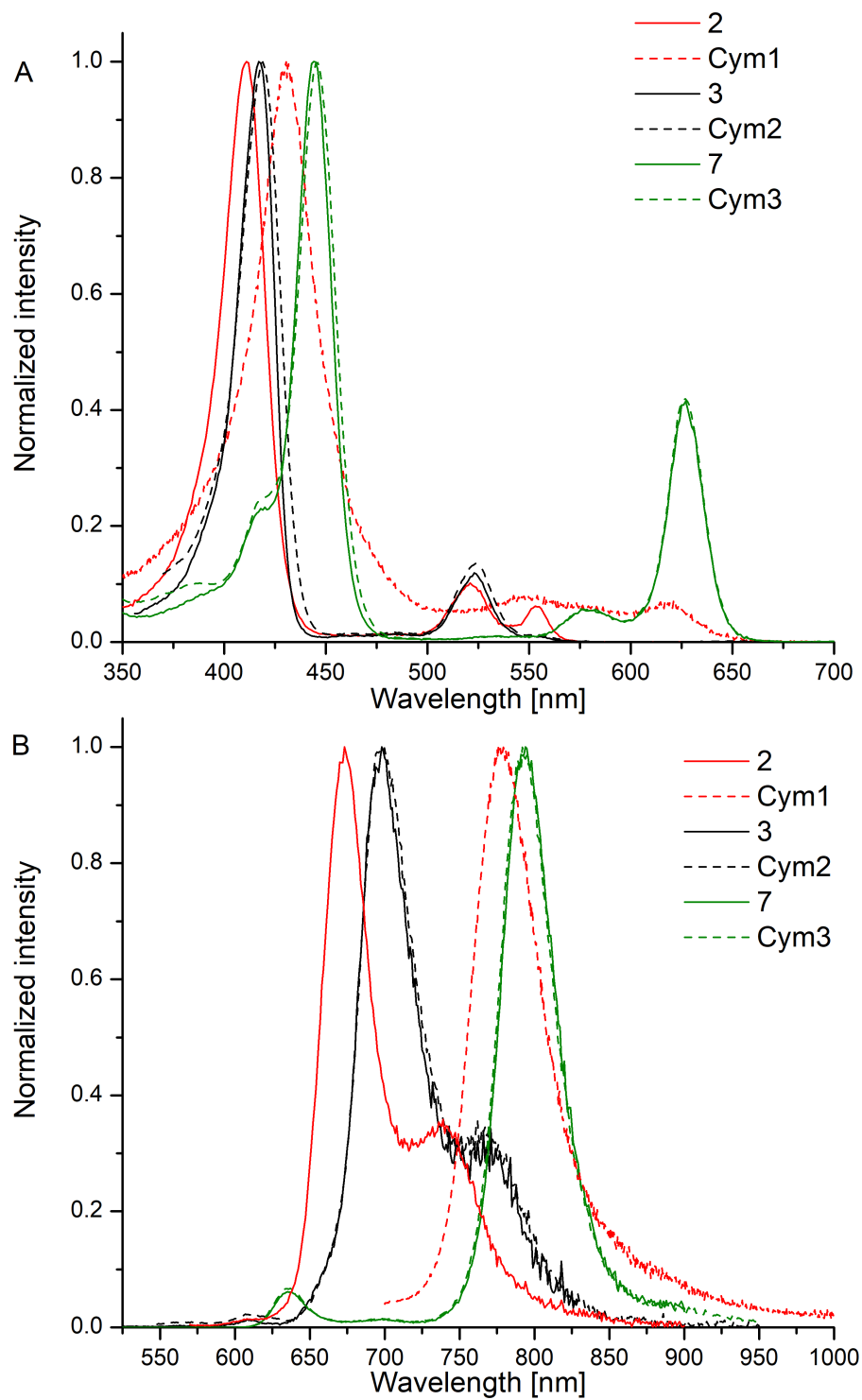
Figure 6.4: Luminescence excitation (A) and emission (B) spectra of the cyclometalated porphyrins (dashed lines) and their precursors (solid lines) in anoxic toluene at 25 °C.

New Indicators for Optical Sensing by Manipulating the Intersystem Crossing in Luminescent Dyes

Table 6.1: Photophysical properties of the cyclometalated Pd(II) porphyrins and their precursors at 298 and 77 K.

Complex	λ_{max} abs [nm][a]	λ_{max} em [nm][b]	τ_0 [µs][b]	ϕ [%][b]	λ_{max} em at 77K [nm][c]	τ_0 at 77 K [µs][c]	ϕ at 77 K [%][c]	ϕ $^1O_2$ [%][a]
2	412, 522	675	698±8	5.1±0.5	661	1620±10	9.9±0.8	70±1
Cym1	432, 620(sh)[d]	780	14.7±2[e]	0.4±0.2	737	16.6±1[e]	1.4±0.6	85±1
3	417, 523	698	540±20	3±0.4	690	1310±10	7.4±1.3	76±1
Cym2	419, 524	700	259±9	2.2±0.1	688	1300±10	6.0±0.3	77±1
7	444, 627	794 (637 TADF)[f]	143±2	2.5±0.1	777	528±1	16.6±1.1	84±4
Cym3	446, 627	792 (635 TADF)[f]	81±2	1.8±0.1	779	526±1	16.3±2.7	82±1

[a] in toluene

[b] in deoxygenated toluene

[c] in toluene+THF (2+3, v+v) frozen glass

[d] sh = shoulder

[e] average lifetimes were calculated from the relative amplitudes (B1, B2) and lifetimes (τ_1, τ_2) of the individual components from two-exponential decay: τ_0=B1*τ_1+B2*τ_2

[f] thermally-activated delayed fluorescence
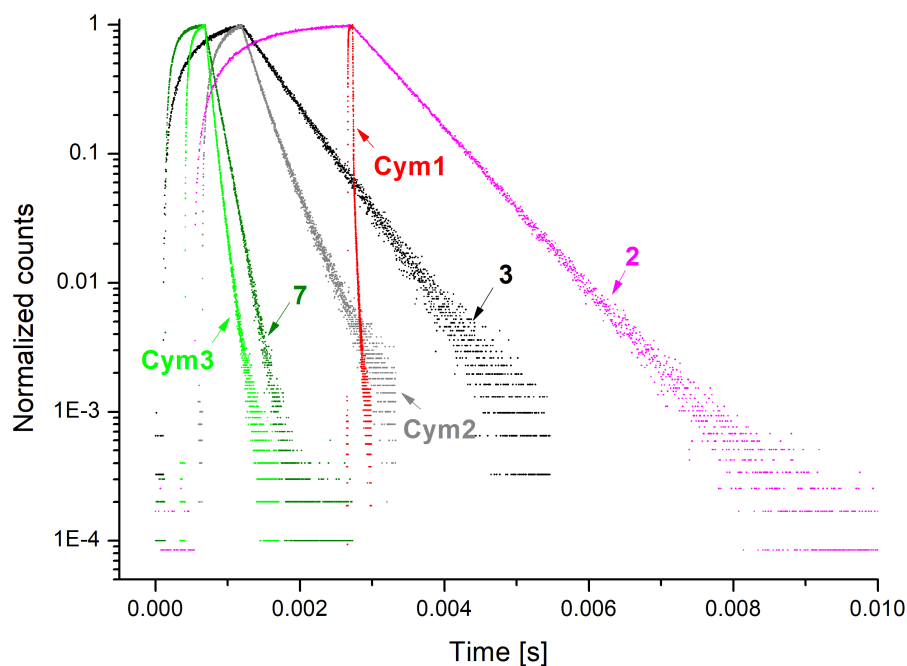
Figure 6.5: Luminescence decays of the cyclometalated porphyrins and their precursors in anoxic toluene at 25 °C.

6.2.4 Photophysical properties at 77K

The experiments conducted in solution at 25 °C indicated that cyclometalation appeared to be a promising tool to control the luminescence lifetime of metalloporphyrins without significantly affecting other photophysical properties. However, the investigations conducted at 77K revealed that all the differences in the decay times between the cyclometalated compounds and non-cyclometalated precursors completely vanish in case of Cym2 and Cym3 (Table 6.1). Therefore, it appears unlikely that the differences observed for these two compounds at room temperature are due to the heavy atom effect of platinum in the cyclometalated motif. Rather, they might be associated with the rotation of the cyclometalated unit that disappear in frozen glass at 77 K and upon immobilization into a rigid polymer matrix (see below). On the other hand, drastic difference in phosphorescence decay times and quantum yields between Cym1 and 2 is preserved at 77K as well (Table 6.1) indicating persistent effect of the cyclometalating unit on the photophysical properties that is rather independent on the measurement conditions.

6.2.5 Photophysical Properties of the Polystyrene-Immobilized Dyes

For opto-electronic applications, dyes are typically immobilized into polymeric matrices. Immobilization may affect the luminescent properties of the emitters. Here, polystyrene was chosen as a matrix due to its high chemical stability and popularity in optical oxygen sensors. The excitation and emission spectra of polystyrene-immobilized dyes (Figure S3) are extremely similar to those measured in toluene. The behavior of the dyes in respect to their luminescence decay times and quantum yields mimics the one observed in frozen glass at 77K: (i) drastic difference in case of Cym1 and 2 and (ii) virtually identical values in case of Cym2 and 3 and in case of Cym3 and 7 (Figure S4, Table 6.2). This again supports the hypothesis on the correlation of the photophysical properties with the possibility of rotation of the cyclometalated group. For Cym2 and Cym3 such rotation is possible in solution but is strongly impeded in rigid media including polystyrene or the frozen glass.

Table 6.2: Photophysical properties of the cyclometalated Pd(II) porphyrins and their precursors immobilized in polystyrene at 25 °C and oxygen-free conditions.

Compound	λ_{max} abs [nm]	λ_{max} em [nm]	τ_0 [µs]	ϕ [%]
2	410, 521	673	1020±10	16.5±0.5
Cym1	428	768	48±1[a]	0.7±0.1
3	418, 525	692	1000±10	11±0.2
Cym2	422, 525	693	945±1	10.4±1.2
7	444, 629	788 (TADF 637)	412±1	6.1±0.1
Cym3	445, 627	792 (TADF 635)	422±1	6.7±0.3

[a] average lifetimes were calculated from the relative amplitudes (B1, B2) and lifetimes (τ_1, τ_2) of the individual components from two-exponential decay: τ_0=B1*τ_1+B2*τ_2

6.2.6 Singlet Oxygen Generation

The generation of singlet oxygen is an important field of research[271] regarding signaling and cell death with regard to photodynamic therapy.[281] Photochemically produced singlet oxygen is used to assess its cytotoxic effect on targeted tissue. Singlet oxygen is mainly generated upon quenching of the triplet state of the photosensitizer and is affected by the match of the energy levels of the sensitizer and quencher, triplet state quantum yields and triplet state lifetime of the dye. A typical method to increase the triplet state population is to increase intersystem crossing via the heavy atom effect. For porphyrins, halogenation has been studied for its effect on singlet oxygen quantum yields.[282] Sensitizers with long excitation wavelength are particularly attractive for photodynamic therapy applications due to good light penetration in tissues.

As can be seen in Table 6.1, $^1O_2$ quantum yields for the new cyclometalated complexes are rather high. The results obtained for Cym1 are of particular interest. In contrast to decrease of the phosphorescence quantum yield, cyclometalation leads to increase of $\phi\left(^1O_2\right)$ to impressive 85 %. Simultaneously, a bathocromic shift of the absorption by about 100 nm makes it possible to excite the cyclometalated complex in the optical window. Further bathochromic shift of the absorption spectra appears to be feasible e.g. via extension of π-conjugation either via introduction of the condensation of phenyl moieties in the β-position or via a cyclometalating unit with extended π-system (quinoline). Moreover, the pentafluorophenyl groups present in Cym 1 represent an interesting possibility of simple post-modification via substitution of p-fluorine atom under mild conditions. In this manner, the sensitizer can be modified with sugars[283] or peptides[284] which would render the dye water-soluble or provide addressable character e.g. for tumors.[285]

6.3 Conclusion

The effect of cyclometalation on three Pd(II) porphyrin structures was investigated. Attachment of the cyclometalated 2-phenylpyridine motif in the *meso*-position of the (benzo)porphyrin (Cym2, Cym3) affects the photophysical properties only in solution with all differences between the cyclometalated compounds and the non-cyclometalated precursors disappearing in rigid frozen glass or rigid polystyrene matrix. On the other hand, cyclometalation involving a pyridine unit in meso-position and β-H of the porphyrin drastically influences the photophysical properties. Orientation of the *meso*-substituent in plane with the porphyrin macrocycle results in extension of the π-system and strong bathochromic shift of the absorption and emission spectra. Cyclometalation is accompanied by more than 20-fold decrease of the phosphorescence decay times and, disappointedly, also by significant deterioration of the emission quantum yield. Nevertheless, the modified dye represents a powerful sensitizer of singlet oxygen. This property together with excitation in the red part of the electromagnetic spectrum and possibly of modification with (bio)molecules via click chemistry can make the dye promising for application in photodynamic therapy.

6.4 Experimental

6.4.1 Materials

Silica gel (0.04-0.063 mm), 1,2,4-trimethylbenzene and PS, av. MW $\approx$ 260,000 Da. were purchased from Acros Organics (www.acros.com); hydrochloric acid 37 %, anhydrous sodium sulfate and sodium hydrogen carbonate from VWR (www.vwr.com); benzaldehyde and pyrrole from abcr (https://www.abcr.de/); propionic acid from Carl Roth (www.roth.de); 2-(4-bromophenyl)acetic acid, 2,4-pentanedione, sodium propionate, and triethylamine from Aldrich (www.sigmaaldrich.com); 4-bromobenzaldehyde, 9,10-dimethylanthracene, DMSO, pentafluorobenzaldehyde, 2-pyridincarboxaldehyde, and 2-(4-tert-butylphenyl)acetic acid from TCI Europe (www.tcichemicals.com). Solvents were purchased from VWR [cyclohexane (CH), ethanol (EtOH), ethyl acetate (EE), methanol (MeOH), toluene (Tol, synthesis grade), all deuterated solvents], Fisher Scientific [dichloromethane (DCM)],) and Roth [chloroform, toluene (HPLC grade, optical measurements)]. Novec 7200 (ethoxy nonafluorobutane) was purchased from 3M (https://www.3m.com/). Polyethylene terephthalate (PET) foils (MELINEX 506) were supplied by Pütz GmbH + Co (www.puetz-folien.com). Pyrrole was freshly distilled before use.

6.4.2 Dye immobilization in PS

Dye (1 wt % with respect to PS) and PS were dissolved in chloroform (7.5 wt % of PS in chloroform). This viscous solution was knife-coated (25 µm thick wet film) onto dust-free 125 µm biaxially oriented polyethylene terephthalate (PET) foils (MELINEX 506). After evaporation of the solvent at room temperature, the sensor foil was dried at 60 °C for 24 h.

6.4.3 Characterization

^{1}H and ^{13}C NMR spectra were recorded on a Bruker AVANCE III spectrometer equipped with an autosampler (300.36 MHz ^{1}H NMR, 75.53 MHz ^{13}C NMR). For mass spectrometric measurements, a matrix-assisted laser desorption/ionization (MALDI)-TOF/TOF (time of flight) spectrometer from Bruker (www.bruker.com) was used. UV-vis spectra were measured on a VARIAN CARY 50 conc. using Hellma Analytics optical glass 10 mm precision cuvettes (www.hellma-analytics.com). Luminescence spectra, quantum yields and luminescence decay times were measured on a Fluorolog 3 spectrofluorometer from HORIBA Scientific equipped with a R2658 photomultiplier from Hamamatsu (www.hamamatsu.com). For measurement under anoxic conditions, screw-capped quartz precision cuvettes from Hellma Analytics were used. Deoxygenation of solutions was achieved by bubbling argon (99.999% purity) through the solution for 10 min and addition of 2 wt % aq Na_2SO_3 solution. Absolute quantum yields were determined using a "Quanta-φ" integrating sphere-based set-up (HORIBA Scientific). Luminescence decays were recorded using a time-correlated single photon counting method on a

Fluorolog 3 spectrofluorometer equipped with a DeltaHub module controlling a SpectraLED-460 (456 nm) laser diode. For data analysis, DAS-6 Analysis software was used. Data were fitted using a mono or biexponential (Cym1) decay model. For the biexponential model, average lifetimes, τ, were calculated from the relative amplitudes (B1, B2) and lifetimes (τ_1, τ_2) of the individual components using the equation $\tau = (B1 \times \tau_1 + B2 \times \tau_2)$. Singlet oxygen quantum yields were determined by a relative method in air-saturated toluene.[282] 9,10-dimethylanthracene was used as a singlet oxygen acceptor and tetraphenylporphyrin as reference photosensitizer (ϕ_Δ=0.63).[286] A solution containing 100 µM DMA and 2-8 µM of photosensitizer was placed in a cuvette equipped with a magnetic stirrer and irradiated with the light of a xenon lamp from a Fluorolog 3 spectrometer. The irradiation wavelength was chosen for each dye/reference pairs to give equal absorbance of both sensitizers at the excitation wavelength. The photooxidation of DMA was monitored via UV-vis spectrometry at 358 nm. The slope from the curve of absorbance vs. time constructed from 3 independent bleaching experiments was compared for each dye with the reference under identical experimental conditions.

6.4.4 Synthesis

Pt and Pd-precursors (K$_2$PtCl$_4$,[287] Pd(PhCN)$_2$Cl$_2$,,[288] [Pt(acac)Cl(DMSO)]),[289] tetrakis-(triphenylphosphine)palladium,[290] tributyl-(2-pyridyl)stannane,[291] and zinc 2-(4-(*tert*-butyl)-phenyl)-acetate[280] were prepared according to literature procedures.

5,10,15-tris(pentafluorophenyl)-20-(pyridin-2-yl)porphyrin (1): In a one-neck round-bottom-flask, propionic acid (270 ml, 3.61 mol) was heated to 130 °C. Pyrrole (5 ml, 72 mmol, 5.9 eq.), 2-pyridinecarboxaldehyde (1.2 ml, 12.2 mmol, 1 eq.) and pentafluorobenzaldehyde (7.51 ml, 60.8 mmol, 5 eq.) were added and the mixture was stirred for 30 minutes. Conversion was monitored via UV-Vis spectroscopy and TLC (silica-gel, Tol+DCM = 5+4). After full conversion, the solvent was removed under reduced pressure. The crude product was purified via column chromatography (silica-gel, Tol+DCM 5+4) and precipitation from DCM upon addition of cyclohexane/ Novec 7200 (10+3) mixture. Yield: 470 mg (5 %) dark purple powder.

Rf value (product) (Tol+DCM 5+4): 0.31

^{1}H NMR (300 MHz, CDCl$_3$): δ 9.17 (d, J = 4.6 Hz, 1H, pyridine), 9.02 – 8.82 (m, 8H, porphyrin, beta-H), 8.27 (d, J = 7.7 Hz, 1H, pyridine), 8.16 (t, J = 7.6 Hz, 1H, pyridine), 7.78 (t, 1H, pyridine), -2.88 (s, 2H, N-H) ppm.

Pd(II) 5,10,15-tris(pentafluorophenyl)-20-(pyridin-2-yl)porphyrin (2): In a Schlenk-tube, free-base porphyrin 1 (160 mg, 0.18 mmol) was dissolved in toluene (30 ml) under argon atmosphere. Pd(PhCN)$_2$Cl$_2$ (104 mg, 0.27 mmol, 1.5 eq.) was added and the solution was

stirred at 105 °C for 3 hours. Conversion was monitored via UV-Vis spectroscopy. After quantitative conversion, the solvent was removed under reduced pressure. The crude product was purified via column chromatography (silica-gel, Tol+DCM 5+4). Yield: 43 mg (24 %) pink solid.

Rf value (product) (Tol+DCM 5+4): 0.15

^{1}H NMR (300 MHz, CDCl$_3$): δ 9.13 (d, J = 4.1 Hz, 1H, pyridine), 8.94 – 8.79 (m, 8H, porphyrin, beta position), 8.25 (d, J = 7.6 Hz, 1H, pyridine), 8.15 (t, J = 7.6 Hz, 1H, pyridine), 7.77 (t, 1H, pyridine) ppm.

Cyclometalated Pd(II) 5,10,15-tris(pentafluorophenyl)-20-(pyridin-2-yl)porphyrin Cym1: In a Schlenk tube, Pd(II)-porphyrin 2 (25 mg, 25.2 µmol, 1 eq.) was dissolved in 1,2,4-trimethylbenzene (15 ml) under Ar-atmosphere. The Pt-precursor, Pt(acac)Cl(DMSO), (18.5 mg, 45.4 µmol, 1.8 eq.) was added and the mixture was stirred at 160 °C for 2 hours. Conversion was monitored via UV-Vis spectroscopy. After full conversion, the solvent was removed under reduced pressure at 50 °C. The crude product was purified via column chromatography (silica-gel, CH+EE 3+1, Rf value (product) (CH+EE 3+1): 0.33). Yield: 3.3 mg (10 %) dark green-brownish solid.

^{1}H NMR (300 MHz, CD$_2$Cl$_2$): δ 9.78 (d, J = 5.8 Hz, 1H, pyridine), 9.28 (d, J = 5.0 Hz, 1H, pyridine), 8.90 – 8.65 (m, 7H, porphyrin, beta-H), 7.99 (t, J = 7.3 Hz, 1H, pyridine), 7.58 – 7.41 (m, J = 13.6, 7.6 Hz, 1H, pyridine), 5.66 (s, 1H, acac, CH), 2.17 (s, 3H, acac, CH$_3$), 2.05 (s, 3H, acac, CH$_3$) ppm.

MALDI TOF: m/z: C$_{48}$H$_{18}$F$_{15}$N$_5$O$_2$PdPt [M+] calc.: 1282.99, found: 1282.97

Pd(II) 5,10,15-triphenyl-20-(4-(pyridin-2-yl)phenyl)porphyrin (3): In a two-neck round-bottom flask, propionic acid (90 ml) was heated to 130 °C under nitrogen atmosphere. Pyrrole (1.5 g, 22 mmol, 6 eq), 4-bromobenzaldehyde (690 mg, 3.7 mmol, 1 eq) and benzaldehyde (1.19 g, 11 mmol, 3 eq) were added under nitrogen counterflow. The reaction mixture was stirred at 130 °C for 25 min. Then air was bubbled through the reaction mixture. The flask was cooled to room temperature and the solvent was removed under reduced pressure. The residue was dissolved in a minimum amount of toluene, filtered through a silica-gel plug and eluted with toluene. The solvent was removed under reduced pressure. The crude product mixture was dissolved in 15 mL of DCM and the precipitated from 200 ml MeOH. Yield: 425 mg, purple powder containing the mixture of tetraphenyl, (4-bromophenyl)-triphenyl, and di-(4-bromophenyl)-di-phenyl porphyrin. In a Schlenk-tube, the product mixture (425 mg, calc.

for (4-bromophenyl)-triphenyl porphyrin: 613 μmol, 1 eq) was dissolved in toluene (30 ml) under Ar atmosphere. Pd(PhCN)$_2$Cl$_2$ (353 mg, 919 μmol, 1.5 eq.) and sodium propionate (295 mg, 3.06 mmol, 5 eq) were added and the reaction mixture was stirred at 110 °C for 45 min. Conversion was monitored via UV-Vis spectra. The reaction mixture was cooled to room temperature and directly poured onto a silica-gel column and eluted with DCM. Yield: 460 mg purple crystalline powder containing the mixture of Pd(II) complexes of tetraphenyl, (4-bromophenyl)-triphenyl, and di-(4-bromophenyl)-di-phenyl porphyrin. The product mixture (460 mg, calc. for Pd(II) (4-bromophenyl)-triphenyl porphyrin: 0.58 mmol, 1 eq) was dissolved in 50 ml of dry toluene under inert conditions. Tetrakis(triphenylphosphine)palladium (67 mg, 58 μmol, 0.1 eq) and tributyl-(2-pyridyl)stannane (424 mg, 1.2 mmol, 2 eq) were added and the mixture was stirred at 100 °C for 24 h. After quantitative conversion monitored by MS. The reaction mixture was cooled to room temperature, directly poured onto a silica-gel column and eluted (gradient starting with Tol to Tol+DCM=1+1). Yield: 184 mg of purple powder.

^{1}H NMR (300 MHz, CDCl$_3$) δ 8.90 – 8.80 (m, 8H), 8.70 (d, J = 4.9 Hz, 1H), 8.38 (d, J = 8.0 Hz, 2H), 8.29 (d, J = 7.9 Hz, 2H), 8.20 – 8.12 (m, 5H), 8.05 (d, J = 8.1 Hz, 1H), 8.01 – 7.97 (m, 1H), 7.92 (t, J = 7.8 Hz, 1H), 7.75 (dd, J = 5.5, 2.7 Hz, 8H), 7.47 (d, J = 7.4 Hz, 1H), 7.40 – 7.34 (m, 1H) ppm.

MALDI TOF: m/z: C$_{49}$H$_{31}$N$_5$Pd [M+] calc.: 795.1632, found: 795.1572.

Cyclometalated Pd(II) 5,10,15-triphenyl-20-(4-(pyridin-2-yl)phenyl)porphyrin Cym2: In a 100 mL Schlenk tube, porphyrin 3 (100 mg, 126 μmol, 1 eq) was suspended in a mixture of 2-ethoxyethanol and water (40 mL, 4+1) under Ar atmosphere and K$_2$PtCl$_4$ was added (52 mg, 126 μmol, 1 eq). The reaction mixture was stirred at 80 °C for 20 h and then it was allowed to cool to room temperature. The chloro-bridged dimer was precipitated from H$_2$O (200 mL). After centrifugation, the precipitate was dissolved in DMSO (30 mL) and stirred at 150 °C for 20 min. The mixture was again cooled to room temperature and precipitated from H$_2$O (200 mL + 7.5 mL sat. aq. NaCl). The residue was dissolved in toluene (12 mL) and triethylamine (127 mg, 1.26 mmol, 10 eq) and 2,4-pentanedione (38 mg, 377 μmol, 3 eq) were added. The mixture was stirred at 100 °C under Ar atmosphere for 24 h. After cooling to room temperature, the reaction mixture was washed with water (20 mL) and then the solvent was removed under reduced pressure. The crude product was purified via flash column chromatography (silica-gel, CH+DCM=1+1). Yield: 14 mg (10 %) purple solid.

^{1}H NMR (300 MHz, CDCl$_3$) δ 9.16 (s, 1H), 9.02 (d, J = 4.9 Hz, 2H), 8.80 (t, J = 2.3 Hz, 6H), 8.41 (s, 1H), 8.19 (d, J = 9.3 Hz, 6H), 7.96 – 7.84 (m, 2H), 7.74 (d, J = 6.7 Hz, 9H), 7.54 (d, J = 8.1 Hz, 1H), 7.38 – 7.33 (m, 1H), 7.13 (d, J = 10.1 Hz, 1H), 5.38 (s, 1H), 2.02 (s,

3H), 1.62 (s, 3H) ppm.

MALDI TOF: m/z: $C_{54}H_{37}N_5O_2PdPt$ [M+] calc.: 1089.1648, found: 1089.1732

Zn(II) 5-(4-bromophenyl)-10,15,20-tri(4-*tert*-butylphenyl)-tetrabenzoporhyrin (4): 2-(4-bromo-phenyl)-acetic acid (1.5 g, 6.99 mmol, 1.5eq), 2-(4-*tert*-butylphenyl)acetic acid (2.24 g, 11.6 mmol, 2.5 eq), zinc 2-(4-(*tert*-butyl)phenyl)acetate (2.08 g, 4.65 mmol, 1 eq) and phthalonitrile (2.38 g, 18.6 mmol, 4 eq) were ground and homogenized with a ceramic pestle in a mortar. Approximately, 750 mg portions of the mixture were weighed in 3 mL glass vials equipped with a stirring bar. The vials were sealed with a metal cap and put in preheated to 160 °C heating block. The mixture was heated to 280 °C within 20 min and kept at this temperature for 40 min. Stirring of the mixture was started at 180 °C. The vials were then removed from the heating block and were allowed to cool to room temperature. The reaction products were dissolved in acetone (500 mL) and precipitated from a mixture of ethanol/water/sat. aq. $NaHCO_3$ (2.5 L, EtOH:H_2O:sat. $NaHCO_3$ = 150+30+1, v+v+v). After centrifugation, the precipitate was dissolved in the minimum amount of acetone (150 mL) and precipitated again from a mixture of ethanol/water/sat. aq. $NaHCO_3$ of the above composition (5*150 mL). The crude product was purified via flash column chromatography (silica-gel, gradient CH+DCM=4+1->1+1). Yield: 237 mg green solid (product mixture with varying number of bromophenyl substituents in the meso position)

^{1}H NMR (300 MHz, CD_2Cl_2) δ 8.16 (d, J = 7.7 Hz, 8H), 7.92 (d, J = 7.9 Hz, 8H), 7.27 – 7.08 (m, 16H), 1.70 (s, 27H) ppm.

5-(4-bromophenyl)-10,15,20-tri(4-*tert*-butylphenyl)-tetrabenzoporhyrin (5) For demetalation, the mixture of Zn(II) meso-tetraaryltetrabenzoporphyrins 4 (170 mg) was dissolved in DCM (100 mL) and conc. HCl was added. The mixture was transferred to a separation funnel and shaken until only the protonated ligand could be observed in the UV-vis spectrum. The solution was then washed with H_2O (1x100 mL), sat. $NaHCO_3$ (1x100 mL) and again H_2O (1x100 mL). The organic layer was dried over Na_2SO_4 and the solvent was removed under reduced pressure. The product was used in the next step without further purification. Yield 160 mg (99 %).

Pd(II) 5-(4-bromophenyl)-10,15,20-tri(4-*tert*-butylphenyl)-tetrabenzoporhyrin (6) In a 100 mL Schlenk-tube, the mixture of *meso*-tetraaryltetrabenzoporphyrins 5 (160 mg, 151 µmol, 1 eq) was dissolved in toluene (30 ml) under Ar atmosphere. Pd(PhCN)$_2$Cl$_2$ (87 mg, 226 µmol, 1.5 eq.) and sodium propionate (72 mg, 753 mmol, 5 eq) were added and the reaction mixture

was stirred at 110 °C for 90 min. Conversion was monitored via UV-Vis spectroscopy. The mixture was cooled to room temperature and filtered through a silica-gel plug (eluted with EE). The crude product was purified via flash column chromatography (silica-gel, CH+DCM=9+1). Yield: 100 mg (57 %) green solid with a blue shimmer.

^{1}H NMR (300 MHz, CD$_2$Cl$_2$) δ 8.14 (m, 8H), 8.04 (d, J = 8.0 Hz, 2H), 7.91 (d, J = 8.0 Hz, 6H), 7.21 (m, 16H), 1.67 (s, 27H) ppm.

Pd(II) 5-(4-(pyridine-2-yl)-phenyl)-10,15,20-tri(4-*tert*-butylphenyl)-tetrabenzoporhyrin (7) The product mixture of Pd(II) *meso*-tetraaryltetrabenzoporphyrins 6 (175 mg, 150 µmol, 1 eq) was dissolved in 15 ml of dry toluene under inert conditions. Tetrakis-(triphenylphosphine)-palladium (17 mg, 15 µmol, 0.1 eq) and tributyl-(2-pyridyl)stannane (11 mg, 300 µmol, 2 eq) were added and the mixture was stirred at 100 °C for 24 h. The reaction mixture was cooled to room temperature and filtered through a silica-gel plug (eluted with EE). The crude product was purified via flash column chromatography (silica-gel, gradient CH+DCM=4+1->1+1). Yield: 32 mg green solid with a blue shimmer.

^{1}H NMR (300 MHz, CD$_2$Cl$_2$) δ 8.87 (d, J = 4.9 Hz, 1H), 8.60 (d, J = 7.9 Hz, 2H), 8.36 (d, J = 8.1 Hz, 2H), 8.15 (m, 6H), 7.92 (m, 7H), 7.47 – 7.36 (m, 1H), 7.22 (m, 17H), 1.68 (s, 27H) ppm.

MALDI TOF: m/z: C$_{77}$H$_{63}$N$_5$Pd [M+] calc.: 1163.4143, found: 1163.2323.

Cyclometalated Pd(II) tetrabenzoporphyrin (10) – Cym3 In a 100 mL Schlenk tube, 9 (29 mg, 25 µmol, 1 eq) was suspended in a mixture of 2-ethoxyethanol and water (10 mL, 9+1) under Ar atmosphere and K$_2$PtCl$_4$ was added (10 mg, 25 µmol, 1 eq). The reaction mixture was stirred at 80 °C for 20 h and then it was allowed to cool to room temperature. The reaction mixture was extracted with DCM (25 mL). The solvent was removed under reduced pressure. The residue was then dissolved in DMSO (15 mL) and stirred at 150 °C for 15 min. The mixture was again cooled to room temperature and precipitated from H$_2$O (75 mL + 1 mL sat. aq. NaCl). The residue was dissolved in toluene (10 mL) and triethylamine (26 mg, 249 µmol, 10 eq) and 2,4-pentanedione (8 mg, 75 µmol, 3 eq) were added. The mixture was stirred at 100 °C under Ar atmosphere for 24 h. The reaction mixture was cooled to room temperature, washed with water (20 mL) and the solvent was removed under reduced pressure. The crude product was purified via flash column chromatography (silica-gel, CH+DCM=1+1). Yield: 16 mg (44 %) green solid.

^{1}H NMR (300 MHz, CD$_2$Cl$_2$) δ 9.22 (d, J = 5.8 Hz, 1H), 8.30 (s, 1H), 8.22 (d, J = 8.5 Hz, 3H), 8.09 (d, J = 6.8 Hz, 3H), 8.01 (d, J = 9.6 Hz, 3H), 7.91 (t, J = 6.7 Hz, 7H), 7.57 (d, J = 8.1 Hz, 2H), 7.27 – 7.12 (m, 17H), 5.41 (s, 1H), 2.03 (s, 3H), 1.67 (s, 27H), 1.64 (s, 3H).

MALDI TOF: m/z: C$_{82}$H$_{69}$N$_5$O$_2$PdPt [M+] calc.: 1457.4161, found: 1457.3115.

6.5 Funding Sources

6.6 Acknowledgment

6.7 Supporting Information

6.7.1 Photophysical Properties

Photophysical Properties in Solution at room temperature
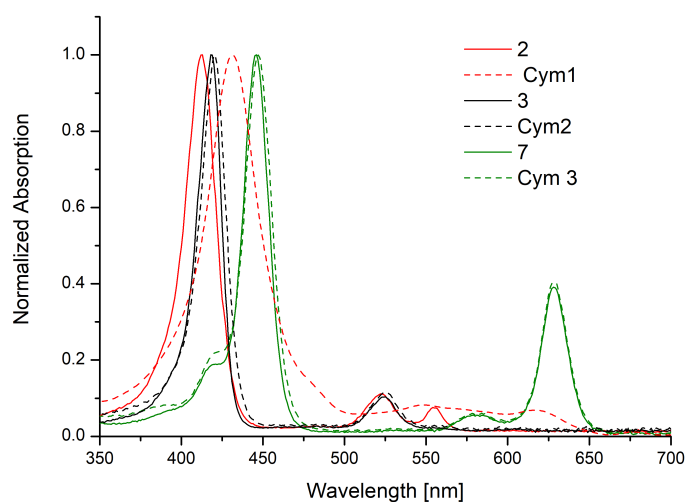
Figure S6.1: Absorption spectra of the cyclometalated porphyrins (dashed lines) and their precursors (solid lines) in toluene at 25 °C.

Measurements at 77 K
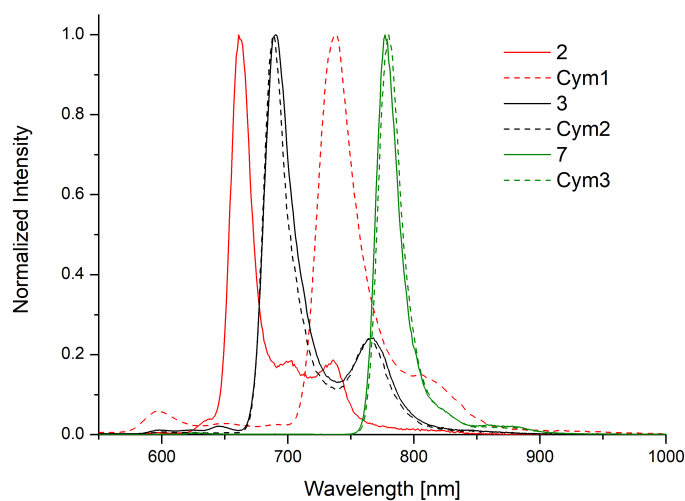
Figure S6.2: Emission spectra of the cyclometalated dyes and their precursors at 77 K in frozen glasses (toluene/THF (4 + 6), v+v).
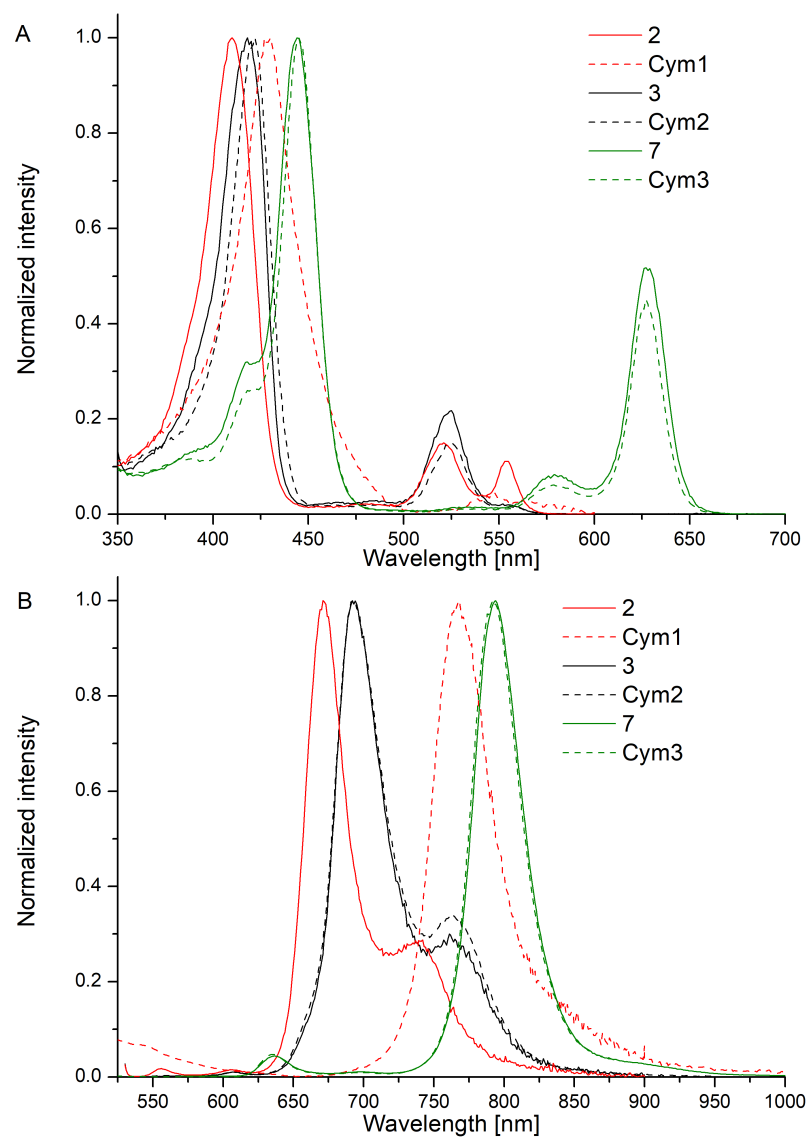
Figure S6.3: Luminescence (A) excitation and (B) emission spectra of the cyclometalated porphyrins (dashed lines) and their precursors (solid lines) immobilized in polystyrene at 25°C.
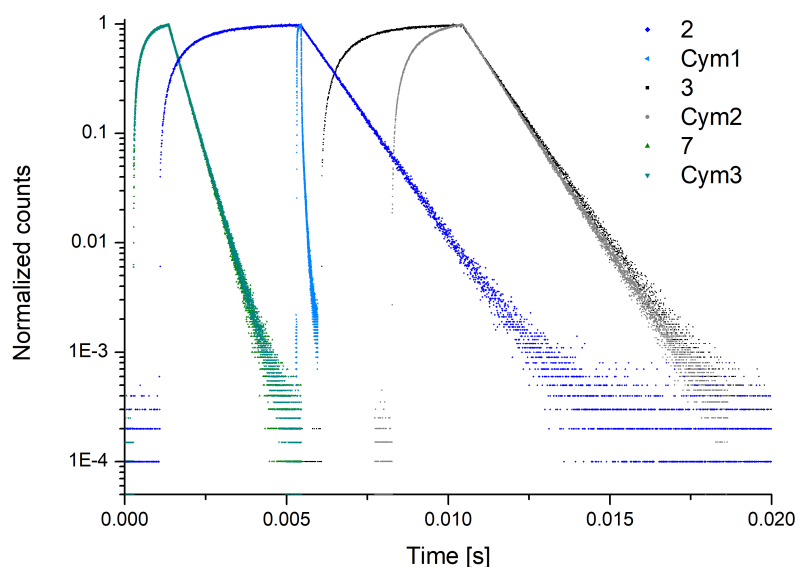
Figure S6.4: Luminescence decay of the cyclometalated porphyrins and their precursors immobilized in polystyrene at 25 °C. The decays were measured under anoxic conditions (aq. 2 wt % Na_2SO_3 solution).

6.7.2 NMR and MS spectra

5,10,15-tris(pentafluorophenyl)-20-(pyridin-2-yl)porphyrin (1)
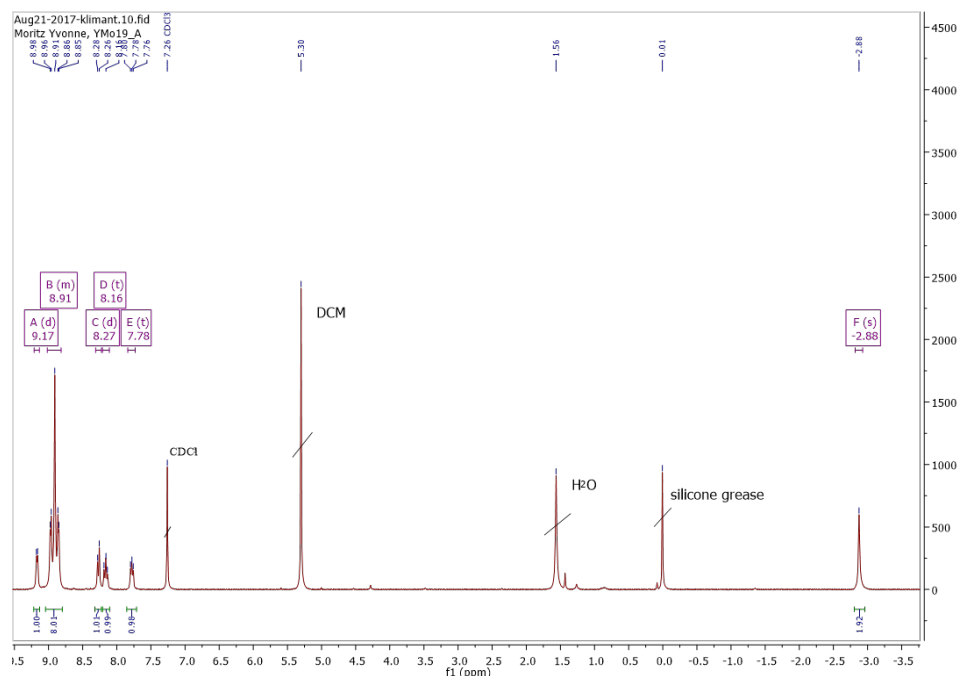
Figure S6.5: ^{1}H-NMR spectrum of 1 in $CDCl_3$.

Pd(II) 5,10,15-tris(pentafluorophenyl)-20-(pyridin-2-yl)porphyrin (2)
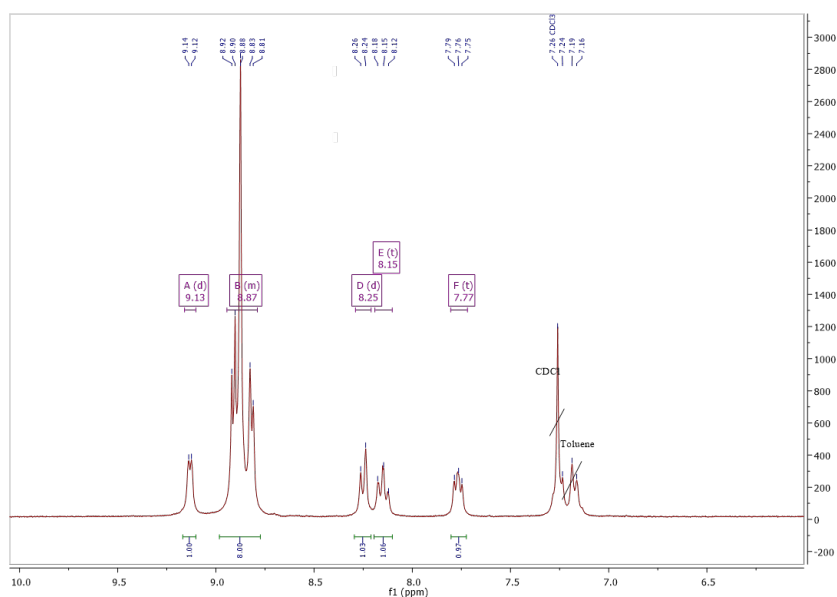
Figure S6.6: ^{1}H-NMR spectrum of 2 in CDCl$_3$.

Cyclometalated Pd(II)
5,10,15-tris(pentafluorophenyl)-20-(pyridin-2-yl)porphyrin – Cym1
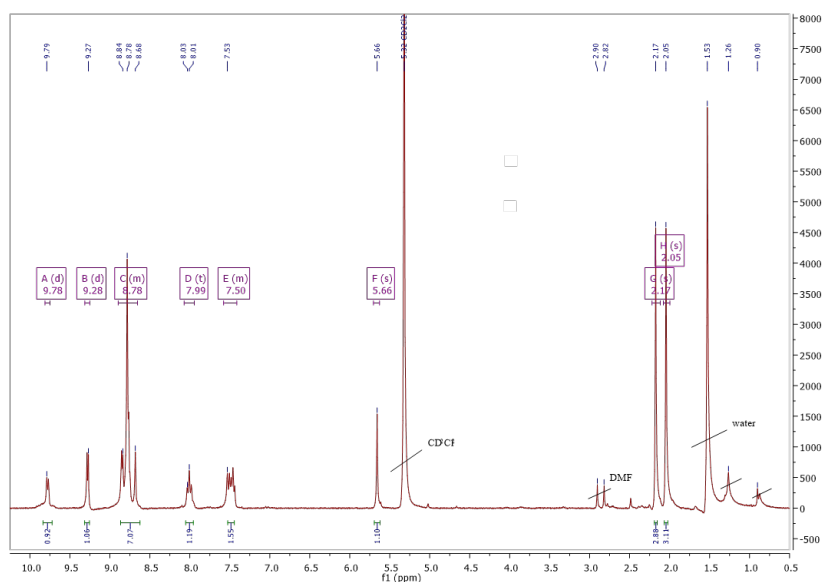
Figure S6.7: ^{1}H-NMR spectrum of Cym1 in CD$_2$Cl$_2$.
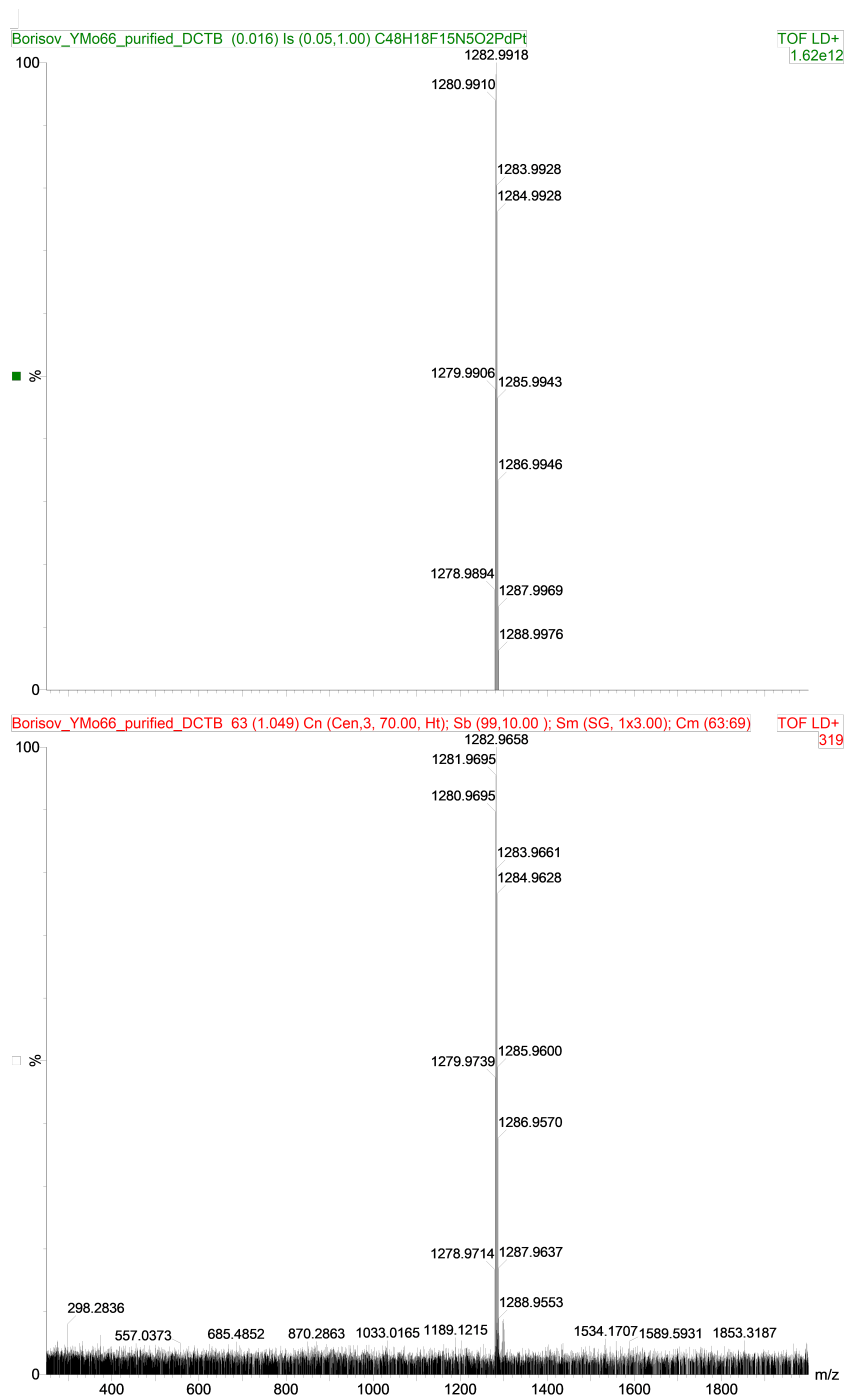
Figure S6.8: MS spectrum (MALDI) of Cym1.
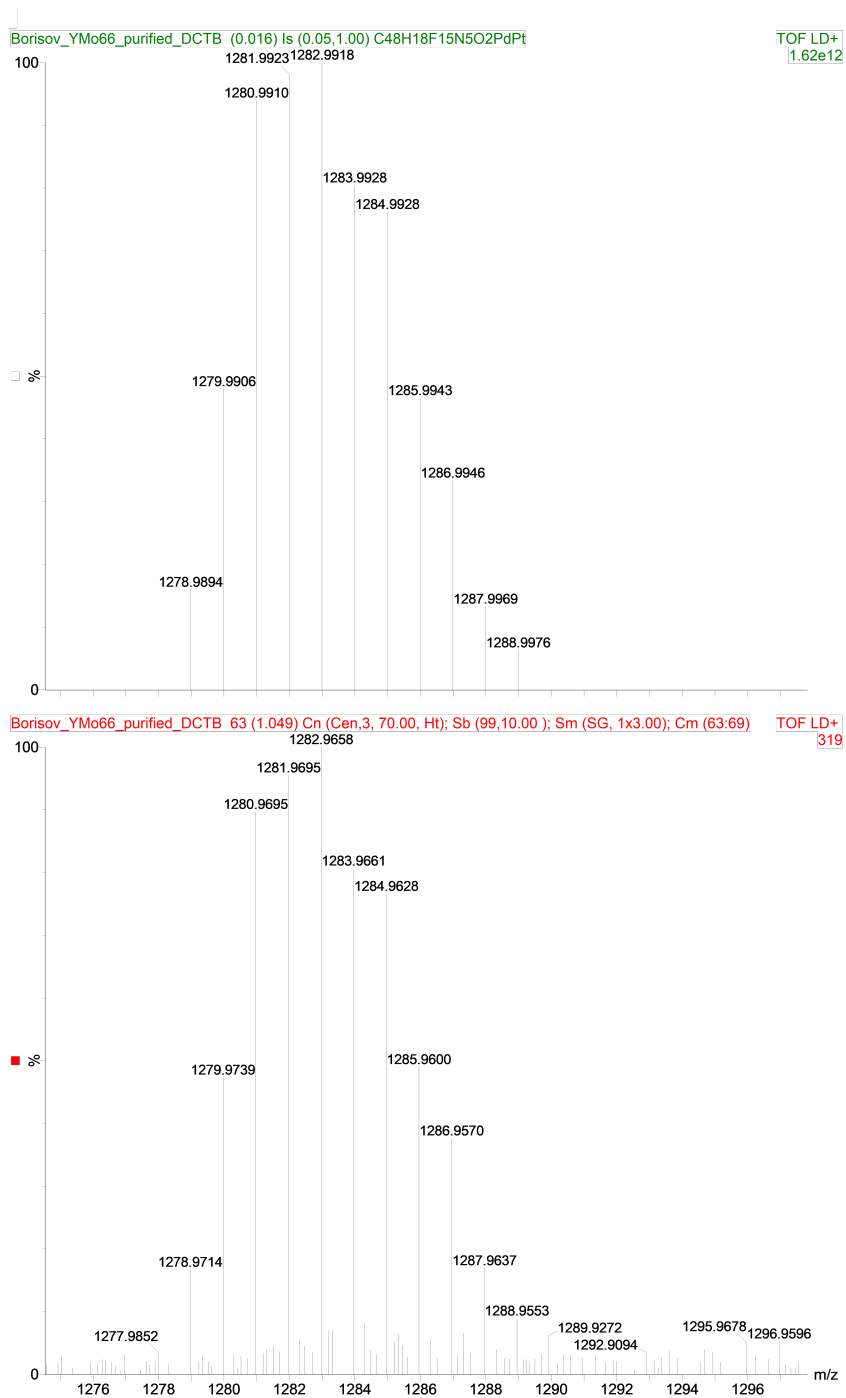
Figure S6.9: Isotope pattern from the MS spectrum of Cym1.

Pd(II) 5,10,15-triphenyl-20-(4-(pyridin-2-yl)phenyl)porphyrin (3)
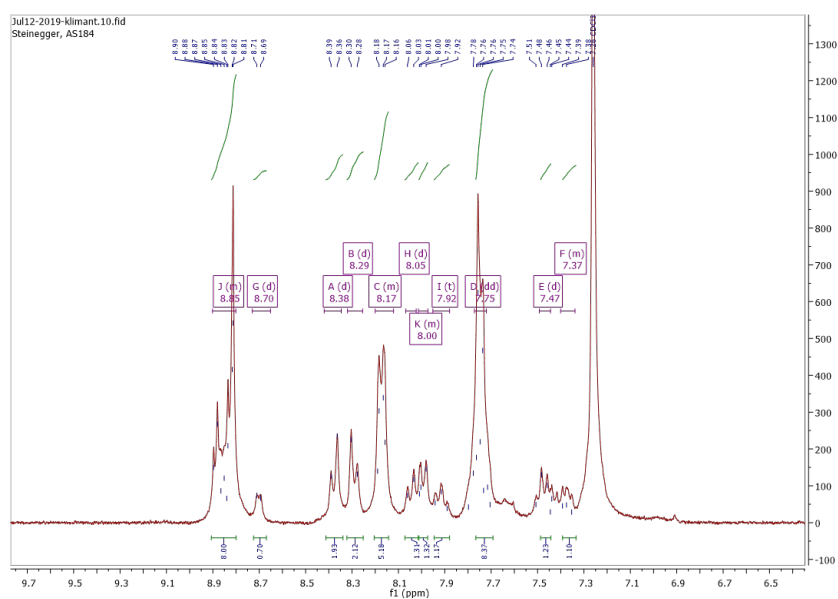
Figure S6.10: ^{1}H-NMR spectrum of 3 in CDCl$_3$.
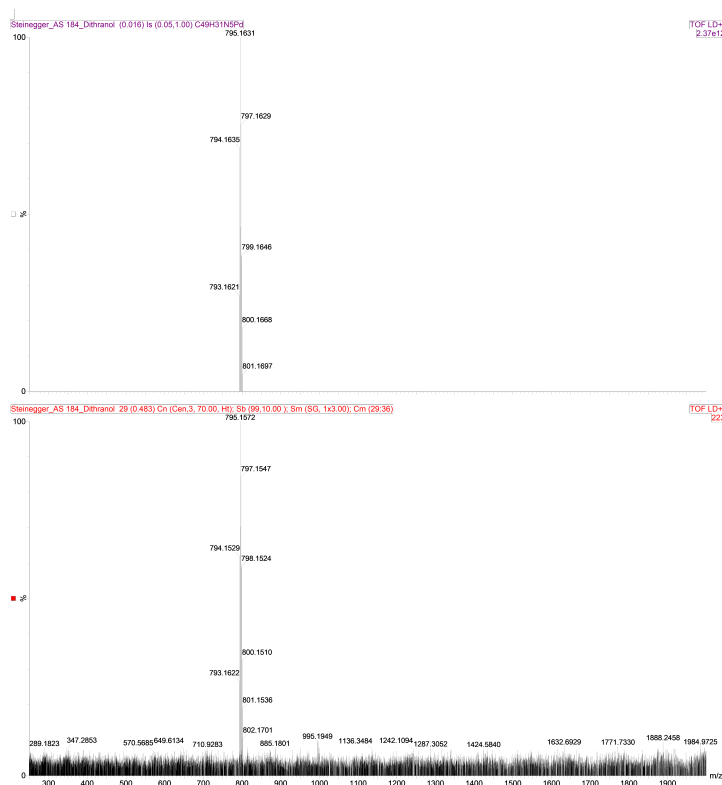
Figure S6.11: MS spectrum (MALDI) of 3.
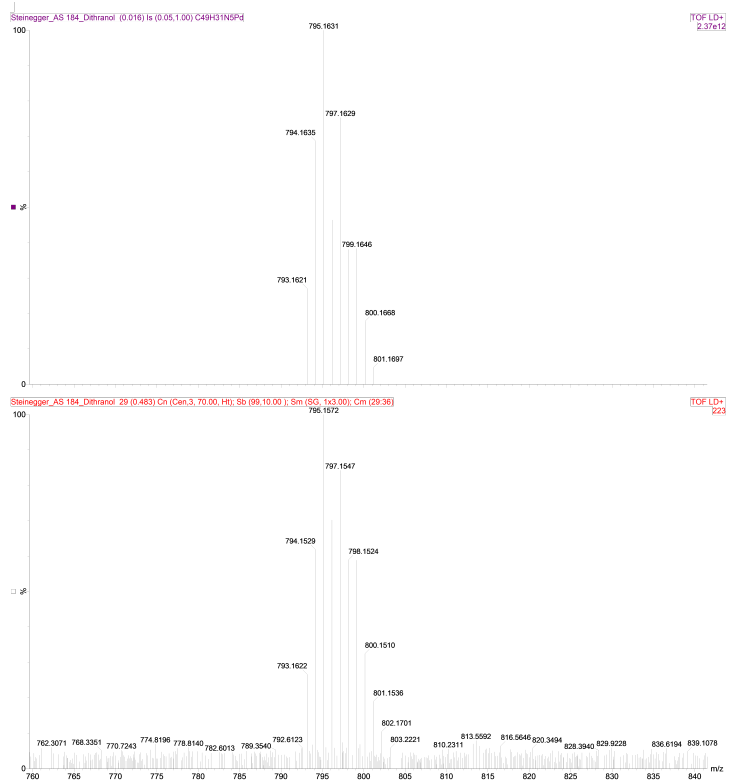
Figure S6.12: Isotope pattern from the MS spectrum of 3.

Cyclometalated Pd(II) 5,10,15-triphenyl-20-(4-(pyridin-2-yl)phenyl)porphyrin – Cym2
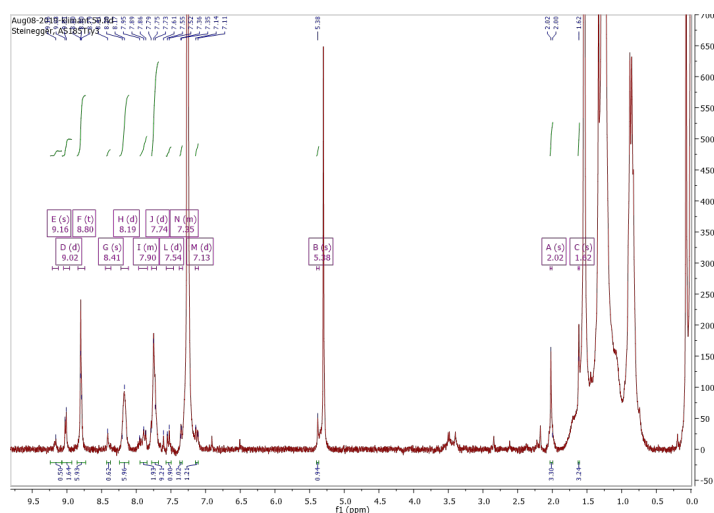
Figure S6.13: ^{1}H-NMR spectrum of Cym2 in CD$_2$Cl$_2$.
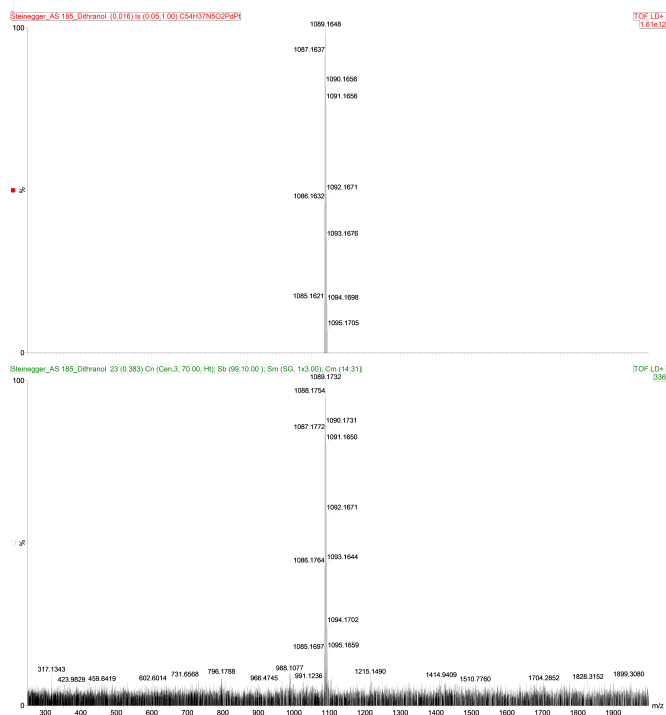
Figure S6.14: MS spectrum (MALDI) of Cym2.
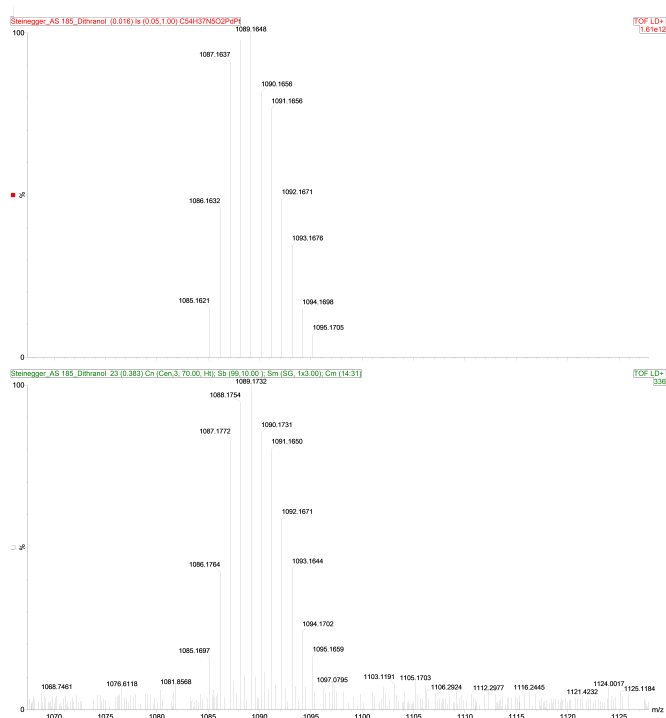
Figure S6.15: Isotope pattern from the MS spectrum of Cym2.

Zn(II) 5-(4-bromophenyl)-10,15,20-tri(4-tert-butylphenyl)-tetrabenzoporhyrin (4)

Figure S6.16: ^{1}H-NMR spectrum of 4 in CD_2Cl_2.

Pd(II) 5-(4-bromophenyl)-10,15,20-tri(4-tert-butylphenyl)-tetrabenzoporhyrin (6)

Figure S6.17: ^{1}H-NMR spectrum of 6 in CD_2Cl_2.

Pd(II)

5-(4-(pyridine-2-yl)-phenyl)-10,15,20-tri(4-tert-butylphenyl)-tetrabenzoporhyrin (7)
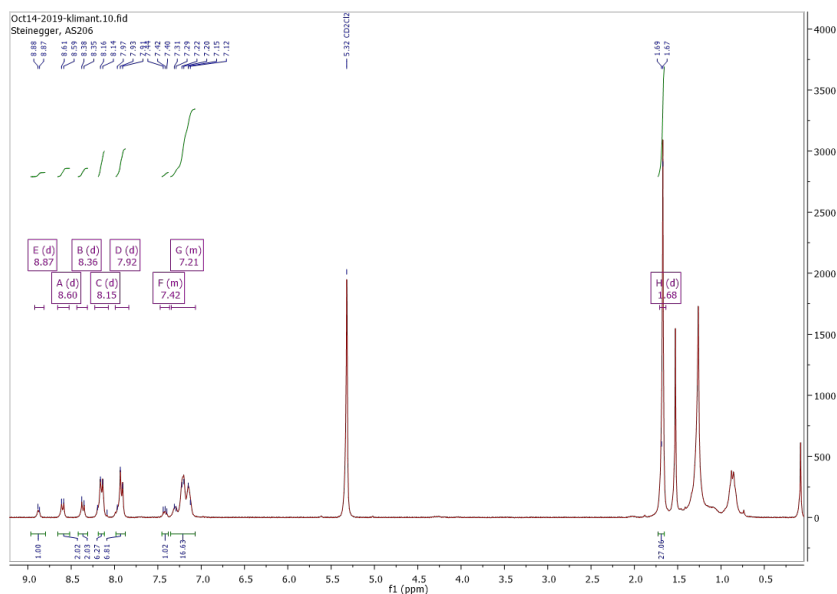
Figure S6.18: ^{1}H-NMR spectrum of 7 in CD_2Cl_2.
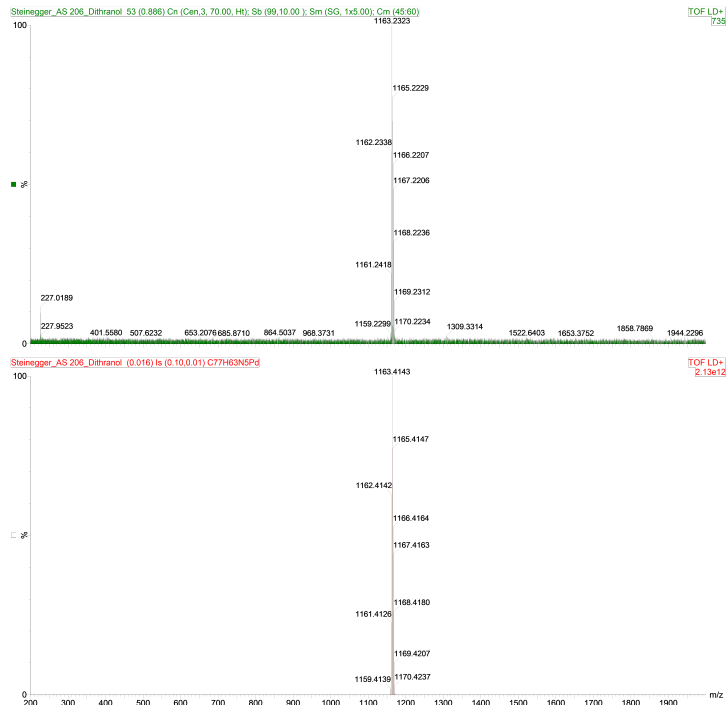
Figure S6.19: MS spectrum (MALDI) of 7.

Figure S6.20: Isotope pattern from the MS spectrum of 9.

Cyclometalated Pd(II)
5-(4-(pyridine-2-yl)-phenyl)-10,15,20-tri(4-tert-butylphenyl)-tetrabenzoporhyrin – Cym3

Figure S6.21: ^{1}H-NMR spectrum of Cym3 in CD_2Cl_2.
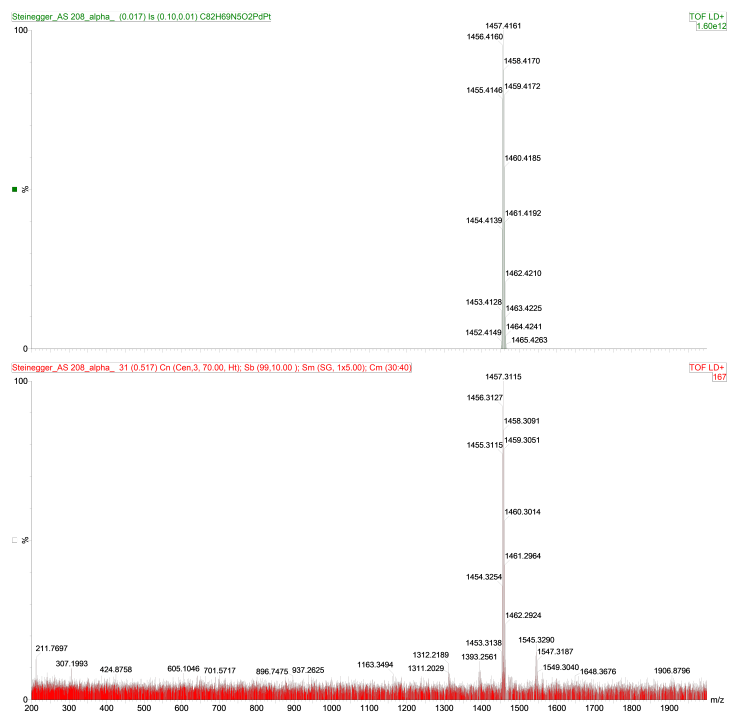
Figure S6.22: MS spectrum (MALDI) of Cym3.
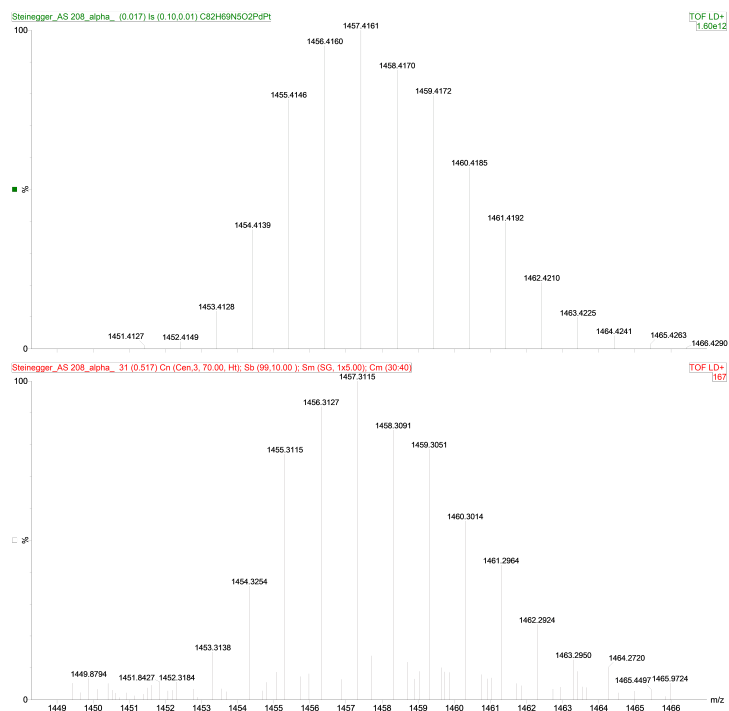
Figure S6.23: Isotope pattern from the MS spectrum of Cym3.

7 Cyclometalation of Naphthalimides

As elaborated in chapter 6, methods to control the photophysical properties are interesting for all dye classes that are intended for application. In general, there are properties that are especially desirable to control. Among these are emissive lifetimes and position of absorption and emission, and consequentially, the Stokes shift.

Cyclometalation was found to produce efficiently phosphorescent Pt(II) and Ir(III) complexes. The heavy atoms Pt and Ir introduce strong spin-orbit coupling that enables intersystem crossing. Efficient intersystem crossing can introduce or enhance phosphorescence. 2-Phenylpyridine structures are known to readily react in cyclometalation reactions and therefore are often introduced in the synthetic pathway to cyclometalated complexes.

Naphthalimides and rylene dyes are prominent fluorescent dyes with diverse application.[292–295] The dyes are structurally closely related and therefore share a similar chemistry. Typically, modification can be achieved via substitution in imide or core position. Introduction of phosphorescence via cyclometalation would drastically prolong the emissive lifetimes and also bathochromically shift the emission. Consequentially, the idea was to investigate the cyclometalation of 1,8-naphthalimide dyes with regard to extend the chemistry to rylene dyes. Especially, substitution with structures for cyclometalation in imide position would be accessible for all rylene dyes.

In literature, naphthalimides were already cyclometalated in the periphery via linker units,[67] but the motif for cyclometalation was not introduced directly at the core or in imide position. In this chapter, the synthesis and properties of these structures are presented.

7.1 Properties of Naphthalimides and Rylene Dyes
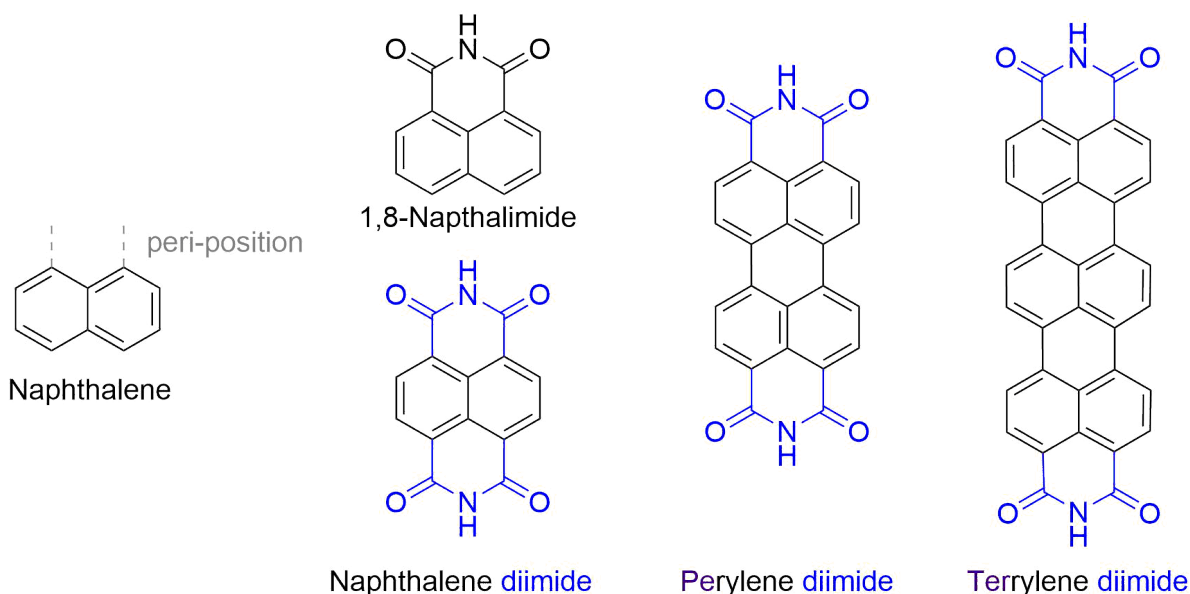
Figure 7.1: Chemical structures of naphthalene and rylene (di)imide dyes and its relation to naphthalene.

A variety of dyes are based on naphthalene as building block (Figure 7.1). Introduction of an imide function in *peri*-position (or 1,8-position) gives 1,8-naphthalimide. Imide substitution in *peri*-position on both sides results in naphthalene diimides. π-extension of the aromatic core with naphthalene building blocks attached in *peri*-position gives Pe**rylene** and Ter**rylene** diimide dyes. The π-extended analouges make up the class of rylene dyes. These rylene dyes are characterized by high molar absorption coefficient, high quantum yields, high photo- and chemical stability. The dyes found application as fluorophores,[292] pigments,[293] optoelectronic devices (organic solar cells,[292,294] organic field-effect transistors,[292,294] light emitting diodes[295]) and photocatalysis.[292]

Substituted 1,8-naphthalimides are prominent dyes that have been commonly used as chromophores for PET-based indicator dyes. They allow simple introduction of the PET group either in imide position or via core substitution. The efficiency of PET varies significantly between the two positions.[39,296] 1,8-Naphthalimides display comparably low brightness due to only moderate molar absorption coefficients (15 000 $M^{-1}cm^{-1}$), even though their quantum yields are close to unity in organic solvents.[39,297] Absorption and emission spectra can be bathochromically shifted by substitution with electron donating amino-groups in 4-position.

7.2 Experimental

7.2.1 6-Bromo-2-(2,6-diisopropylphenyl)-1*H*-benzo[*de*]isoquinoline-1,3(2*H*)-dione - 1

Procedure analogously to: Yu, J.; Gao, Y.; Jiang, S.; Sun, F. Naphthalimide Aryl Sulfide Derivative Norrish Type I Photoinitiators with Excellent Stability to Sunlight under Near-UV LED. *Macromolecules* **2019**, *52*, Publisher: American Chemical Society, 1707–1717.

A solution of 961.7 mg (2.5 mmol, 1 eq) 4-bromo-1,8-naphthalic anhydride and 13.61 mL (72.16 mmol, 29 eq) 2,6 diisopropylaniline in acetic acid (143 mL) was stirred at 110 °C for 18 h. Then the solvent was removed under reduced pressure. The crude product was purified via column chromatography (silica gel, CH+EE = 17+1, v+v) and recrystallization from CH.

Yield: 292 mg (30 %), colourless solid.

MS APCI: m/z: $[M + H]^+$ calc.: 436.35, found: 436

^{1}H NMR shifts (300 MHz, CDCl$_3$) δ 8.73 (d, J = 7.3 Hz, 1H), 8.67 (d, J = 8.6 Hz, 1H), 8.49 (d, J = 7.8 Hz, 1H), 8.10 (d, J = 7.6 Hz, 1H), 7.91 (t, J = 7.9 Hz, 1H), 7.47 (d, J = 7.7 Hz, 1H), 7.33 (d, J = 7.7 Hz, 2H), 2.71 (p, J = 6.8 Hz, 2H), 1.15 (d, J = 6.8 Hz, 12H) ppm.

^{13}C NMR shifts (76 MHz, CDCl$_3$) δ 145.76, 133.74, 132.72, 131.89, 131.34, 131.07, 130.79, 129.77, 128.34, 124.21, 123.32, 122.44, 29.32, 24.11 ppm.

7.2.2 2-(2,6-diisopropylphenyl)-6-(4-(pyridin-2-yl)phenyl)- 1*H* -benzo[*de*]isoquinoline- 1,3(2*H*)-dione - N1

Procedure analogously to: Kumar, M.; Kumar, N.; Bhalla, V.; Singh, H.; Sharma, P. R.; Kaur, T. Naphthalimide Appended Rhodamine Derivative: Through Bond Energy Transfer for Sensing of Hg2+ Ions. *Organic Letters* **2011**, *13*, Publisher: American Chemical Society, 1422–1425.

467.4 mg (1.07 mmol) of **1**, 213.5 mg (759.4 µmol, 0.71 eq) of 4-(2-Pyridyl)phenylboronic acid pinacol ester and 294.2 mg (2.13 mmol, 2 eq) of K$_2$CO$_3$ were dissolved in a mixture of dioxane (5.3 ml) and water (1.3 mL). The reaction mixture was refluxed at 100 °C for 25 h under argon atmosphere. Dioxane was removed under reduced pressure. Water (10 mL) was added to the residue and then the product was extracted with DCM (3 x 20 mL). The organic layer was dried over Na$_2$SO$_4$. The product was then purified via column chromatography (silica gel, CH+EA = 4+1, v+v) and recrystallization from CH.

Yield: 226 mg (58 %), yellow solid.

MS APCI: m/z: $[M + H]^+$ calc.: 510.64, found: 511.3

^{1}H NMR shifts (300 MHz, CDCl$_3$) δ 8.82 – 8.65 (m, 3H), 8.41 (d, J = 8.5 Hz, 1H), 8.22 (d, J = 7.9 Hz, 2H), 7.90 – 7.73 (m, 4H), 7.67 (d, J = 8.0 Hz, 2H), 7.53 – 7.44 (m, 1H), 7.38 – 7.28 (m, 3H), 2.79 (hept, J = 6.6 Hz, 2H), 1.24 – 1.08 (m, 12H) ppm.

^{13}C NMR shifts (76 MHz, CDCl$_3$) δ 164.47, 164.25, 156.81, 150.09, 146.89, 145.83, 139.87, 139.52, 137.10, 133.03, 131.92, 131.48, 131.03, 130.50, 129.65, 129.52, 128.03, 127.43, 127.17, 124.17, 123.12, 122.72, 122.10, 120.81, 29.33, 24.14 ppm.

7.2.3 Cyclometalated 2-(2,6-diisopropylphenyl)-6-(4-(pyridin-2-yl)phenyl)-1*H*-benzo[*de*]isoquinoline-1,3(2*H*)-dione - N1-Cym

Procedure analogously to: Wu, W.; Wu, W.; Ji, S.; Guo, H.; Song, P.; Han, K.; Chi, L.; Shao, J.; Zhao, J. Tuning the emission properties of cyclometalated platinum(II) complexes by intramolecular electron-sink/arylethynylated ligands and its application for enhanced luminescent oxygen sensing. *Journal of Materials Chemistry* **2010**, *20*, 9775.

93 mg (182.13 µmol, 1.9 eq) of compound N1 and 39.9 mg (96.1 µmol, 1 eq) of K$_2$PtCl$_4$ were added to a mixture of 2-ethoxyethanol (3 mL) and water (0.7 mL). The reaction mixture was stirred at 80 °C under argon atmosphere for 22 h. Water (7 mL) was added to the residue and after centrifugation, the red precipitate was collected. 5 ml ethoxyethanol, 110 mg Na$_2$CO$_3$ (1.04 mmol, 11.4 eq.) and 30 µl acetylacetone (294 µmol, 3 eq) were added to the precipitate. The reaction mixture was then stirred at 100 °C for 20 h. Water (10 mL) was added to the reaction mixture and the product was extracted with DCM (3 x 20 mL).The organic layer was dried over Na$_2$SO$_4$. The product was then purified via column chromatography (silica gel, DCM+CH = 2+1, v+v) and precipitation (dissolved in DCM, precipitated from a mixture of H$_2$O+MeOH = 1+9, v+v).

Yield: 38 mg (26.9 %) yellow solid.

MALDI TOF: m/z: $[M^+]$ calc.: 804.24, found: 804.15.

^{1}H NMR shifts (300 MHz, CD$_2$Cl$_2$) δ 9.15 – 8.98 (m, 1H), 8.68 (dd, J = 9.2, 7.1 Hz, 2H), 8.52 (d, J = 8.5 Hz, 1H), 8.02 – 7.84 (m, 2H), 7.85 – 7.71 (m, 3H), 7.67 (d, J = 7.9 Hz, 1H), 7.51 (t, J = 7.7 Hz, 1H), 7.35 (d, J = 7.7 Hz, 2H), 7.32 – 7.18 (m, 2H), 5.51 (s, 1H), 2.77 (h, J = 6.9 Hz, 2H), 2.03 (s, 3H), 1.88 (s, 3H), 1.19 – 1.04 (m, 12H) ppm.

^{13}C NMR shifts (76 MHz, CD$_2$Cl$_2$) δ 186.64, 184.64, 164.93, 164.73, 148.66, 147.89, 146.55, 139.98, 139.71, 139.02, 133.90, 132.04, 131.89, 131.57, 130.83, 129.70, 128.20, 125.74, 124.40, 123.24, 122.36, 121.95, 119.32, 29.52, 28.41, 27.26, 24.11 ppm.

7.2.4 6-(bis(2-ethylhexyl)amino)-1H,3H-benzo[de]isochromene-1,3-dione - 2

A 10 mL Schlenk tube was charged with 500 mg (1.8 mmol, 1 eq) of 6-bromo-1H,3H-benzo[de]isochromene-1,3-dione, 1.09g (4.5 mmol, 2.5 eq) of bis(2-ethylhexyl)amine, 23 mg (90 µmol, 0.05eq) of copper(II) sulfate pentahydrate and 5 mL of DMF. The reaction mixture was stirred at 160°C for 16 h. Then the reaction mixture was allowed to cool down to room temperature and water (15 mL) was added. The product was extracted with DCM (35 mL). The organic layer was washed with water (2x50 mL) and then dried over Na$_2$SO$_4$. The solvent was removed under reduced pressure. The product was purified via flash column chromatography (silica gel, gradient CH+EE=15+1 to CH+EE=10+1).

Yield: 203 mg (26 %), orange oil that crystallized upon longer storage. ^{1}H NMR (300 MHz, CDCl$_3$) δ 8.56 (d, J = 7.2 Hz, 1H), 8.42 (t, J = 8.5 Hz, 2H), 7.65 (t, J = 7.9 Hz, 1H), 7.17 (d, J = 8.4 Hz, 1H), 3.42 (d, J = 7.1 Hz, 4H), 1.78 (p, J = 6.0 Hz, 2H), 1.17 (q, J = 10.9, 8.4 Hz, 12H), 0.77 (d, J = 7.7 Hz, 9H). ^{13} NMR (76 MHz, CDCl$_3$) δ 161.88, 160.84, 158.11, 134.60, 133.35, 132.79, 126.05, 124.92, 119.60, 116.29, 109.11, 57.27, 37.59, 30.90, 28.59, 24.19, 23.16, 14.14, 10.55.

7.2.5 6-(bis(2-ethylhexyl)amino)-2-(4-(pyridin-2-yl)phenyl)-1H-benzo[de]isoquinoline-1,3(2H)-dione - N2

A 10 mL Schlenk tube was charged with 50 mg (114 µmol, 1 eq) of 2, 22 mg (126 µmol, 1.1 eq) of 4-(2-pyridiyl)aniline and 2 mL acetic acid under Ar counterflow. The reaction mixture was stirred at 130°C. After 24 h, 1 eq of 4-(2-pyridiyl)aniline was added and further stirred at 130°C. After another 24 h, the solvent was removed under reduced pressure and washed with water (3 x 15 mL). The product was purified via flash column chromatography (silica gel, CH+EE = 4+1, v+v).

Yield: 17 mg (25 %), yellow solid.

^{1}H NMR (300 MHz, CDCl$_3$) δ 8.73 (d, J = 4.8 Hz, 1H), 8.62 (d, J = 7.2 Hz, 1H), 8.50 (d, J = 8.2 Hz, 1H), 8.44 (d, J = 8.6 Hz, 1H), 8.17 (d, J = 8.1 Hz, 2H), 7.78 (d, J = 5.1 Hz, 2H),

7.66 (t, J = 7.8 Hz, 1H), 7.43 (d, J = 8.1 Hz, 2H), 7.22 (d, J = 9.1 Hz, 2H), 3.40 (d, J = 7.1 Hz, 4H), 1.78 (h, J = 5.9 Hz, 2H), 1.21 (m, 16H), 0.76 (m, 12H).

MS APCI: $[M + H]^+$ calc.: 590.37, found: 590.4

7.2.6 Cyclometalated 6-(bis(2-ethylhexyl)amino)-2-(4-(pyridin-2-yl)phenyl)-1*H*-benzo[*de*]isoquinoline-1,3(2*H*)-dione - N2-Cym

50 mg (85 µmol, 2 eq) of compound N2 and 18 mg (42 µmol, 1 eq) of K_2PtCl_4 were added to a mixture of 2-ethoxyethanol (6 mL) and water (2 mL). The reaction mixture was stirred at 80 °C under argon atmosphere for 20 h. Then water (10 mL) was added to the reaction mixture. The precipitate was collected via filtration and washed with water (2 x 10 mL). Subsequently, 2 mL of 2-ethoxyethanol, 13 µL (127 µmol, 3 eq) of acetylacetone and 45 mg (424 µmol, 10 eq) of Na_2CO_3 were added to the precipitate and stirred at 100°C for 24 h. Water (10 mL) was added to the reaction mixture and the product was extracted with DCM (3 x 20 mL). The organic layer was washed with brine (1 x 20 mL) and dried over Na_2SO_4. It was attempted to purify the product via column chromatography (silica gel, DCM+CH = 4+1, v+v). Side products and educt could be removed but the product slowly degraded during chromatography. NMR and MS indicated that the main fraction is product but degradation products could not be removed. MALDI TOF: m/z: $[M+H]^+$ calc.: 883.38, found: 883.47

7.3 Results
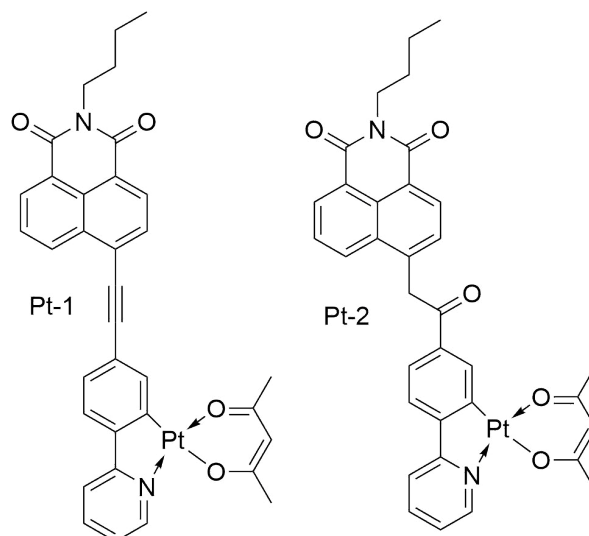
Figure 7.2: Chemical structures of literature known cyclometalated 1,8-naphthalimides.
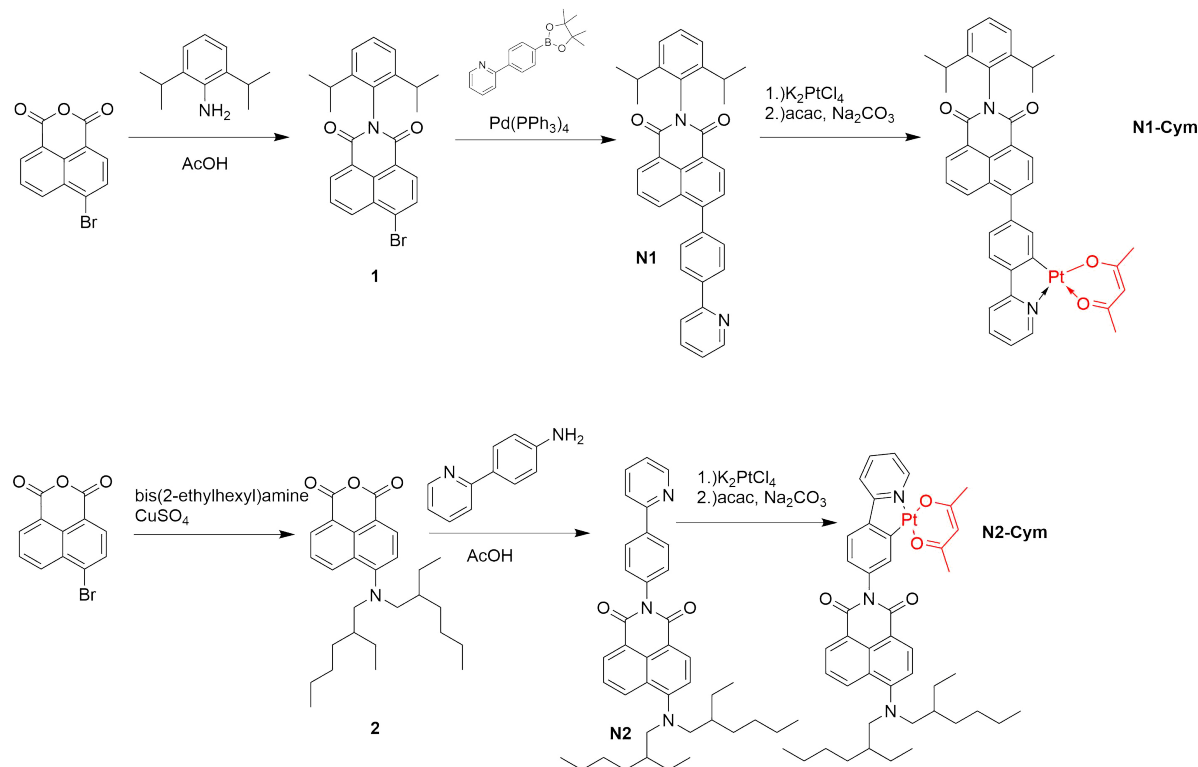
Figure 7.3: Reaction structures for the preparation of cyclometalated 1,8-naphthalimides.

In literature, 1,8-naphthalimides have been cyclometalated in 4-position via alkyne, or CH_2-C=O linker units(7.2).[67] These structures simultaneously display room temperature phosphorescence and fluorescence. However, cyclometalation was never reported at 4-position without a linker

group (Figure 7.3, N1-Cym) or in imide position (Figure 7.3, N2-Cym). Especially the substitution with structures for cyclometalation in imide position (N2-Cym) would be accessible for all rylene dyes. The idea was to investigate the cyclometalation of 1,8-naphthalimide dyes with regard to extend the chemistry to rylene dyes.

Synthesis of N1-Cym and N2-Cym was done analogously to literature known naphthalimide chemistry and standard cyclometalation procedures (Figure 7.3). For N1-Cym, the poor solubility was problematic for purification via column chromatography. N2-Cym could not be obtained in pure form, because it slowly decomposed during chromatography.

For both cyclometalated structures, the absorption spectra are hardly affected (Figures 7.4 and 7.5). A slight shoulder appears at 420 nm that can be attributed to a charge-transfer band for N1-Cym. Excitation remains efficient only in the UV (N1-Cym) to blue region (N2-Cym).

For N1-Cym, room temperature phosphorescence (λ_{max}, em=609 nm) is generated analogously to the reported structures (Table 7.1, Figure 7.4). In solution, the quantum yield of phosphorescence is moderate with 7 %, but is higher than for Pt-1 (0.06/1.1% (relative quantum yield, different standards)) and comparable to Pt-2 (0.38/18.2%).[67] However, fluorescence is absent. Incorporated into polystyrene, the phosphorescence quantum yield increases to 25 % for N1-Cym. Compared to literature, the phosphorescence decay time is longer (62 µs (N1-Cym) > 7(Pt-1)/26(Pt-2) µs).[67] The emission of N1-Cym lies between the emission peaks of the literature representatives with an alkyne linker unit Pt-1 (λ_{max}, em=640 nm)[67] and an CH$_2$-C=O linker unit Pt-2 (λ_{max}, em=540 nm).[67] This may be reasoned by the varying extent of additional π-conjugation.

Compound N2-Cym could not be obtained in completely pure form. The NMR spectrum contains the typical peaks for cyclometalated structures (acac ligand) and MS indicates that main fraction is product but the compound slowly degrades during chromatography. Unfortunately, cyclometalation of N2 had no interesting effects on the properties (Table 7.1, 7.5). It was hypothesized that this is due to the rotation of the substituent in imide position (c.f. section 7.4). This rotation may prevent phosphorescence by promoting radiationless deactivation processes compared to intersystem crossing.

The tedious and difficult purification of N1-Cym and N2-Cym, however, suggested not to extend the chemistry to rylene dyes as they suffer from even poorer solubility and itself are hard to purify. For N1-Cym, the solubility may be improved by alkyl substitution. This would make purification easier, yet, moderate phosphorescence quantum yield and UV excitation remain unattractive features for application.

Table 7.1: Summary of the photophysical properties of cyclometalated 1,8-naphthalimides compared to its precursors in toluene at 25 °C. F - Fluorescence; P - Phosphorescence

	abs$_{max}$ [nm]	em$_{max}$ [nm]	τ_0	QY [%]
N1	360	425	-	F 99
N1-Cym	366	609	62 μs	P 7
N2	426	498	-	F 81
N2-Cym	425	498	-	F 34
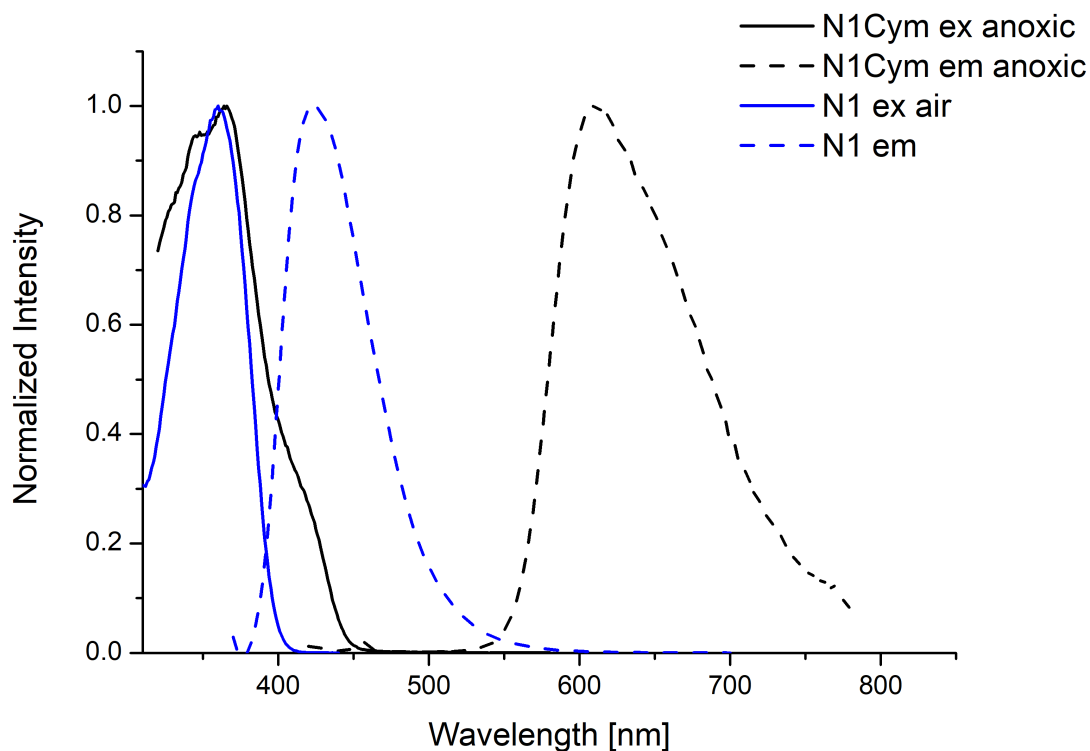
Figure 7.4: Normalized excitation and emission spectra of N1 and N1-Cym.
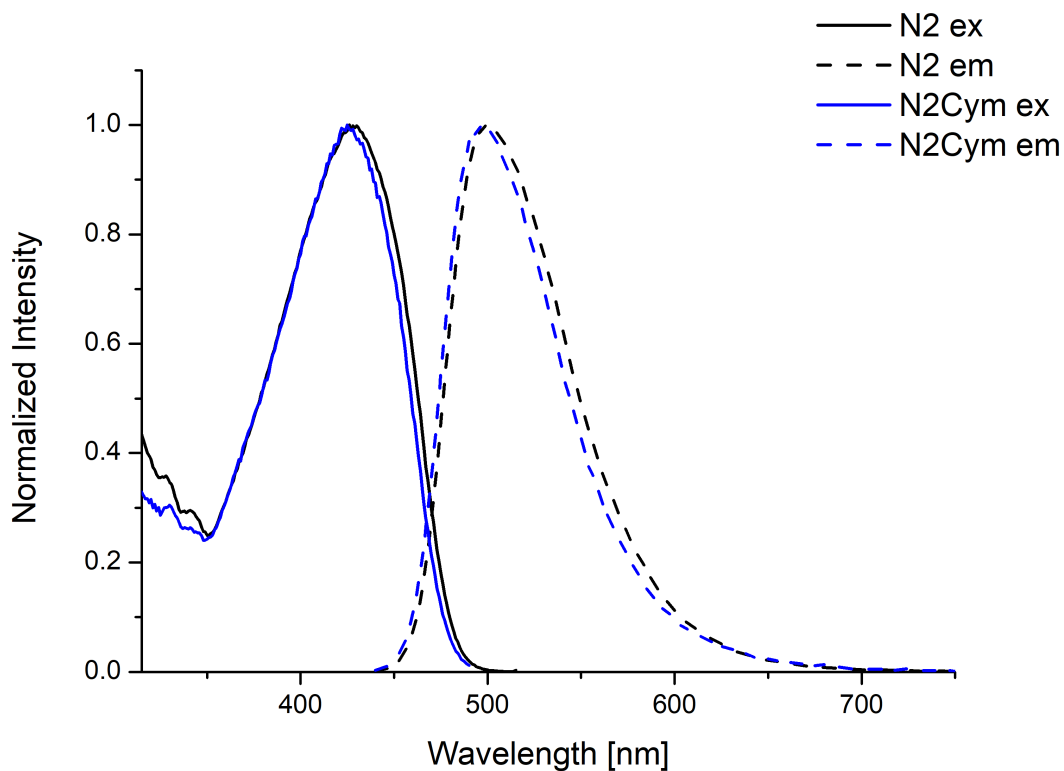
Figure 7.5: Normalized excitation and emission spectra of N2 and N2-Cym.

7.4 Unsuccessful Synthetic Route
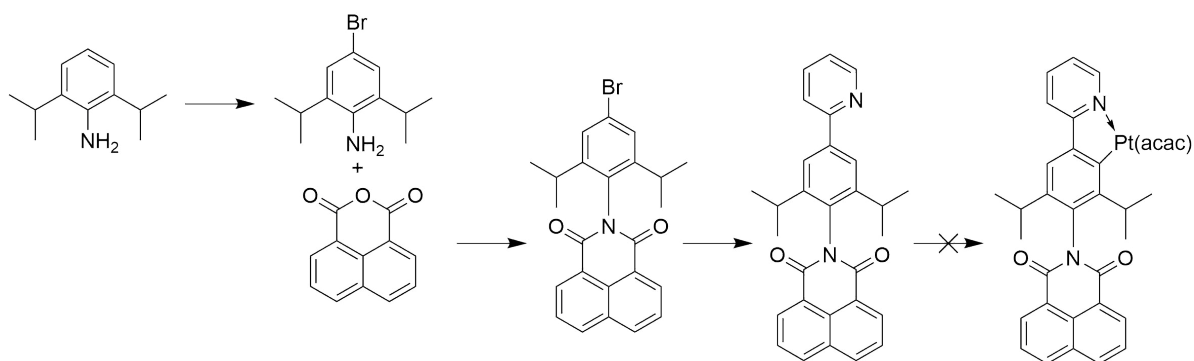
Figure 7.6: Reaction scheme for the preparation of another cyclometalated 1,8-naphthalimide.

The structure for cyclometalation in compound N2 is able to rotate around the C-N bond from the imide position to the phenyl group. It was hypothesized that this rotation prevents phosphorescence by promoting radiationless deactivation processes compared to intersystem crossing. Two isopropyl groups in ortho-position to the C-N bond should prevent rotation (Figure 7.6). However, no cyclometalated product could be isolated from reaction mixtures.

The reaction was abandoned.

7.5 NMR and MS spectra
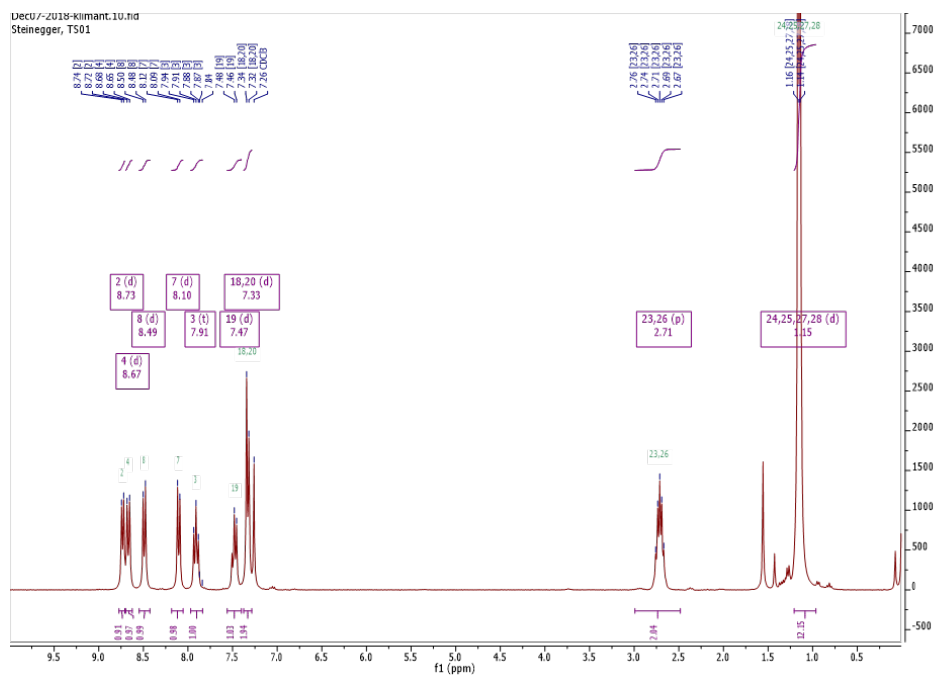
Figure 7.7: ^{1}H-NMR spectrum of 1 in CDCl$_3$.
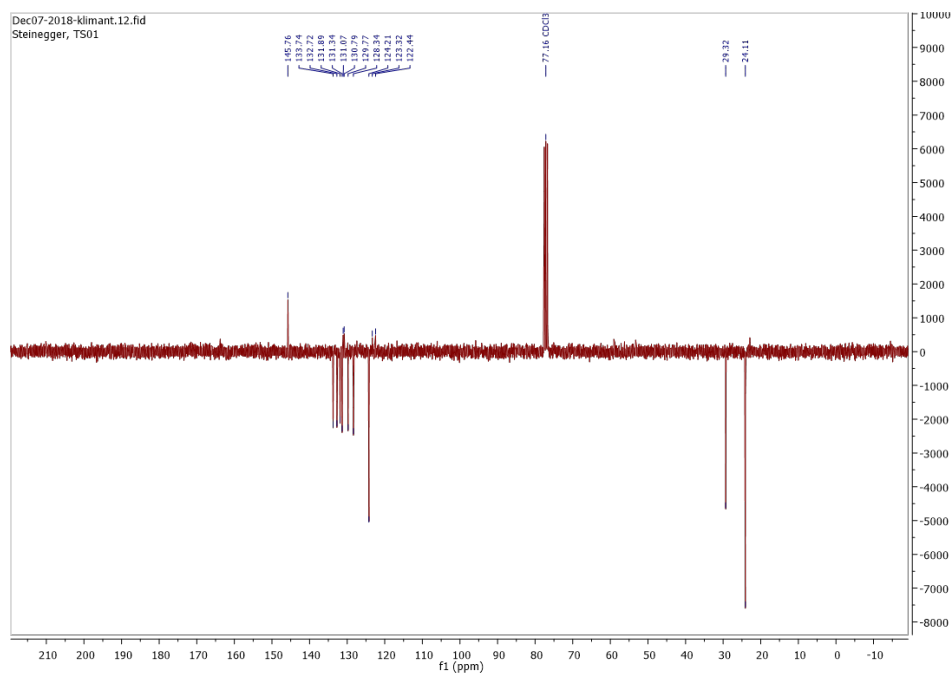
Figure 7.8: ^{13}C-NMR spectrum of 1 in CDCl$_3$.

Figure 7.9: ^{1}H-NMR spectrum of N1 in CDCl$_3$.

Figure 7.10: ^{13}C-NMR spectrum of N1 in CDCl$_3$.

Figure 7.11: ^{1}H-NMR spectrum of N1-Cym in CD_2Cl_2.

Figure 7.12: ^{13}C-NMR spectrum of N1-Cym in CD_2Cl_2.

New Indicators for Optical Sensing by Manipulating the Intersystem Crossing in Luminescent Dyes
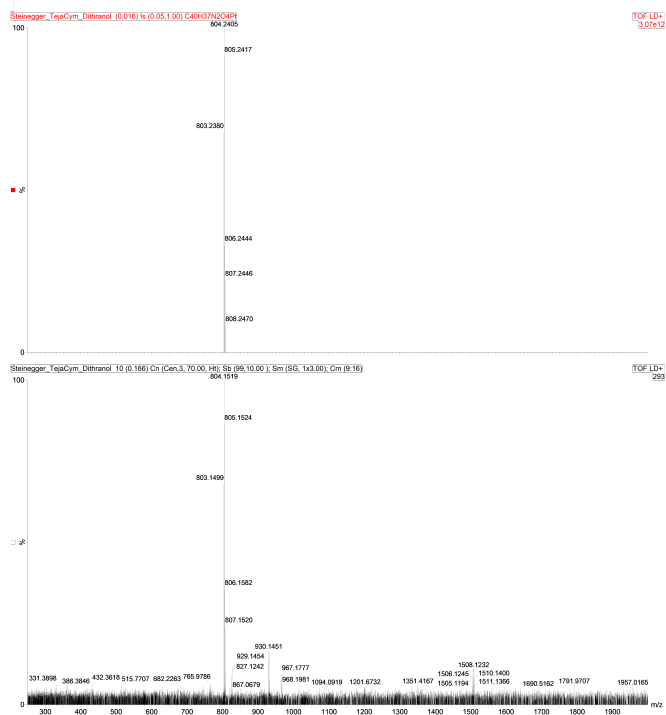
Figure 7.13: MS spectrum (MALDI) of N1-Cym.
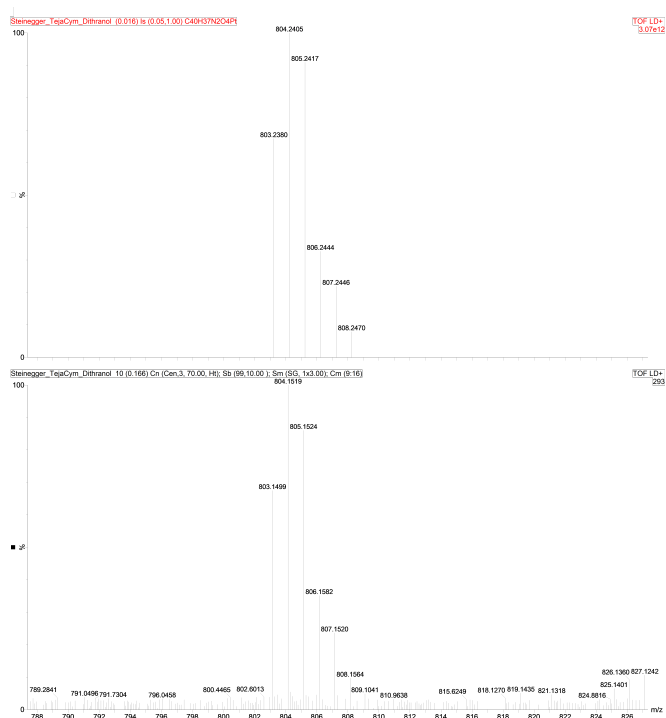
Figure 7.14: Isotope pattern from the MS spectrum of N1-Cym.
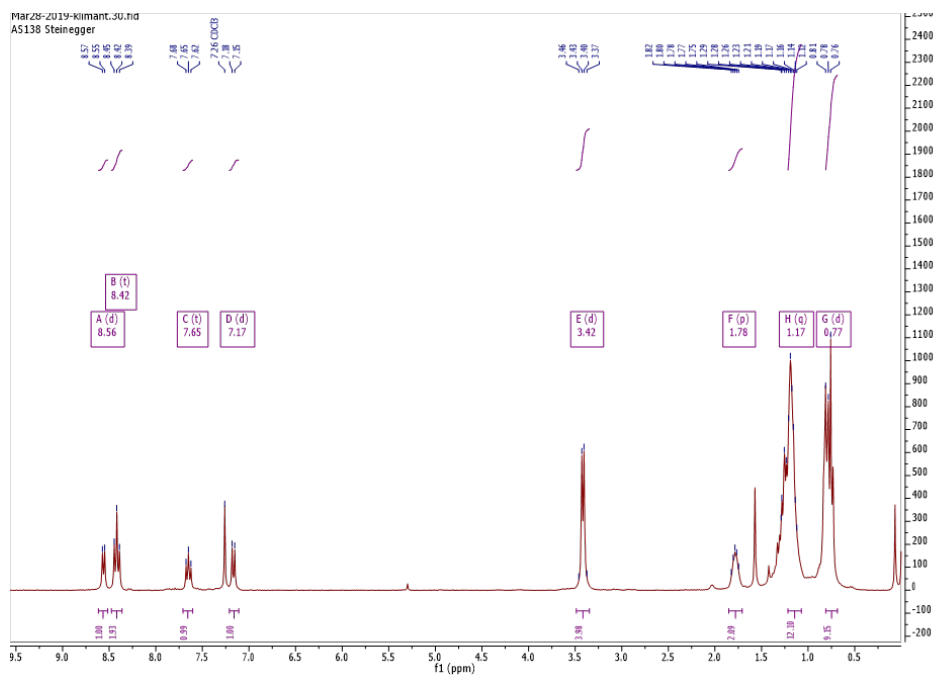
Figure 7.15: ^{1}H-NMR spectrum of 2 in CDCl$_3$.
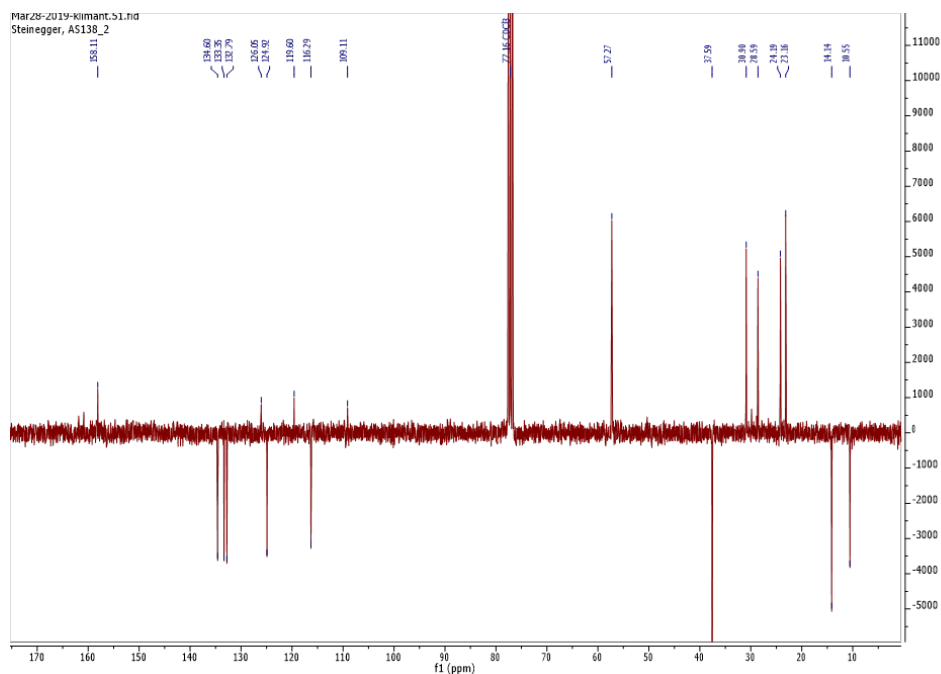
Figure 7.16: ^{13}C-NMR spectrum of 2 in CDCl$_3$.

New Indicators for Optical Sensing by Manipulating the Intersystem Crossing in
Luminescent Dyes
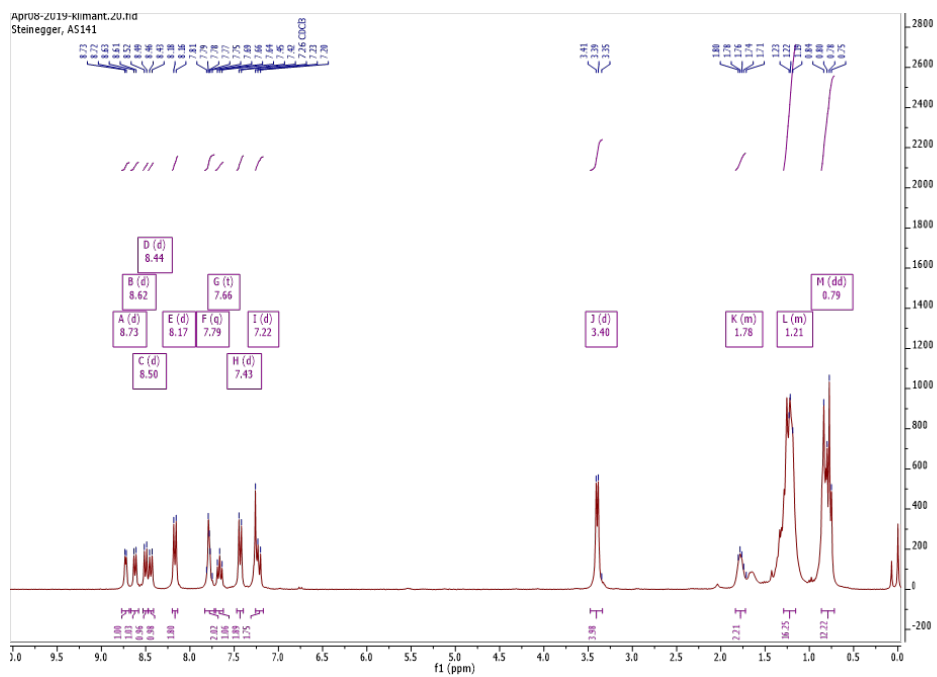
Figure 7.17: ^{1}H-NMR spectrum of N2 in CDCl$_3$.
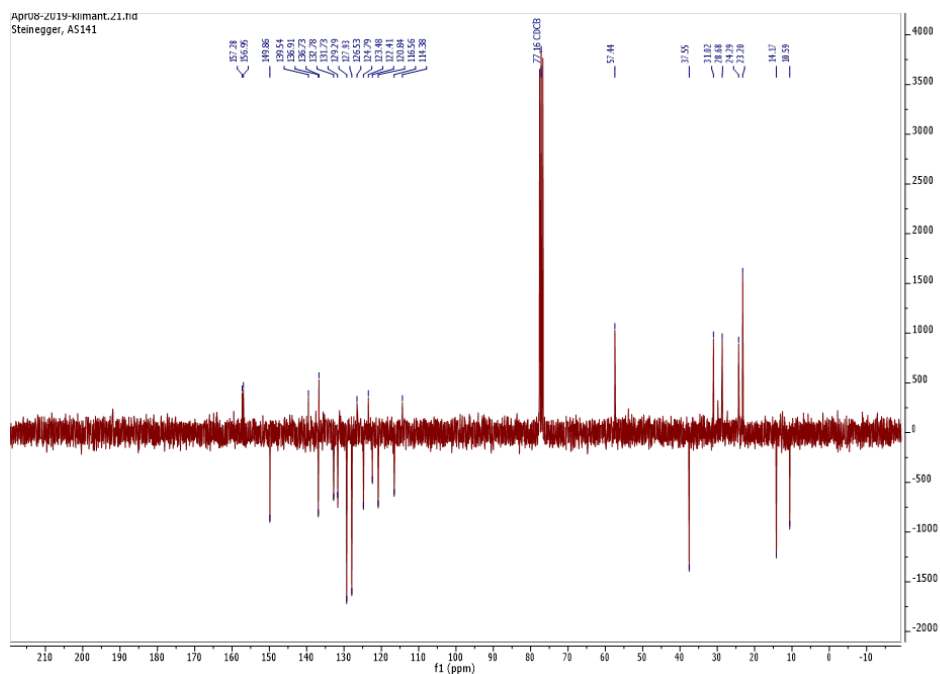
Figure 7.18: ^{13}C-NMR spectrum of N2 in CDCl$_3$.
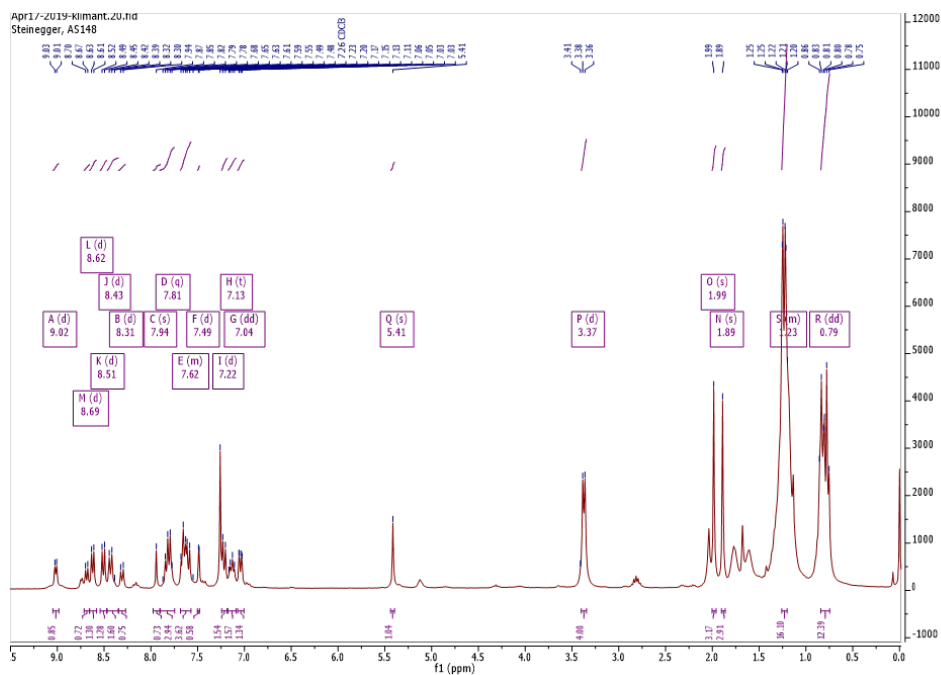
Figure 7.19: ^{1}H-NMR spectrum of N2-Cym in CDCl$_3$.
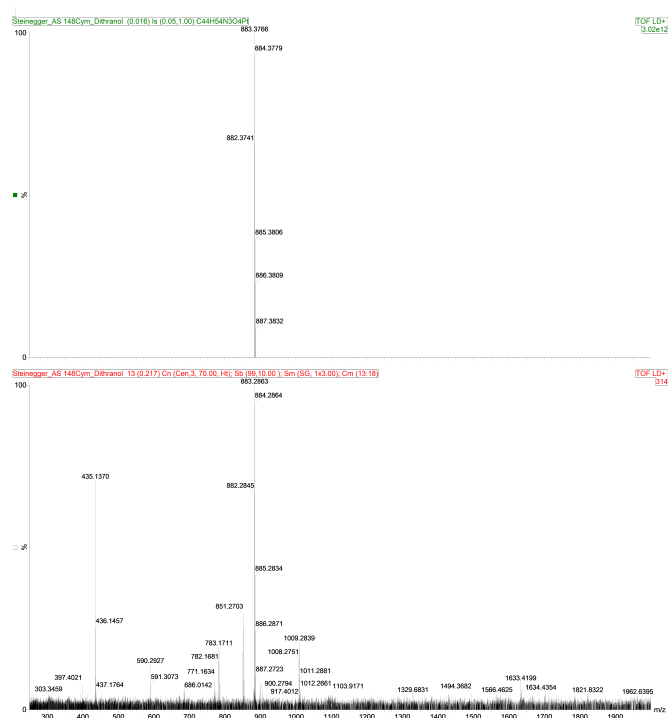
Figure 7.20: MS spectrum (MALDI) of N2-Cym.
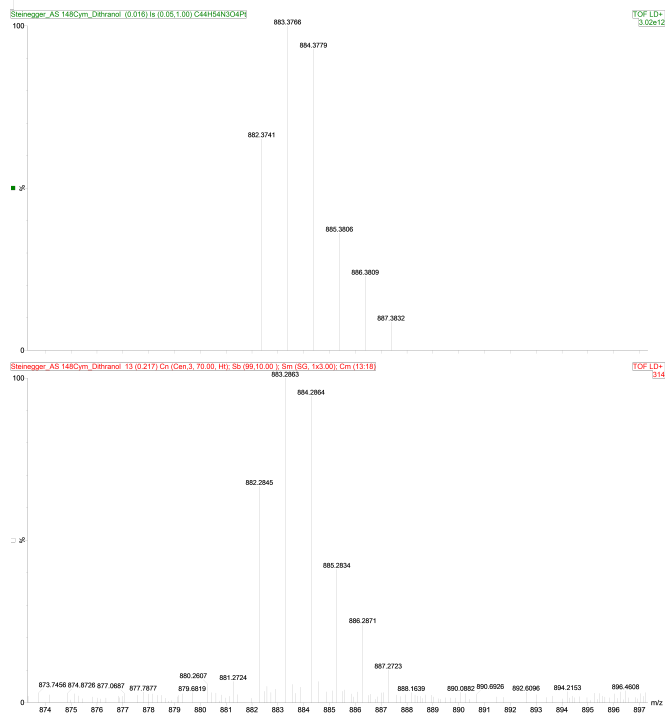
Figure 7.21: Isotope pattern from the MS spectrum of N2-Cym.

8 Summary and Conclusion

This thesis presents advances in optical luminescent sensing based on new materials and application of a new data processing method for dual sensing. Regarding the materials, this includes the synthesis, modification and application of a variety of dye classes (anthraquinones, dicyanobenzenes, Schiff bases, metallo(benzo)porphyrins) as temperature indicators and a simple method to eliminate oxygen cross-sensitivity for these sensing materials. A software algorithm, called dualSense and developed at the institute, was for the first time applied for evaluation and data processing of dual sensors. It enabled the simultaneous determination of oxygen and temperature using a single indicator and single-wavelength readout.

In chapter 3, two classes of TADF of emitters were investigated for their performance in optical oxygen and temperature sensing. The classes are carbazole-substituted dicyanobenzenes and anthraquinone based intramolecular charge-transfer dyes. Literature known representative and systematically modified derivatives were prepared and thoroughly characterized. These dyes show excellent tunability of photophysical properties and especially, the anthraquinone dyes display TADF lifetimes tunable over a broad range (11-583 µs in toluene). The temperature sensitivity of the TADF decay time was found to be in the range from -1.4 to -3.7% change of TADF lifetime per K. Oxygen cross-talk was minimized by immobilizing the dyes into virtually gas impermeable poly(vinylidene chloride-*co*-acrylonitrile). The sensing materials compare favorably to the most sensitive optical thermometers based on decay time changes reported in literature. The applicability in imaging applications for biology or medicine was demonstrated by incorporation into cell penetrating polymeric nanoparticles that display excellent temperature-sensitivity with only minor cross-talk to oxygen.

In chapter 4, highly sensitive materials for optical thermometry based on TADF-emitting Zn(II) Schiff base complexes are presented. These complexes are characterized by high molar absorption coefficients and high temperature sensitivity of TADF decay time exceeding 3.5%/K at 25 °C. Respective sensing materials allow self-referenced temperature measurement with a resolution better than 0.03 °C. Additionally, a new simple method to eliminate oxygen cross-sensitivity was applied to the sensing material based on the TADF-emitting Zn(II) Schiff. Oxygen cross-sensitivity is an inherent downside of most temperature indicators with long luminescence decay times. Here, oxygen cross-talk was completely eliminated by adding a layer of an oxygen-scavenging off-stoichiometry thiol-ene polymer combined with a gas barrier made of poly(vinylidene chloride-*co*-acrylonitrile). The oxygen-scavenging capabilities of the OSTE

layer were monitored for more than 60 days during storage under ambient air. The results demonstrate the suitability of the new sensor for long-term temperature monitoring.

In chapter 5, an alkylsulfone-substituted Zn(II)-*meso*-tetraphenyltetrabenzoporphyrin is presented as an indicator that allows simultaneous measurement of oxygen and temperature at a single wavelength. Despite poor quantum yield, the dye features good brightness due to exceptionally hight molar absorption coefficients. Additionally, the full emission peak/brightness of the indicator can be utilized due to the good separation of Soret-excitation and emission bands. The dual sensing is enabled by the simultaneous emission of prompt and delayed fluorescence. The prompt fluorescence acts as an intrinsic reference as it is neither significantly affected by oxygen nor temperature. Delayed fluorescence is differently affected by oxygen and temperature. Oxygen quenching decreases the decay time and intensity of delayed fluorescence. On the other hand, temperature decreases the decay time but increases the intensity. By using multifrequency phase fluorometry and sophisticated data processing, oxygen and temperature can measured with a single indicator using only a single wavelength readout.

Chapter 6 describes the effects of cyclometalation on three Pd(II) porphyrin structures. The porphyrins were modified with the 2-phenylpyridine or 2-pyridyl motif in meso-position to enable cyclometalation. The cyclometalated 2-phenylpyridine motif in meso-position affects the photophysical properties only in solution. In rigid matrices such as frozen glass or polystyrene, the differences between the cyclometalated dyes and the non-cyclometalated precursors disappear completly. Cyclometalation with the 2-pyridyl motive in meso-position drastically affects the photophysical properties. It results in a strong bathochromic shift and 20-fold decrease of the phosphorescence decay times, but unfortunately also in significant deterioration of the emission quantum yield. The dye, however, is a powerful sensitizer of singlet oxygen. The high singlet oxygen quantum yield together with excitation in the red part of the electromagnetic spectrum may be promising for application in photodynamic therapy. Additionally, the pentafluorophenyl substitution allows simple modification with (bio)molecules via click chemistry.

The short chapter 7 presents the photophysical properties of two cyclometalated 1,8-naphthalimide structures. The naphthalimides were modified with motifs for cyclometalation in 4-position and in imide position. The cyclometalation in 4-position of a directly connected 2-phenylpyridine unit generates room temperature phosphorescence. In contrast to literature known representatives, where the cyclometalation motif is connected via a linker-unit, no simultaneous fluorescence can be observed. The cyclometalation of a 2-phenylpyridine unit connected in imide position has no effect on the photophysical properties except for a decrease in quantum yield.

9 Curriculum Vitae

Personal Data

Name:	Andreas Steinegger, BSc MSc
Address:	Wartingergasse 15, 8010 Graz
Telephone:	+436603159328
E-Mail:	andr.steinegger@gmail.com
Nationality:	Austria
Date of Birth:	February 5th, 1992

Education

Feb 2017 - Dec 2020	**PhD student** in Technical Chemistry - Graz University of Technology
	PhD Thesis at the Institute of Analytical Chemistry and Food Chemistry
	Supervision: Ass. Prof. kand. Sergey Borisov
	"New Indicators for Optical Sensing by Manipulating the Intersystem Crossing in Luminescent Dyes"
Oct 2014- Dec 2016	**Master program** in Chemistry - Graz University of Technology
	Master's Thesis at the Institute of Analytical Chemistry and Food Chemistry
	Supervision: Ass. Prof. kand. Sergey Borisov
	"Thermally Activated Delayed Fluorescence Dyes as New Indicators for Optical Sensors"
	Master of Science (MSc) with distinction
Oct 2011 - Oct 2014	**Bachelor program** in Chemistry - Graz University of Technology
	Bachelor's Thesis at the Institute of Organic Chemistry
	Supervision: Prof. Rolf Breinbauer
	"Synthesis of building blocks for a modular synthesis of teraryl-based α-helix mimetics"
	Bachelor of Science (BSc) with distinction
Jun 2010	**Matura** – BG/BRG Leoben 1 (with distinction)

Scholarships

Jan 2015 **Merit-Based Scholarship** – Graz University of Technology

April 2017 **DOC Scholarship** - Austrian Academy of Sciences (ÖAW)

List of Publications in Peer Reviewed Journals

First Author

Steinegger, A.; Klimant, I.; Borisov, S. M. Purely Organic Dyes with Thermally Activated Delayed Fluorescence-A Versatile Class of Indicators for Optical Temperature Sensing. *Advanced Optical Materials* **2017**, 1700372

Steinegger, A.; Borisov, S. M. Zn(II) Schiff Bases: Bright TADF Emitters for Self-referenced Decay Time-Based Optical Temperature Sensing. *ACS Omega* **2020**, *5*, Publisher: American Chemical Society, 7729–7737

Zieger, S. E.; Steinegger, A.; Klimant, I.; Borisov, S. M. TADF-Emitting Zn(II)-Benzoporphyrin: An Indicator for Simultaneous Sensing of Oxygen and Temperature. *ACS Sensors* **2020**, *5*, Publisher: American Chemical Society, 1020–1027 - shared first authorship.

Steinegger, A.; Wolfbeis, O. S.; Borisov, S. M. Optical Sensors for pH Values: Spectroscopies, Materials, and Applications. *Chemical Reviews* - accepted

Co-Author

Weber, S.; Rath, T.; Fellner, K.; Fischer, R.; Resel, R.; Kunert, B.; Dimopoulos, T.; Steinegger, A.; Trimmel, G. Influence of the Iodide to Bromide Ratio on Crystallographic and Optoelectronic Properties of Rubidium Antimony Halide Perovskites. *ACS Applied Energy Materials* **2019**, *2*, Publisher: American Chemical Society, 539–547

Urstöger, G.; Simoes, M. G.; Steinegger, A.; Schennach, R.; Hirn, U. Evaluating the degree of molecular contact between cellulose fiber surfaces using FRET microscopy. *Cellulose* **2019**, *26*, 7037–7050

Urstöger, G.; Steinegger, A.; Schennach, R.; Hirn, U. Spectroscopic Investigation of DCCH and FTSC as a potential pair for Förster Resonance Energy Transfer in different solvents. *PLOS ONE* **2020**, *15*, Publisher: Public Library of Science, e0228543

10 References

(1) Xiong, X.; Song, F.; Wang, J.; Zhang, Y.; Xue, Y.; Sun, L.; Jiang, N.; Gao, P.; Tian, L.; Peng, X. Thermally Activated Delayed Fluorescence of Fluorescein Derivative for Time-Resolved and Confocal Fluorescence Imaging. *Journal of the American Chemical Society* **2014**, *136*, 9590–9597.

(2) Fister, J. C.; Rank, D.; Harris, J. M. Delayed Fluorescence Optical Thermometry. *Analytical Chemistry* **1995**, *67*, 4269–4275.

(3) Baleizão, C.; Nagl, S.; Borisov, S. M.; Schäferling, M.; Wolfbeis, O. S.; Berberan-Santos, M. N. An Optical Thermometer Based on the Delayed Fluorescence of C70. *Chemistry - A European Journal* **2007**, *13*, 3643–3651.

(4) Baleizão, C.; Nagl, S.; Schäferling, M.; Berberan-Santos, M. N.; Wolfbeis, O. S. Dual Fluorescence Sensor for Trace Oxygen and Temperature with Unmatched Range and Sensitivity. *Analytical Chemistry* **2008**, *80*, 6449–6457.

(5) Augusto, V.; Baleizão, C.; Berberan-Santos, M. N.; Farinha, J. P. S. Oxygen-proof fluorescence temperature sensing with pristine C $_{70}$ encapsulated in polymernanoparticles. *J. Mater. Chem.* **2010**, *20*, 1192–1197.

(6) Quaranta, M.; Borisov, S. M.; Klimant, I. Indicators for optical oxygen sensors. *Bioanalytical Reviews* **2012**, *4*, 115–157.

(7) Lehner, P.; Larndorfer, C.; Garcia-Robledo, E.; Larsen, M.; Borisov, S. M.; Revsbech, N.-P.; Glud, R. N.; Canfield, D. E.; Klimant, I. LUMOS - A Sensitive and Reliable Optode System for Measuring Dissolved Oxygen in the Nanomolar Range. *PLOS ONE* **2015**, *10*, ed. by D'Auria, S., e0128125.

(8) Valeur, B., *Molecular fluorescence: principles and applications*, OCLC: ocm45541665; Wiley-VCH: Weinheim ; New York, 2002; 387 pp.

(9) Pawlicki, M.; Collins, H. A.; Denning, R. G.; Anderson, H. L. Two-Photon Absorption and the Design of Two-Photon Dyes. *Angewandte Chemie International Edition* **2009**, *48*, 3244–3266.

(10) Jenkins, J.; Borisov, S. M.; Papkovsky, D. B.; Dmitriev, R. I. Sulforhodamine Nanothermometer for Multiparametric Fluorescence Lifetime Imaging Microscopy. *Analytical Chemistry* **2016**, *88*, 10566–10572.

(11) Wolfbeis, O. S. In, Chemical, Biochemical, and Environmental Fiber Sensors II, International Society for Optics and Photonics: 1991; Vol. 1368, pp 218–222.

(12) Baleizão, C.; Berberan-Santos, M. N. Thermally activated delayed fluorescence as a cycling process between excited singlet and triplet states: Application to the fullerenes. *The Journal of Chemical Physics* **2007**, *126*, 204510.

(13) Yang, Z.; Mao, Z.; Xie, Z.; Zhang, Y.; Liu, S.; Zhao, J.; Xu, J.; Chi, Z.; Aldred, M. P. Recent advances in organic thermally activated delayed fluorescence materials. *Chem. Soc. Rev.* **2017**, *46*, 915–1016.

(14) Wong, M. Y.; Zysman-Colman, E. Purely Organic Thermally Activated Delayed Fluorescence Materials for Organic Light-Emitting Diodes. *Advanced Materials* **2017**, 1605444.

(15) Im, Y.; Kim, M.; Cho, Y. J.; Seo, J.-A.; Yook, K. S.; Lee, J. Y. Molecular Design Strategy of Organic Thermally Activated Delayed Fluorescence Emitters. *Chemistry of Materials* **2017**, *29*, 1946–1963.

(16) Hirata, S. Recent Advances in Materials with Room Temperature Phosphorescence: Photophysics for Triplet Exciton Stabilization. *Advanced Optical Materials* **2017**, 1700116.

(17) Yeh, A. T.; Shank, C. V.; McCusker, J. K. Ultrafast Electron Localization Dynamics Following Photo-Induced Charge Transfer. *Science* **2000**, *289*, 935.

(18) Mukherjee, S.; Thilagar, P. Recent advances in purely organic phosphorescent materials. *Chem. Commun.* **2015**, *51*, 10988–11003.

(19) Huo, S.; Carroll, J.; Vezzu, D. A. K. Design, Synthesis, and Applications of Highly Phosphorescent Cyclometalated Platinum Complexes. *Asian Journal of Organic Chemistry* **2015**, *4*, 1210–1245.

(20) DaCosta, M. V.; Doughan, S.; Han, Y.; Krull, U. J. Lanthanide upconversion nanoparticles and applications in bioassays and bioimaging: A review. *Analytica Chimica Acta* **2014**, *832*, 1–33.

(21) Wang, F.; Liu, X. Recent advances in the chemistry of lanthanide-doped upconversion nanocrystals. *Chemical Society Reviews* **2009**, *38*, 976.

(22) Wen, S.; Zhou, J.; Zheng, K.; Bednarkiewicz, A.; Liu, X.; Jin, D. Advances in highly doped upconversion nanoparticles. *Nature Communications* **2018**, *9*, 2415.

(23) Wiesholler, L. M.; Frenzel, F.; Grauel, B.; Würth, C.; Resch-Genger, U.; Hirsch, T. Yb,Nd,Er-doped upconversion nanoparticles: 980 nm *versus* 808 nm excitation. *Nanoscale* **2019**, *11*, 13440–13449.

(24) Klimant, I.; Huber, C.; Liebsch, G.; Neurauter, G.; Stangelmayer, A.; Wolfbeis, O. S. In *New Trends in Fluorescence Spectroscopy: Applications to Chemical and Life Sciences*, Valeur, B., Brochon, J.-C., Eds.; Springer Berlin Heidelberg: Berlin, Heidelberg, 2001, pp 257–274.

(25) Larndorfer, C.; Borisov, S. M.; Lehner, P.; Klimant, I. The effect of high light intensities on luminescence lifetime based oxygen sensing. *The Analyst* **2014**, *139*, 6569–6579.

(26) Woods, R. J.; Scypinski, S.; Love, L. J. C. Transient digitizer for the determination of microsecond luminescence lifetimes. *Analytical Chemistry* **1984**, *56*, 1395–1400.

(27) Feng, J.; Tian, K.; Hu, D.; Wang, S.; Li, S.; Zeng, Y.; Li, Y.; Yang, G. A Triarylboron-Based Fluorescent Thermometer: Sensitive Over a Wide Temperature Range. *Angewandte Chemie International Edition* **2011**, *50*, 8072–8076.

(28) Khalid, A. H.; Kontis, K. Thermographic Phosphors for High Temperature Measurements: Principles, Current State of the Art and Recent Applications. *Sensors* **2008**, *8*, 5673–5744.

(29) Wang, X.-d.; Wolfbeis, O. S.; Meier, R. J. Luminescent probes and sensors for temperature. *Chemical Society Reviews* **2013**, *42*, 7834–7869.

(30) Lippitsch, M. E. Optical sensors based on fluorescence anisotropy. *Sensors and Actuators B: Chemical* **1993**, *11*, 499–502.

(31) Carraway, E. R.; Demas, J. N.; DeGraff, B. A. Luminescence quenching mechanism for microheterogeneous systems. *Analytical Chemistry* **1991**, *63*, 332–336.

(32) Han, J.; Burgess, K. Fluorescent Indicators for Intracellular pH. *Chemical Reviews* **2010**, *110*, 2709–2728.

(33) Whitaker, J. E.; Haugland, R. P.; Prendergast, F. G. Spectral and photophysical studies of benzo[c]xanthene dyes: Dual emission pH sensors. *Analytical Biochemistry* **1991**, *194*, 330–344.

(34) Clarke, Y.; Xu, W.; Demas, J. N.; DeGraff, B. A. Lifetime-Based pH Sensor System Based on a Polymer-Supported Ruthenium(II) Complex. *Analytical Chemistry* **2000**, *72*, 3468–3475.

(35) Sabnis, R. W. In *Handbook of Fluorescent Dyes and Probes*, Section: 90 _eprint: https://onlinelibrary.wiley.com/doi/pdf/10.1002/9781119007104.ch90; John Wiley & Sons, Ltd: 2015, pp 253–262.

(36) Wu, S.; Li, Z.; Han, J.; Han, S. Dual colored mesoporous silica nanoparticles with pH activable rhodamine-lactam for ratiometric sensing of lysosomal acidity. *Chemical Communications* **2011**, *47*, 11276.

(37) Aigner, D.; Ungerböck, B.; Mayr, T.; Saf, R.; Klimant, I.; Borisov, S. M. Fluorescent materials for pH sensing and imaging based on novel 1, 4-diketopyrrolo-[3, 4-c] pyrrole dyes. *Journal of Materials Chemistry C* **2013**, *1*, 5685–5693.

(38) Valeur, B. Design principles of fluorescent molecular sensors for cation recognition. *Coordination Chemistry Reviews* **2000**, *205*, 3–40.

(39) De Silva, A. P.; Gunaratne, H. Q. N.; Habib-Jiwan, J.-L.; McCoy, C. P.; Rice, T. E.; Soumillion, J.-P. New Fluorescent Model Compounds for the Study of Photoinduced Electron Transfer: The Influence of a Molecular Electric Field in the Excited State. *Angewandte Chemie International Edition in English* **1995**, *34*, 1728–1731.

(40) Escudero, D. Revising Intramolecular Photoinduced Electron Transfer (PET) from First-Principles. *Accounts of Chemical Research* **2016**, *49*, 1816–1824.

(41) Yuan, L.; Lin, W.; Zheng, K.; Zhu, S. FRET-Based Small-Molecule Fluorescent Probes: Rational Design and Bioimaging Applications. *Accounts of Chemical Research* **2013**, *46*, Publisher: American Chemical Society, 1462–1473.

(42) Chen, G.; Song, F.; Xiong, X.; Peng, X. Fluorescent Nanosensors Based on Fluorescence Resonance Energy Transfer (FRET). *Industrial & Engineering Chemistry Research* **2013**, *52*, 11228–11245.

(43) Dalfen, I.; Dmitriev, R. I.; Holst, G.; Klimant, I.; Borisov, S. M. Background-free fluorescence decay time sensing and imaging of pH with highly photostable diazaoxotri-angulenium dyes. *Analytical Chemistry* **2018**, DOI: `10.1021/acs.analchem.8b02534`.

(44) Modi, S.; G, S. M.; Goswami, D.; Gupta, G. D.; Mayor, S.; Krishnan, Y. A DNA nanomachine that maps spatial and temporal pH changes inside living cells. *Nature Nanotechnology* **2009**, *4*, 325–330.

(45) Huang, J.; Ying, L.; Yang, X.; Yang, Y.; Quan, K.; Wang, H.; Xie, N.; Ou, M.; Zhou, Q.; Wang, K. Ratiometric Fluorescent Sensing of pH Values in Living Cells by Dual-Fluorophore-Labeled i-Motif Nanoprobes. *Analytical Chemistry* **2015**, *87*, 8724–8731.

(46) Chen, C.; Zhang, P.; Zhang, L.; Gao, D.; Gao, G.; Yang, Y.; Li, W.; Gong, P.; Cai, L. Long-decay near-infrared-emitting doped quantum dots for lifetime-based in vivo pH imaging. *Chemical Communications* **2015**, *51*, 11162–11165.

(47) Hong, S. W.; Kim, K. H.; Huh, J.; Ahn, C.-H.; Jo, W. H. Design and Synthesis of a New pH Sensitive Polymeric Sensor Using Fluorescence Resonance Energy Transfer. *Chemistry of Materials* **2005**, *17*, 6213–6215.

(48) Wan, X.; Liu, S. Fluorescent water-soluble responsive polymers site-specifically labeled with FRET dyes possessing pH- and thermo-modulated multicolor fluorescence emissions as dual ratiometric probes. *Journal of Materials Chemistry* **2011**, *21*, 10321–10329.

(49) Fabbrizzi, L.; Licchelli, M.; Pallavicini, P.; Perotti, A.; Taglietti, A.; Sacchi, D. Fluorescent Sensors for Transition Metals Based on Electron-Transfer and Energy-Transfer Mechanisms. *Chemistry – A European Journal* **1996**, *2*, Publisher: John Wiley & Sons, Ltd, 75–82.

(50) Marín, M. J.; Galindo, F.; Thomas, P.; Russell, D. A. Localized Intracellular pH Measurement Using a Ratiometric Photoinduced Electron-Transfer-Based Nanosensor. *Angewandte Chemie International Edition* **2012**, *51*, 9657–9661.

(51) Gong, Y.-J.; Zhang, X.-B.; Zhang, C.-C.; Luo, A.-L.; Fu, T.; Tan, W.; Shen, G.-L.; Yu, R.-Q. Through Bond Energy Transfer: A Convenient and Universal Strategy toward Efficient Ratiometric Fluorescent Probe for Bioimaging Applications. *Analytical Chemistry* **2012**, *84*, Publisher: American Chemical Society, 10777–10784.

(52) Pietsch, C.; Schubert, U. S.; Hoogenboom, R. Aqueous polymeric sensors based on temperature-induced polymer phase transitions and solvatochromic dyes. *Chemical Communications* **2011**, *47*, 8750.

(53) McCurley, M. An optical biosensor using a fluorescent, swelling sensing element. *Biosensors and Bioelectronics* **1994**, *9*, 527–533.

(54) Reichardt, C.; Welton, T., *Solvents and Solvent Effects in Organic Chemistry*; Wiley-VCH Verlag GmbH & Co. KGaA: Weinheim, Germany, 2010.

(55) Dimroth, K.; Reichardt, C.; Siepmann, T.; Bohlmann, F. Über Pyridinium-N-phenol-betaine und ihre Verwendung zur Charakterisierung der Polarität von Lösungsmitteln. *Justus Liebigs Annalen der Chemie* **1963**, *661*, Publisher: John Wiley & Sons, Ltd, 1–37.

(56) Chang, Q.; Murtaza, Z.; Lakowicz, J. R.; Rao, G. A fluorescence lifetime-based solid sensor for water. *Analytica Chimica Acta* **1997**, *350*, 97–104.

(57) Niu, C.-G.; Guan, A.-L.; Zeng, G.-M.; Liu, Y.-G.; Li, Z.-W. Fluorescence water sensor based on covalent immobilization of chalcone derivative. *Analytica Chimica Acta* **2006**, *577*, 264–270.

(58) Kessler, M. A.; Gailer, J. G.; Wolfbeis, O. S. Optical sensor for on-line determination of solvent mixtures based on a fluorescent solvent polarity probe. *Sensors and Actuators B: Chemical* **1991**, *3*, 267–272.

(59) Fischer, L. H.; Harms, G. S.; Wolfbeis, O. S. Upconverting Nanoparticles for Nanoscale Thermometry. *Angewandte Chemie International Edition* **2011**, *50*, 4546–4551.

(60) Rocha, J.; Brites, C. D. S.; Carlos, L. D. Lanthanide Organic Framework Luminescent Thermometers. *Chemistry - A European Journal* **2016**, DOI: `10.1002/chem.201600860`.

(61) Wang, X.-d.; Wolfbeis, O. S. Optical methods for sensing and imaging oxygen: materials, spectroscopies and applications. *Chem. Soc. Rev.* **2014**, *43*, 3666–3761.

(62) Borisov, S.; Nuss, G.; Haas, W.; Saf, R.; Schmuck, M.; Klimant, I. New NIR-emitting complexes of platinum(II) and palladium(II) with fluorinated benzoporphyrins. *Journal of Photochemistry and Photobiology A: Chemistry* **2009**, *201*, 128–135.

(63) Koren, K.; Borisov, S. M.; Saf, R.; Klimant, I. Strongly Phosphorescent Iridium(III)-Porphyrins - New Oxygen Indicators with Tuneable Photophysical Properties and Functionalities. *European Journal of Inorganic Chemistry* **2011**, *2011*, 1531–1534.

(64) Omae, I. Application of five-membered ring products of cyclometalation reactions as sensing materials in sensing devices. *Journal of Organometallic Chemistry* **2016**, *823*, 50–75.

(65) Amao, Y.; Ishikawa, Y.; Okura, I. Green luminescent iridium (III) complex immobilized in fluoropolymer film as optical oxygen-sensing material. *Analytica chimica acta* **2001**, *445*, 177–182.

(66) Vander Donckt, E.; Camerman, B.; Herne, R.; Vandeloise, R. Fibre-optic oxygen sensor based on luminescence quenching of a Pt (II) complex embedded in polymer matrices. *Sensors and Actuators B: Chemical* **1996**, *32*, 121–127.

(67) Wu, W.; Wu, W.; Ji, S.; Guo, H.; Song, P.; Han, K.; Chi, L.; Shao, J.; Zhao, J. Tuning the emission properties of cyclometalated platinum(II) complexes by intramolecular electron-sink/arylethynylated ligands and its application for enhanced luminescent oxygen sensing. *Journal of Materials Chemistry* **2010**, *20*, 9775.

(68) Dixon, I. M.; Collin, J.-P.; Sauvage, J.-P.; Flamigni, L.; Encinas, S.; Barigelletti, F. A family of luminescent coordination compounds: iridium(iii) polyimine complexes. *Chemical Society Reviews* **2000**, *29*, 385–391.

(69) Chi, Y.; Chou, P.-T. Transition-metal phosphors with cyclometalating ligands: fundamentals and applications. *Chem. Soc. Rev.* **2010**, *39*, 638–655.

(70) Williams, J. A. G.; Develay, S.; Rochester, D.; Murphy, L. Optimising the luminescence of platinum(II) complexes and their application in organic light emitting devices (OLEDs). *Coordination Chemistry Reviews* **2008**, *252*, 2596–2611.

(71) Murphy, L.; Williams, J. A. G. In *Molecular Organometallic Materials for Optics*, Bozec, H., Guerchais, V., Eds.; Springer Berlin Heidelberg: Berlin, Heidelberg, 2010, pp 75–111.

(72) Borisov, S. M.; Klimant, I. Ultrabright Oxygen Optodes Based on Cyclometalated Iridium(III) Coumarin Complexes. *Analytical Chemistry* **2007**, *79*, 7501–7509.

(73) Amao, Y.; Okura, I.; Miyashita, T. Optical Oxygen Sensing Based on the Luminescence Quenching of Europium(III) Complex Immobilized in Fluoropolymer Film. *Bulletin of the Chemical Society of Japan* **2000**, *73*, 2663–2668.

(74) Borisov, S. M.; Klimant, I. New luminescent oxygen-sensing and temperature-sensing materials based on gadolinium(III) and europium(III) complexes embedded in an acridone–polystyrene conjugate. *Analytical and Bioanalytical Chemistry* **2012**, *404*, 2797–2806.

(75) Borisov, S. M.; Fischer, R.; Saf, R.; Klimant, I. Exceptional Oxygen Sensing Properties of New Blue Light-Excitable Highly Luminescent Europium(III) and Gadolinium(III) Complexes. *Advanced Functional Materials* **2014**, *24*, 6548–6560.

(76) Amao, Y.; Ishikawa, Y.; Okura, I.; Miyashita, T. Optical Oxygen Sensing Material: Terbium(III) Complex Adsorbed Thin Film. *Bulletin of the Chemical Society of Japan* **2001**, *74*, 2445–2449.

(77) Borisov, S. M.; Pommer, R.; Svec, J.; Peters, S.; Novakova, V.; Klimant, I. New red-emitting Schiff base chelates: promising dyes for sensing and imaging of temperature and oxygen *via* phosphorescence decay time. *Journal of Materials Chemistry C* **2018**, *6*, 8999–9009.

(78) Zach, P. W.; Freunberger, S. A.; Klimant, I.; Borisov, S. M. Electron-Deficient Near-Infrared Pt(II) and Pd(II) Benzoporphyrins with Dual Phosphorescence and Unusually Efficient Thermally Activated Delayed Fluorescence: First Demonstration of Simultaneous Oxygen and Temperature Sensing with a Single Emitter. *ACS Applied Materials & Interfaces* **2017**, *9*, 38008–38023.

(79) Zieger, S. E.; Steinegger, A.; Klimant, I.; Borisov, S. M. TADF-Emitting Zn(II)-Benzoporphyrin: An Indicator for Simultaneous Sensing of Oxygen and Temperature. *ACS Sensors* **2020**, *5*, Publisher: American Chemical Society, 1020–1027.

(80) Kochmann, S.; Baleizão, C.; Berberan-Santos, M. N.; Wolfbeis, O. S. Sensing and imaging of oxygen with parts per billion limits of detection and based on the quenching of the delayed fluorescence of 13C70 fullerene in polymer hosts. *Analytical chemistry* **2013**, *85*, Publisher: ACS Publications, 1300–1304.

(81) Nagl, S.; Baleizao, C.; Borisov, S. M.; Schäferling, M.; Berberan-Santos, M. N.; Wolfbeis, O. S. Optical sensing and imaging of trace oxygen with record response. *Angewandte Chemie International Edition* **2007**, *46*, Publisher: Wiley Online Library, 2317–2319.

(82) Mills, A. Controlling the sensitivity of optical oxygen sensors. *Sensors and Actuators B: Chemical* **1998**, *51*, 60–68.

(83) Baron, A. E.; Danielson, J. D. S.; Gouterman, M.; Wan, J. R.; Callis, J. B.; McLachlan, B. Submillisecond response times of oxygen-quenched luminescent coatings. *Review of Scientific Instruments* **1993**, *64*, 3394–3402.

(84) Lin, H.-W. et al. Novel oxygen sensor based on terfluorene thin-film and its enhanced sensitivity by stimulated emission. *Journal of Materials Chemistry* **2012**, *22*, 13446.

(85) Xu, W.; Schmidt, R.; Whaley, M.; Demas, J.; DeGraff, B.; Karikari, E.; Famer, B. Oxygen sensors based on luminescence quenching: interactions of pyrene with the polymer supports. *Analytical Chemistry* **1995**, *67*, Publisher: ACS Publications, 3172–3180.

(86) McDonagh, C.; Bowe, P.; Mongey, K.; MacCraith, B. Characterisation of porosity and sensor response times of sol–gel-derived thin films for oxygen sensor applications. *Journal of Non-Crystalline Solids* **2002**, *306*, 138–148.

(87) Klimant, I.; Ruckruh, F.; Liebsch, G.; Stangelmayer, A.; Wolfbeis, O. S. Fast Response Oxygen Micro-Optodes Based on Novel Soluble Ormosil Glasses. *Microchimica Acta* **1999**, *131*, 35–46.

(88) Wolfbeis, O. S.; Offenbacher, H.; Kroneis, H.; Marsoner, H. A fast responding fluorescence sensor for oxygen. *Mikrochimica Acta* **1984**, *82*, 153–158.

(89) Bhanu, V. A.; Kishore, K. Role of oxygen in polymerization reactions. *Chemical Reviews* **1991**, *91*, 99–117.

(90) Nakano, T.; Hoshi, K.; Baba, S. Effect of background gas environment on oxygen incorporation in TiN films deposited using UHV reactive magnetron sputtering. *Vacuum* **2008**, *83*, 467–469.

(91) Berger, H. Contamination due to process gases. *Microelectronic Engineering* **1991**, *10*, 259–267.

(92) Banerjee, S.; Kelly, C.; Kerry, J. P.; Papkovsky, D. B. High throughput non-destructive assessment of quality and safety of packaged food products using phosphorescent oxygen sensors. *Trends in Food Science & Technology* **2016**, *50*, 85–102.

(93) Bergersen, F. J.; Turner, G. Bacteroids from soybean root nodules: respiration and N2-fixation in flow-chamber reactions with oxyleghaemoglobin. *Proceedings of the Royal Society of London. B. Biological Sciences* **1990**, *238*, Publisher: The Royal Society London, 295–320.

(94) Lehner, P.; Staudinger, C.; Borisov, S. M.; Klimant, I. Ultra-sensitive optical oxygen sensors for characterization of nearly anoxic systems. *Nature communications* **2014**, *5*, Publisher: Nature Publishing Group, 1–6.

(95) Amao, Y.; Tabuchi, Y.; Yamashita, Y.; Kimura, K. Novel optical oxygen sensing material: metalloporphyrin dispersed in fluorinated poly(aryl ether ketone) films. *European Polymer Journal* **2002**, *38*, 675–681.

(96) Borisov, S. M.; Lehner, P.; Klimant, I. Novel optical trace oxygen sensors based on platinum(II) and palladium(II) complexes with 5,10,15,20-meso-tetrakis-(2,3,4,5,6-pentafluorphenyl)-porphyrin covalently immobilized on silica-gel particles. *Analytica Chimica Acta* **2011**, *690*, 108–115.

(97) Lehner, P.; Staudinger, C.; Borisov, S. M.; Regensburger, J.; Klimant, I. Intrinsic Artefacts in Optical Oxygen Sensors-How Reliable are our Measurements? *Chemistry - A European Journal* **2015**, *21*, 3978–3986.

(98) Allison, S. W.; Gillies, G. T. Remote thermometry with thermographic phosphors: Instrumentation and applications. *Review of Scientific Instruments* **1997**, *68*, 2615–2650.

(99) Chambers, M.; Clarke, D. Doped Oxides for High-Temperature Luminescence and Lifetime Thermometry. *Annual Review of Materials Research* **2009**, *39*, 325–359.

(100)   McLaurin, E. J.; Bradshaw, L. R.; Gamelin, D. R. Dual-Emitting Nanoscale Temperature Sensors. *Chemistry of Materials* **2013**, *25*, 1283–1292.

(101)   Jaque, D.; Vetrone, F. Luminescence nanothermometry. *Nanoscale* **2012**, *4*, 4301–4326.

(102)   Brites, C. D. S.; Lima, P. P.; Silva, N. J. O.; Millán, A.; Amaral, V. S.; Palacio, F.; Carlos, L. D. Thermometry at the nanoscale. *Nanoscale* **2012**, *4*, 4799–4829.

(103)   Dramićanin, M. D. Sensing temperature via downshifting emissions of lanthanide-doped metal oxides and salts. A review. *Methods and Applications in Fluorescence* **2016**, *4*, 042001.

(104)   Dramićanin, M., *Luminescence thermometry: methods, materials, and applications*, OCLC: 1034724325, 2018.

(105)   Brites, C. D. S.; Balabhadra, S.; Carlos, L. D. Lanthanide-Based Thermometers: At the Cutting-Edge of Luminescence Thermometry. *Advanced Optical Materials* **2019**, *7*, 1801239.

(106)   Duong, H. D.; Rhee, J. I. Exploitation of thermo-effect of rhodamine B entrapped in sol–gel matrix and silica gel for temperature detection. *Sensors and Actuators B: Chemical* **2007**, *124*, 18–23.

(107)   Homma, M.; Takei, Y.; Murata, A.; Inoue, T.; Takeoka, S. A ratiometric fluorescent molecular probe for visualization of mitochondrial temperature in living cells. *Chemical Communications* **2015**, *51*, Publisher: Royal Society of Chemistry, 6194–6197.

(108)   Ross, D.; Gaitan, M.; Locascio, L. E. Temperature Measurement in Microfluidic Systems Using a Temperature-Dependent Fluorescent Dye. *Analytical Chemistry* **2001**, *73*, 4117–4123.

(109)   Benninger, R. K.; Ko*c*, Y.; Hofmann, O.; Requejo-Isidro, J.; Neil, M. A.; French, P. M.; deMello, A. J. Quantitative 3D mapping of fluidic temperatures within microchannel networks using fluorescence lifetime imaging. *Analytical chemistry* **2006**, *78*, Publisher: ACS Publications, 2272–2278.

(110)   Kitamura, N.; Hosoda, Y.; Ueno, K.; IWATA, S. An application of plastic microchannel-microheater chips to a thermal synthetic reaction. *Analytical sciences* **2004**, *20*, Publisher: The Japan Society for Analytical Chemistry, 783–786.

(111)   Gallery, J.; Gouterman, M.; Callis, J.; Khalil, G.; McLachlan, B.; Bell, J. Luminescent thermometry for aerodynamic measurements. *Review of Scientific Instruments* **1994**, *65*, 712–720.

(112)   Chandrasekharan, N.; Kelly, L. A. A dual fluorescence temperature sensor based on perylene/exciplex interconversion. *Journal of the American Chemical Society* **2001**, *123*, Publisher: ACS Publications, 9898–9899.

(113) Baker, G. A.; Baker, S. N.; McCleskey, T. M. Noncontact two-color luminescence thermometry based on intramolecular luminophore cyclization within an ionic liquid. *Chemical Communications* **2003**, 2932–2933.

(114) Pragst, F.; Hamann, H.-J.; Teuchner, K.; Naether, M.; Becker, W.; Daehne, S. Steady state and laser spectroscopic investigations on the intramolecular exciplex formation of 1-(Np-anisyl-N-methyl)-amino-3-anthryl-(9)-propane. *Chemical Physics Letters* **1977**, *48*, Publisher: Elsevier, 36–39.

(115) Steinegger, A.; Borisov, S. M. Zn(II) Schiff Bases: Bright TADF Emitters for Self-referenced Decay Time-Based Optical Temperature Sensing. *ACS Omega* **2020**, *5*, Publisher: American Chemical Society, 7729–7737.

(116) Stehr, J.; Lupton, J. M.; Reufer, M.; Raschke, G.; Klar, T. A.; Feldmann, J. Sub-Microsecond Molecular Thermometry Using Thermal Spin Flips. *Advanced Materials* **2004**, *16*, Publisher: Wiley Online Library, 2170–2174.

(117) Fischer, L. H.; Karakus, C.; Meier, R. J.; Risch, N.; Wolfbeis, O. S.; Holder, E.; Schäferling, M. Referenced Dual Pressure-and Temperature-Sensitive Paint for Digital Color Camera Read Out. *Chemistry–A European Journal* **2012**, *18*, 15706–15713.

(118) Khalil, G. E.; Lau, K.; Phelan, G. D.; Carlson, B.; Gouterman, M.; Callis, J. B.; Dalton, L. R. Europium beta-diketonate temperature sensors: Effects of ligands, matrix, and concentration. *Review of Scientific Instruments* **2004**, *75*, 192–206.

(119) Cao, B.; He, Y.; Feng, Z.; Li, Y.; Dong, B. Optical temperature sensing behavior of enhanced green upconversion emissions from Er–Mo:Yb2Ti2O7 nanophosphor. *Sensors and Actuators B: Chemical* **2011**, *159*, 8–11.

(120) Shao, Q.; Lin, H.; Hu, J.; Dong, Y.; Jiang, J. Temperature-dependent photoluminescence properties of deep-red emitting Mn4+-activated magnesium fluorogermanate phosphors. *Journal of Alloys and Compounds* **2013**, *552*, 370–375.

(121) Grattan, K. T. V.; Selli, R. K.; Palmer, A. W. Ruby decay-time fluorescence thermometer in a fiber-optic configuration. *Review of Scientific Instruments* **1988**, *59*, 1328–1335.

(122) Aizawa, H.; Ohishi, N.; Ogawa, S.; Watanabe, E.; Katsumata, T.; Komuro, S.; Morikawa, T.; Toba, E. Characteristics of chromium doped spinel crystals for a fiber-optic thermometer application. *Review of Scientific Instruments* **2002**, *73*, 3089–3092.

(123) Borisov, S. M.; Gatterer, K.; Bitschnau, B.; Klimant, I. Preparation and Characterization of Chromium(III)-Activated Yttrium Aluminum Borate: A New Thermographic Phosphor for Optical Sensing and Imaging at Ambient Temperatures. *The Journal of Physical Chemistry C* **2010**, *114*, 9118–9124.

(124) Wang, X.; Liu, Q.; Bu, Y.; Liu, C.-S.; Liu, T.; Yan, X. Optical temperature sensing of rare-earth ion doped phosphors. *RSC Adv.* **2015**, *5*, 86219–86236.

(125) Kuno, M.; Fromm, D. P.; Hamann, H. F.; Gallagher, A.; Nesbitt, D. J. Nonexponential "blinking" kinetics of single CdSe quantum dots: A universal power law behavior. *The journal of chemical physics* **2000**, *112*, 3117–3120.

(126) Liang, R.; Tian, R.; Shi, W.; Liu, Z.; Yan, D.; Wei, M.; Evans, D. G.; Duan, X. A temperature sensor based on CdTe quantum dots–layered double hydroxide ultrathin films via layer-by-layer assembly. *Chemical Communications* **2013**, *49*, 969–971.

(127) McLaurin, E. J.; Vlaskin, V. A.; Gamelin, D. R. Water-Soluble Dual-Emitting Nanocrystals for Ratiometric Optical Thermometry. *Journal of the American Chemical Society* **2011**, *133*, 14978–14980.

(128) Haro-González, P.; Martínez-Maestro, L.; Martín, I. R.; García-Solé, J.; Jaque, D. High-Sensitivity Fluorescence Lifetime Thermal Sensing Based on CdTe Quantum Dots. *Small* **2012**, *8*, 2652–2658.

(129) Pugh-Thomas, D.; Walsh, B. M.; Gupta, M. C. CdSe (ZnS) nanocomposite luminescent high temperature sensor. *Nanotechnology* **2011**, *22*, Publisher: IOP Publishing, 185503.

(130) Vetrone, F.; Naccache, R.; Zamarrón, A.; Juarranz de la Fuente, A.; Sanz-Rodríguez, F.; Martinez Maestro, L.; Martín Rodriguez, E.; Jaque, D.; García Solé, J.; Capobianco, J. A. Temperature Sensing Using Fluorescent Nanothermometers. *ACS Nano* **2010**, *4*, 3254–3258.

(131) Singh, S. K.; Kumar, K.; Rai, S. Er3+/Yb3+ codoped Gd2O3 nano-phosphor for optical thermometry. *Sensors and Actuators A: Physical* **2009**, *149*, 16–20.

(132) Geitenbeek, R. G.; Prins, P. T.; Albrecht, W.; van Blaaderen, A.; Weckhuysen, B. M.; Meijerink, A. NaYF $_4$:Er $^{3+}$,Yb $^{3+}$ /SiO $_2$ Core/Shell Upconverting Nanocrystals for Luminescence Thermometry up to 900 K. *The Journal of Physical Chemistry C* **2017**, *121*, 3503–3510.

(133) Dong, N.-N. et al. NIR-to-NIR Two-Photon Excited CaF $_2$:Tm $^{3+}$,Yb $^{3+}$ Nanoparticles: Multifunctional Nanoprobes for Highly Penetrating Fluorescence Bio-Imaging. *ACS Nano* **2011**, *5*, 8665–8671.

(134) Cui, Y.; Zou, W.; Song, R.; Yu, J.; Zhang, W.; Yang, Y.; Qian, G. A ratiometric and colorimetric luminescent thermometer over a wide temperature range based on a lanthanide coordination polymer. *Chem. Commun.* **2014**, *50*, 719–721.

(135) Zhou, J.; Mishra, K.; Bhagat, V.; Joy, A.; Becker, M. L. Thermoresponsive dual emission nanosensor based on quantum dots and dye labeled poly(N-isopropylacrylamide). *Polymer Chemistry* **2015**, *6*, 2813–2816.

(136) Gota, C.; Uchiyama, S.; Yoshihara, T.; Tobita, S.; Ohwada, T. Temperature-Dependent Fluorescence Lifetime of a Fluorescent Polymeric Thermometer, Poly(*N* -isopropylacrylamide), Labeled by Polarity and Hydrogen Bonding Sensitive 4-Sulfamoyl-7-aminobenzofurazan. *The Journal of Physical Chemistry B* **2008**, *112*, 2829–2836.

(137) Graham, E. M.; Iwai, K.; Uchiyama, S.; Prasanna de Silva, A.; Magennis, S. W.; Jones, A. C. Quantitative mapping of aqueous microfluidic temperature with sub-degree resolution using fluorescence lifetime imaging microscopy. *Lab on a Chip* **2010**, *10*, 1267.

(138) Borisov, S. M.; Krause, C.; Arain, S.; Wolfbeis, O. S. Composite Material for Simultaneous and Contactless Luminescent Sensing and Imaging of Oxygen and Carbon Dioxide. *Advanced Materials* **2006**, *18*, 1511–1516.

(139) Bustamante, N.; Ielasi, G.; Bedoya, M.; Orellana, G. Optimization of Temperature Sensing with Polymer-Embedded Luminescent Ru(II) Complexes. *Polymers* **2018**, *10*, 234.

(140) Peng, H.; Stich, M. I. J.; Yu, J.; Sun, L.-n.; Fischer, L. H.; Wolfbeis, O. S. Luminescent Europium(III) Nanoparticles for Sensing and Imaging of Temperature in the Physiological Range. *Advanced Materials* **2010**, *22*, 716–719.

(141) Fischer, L. H.; Borisov, S. M.; Schaeferling, M.; Klimant, I.; Wolfbeis, O. S. Dual sensing of pO2 and temperature using a water-based and sprayable fluorescent paint. *The Analyst* **2010**, *135*, 1224.

(142) Brübach, J.; Feist, J. P.; Dreizler, A. Characterization of manganese-activated magnesium fluorogermanate with regards to thermographic phosphor thermometry. *Measurement Science and Technology* **2008**, *19*, 025602.

(143) Allison, S. W.; Gillies, G. T.; Rondinone, A. J.; Cates, M. R. Nanoscale thermometry via the fluorescence of YAG: Ce phosphor particles: measurements from 7 to 77 C. *Nanotechnology* **2003**, *14*, 859.

(144) Steinegger, A.; Klimant, I.; Borisov, S. M. Purely Organic Dyes with Thermally Activated Delayed Fluorescence-A Versatile Class of Indicators for Optical Temperature Sensing. *Advanced Optical Materials* **2017**, 1700372.

(145) Lv, Y.; Jin, Y.; Wu, H.; Liu, D.; Xiong, G.; Ju, G.; Chen, L.; Hu, Y. An All-Optical Ratiometric Thermometer Based on Reverse Thermal Response from Interplay among Diverse Emission Centers and Traps with High-Temperature Sensitivity. *Industrial & Engineering Chemistry Research* **2019**, *58*, 21242–21251.

(146) Rao, X.; Song, T.; Gao, J.; Cui, Y.; Yang, Y.; Wu, C.; Chen, B.; Qian, G. A Highly Sensitive Mixed Lanthanide Metal–Organic Framework Self-Calibrated Luminescent Thermometer. *Journal of the American Chemical Society* **2013**, *135*, 15559–15564.

(147) Liu, X.; Akerboom, S.; Jong, M. d.; Mutikainen, I.; Tanase, S.; Meijerink, A.; Bouwman, E. Mixed-Lanthanoid Metal–Organic Framework for Ratiometric Cryogenic Temperature Sensing. *Inorganic Chemistry* **2015**, *54*, 11323–11329.

(148) Chen, D.; Xu, M.; Huang, P. Core@shell upconverting nanoarchitectures for luminescent sensing of temperature. *Sensors and Actuators B: Chemical* **2016**, *231*, 576–583.

(149) Cui, Y.; Song, R.; Yu, J.; Liu, M.; Wang, Z.; Wu, C.; Yang, Y.; Wang, Z.; Chen, B.; Qian, G. Dual-Emitting MOF Dye Composite for Ratiometric Temperature Sensing. *Advanced Materials* **2015**, *27*, 1420–1425.

(150) Tian, Y.; Tian, B.; Huang, P.; Wang, L.; Chen, B. Size-dependent upconversion luminescence and temperature sensing behavior of spherical Gd 2 O 3: Yb 3+/Er 3+ phosphor. *Rsc Advances* **2015**, *5*, Publisher: Royal Society of Chemistry, 14123–14128.

(151) Albrecht, M. Cyclometalation Using d-Block Transition Metals: Fundamental Aspects and Recent Trends. *Chemical Reviews* **2010**, *110*, 576–623.

(152) Williams, J. A. G. In *Photochemistry and Photophysics of Coordination Compounds II*, Balzani, V., Campagna, S., Eds.; Springer Berlin Heidelberg: Berlin, Heidelberg, 2007, pp 205–268.

(153) Shafikov, M. Z.; Daniels, R.; Pander, P.; Dias, F. B.; Williams, J. A. G.; Kozhevnikov, V. N. Dinuclear Design of a Pt(II) Complex Affording Highly Efficient Red Emission: Photophysical Properties and Application in Solution-Processible OLEDs. *ACS Applied Materials & Interfaces* **2019**, *11*, 8182–8193.

(154) Lanoë, P.-H.; Tong, C. M.; Harrington, R. W.; Probert, M. R.; Clegg, W.; Williams, J. G.; Kozhevnikov, V. N. Ditopic bis-terdentate cyclometallating ligands and their highly luminescent dinuclear iridium (III) complexes. *Chemical Communications* **2014**, *50*, Publisher: Royal Society of Chemistry, 6831–6834.

(155) Daniels, R. E.; Culham, S.; Hunter, M.; Durrant, M. C.; Probert, M. R.; Clegg, W.; Williams, J. G.; Kozhevnikov, V. N. When two are better than one: bright phosphorescence from non-stereogenic dinuclear iridium (III) complexes. *Dalton Transactions* **2016**, *45*, Publisher: The Royal Society of Chemistry, 6949–6962.

(156) Kozhevnikov, V. N.; Durrant, M. C.; Williams, J. A. G. Highly Luminescent Mixed-Metal Pt(II)/Ir(III) Complexes: Bis-Cyclometalation of 4,6-Diphenylpyrimidine As a Versatile Route to Rigid Multimetallic Assemblies. *Inorganic Chemistry* **2011**, *50*, Publisher: American Chemical Society, 6304–6313.

(157) Turnbull, G.; Williams, J. A. G.; Kozhevnikov, V. N. Rigidly linking cyclometallated Ir(iii) and Pt(ii) centres: an efficient approach to strongly absorbing and highly phosphorescent red emitters. *Chemical Communications* **2017**, *53*, Publisher: The Royal Society of Chemistry, 2729–2732.

(158) Culham, S.; Lanoë, P.-H.; Whittle, V. L.; Durrant, M. C.; Williams, J. A. G.; Kozhevnikov, V. N. Highly Luminescent Dinuclear Platinum(II) Complexes Incorporating Bis-Cyclometallating Pyrazine-Based Ligands: A Versatile Approach to Efficient Red Phosphors. *Inorganic Chemistry* **2013**, *52*, 10992–11003.

(159)   Ashen-Garry, D.; Selke, M. Singlet Oxygen Generation by Cyclometalated Complexes and Applications. *Photochemistry and Photobiology* **2014**, *90*, Publisher: John Wiley & Sons, Ltd, 257–274.

(160)   Van der Boom, M. E.; Milstein, D. Cyclometalated Phosphine-Based Pincer Complexes: Mechanistic Insight in Catalysis, Coordination, and Bond Activation. *Chemical Reviews* **2003**, *103*, 1759–1792.

(161)   Mauro, M.; Aliprandi, A.; Septiadi, D.; Kehr, N. S.; De Cola, L. When self-assembly meets biology: luminescent platinum complexes for imaging applications. *Chem. Soc. Rev.* **2014**, *43*, 4144–4166.

(162)   You, Y. Phosphorescence bioimaging using cyclometalated Ir(III) complexes. *Current Opinion in Chemical Biology* **2013**, *17*, 699–707.

(163)   Cave, G. W. V.; Fanizzi, F. P.; Deeth, R. J.; Errington, W.; Rourke, J. P. CH Activation Induced by Water. Monocyclometalated to Dicyclometalated: CNC Tridentate Platinum Complexes. *Organometallics* **2000**, *19*, Publisher: American Chemical Society, 1355–1364.

(164)   Ghedini, M.; Pucci, D.; Crispini, A.; Barberio, G. Oxidative Addition to Cyclometalated Azobenzene Platinum(II) Complexes: A Route to Octahedral Liquid Crystalline Materials. *Organometallics* **1999**, *18*, 2116–2124.

(165)   Thomas III, S. W.; Yagi, S.; Swager, T. M. Towards chemosensing phosphorescent conjugated polymers: cyclometalated platinum(ii) poly(phenylene)s. *Journal of Materials Chemistry* **2005**, *15*, 2829.

(166)   Hudson, Z. M.; Blight, B. A.; Wang, S. Efficient and High Yield One-Pot Synthesis of Cyclometalated Platinum(II) -Diketonates at Ambient Temperature. *Organic Letters* **2012**, *14*, 1700–1703.

(167)   Flamigni, L.; Barbieri, A.; Sabatini, C.; Ventura, B.; Barigelletti, F. In *Photochemistry and Photophysics of Coordination Compounds II*, Balzani, V., Campagna, S., Eds.; Springer Berlin Heidelberg: Berlin, Heidelberg, 2007, pp 143–203.

(168)   Reijenga, J. C.; Gagliardi, L. G.; Kenndler, E. Temperature dependence of acidity constants, a tool to affect separation selectivity in capillary electrophoresis. *Journal of Chromatography A* **2007**, *1155*, 142–145.

(169)   Rayer, A. V.; Sumon, K. Z.; Jaffari, L.; Henni, A. Dissociation Constants (p K_a) of Tertiary and Cyclic Amines: Structural and Temperature Dependences. *Journal of Chemical & Engineering Data* **2014**, *59*, 3805–3813.

(170)   Lobnik, A.; Oehme, I.; Murkovic, I.; Wolfbeis, O. S. pH optical sensors based on sol–gels: Chemical doping versus covalent immobilization. *Analytica Chimica Acta* **1998**, *367*, 159–165.

(171) Starannikova, L.; Khodzhaeva, V.; Yampolskii, Y. Mechanism of aging of poly[1-(trimethylsilyl)-1-propyne] and its effect on gas permeability. *Journal of Membrane Science* **2004**, *244*, 183–191.

(172) Enko, B.; Borisov, S. M.; Regensburger, J.; Bäumler, W.; Gescheidt, G.; Klimant, I. Singlet Oxygen-Induced Photodegradation of the Polymers and Dyes in Optical Sensing Materials and the Effect of Stabilizers on These Processes. *The Journal of Physical Chemistry A* **2013**, *117*, Publisher: American Chemical Society, 8873–8882.

(173) Demchenko, A. P. Photobleaching of organic fluorophores: quantitative characterization, mechanisms, protection. *Methods and Applications in Fluorescence* **2020**, *8*, 022001.

(174) Müller, B. J.; Steinmann, N.; Borisov, S. M.; Klimant, I. Ammonia sensing with fluoroionophores – A promising way to minimize interferences caused by volatile amines. *Sensors and Actuators B: Chemical* **2018**, *255*, 1897–1901.

(175) Bakker, E.; Bühlmann, P.; Pretsch, E. Carrier-based ion-selective electrodes and bulk optodes. 1. General characteristics. *Chemical Reviews* **1997**, *97*, 3083–3132.

(176) Yin, J.; Hu, Y.; Yoon, J. Fluorescent probes and bioimaging: alkali metals, alkaline earth metals and pH. *Chem. Soc. Rev.* **2015**, *44*, 4619–4644.

(177) Wencel, D.; Abel, T.; McDonagh, C. Optical Chemical pH Sensors. *Analytical Chemistry* **2014**, *86*, 15–29.

(178) Ding, Y.; Tang, Y.; Zhu, W.; Xie, Y. Fluorescent and colorimetric ion probes based on conjugated oligopyrroles. *Chem. Soc. Rev.* **2015**, *44*, 1101–1112.

(179) Mistlberger, G.; Crespo, G. A.; Bakker, E. Ionophore-Based Optical Sensors. *Annual Review of Analytical Chemistry* **2014**, *7*, 483–512.

(180) Mills, A.; Hodgen, S. In *Topics in Fluorescence Spectroscopy*; Springer: 2005, pp 119–161.

(181) Chu, C.-S.; Lo, Y.-L.; Sung, T.-W. Review on recent developments of fluorescent oxygen and carbon dioxide optical fiber sensors. *Photonic Sensors* **2011**, *1*, 234–250.

(182) Schäferling, M. The Art of Fluorescence Imaging with Chemical Sensors. *Angewandte Chemie International Edition* **2012**, *51*, 3532–3554.

(183) Kerry, J.; O'Grady, M.; Hogan, S. Past, current and potential utilisation of active and intelligent packaging systems for meat and muscle-based products: A review. *Meat Science* **2006**, *74*, 113–130.

(184) Mills, A. Oxygen indicators and intelligent inks for packaging food. *Chemical Society Reviews* **2005**, *34*, 1003.

(185) Papkovsky, D. B.; Papkovskaia, N.; Smyth, A.; Kerry, J.; Ogurtsov, V. I. Phosphorescent Sensor Approach for Non-Destructive Measurement of Oxygen in Packaged Foods: Optimisation of Disposable Oxygen Sensors and their Characterization Over a Wide Temperature Range. *Analytical Letters* **2000**, *33*, 1755–1777.

(186)   *Temperature measurement*, 2nd ed; Michalski, L., Michalski, L., Eds.; J. Wiley: Chichester ; New York, 2001, 501 pp.

(187)   Wang, C.; Xu, R.; Tian, W.; Jiang, X.; Cui, Z.; Wang, M.; Sun, H.; Fang, K.; Gu, N. Determining intracellular temperature at single-cell level by a novel thermocouple method. *Cell Research* **2011**, *21*, 1517–1519.

(188)   Chen, Z.; Zhang, K. Y.; Tong, X.; Liu, Y.; Hu, C.; Liu, S.; Yu, Q.; Zhao, Q.; Huang, W. Phosphorescent Polymeric Thermometers for In Vitro and In Vivo Temperature Sensing with Minimized Background Interference. *Advanced Functional Materials* **2016**, *26*, 4386–4396.

(189)   Brübach, J.; Pflitsch, C.; Dreizler, A.; Atakan, B. On surface temperature measurements with thermographic phosphors: A review. *Progress in Energy and Combustion Science* **2013**, *39*, 37–60.

(190)   Cao, C.; Liu, X.; Qiao, Q.; Zhao, M.; Yin, W.; Mao, D.; Zhang, H.; Xu, Z. A twisted-intramolecular-charge-transfer (TICT) based ratiometric fluorescent thermometer with a mega-Stokes shift and a positive temperature coefficient. *Chem. Commun.* **2014**, *50*, 15811–15814.

(191)   Okabe, K.; Inada, N.; Gota, C.; Harada, Y.; Funatsu, T.; Uchiyama, S. Intracellular temperature mapping with a fluorescent polymeric thermometer and fluorescence lifetime imaging microscopy. *Nature Communications* **2012**, *3*, 705–713.

(192)   Albers, A. E.; Chan, E. M.; McBride, P. M.; Ajo-Franklin, C. M.; Cohen, B. E.; Helms, B. A. Dual-Emitting Quantum Dot/Quantum Rod-Based Nanothermometers with Enhanced Response and Sensitivity in Live Cells. *Journal of the American Chemical Society* **2012**, *134*, 9565–9568.

(193)   Yang, J.-M.; Yang, H.; Lin, L. Quantum Dot Nano Thermometers Reveal Heterogeneous Local Thermogenesis in Living Cells. *ACS Nano* **2011**, *5*, 5067–5071.

(194)   Donner, J. S.; Thompson, S. A.; Kreuzer, M. P.; Baffou, G.; Quidant, R. Mapping Intracellular Temperature Using Green Fluorescent Protein. *Nano Letters* **2012**, *12*, 2107–2111.

(195)   Wang, H.; Xie, L.; Peng, Q.; Meng, L.; Wang, Y.; Yi, Y.; Wang, P. Novel Thermally Activated Delayed Fluorescence Materials-Thioxanthone Derivatives and Their Applications for Highly Efficient OLEDs. *Advanced Materials* **2014**, *26*, 5198–5204.

(196)   Xu, S.; Liu, T.; Mu, Y.; Wang, Y.-F.; Chi, Z.; Lo, C.-C.; Liu, S.; Zhang, Y.; Lien, A.; Xu, J. An Organic Molecule with Asymmetric Structure Exhibiting Aggregation-Induced Emission, Delayed Fluorescence, and Mechanoluminescence. *Angewandte Chemie International Edition* **2015**, *54*, 874–878.

(197) Cho, Y. J.; Jeon, S. K.; Chin, B. D.; Yu, E.; Lee, J. Y. The Design of Dual Emitting Cores for Green Thermally Activated Delayed Fluorescent Materials. *Angewandte Chemie International Edition* **2015**, *54*, 5201–5204.

(198) Kim, M.; Jeon, S. K.; Hwang, S.-H.; Lee, S.-s.; Yu, E.; Lee, J. Y. Highly efficient and color tunable thermally activated delayed fluorescent emitters using a "twin emitter" molecular design. *Chem. Commun.* **2016**, *52*, 339–342.

(199) Lee, J.; Shizu, K.; Tanaka, H.; Nakanotani, H.; Yasuda, T.; Kaji, H.; Adachi, C. Controlled emission colors and singlet–triplet energy gaps of dihydrophenazine-based thermally activated delayed fluorescence emitters. *J. Mater. Chem. C* **2015**, *3*, 2175–2181.

(200) Xie, G.; Li, X.; Chen, D.; Wang, Z.; Cai, X.; Chen, D.; Li, Y.; Liu, K.; Cao, Y.; Su, S.-J. Evaporation- and Solution-Process-Feasible Highly Efficient Thianthrene-9,9,10,10-Tetraoxide-Based Thermally Activated Delayed Fluorescence Emitters with Reduced Efficiency Roll-Off. *Advanced Materials* **2016**, *28*, 181–187.

(201) Wang, S.; Yan, X.; Cheng, Z.; Zhang, H.; Liu, Y.; Wang, Y. Highly Efficient Near-Infrared Delayed Fluorescence Organic Light Emitting Diodes Using a Phenanthrene-Based Charge-Transfer Compound. *Angewandte Chemie International Edition* **2015**, *54*, 13068–13072.

(202) Wang, F.; Hu, J.; Cao, X.; Yang, T.; Tao, Y.; Mei, L.; Zhang, X.; Huang, W. A low-cost phenylbenzoimidazole containing electron transport material for efficient green phosphorescent and thermally activated delayed fluorescent OLEDs. *J. Mater. Chem. C* **2015**, *3*, 5533–5540.

(203) Tanaka, H.; Shizu, K.; Miyazaki, H.; Adachi, C. Efficient green thermally activated delayed fluorescence (TADF) from a phenoxazine–triphenyltriazine (PXZ–TRZ) derivative. *Chemical Communications* **2012**, *48*, 11392–11394.

(204) Ni, F.; Wu, Z.; Zhu, Z.; Chen, T.; Wu, K.; Zhong, C.; An, K.; Wei, D.; Ma, D.; Yang, C. Teaching an old acceptor new tricks: rationally employing 2,1,3-benzothiadiazole as input to design a highly efficient red thermally activated delayed fluorescence emitter. *J. Mater. Chem. C* **2017**, *5*, 1363–1368.

(205) Li, B.; Nomura, H.; Miyazaki, H.; Zhang, Q.; Yoshida, K.; Suzuma, Y.; Orita, A.; Otera, J.; Adachi, C. Dicarbazolyldicyanobenzenes as Thermally Activated Delayed Fluorescence Emitters: Effect of Substitution Position on Photoluminescent and Electroluminescent Properties. *Chemistry Letters* **2014**, *43*, 319–321.

(206) Hatakeyama, T.; Shiren, K.; Nakajima, K.; Nomura, S.; Nakatsuka, S.; Kinoshita, K.; Ni, J.; Ono, Y.; Ikuta, T. Ultrapure Blue Thermally Activated Delayed Fluorescence Molecules: Efficient HOMO-LUMO Separation by the Multiple Resonance Effect. *Advanced Materials* **2016**, *28*, 2777–2781.

(207) Méhes, G.; Nomura, H.; Zhang, Q.; Nakagawa, T.; Adachi, C. Enhanced Electroluminescence Efficiency in a Spiro-Acridine Derivative through Thermally Activated Delayed Fluorescence. *Angewandte Chemie International Edition* **2012**, *51*, 11311–11315.

(208) Zhu, Y.; Zhang, Y.; Yao, B.; Wang, Y.; Zhang, Z.; Zhan, H.; Zhang, B.; Xie, Z.; Wang, Y.; Cheng, Y. Synthesis and Electroluminescence of a Conjugated Polymer with Thermally Activated Delayed Fluorescence. *Macromolecules* **2016**, *49*, 4373–4377.

(209) Uoyama, H.; Goushi, K.; Shizu, K.; Nomura, H.; Adachi, C. Highly efficient organic light-emitting diodes from delayed fluorescence. *Nature* **2012**, *492*, 234–238.

(210) Li, J.; Nakagawa, T.; MacDonald, J.; Zhang, Q.; Nomura, H.; Miyazaki, H.; Adachi, C. Highly Efficient Organic Light-Emitting Diode Based on a Hidden Thermally Activated Delayed Fluorescence Channel in a Heptazine Derivative. *Advanced Materials* **2013**, *25*, 3319–3323.

(211) Mayr, C.; Lee, S. Y.; Schmidt, T. D.; Yasuda, T.; Adachi, C.; Brütting, W. Efficiency Enhancement of Organic Light-Emitting Diodes Incorporating a Highly Oriented Thermally Activated Delayed Fluorescence Emitter. *Advanced Functional Materials* **2014**, *24*, 5232–5239.

(212) Tao, Y.; Yuan, K.; Chen, T.; Xu, P.; Li, H.; Chen, R.; Zheng, C.; Zhang, L.; Huang, W. Thermally Activated Delayed Fluorescence Materials Towards the Breakthrough of Organoelectronics. *Advanced Materials* **2014**, *26*, 7931–7958.

(213) Xie, Y.; Li, Z. Thermally Activated Delayed Fluorescent Polymers. *Journal of Polymer Science Part A: Polymer Chemistry* **2017**, *55*, 575–584.

(214) Zhang, Q.; Kuwabara, H.; Potscavage, W. J.; Huang, S.; Hatae, Y.; Shibata, T.; Adachi, C. Anthraquinone-Based Intramolecular Charge-Transfer Compounds: Computational Molecular Design, Thermally Activated Delayed Fluorescence, and Highly Efficient Red Electroluminescence. *Journal of the American Chemical Society* **2014**, *136*, 18070–18081.

(215) *Polymer handbook, 4th edition*, 4th ed; Brandrup, J., Immergut, E. H., Grulke, E. A., Eds., OCLC: ocm56457312; Wiley: New York ; Chichester, 2004, 2 pp.

(216) Wessling, R. A.; Gibbs, D. S.; Obi, B. E.; Beyer, D. E.; DeLassus, P. T.; Howell, B. A. In *Encyclopedia of Polymer Science and Technology*; John Wiley & Sons, Inc.: Hoboken, 2002, pp 458–510.

(217) Borisov, S. M.; Nuss, G.; Klimant, I. Red Light-Excitable Oxygen Sensing Materials Based on Platinum(II) and Palladium(II) Benzoporphyrins. *Analytical Chemistry* **2008**, *80*, 9435–9442.

(218) Liebsch, G.; Klimant, I.; Wolfbeis, O. S. Luminescence Lifetime Temperature Sensing Based on Sol-Gels and Poly(acrylonitrile)s Dyed with Ruthenium Metal-Ligand Complexes. *Advanced Materials* **1999**, *11*, 1296–1299.

(219) Dmitriev, R. I.; Zhdanov, A. V.; Jasionek, G.; Papkovsky, D. B. Assessment of Cellular Oxygen Gradients with a Panel of Phosphorescent Oxygen-Sensitive Probes. *Analytical Chemistry* **2012**, *84*, 2930–2938.

(220) Kürner, J. M.; Klimant, I.; Krause, C.; Preu, H.; Kunz, W.; Wolfbeis, O. S. Inert phosphorescent nanospheres as markers for optical assays. *Bioconjugate chemistry* **2001**, *12*, 883–889.

(221) Holst, G.; Kohls, O.; Klimant, I.; König, B.; Kühl, M.; Richter, T. A modular luminescence lifetime imaging system for mapping oxygen distribution in biological samples. *Sensors and Actuators B: Chemical* **1998**, *51*, 163–170.

(222) Stich, M. I. J.; Fischer, L. H.; Wolfbeis, O. S. Multiple fluorescent chemical sensing and imaging. *Chemical Society Reviews* **2010**, *39*, 3102.

(223) Nagl, S.; Wolfbeis, O. S. Optical multiple chemical sensing: status and current challenges. *The Analyst* **2007**, *132*, 507.

(224) Gosse, C.; Bergaud, C.; Löw, P. In *Thermal Nanosystems and Nanomaterials*, Volz, S., Ed.; Springer Berlin Heidelberg: Berlin, Heidelberg, 2009; Vol. 118, pp 301–341.

(225) Samy, R.; Glawdel, T.; Ren, C. L. Method for Microfluidic Whole-Chip Temperature Measurement Using Thin-Film Poly(dimethylsiloxane)/Rhodamine B. *Analytical Chemistry* **2008**, *80*, 369–375.

(226) Barilero, T.; Le Saux, T.; Gosse, C.; Jullien, L. Fluorescent Thermometers for Dual-Emission-Wavelength Measurements: Molecular Engineering and Application to Thermal Imaging in a Microsystem. *Analytical Chemistry* **2009**, *81*, 7988–8000.

(227) Seger-Sauli, U.; Panayiotou, M.; Schnydrig, S.; Jordan, M.; Renaud, P. Temperature measurements in microfluidic systems: Heat dissipation of negative dielectrophoresis barriers. *ELECTROPHORESIS* **2005**, *26*, 2239–2246.

(228) Otto, S.; Scholz, N.; Behnke, T.; Resch-Genger, U.; Heinze, K. Thermo-Chromium: A Contactless Optical Molecular Thermometer. *Chemistry – A European Journal* **2017**, *23*, _eprint: https://onlinelibrary.wiley.com/doi/pdf/10.1002/chem.201701726, 12131–12135.

(229) Karakus, C.; Fischer, L. H.; Schmeding, S.; Hummel, J.; Risch, N.; Schäferling, M.; Holder, E. Oxygen and temperature sensitivity of blue to green to yellow light-emitting Pt (II) complexes. *Dalton Transactions* **2012**, *41*, 9623–9632.

(230) Maruszewski, K.; Andrzejewski, D.; Strek, W. Thermal sensor based on luminescence of Ru (bpy) 32+ entrapped in sol-gel glasses. *Journal of luminescence* **1997**, *72*, 226–228.

(231) Khalil, G. E.; Costin, C.; Crafton, J.; Jones, G.; Grenoble, S.; Gouterman, M.; Callis, J. B.; Dalton, L. R. Dual-luminophor pressure-sensitive paint. *Sensors and Actuators B: Chemical* **2004**, *97*, 13–21.

(232) Mitsuishi, M.; Kikuchi, S.; Miyashita, T.; Amao, Y. Characterization of an ultrathin polymer optode and its application to temperature sensors based on luminescent europium complexes. *Journal of Materials Chemistry* **2003**, *13*, 2875–2879.

(233) Borisov, S. M.; Klimant, I. Blue LED excitable temperature sensors based on a new europium (III) chelate. *Journal of fluorescence* **2008**, *18*, 581–589.

(234) Zelelow, B.; Khalil, G. E.; Phelan, G.; Carlson, B.; Gouterman, M.; Callis, J. B.; Dalton, L. R. Dual luminophor pressure sensitive paint. *Sensors and Actuators B: Chemical* **2003**, *96*, 304–314.

(235) Peng, H.-S.; Huang, S.-H.; Wolfbeis, O. S. Ratiometric fluorescent nanoparticles for sensing temperature. *Journal of Nanoparticle Research* **2010**, *12*, 2729–2733.

(236) Park, Y.; Koo, C.; Chen, H.-Y.; Han, A.; Son, D. H. Ratiometric temperature imaging using environment-insensitive luminescence of Mn-doped core–shell nanocrystals. *Nanoscale* **2013**, *5*, 4944–4950.

(237) Sung, T.-W.; Lo, Y.-L. Dual sensing of temperature and oxygen using PtTFPP-doped CdSe/SiO2 core–shell nanoparticles. *Sensors and Actuators B: Chemical* **2012**, *173*, 406–413.

(238) Hsia, C.-H.; Wuttig, A.; Yang, H. An accessible approach to preparing water-soluble Mn2+-doped (CdSSe) ZnS (core) shell nanocrystals for ratiometric temperature sensing. *ACS nano* **2011**, *5*, 9511–9522.

(239) Stich, M. I. J.; Nagl, S.; Wolfbeis, O. S.; Henne, U.; Schaeferling, M. A Dual Luminescent Sensor Material for Simultaneous Imaging of Pressure and Temperature on Surfaces. *Advanced Functional Materials* **2008**, *18*, 1399–1406.

(240) Sano, S.; Yuuki, T.; Hyakutake, T.; Morita, K.; Sakaue, H.; Arai, S.; Matsumoto, H.; Michinobu, T. Temperature compensation of pressure-sensitive luminescent polymer sensors. *Sensors and Actuators B: Chemical* **2018**, *255*, 1960–1966.

(241) Lam, H.; Rao, G.; Loureiro, J.; Tolosa, L. Dual optical sensor for oxygen and temperature based on the combination of time domain and frequency domain techniques. *Talanta* **2011**, *84*, 65–70.

(242) Borisov, S. M.; Wolfbeis, O. S. Temperature-Sensitive Europium(III) Probes and Their Use for Simultaneous Luminescent Sensing of Temperature and Oxygen. *Analytical Chemistry* **2006**, *78*, 5094–5101.

(243) Köse, M. E.; Carroll, B. F.; Schanze, K. S. Preparation and Spectroscopic Properties of Multiluminophore Luminescent Oxygen and Temperature Sensor Films. *Langmuir* **2005**, *21*, 9121–9129.

(244) Sticker, D. et al. Oxygen Management at the Microscale: A Functional Biochip Material with Long-Lasting and Tunable Oxygen Scavenging Properties for Cell Culture Applications. *ACS Applied Materials & Interfaces* **2019**, *11*, 9730–9739.

(245) Kheria, S.; Rayavarapu, S.; Kotmale, A. S.; Shinde, D. R.; Gonnade, R. G.; Sanjayan, G. J. Coumarin-Appended Stable Fluorescent Self-Complementary Quadruple-Hydrogen-Bonded Molecular Duplexes. *The Journal of Organic Chemistry* **2017**, *82*, 6403–6408.

(246) Sun, J.; Sun, J.; Mi, W.; Xue, P.; Zhao, J.; Zhai, L.; Lu, R. Self-assembling and piezofluorochromic properties of tert-butylcarbazole-based Schiff bases and the difluoroboron complex. *Dyes and Pigments* **2017**, *136*, 633–640.

(247) Coyle, L. M.; Gouterman, M. Correcting lifetime measurements for temperature. *Sensors and Actuators B: Chemical* **1999**, *61*, 92–99.

(248) Chu, C.-S.; Lin, T.-H. Ratiometric optical sensor for dual sensing of temperature and oxygen. *Sensors and Actuators B: Chemical* **2015**, *210*, 302–309.

(249) Collier, B. B.; McShane, M. J. Temperature Compensation of Oxygen Sensing Films Utilizing a Dynamic Dual Lifetime Calculation Technique. *IEEE Sensors Journal* **2014**, *14*, 2755–2764.

(250) Köse, M. E.; Omar, A.; Virgin, C. A.; Carroll, B. F.; Schanze, K. S. Principal component analysis calibration method for dual-luminophore oxygen and temperature sensor films: Application to luminescence imaging. *Langmuir* **2005**, *21*, 9110–9120.

(251) Hradil, J.; Davis, C.; Mongey, K.; McDonagh, C.; MacCraith, B. D. Temperature-corrected pressure-sensitive paint measurements using a single camera and a dual-lifetime approach. *Measurement Science and Technology* **2002**, *13*, 1552–1557.

(252) Lin, F.; Li, F.; Lai, Z.; Cai, Z.; Wang, Y.; Wolfbeis, O. S.; Chen, X. Mn [II] -Doped Cesium Lead Chloride Perovskite Nanocrystals: Demonstration of Oxygen Sensing Capability Based on Luminescent Dopants and Host-Dopant Energy Transfer. *ACS Applied Materials & Interfaces* **2018**, *10*, 23335–23343.

(253) Fischer, L. H.; Stich, M. I. J.; Wolfbeis, O. S.; Tian, N.; Holder, E.; Schäferling, M. Red- and Green-Emitting Iridium(III) Complexes for a Dual Barometric and Temperature-Sensitive Paint. *Chemistry - A European Journal* **2009**, *15*, 10857–10863.

(254) Kocincova, A. S.; Borisov, S. M.; Krause, C.; Wolfbeis, O. S. Fiber-Optic Microsensors for Simultaneous Sensing of Oxygen and pH, and of Oxygen and Temperature. *Analytical Chemistry* **2007**, *79*, 8486–8493.

(255) Basu, B. B. J.; Vasantharajan, N. Temperature dependence of the luminescence lifetime of a europium complex immobilized in different polymer matrices. *Journal of Luminescence* **2008**, *128*, 1701–1708.

(256) Basu, B. J.; Venkatraman, S. Fabrication of a bi-luminophore temperature sensitive coating by embedding europium thenoyltrifluoroacetonate (EuTTA) and perylene in polystyrene. *Journal of fluorescence* **2009**, *19*, 479.

(257) Sun, L.-N.; Yu, J.; Peng, H.; Zhang, J. Z.; Shi, L.-Y.; Wolfbeis, O. S. Temperature-Sensitive Luminescent Nanoparticles and Films Based on a Terbium (III) Complex Probe. *The Journal of Physical Chemistry C* **2010**, *114*, 12642–12648.

(258) Yu, J.; Sun, L.; Peng, H.; Stich, M. I. Luminescent terbium and europium probes for lifetime based sensing of temperature between 0 and 70 C. *Journal of Materials Chemistry* **2010**, *20*, 6975–6981.

(259) Jorge, P.; Maule, C.; Silva, A.; Benrashid, R.; Santos, J.; Farahi, F. Dual sensing of oxygen and temperature using quantum dots and a ruthenium complex. *Analytica Chimica Acta* **2008**, *606*, 223–229.

(260) Chu, C.-S.; Lin, T.-H. A new portable optical sensor for dual sensing of temperature and oxygen. *Sensors and Actuators B: Chemical* **2014**, *202*, 508–515.

(261) Borisov, S. M.; Neurauter, G.; Schroeder, C.; Klimant, I.; Wolfbeis, O. S. Modified dual lifetime referencing method for simultaneous optical determination and sensing of two analytes. *Applied spectroscopy* **2006**, *60*, 1167–1173.

(262) Stehning, C.; Holst, G. Addressing Multiple Indicators on a Single Optical Fiber—Digital Signal Processing Approaches for Temperature Compensated Oxygen Sensing. *IEEE Sensors Journal* **2004**, *4*, 153–159.

(263) Carraway, E. R.; Demas, J. N.; DeGraff, B. A.; Bacon, J. R. Photophysics and photochemistry of oxygen sensors based on luminescent transition-metal complexes. *Analytical Chemistry* **1991**, *63*, 337–342.

(264) Kalinowski, J.; Fattori, V.; Cocchi, M.; Williams, J. G. Light-emitting devices based on organometallic platinum complexes as emitters. *Coordination Chemistry Reviews* **2011**, *255*, 2401–2425.

(265) Zhao, Q.; Huang, C.; Li, F. Phosphorescent heavy-metal complexes for bioimaging. *Chemical Society Reviews* **2011**, *40*, 2508.

(266) Zhao, Q.; Li, F.; Huang, C. Phosphorescent chemosensors based on heavy-metal complexes. *Chemical Society Reviews* **2010**, *39*, 3007.

(267) Papkovsky, D. B.; O'Riordan, T. C. Emerging Applications of Phosphorescent Metalloporphyrins. *Journal of Fluorescence* **2005**, *15*, 569–584.

(268) Zhao, J.; Wu, W.; Sun, J.; Guo, S. Triplet photosensitizers: from molecular design to applications. *Chemical Society Reviews* **2013**, *42*, Publisher: The Royal Society of Chemistry, 5323–5351.

(269) O'Connor, A. E.; Gallagher, W. M.; Byrne, A. T. Porphyrin and nonporphyrin photosensitizers in oncology: preclinical and clinical advances in photodynamic therapy. *Photochemistry and photobiology* **2009**, *85*, Publisher: Wiley Online Library, 1053–1074.

(270) To, W.-P.; Zou, T.; Sun, R. W.-Y.; Che, C.-M. Light-induced catalytic and cytotoxic properties of phosphorescent transition metal compounds with a d8 electronic configuration. *Philosophical Transactions of the Royal Society A: Mathematical, Physical and Engineering Sciences* **2013**, *371*, Publisher: Royal Society, 20120126.

(271) DeRosa, M. C.; Crutchley, R. J. Photosensitized singlet oxygen and its applications. *Coordination Chemistry Reviews* **2002**, *233-234*, 351–371.

(272) Xuan, J.; Xiao, W.-J. Visible-Light Photoredox Catalysis. *Angewandte Chemie International Edition* **2012**, *51*, Publisher: John Wiley & Sons, Ltd, 6828–6838.

(273) Shi, L.; Xia, W. Photoredox functionalization of C–H bonds adjacent to a nitrogen atom. *Chemical Society Reviews* **2012**, *41*, Publisher: The Royal Society of Chemistry, 7687–7697.

(274) Singh-Rachford, T. N.; Castellano, F. N. Photon upconversion based on sensitized triplet–triplet annihilation. *Coordination Chemistry Reviews* **2010**, *254*, 2560–2573.

(275) Zang, L.; Zhao, H.; Hua, J.; Qin, F.; Zheng, Y.; Zhang, Z.; Cao, W. Ratiometric oxygen sensing using the tunable ratio of phosphorescence to fluorescence emissions from gadolinium porphyrin and porphyrin. *Journal of Luminescence* **2017**, *183*, 452–457.

(276) Zang, L.; Zhao, H.; Hua, J.; Cao, W.; Qin, F.; Yao, J.; Tian, Y.; Zheng, Y.; Zhang, Z. Comparison study on the influence of the central metal ions in palladium(ii)- and gadolinium(iii)-porphyrins for phosphorescence-based oxygen sensing. *Journal of Materials Chemistry C* **2016**, *4*, Publisher: The Royal Society of Chemistry, 9581–9587.

(277) Lowry, M. S.; Bernhard, S. Synthetically Tailored Excited States: Phosphorescent, Cyclometalated Iridium(III) Complexes and Their Applications. *Chemistry – A European Journal* **2006**, *12*, Publisher: John Wiley & Sons, Ltd, 7970–7977.

(278) Evans, R. C.; Douglas, P.; Winscom, C. J. Coordination complexes exhibiting room-temperature phosphorescence: Evaluation of their suitability as triplet emitters in organic light emitting diodes. *Coordination Chemistry Reviews* **2006**, *250*, 2093–2126.

(279) Lindsey, J. S. Synthetic Routes to *meso* -Patterned Porphyrins. *Accounts of Chemical Research* **2010**, *43*, 300–311.

(280) Hutter, L. H.; Müller, B. J.; Koren, K.; Borisov, S. M.; Klimant, I. Robust optical oxygen sensors based on polymer-bound NIR-emitting platinum(ii)–benzoporphyrins. *Journal of Materials Chemistry C* **2014**, *2*, Publisher: The Royal Society of Chemistry, 7589–7598.

(281) Ogilby, P. R. Singlet oxygen: there is indeed something new under the sun. *Chemical Society Reviews* **2010**, *39*, Publisher: The Royal Society of Chemistry, 3181–3209.

(282) Nifiatis, F.; C Athas, J.; Don Dasitha Gunaratne, K.; Gurung, Y.; Mae Monette, K.; Joseph Shivokevich, P. Substituent effects of porphyrin on singlet oxygen generation quantum yields. *The Open Spectroscopy Journal* **2011**, *5*.

(283) Dmitriev, R. I.; Kondrashina, A. V.; Koren, K.; Klimant, I.; Zhdanov, A. V.; Pakan, J. M. P.; McDermott, K. W.; Papkovsky, D. B. Small molecule phosphorescent probes for O2 imaging in 3D tissue models. *Biomaterials Science* **2014**, *2*, Publisher: The Royal Society of Chemistry, 853–866.

(284) Dmitriev, R. I.; O'Donnell, N.; Papkovsky, D. B. Metallochelate Coupling of Phosphorescent Pt-Porphyrins to Peptides, Proteins, and Self-Assembling Protein Nanoparticles. *Bioconjugate Chemistry* **2016**, *27*, Publisher: American Chemical Society, 439–445.

(285) Biscaglia, F.; Gobbo, M. Porphyrin–peptide conjugates in biomedical applications. *Peptide Science* **2018**, *110*, Publisher: John Wiley & Sons, Ltd, e24038.

(286) Redmond, R. W.; Gamlin, J. N. A Compilation of Singlet Oxygen Yields from Biologically Relevant Molecules. *Photochemistry and Photobiology* **1999**, *70*, Publisher: John Wiley & Sons, Ltd, 391–475.

(287) Brauer, G.; Stecher, P. G.; Scripta Technica, i., *Handbook of preparative inorganic chemistry Volume 2 Volume 2*, OCLC: 846979527; Academic Press: New York, 1965.

(288) Tsuji, J.; Guo, H.; Ma, S.; Roman, D. S. In *Encyclopedia of Reagents for Organic Synthesis*, _eprint: https://onlinelibrary.wiley.com/doi/pdf/10.1002/047084289X.rb101.pub3; American Cancer Society: 2015, pp 1–27.

(289) De Pascali, S. A.; Lugoli, F.; De Donno, A.; Fanizzi, F. P. Mutagenic Tests Confirm That New Acetylacetonate Pt(II) Complexes Induce Apoptosis in Cancer Cells Interacting with Nongenomic Biological Targets. *Metal-based drugs* **2011**, *2011*, 763436.

(290) Armarego, W. L. F.; Chai, C. L. L., *Purification of laboratory chemicals*, 5th ed, OCLC: ocm52733960; Butterworth-Heinemann: Amsterdam ; Boston, 2003; 609 pp.

(291) Hoang, T. N. Y.; Humbert-Droz, M.; Dutronc, T.; Guénée, L.; Besnard, C.; Piguet, C. A Polyaromatic Terdentate Binding Unit with Fused 5,6-Membered Chelates for Complexing s-, p-, d-, and f-Block Cations. *Inorganic Chemistry* **2013**, *52*, Publisher: American Chemical Society, 5570–5580.

(292) Chen, S.; Slattum, P.; Wang, C.; Zang, L. Self-Assembly of Perylene Imide Molecules into 1D Nanostructures: Methods, Morphologies, and Applications. *Chemical Reviews* **2015**, *115*, Publisher: American Chemical Society, 11967–11998.

(293) Nagao, Y. Synthesis and properties of perylene pigments. *Progress in Organic Coatings* **1997**, *31*, 43–49.

(294) Zhan, X.; Facchetti, A.; Barlow, S.; Marks, T. J.; Ratner, M. A.; Wasielewski, M. R.; Marder, S. R. Rylene and Related Diimides for Organic Electronics. *Advanced Materials* **2011**, *23*, Publisher: John Wiley & Sons, Ltd, 268–284.

(295) Golshan, M.; Rostami-Tapeh-Esmail, E.; Salami-Kalajahi, M.; Roghani-Mamaqani, H. A review on synthesis, photophysical properties, and applications of dendrimers with perylene core. *European Polymer Journal* **2020**, *137*, 109933.

(296) Daffy, L. M.; de Silva, A. P.; Gunaratne, H. N.; Huber, C.; Lynch, P. M.; Werner, T.; Wolfbeis, O. S. Arenedicarboximide building blocks for fluorescent photoinduced electron transfer pH sensors applicable with different media and communication wavelengths. *Chemistry–A European Journal* **1998**, *4*, 1810–1815.

(297) Duke, R. M.; Veale, E. B.; Pfeffer, F. M.; Kruger, P. E.; Gunnlaugsson, T. Colorimetric and fluorescent anion sensors: an overview of recent developments in the use of 1,8-naphthalimide-based chemosensors. *Chemical Society Reviews* **2010**, *39*, 3936.

(298) Yu, J.; Gao, Y.; Jiang, S.; Sun, F. Naphthalimide Aryl Sulfide Derivative Norrish Type I Photoinitiators with Excellent Stability to Sunlight under Near-UV LED. *Macromolecules* **2019**, *52*, Publisher: American Chemical Society, 1707–1717.

(299) Kumar, M.; Kumar, N.; Bhalla, V.; Singh, H.; Sharma, P. R.; Kaur, T. Naphthalimide Appended Rhodamine Derivative: Through Bond Energy Transfer for Sensing of Hg2+ Ions. *Organic Letters* **2011**, *13*, Publisher: American Chemical Society, 1422–1425.

(300) Weber, S.; Rath, T.; Fellner, K.; Fischer, R.; Resel, R.; Kunert, B.; Dimopoulos, T.; Steinegger, A.; Trimmel, G. Influence of the Iodide to Bromide Ratio on Crystallographic and Optoelectronic Properties of Rubidium Antimony Halide Perovskites. *ACS Applied Energy Materials* **2019**, *2*, Publisher: American Chemical Society, 539–547.

(301) Urstöger, G.; Simoes, M. G.; Steinegger, A.; Schennach, R.; Hirn, U. Evaluating the degree of molecular contact between cellulose fiber surfaces using FRET microscopy. *Cellulose* **2019**, *26*, 7037–7050.

(302) Urstöger, G.; Steinegger, A.; Schennach, R.; Hirn, U. Spectroscopic Investigation of DCCH and FTSC as a potential pair for Förster Resonance Energy Transfer in different solvents. *PLOS ONE* **2020**, *15*, Publisher: Public Library of Science, e0228543.

List of Figures

List of Tables